DESIGN AND MECHANISTIC UNDERSTANDING OF ZEIN NANOCOMPOSITE FILMS AND THEIR IMPLEMENTATION IN AN AMPEROMETRIC BIOSENSOR FOR DETECTION OF GLIADIN

by

Tahrima Binte Rouf

A Dissertation

Submitted to the Faculty of Purdue University

In Partial Fulfillment of the Requirements for the degree of

Doctor of Philosophy

Department of Food Science

West Lafayette, Indiana

December 2019

THE PURDUE UNIVERSITY GRADUATE SCHOOL
STATEMENT OF COMMITTEE APPROVAL

Dr. Jozef Kokini, Chair
Department of Food Science

Dr. Yuan Yao
Department of Food Science

Dr. Carlos Corvalan
Department of Food Science

Dr. Gudrun Schmidt
Department of Chemistry

Dr. Lia Stanciu
School of Materials Engineering

Approved by:
Dr. Arun K. Bhunia
Head of the Graduate Program

Dedicated to my parents Zannatun Nahar and Abdur Rouf, for their infinite love, support and encouragement.

ACKNOWLEDGMENTS

First and foremost, I want to convey my deepest appreciation to my mentor, Dr. Jozef Kokini, a reputable, competent and ingenious scholar, who has enlightened me with his responsible attitude towards research, knowledgeable learning and perceptive ideas, not only in my graduate study, but also in my future career. I am incredibly thankful for his kindness and understanding, for all the time he has devoted to me and for his tremendous support that has led me on this journey to develop my research skills.

I would like to express my heartfelt gratitude towards my PhD advisory committee members, Dr. Yuan Yao, Dr. Gudrun Schmidt, Dr. Carlos Corvalan and Dr. Lia Stanciu. I greatly appreciate their valuable time, constructive comments, and immense support that significantly helped me to accomplish my research goals, improve the quality of the dissertation and overcome the interdisciplinary challenges associated with the work.

I could not have reached this milestone without the unconditional friendship and support of all my lab mates, Hazal, Merve, Luis, Jose, Neslihan, Gamze, Ozlem, Ali, Fei, Xingfei. All of them in one way or another have encouraged me, taught me and pushed me forward, which helped me immensely throughout the process. To my new lab mates Harrison and Cindy, even though the times we spend together were short, I enjoyed the company.

A big thank you to Susana Diaz, who really helped me through the very difficult electrochemical sensor work. I would also like to acknowledge my two undergraduate students Nathalia Olivera and Nathania Dianda, who made my experience as a mentor an enjoyable one, who intellectually challenged me to become a better teacher and researcher and made me proud through their hard work and dedication to research.

My eternal appreciation to my parents Zannatun Nahar and Abdur Rouf, I have accomplished what I am today thanks to your love and guidance. Finally, I want to express my heartfelt thanks to my husband, Arif Mohaimin Sadri, for never giving up on me and giving me the support and encouragement to overcome this challenging period of my life.

TABLE OF CONTENTS

LIST OF TABLES

LIST OF FIGURES

ABSTRACT

Author: Rouf, Tahrima B. PhD
Institution: Purdue University
Degree Received: December 2019
Title: Design and Mechanistic Understanding of Zein Nanocomposite Films and Their Implementation in an Amperometric Biosensor for Detection of Gliadin
Major Professor: Dr. Jozef Kokini

Zein is a major storage protein of corn, with unique amphiphilic film forming properties. It is insoluble in water, but soluble in 70% ethanol and acetic acid, and has been declared 'generally recognized as safe' (GRAS) by the FDA. Due to new advances in food nanotechnology, zein is being investigated for various applications such as biodegradable packaging, oral delivery of proteins and peptides, scaffold for tissue engineering, as well as biodegradable sensor platforms. The time consuming and highly complicated methods for toxin and allergen analysis in the food industry necessitates the need for a rapid, selective, compact and easy-to-use method of detection for analytes. In the scope of this dissertation, we investigated the feasibility of functional zein nanocomposite films and formation of a zein nanocomposite sensor assembly for rapid and highly selective electrochemical measurements of food toxins and allergens. Fabrication of a zein based electrochemical amperometric sensor assembly was studied, first through the comparison of various zein film characteristics changes with the application of Laponite®, graphene oxide and carbon nanotube nanoparticles, followed by a proof-of-concept study by detecting the gluten allergen protein gliadin.

To mechanistically study the functional zein nanocomposite films, Laponite®, a silica nanoparticle, was added in the presence of 70% ethanol solvent and oleic acid plasticizer. The films were studied using various characterization techniques like transmission electron microscopy (TEM), Fourier transform infrared spectroscopy (FTIR), atomic force microscopy (AFM), thermogravimetric analysis (TGA), differential scanning calorimetry (DSC), water contact angle measurements etc. Through Si-N bond formation between Laponite® and zein, fabricated zein nanocomposite films showed increase in surface hydrophobicity, water vapor barrier properties, tensile strength and Young's modulus. Graphene oxide (GO), a carbon nanoparticle, was also incorporated into zein through the solvent casting process. Uniform dispersion of GO nanoparticles within zein matrix were confirmed up to 1% GO loading, and covalent and hydrogen bonding

mechanisms were proposed. Similar to zein-Laponite® (Z-LAP) nanocomposites, zein-GO (Z-GO) showed increase in hydrophobic tendencies, rougher surface and a 300% improvement in Young's modulus and 180% improvement in tensile strength at only 3% GO loading. Both nanoparticles increased tensile strength, thermal stability and water vapor barrier property of the films, indicating a potential for food packaging as an alternative application for the nanocomposite films.

Finally, the research focused on the fabrication of an electrochemical amperometric sensor, capable of detecting the protein gliadin, which is responsible for the allergic reaction with people having celiac disease. Novel biodegradable coatings made from zein nanocomposites: zein-graphene oxide, zein-Laponite® and zein-multiwalled carbon nanotubes (Z-CNT) using drop casting technique were tested for fabricating the electrochemical sensors using cyclic voltammetry (CV), electrochemical impedance spectroscopy (EIS) and square wave voltammetry (SWV) techniques. As Z-CNT produced the strongest signals compared to other nanomaterials, the active tip of the electrochemical sensor was functionalized through a sequence of layer by layer deposition of Z-CNT nanocomposite, antibody and target analyte. Here, Z-CNT acts as a natural linker molecule with large number of functional groups, that causes immobilization of capture antibody and target, to ensure high sensor performance. Both CV curves and SWV curves indicated successful sequential immobilization of gliadin antibody onto the Z-CNT coated electrode. The Z-CNT biosensor was successfully able to give CV signals for gliadin toxins for as low as 0.5 ppm and was highly specific for gliadin in the presence of other interfering molecules, and remained stable over a 30-day period. The low-cost, thin, conductive zein films offered a promising alternative for protein immobilization platforms used in sensors and can be extended to other matrices in biosensors as well as other functional film applications.

CHAPTER 1. INTRODUCTION

Zein, a by-product of ethanol production from corn, that has multifaceted application as a biopolymer due to its free-standing amphiphilic film forming ability, is a strong candidate for environmentally sustainable polymers. Zein has been the material of use in several markets, including, coatings, adhesives, painting, fabrics, plastics and packaging films, since its first commercialized in 1939 [1]. However, usage of zein in several industries have dramatically declined, since the development of cheaper petroleum-based polymers [1-3]. The rising environmental concern due to the use of limited fossil fuel dependent petroleum-based polymers has renewed attention to zein as a twenty-first century industrial biopolymer. Since U.S. is the number one corn producer in the world and more than half of the corn produced in U.S. is for fuel ethanol production, increasing value of zein would also reduce cost of ethanol production [4]. Applying zein to wider implementation sectors as well as enhancing zein properties would therefore improve the quality and demand of zein, motivating the bioethanol industry to develop more efficient and affordable methods of zein extraction.

Developing innovative methods to transform zein protein into more useful commodities, such as eco-friendly biodegradable packaging materials or reusable biological detectors, will expand the use of zein and minimize environmental and economic concerns. Even though zein has multidimensional film forming properties, the brittle nature of the zein films can be a drawback, which can be compensated by using plasticizers and/or different functional nanomaterials. In-depth discussion related to the previous studies of zein, zein structure, effect of solvent, plasticizer and nanomaterial addition, as well as current and potential future applications for zein have been presented in chapter 2. A potential candidate for zein functionalization is graphene oxide, which is well-known for its functionalizing properties towards various biopolymers. Chapter 3 provides an in-depth review of the various biopolymer-graphene oxide nanocomposite studies, and the effect of solvent polarity as a driving factor for efficient nanocomposite fabrication.

The first objective of this study was to investigate the effect of Laponite®, a silica nanoparticle, addition on the mechanical, thermal, barrier and surface properties of zein films. Laponite® is a GRAS material known for its functionalizing properties and use in biomedical applications. To understand the underlying chemistry of nanocomposite formation and examine

the films for value added applications, the films were studied using an array of various spectroscopic techniques. Findings from the zein-Laponite® nanocomposite study has been presented in Chapter 4, which discussed the possible mechanism for binding of zein with the silicate clay, as well as, the chemistry for various property enhancement of zein as a result of nanocomposite formation.

Graphene oxide (GO), which is an oxidative form of graphene, is also a material of interest due to formation of durable, lightweight polymer and biopolymer nanocomposite. The second objective of this study was to functionalize zein with a GO nanomaterial and thoroughly examine the effects of nanomaterial addition on the overall properties of zein. In chapter 5, detailed investigation was undertaken to study the changes in thermal, mechanical, barrier and surface properties of zein-graphene oxide nanocomposites, propose a nanocomposite formation mechanism as well as to understand the binding techniques of zein, plasticizer and the nanomaterials.

In recent years, innovative work in the area of biosensors have increased interest for their beneficial properties as analytical instruments, particularly, their potential for scaling down, low-cost, portability and user friendliness, compared to other conventional lab-based techniques [5, 6]. However, efficient disposal and waste management of these non-biodegradable sensors can become an issue for mass-scale, every-day-use applications. Researchers are currently facing the challenge to find multipurpose sustainable biosensors that are inexpensive and offer implantability. To conquer these difficulties scientists concentrated their attention towards biodegradable biopolymer nanocomposites-biosensors. In this dissertation, zein was investigated as a potential platform for biodegradable biosensor development.

The various functional groups present in zein can act as an anchoring molecule for the biological element (antibody) against a specific target analyte. The electrochemical signal resulting from the capturing of target by antibody immobilized by zein can be used to detect the presence of analyte in food materials. In order for the detection method to be highly sensitive, the electrochemical signal produced from zein sensor platform needs to be of high intensity. Since zein is an insulating polymer, it is highly critical to improve the conductive property of zein through the addition of conductive nanoparticles. Therefore, the third objective of this research was to enhance the conductive property of zein through addition of graphene oxide, Laponite® and carbon nanotubes, and to optimize design and fabrication of an electrochemical sensor. In this

research, an electrochemical method namely cyclic voltammetry (CV) was used for the electrochemical detection. Upon incubation of the antibody functionalized sensor assembly in target solution, the cyclic voltammogram changes considerably with a decrease of oxidation peak current and an increase of reduction peak current, hence, the electrochemical signal could be utilized as an effective biosensor for target recognition. The fourth and final objective of this study was to use the as-fabricated zein nanocomposite sensor for the detection of gliadin, a food toxin responsible for allergic reaction in patients suffering from celiac disease. Since continuous ingestion of gliadin in celiac disease patients can cause allergic response leading to a large number of complications, such as growth retardation in children, decreasing bone mineral density in patients with osteoporosis, and miscarriage and infertility in women, continuous monitoring of the gluten levels in the product lines of food industry is crucial. Zein-CNT platform was utilized for direct detection of gliadin solutions at different concentrations to obtain a calibration curve. In chapter 6, the outcomes of this study have been thoroughly discussed in an impactful manner to utilize the findings and extend application in other aspects of sensor and functional film research.

CHAPTER 2. LITERATURE REVIEW

2.1 Zein

Zein is a prolamin of corn, which can be found in the rough endoplasmic reticulum of the corn kernel. Zein constitutes 50-70% of the whole protein body and is insoluble in water, but soluble in other solvents like 70% ethanol or acetic acid. Since its discovery by Gorham in 1821 [7], it has mainly been used as an industrial polymer and it started being commercially produced in 1939 [3]. Corn processing by-products e.g. corn gluten meal (CGM), distillers dried grains (DDG), distillers dried grains soluble (DDGS) and corn gluten feed (CGF) are some of the protein-rich sources for zein extraction [3].

Zein can be divided into α-zein, β-zein, γ-zein, and δ-zein, based on their molecular weights and varying amino acid compositions, as seen in **Table 2.1**. [8]. Based on these differences the organization of the protein body can change and also affect the extractability [9]. The most abundant subfraction of zein is α-zein, which constitutes 70% of the protein, followed by γ-zein which constitutes 20%, while the remaining 5-10 % is comprised of both δ and β -zein. As α-zein is the most abundantly found zein fraction, it has been thoroughly studied. Recently γ-zein has also become the focus of research due to its rich concentration of cysteine amino acids [10-12]. Due to α-zein being abundant and well-studied, it was chosen for the nanocomposite formation and sensor assembly fabrication work in this research.

Table 2.1. Amino acid profile of zein protein subfractions.

Amino Acids (% mol)	α-zein		γ-zein		β-zein	δ-zein	
	19 kDa	22 kDa	16 kDa	27 kDa	15 kDa	10 kDa	18 kDa
Alanine (Ala)	14.6	13.7	7.9	4.9	13.8	5.5	5.4
Arginine (Arg)	1.2	1.0	1.8	2.5	3.1	0.0	0.0
Asparagine (Asn)	4.7	3.9	0.6	0.0	1.9	2.4	1.1
Aspartic Acid (Asp)	0.0	0.0	0.0	0.0	0.6	0.8	0.5
Cysteine (Cys)	1.2	1.0	7.3	7.4	4.4	3.9	1.6
Glutamine (Gln)	19.3	16.6	18.9	1.0	16.2	11.8	8.6
Glutamic Acid (Glu)	0.6	0.5	1.8	14.7	1.9	0.0	0.5
Glycine (Gly)	1.2	1.5	9.1	6.4	8.8	3.1	2.7
Histidine (His)	1.2	0.5	2.4	7.8	0.0	0.0	1.1
Isoleucine (Iso)	4.1	4.9	0.6	2.0	0.6	4.7	4.9

Table 2.1. Continued

Amino Acids (% mol)	α-zein		γ-zein		β-zein	δ-zein	
	19 kDa	22 kDa	16 kDa	27 kDa	15 kDa	10 kDa	18 kDa
Leucine (Leu)	19.9	17.6	8.5	9.3	10.0	9.4	5.4
Lysine (Lys)	0.0	0.5	0.0	0.0	0.0	0.0	0.5
Methionine (Met)	0.0	1.5	1.8	0.5	11.2	22.8	26.9
Phenylalanine (Phe)	4.7	7.3	4.3	1.0	0.0	3.9	2.7
Proline (Pro)	11.1	9.8	15.2	25.0	8.8	15.7	17.2
Serine (Ser)	7.6	7.8	5.5	3.9	5.0	6.3	9.1
Threonine (Thr)	1.8	4.4	3.7	4.4	2.5	3.1	5.9
Tryptophan (Trp)	0.0	0.0	0.6	0.0	0.0	0.0	1.1
Tyrosine (Tyr)	4.1	3.4	4.9	2.0	8.8	0.8	1.6
Valine (Val)	2.9	4.4	4.9	7.4	2.5	3.9	3.2

2.2 Zein Structure

One of the earliest and most well-known study on the structural model for zein was conducted by Argos et al. [13], who investigate the secondary structure, as well as the amino acid sequence of α-zein using circular dichroism (CD). Using far UV light as the light source and 70% methanol as the solvent, they identified the secondary structure of zein, having approximately 59% α-helix, 41% β-turn and 0% β-sheet structures. Later studies by other researchers agreed on the high helical content but disagreed on the 0% β-sheet structures. Argos et al. [13], proposed that zein constitutes of rod-like structures formed by 9 repeat sequences of α-helices organized in an antiparallel fashion, linked together by polar glutamine turns, as shown in **Fig. 2.1**(a). While the turns are mainly comprised of polar glutamine amino acids, the 9 helices are composed of non-polar leucine, alanine and proline amino acid residues. Based on the number of amino acids in C-terminus, α-zein was further classified into two subfractions 19kDa and 22kDa, whose C-terminus has the larger number of amino acids. Garrett et al. 1993 applied statistical modeling, and found results in agreement with Argos et al. [13] regarding zein having antiparallelly connected hydrophobic helices [11]. They reported that both 22 kDa and 19 kDa α-zein have identical length in the C-terminus, however, an additional tenth unit is formed in the 22 kDa α-zein. The researchers proposed a triangular or a hexagonal net structure, and declared Argos's circular wheel model inaccurate. Nevertheless, both studied proposed an overall globular shape of α-zein in 70% methanol [13, 14].

Tatham et al. [15], used 70% methanol solvent and applied CD using far UV range wavelength and reported a 50% α-helix content, akin to Argos et al.'s study [13], but proposed a different dimensional ratio (9.9 nm x 0.35 nm) of zein prolate ellipsoid structure. While studying the purity of α-zein extracted from corn flour using CD, Cabra et al. [16], reported a 56% α-helix for α-zein and a 40% α-helix content for Z19 zein in 70% aqueous methanol. Although the α-helices percentage was similar to Argos et al.'s study [13], the β-sheet contents (7% for α-zein) were not similar at all and rather showed consistency with the study by Tatham et al. [15]. In addition, the random coil structure of α-zein and pure Z19 were reported to be 8% and 15.4% respectively, but β-turns were not mentioned and reported as "undetermined" structures [16].

Matsushima et al. [17] investigated the structure of α-zein solubilized in 70% ethanol using small angle x-ray scattering (SAXS) and dismissed the globular structure of zein and reported a linear model [17]. SAXS also confirmed that helical repeat units are connected by glutamine rich turns, and a tenth repeat unit is present in the 22 kDa fraction, as shown in **Fig. 2.1** (b).

Based on amino acid sequence and all the previous zein secondary structure analysis, Li et al. [18] used SAXS and CD to propose a model for zein in acetic acid solution. An oblate ellipsoid shape for Z19 component of α-zein was proposed with folded dimensions of c = 2.3, b = 4.5 nm and a = 5.9 nm, while a globular shape for Z22 was reported with dimensions of c = 3.4 nm, b = 5.0 nm and a = 5.8 nm as shown in **Fig. 2.1** (c). SAXS results indicated that the scaling behavior of zein in acetic acid solution is similar to that of a rod-like molecule [18].

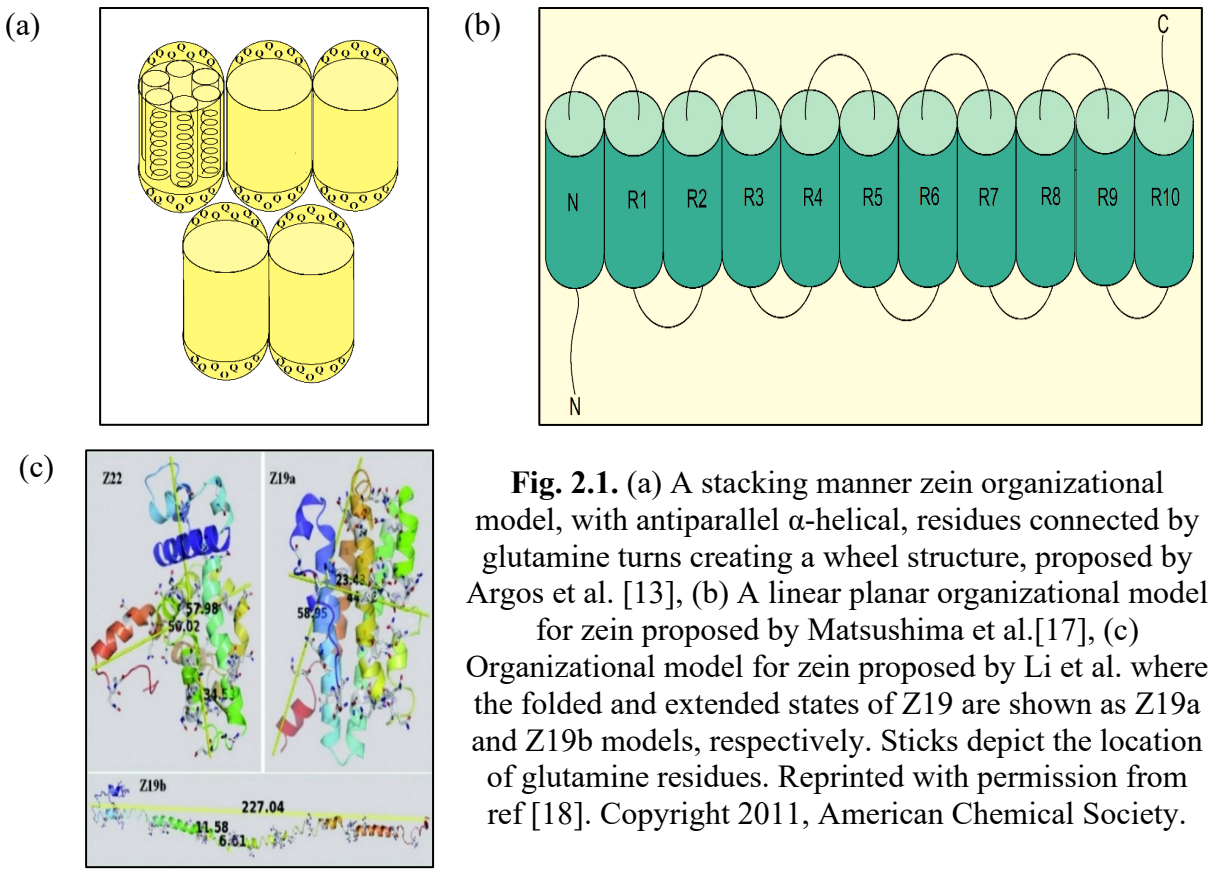

Fig. 2.1. (a) A stacking manner zein organizational model, with antiparallel α-helical, residues connected by glutamine turns creating a wheel structure, proposed by Argos et al. [13], (b) A linear planar organizational model for zein proposed by Matsushima et al.[17], (c) Organizational model for zein proposed by Li et al. where the folded and extended states of Z19 are shown as Z19a and Z19b models, respectively. Sticks depict the location of glutamine residues. Reprinted with permission from ref [18]. Copyright 2011, American Chemical Society.

Later studies [15, 18–20] all build upon the previous models by Argos and Matsushima, and they all agree on the basic structure of zein with hydrophobic helices connected by glutamine turns [21]. Other than this, the studies cannot agree on any other aspects, and this difference of opinion can be attributed to the variety of sources of corn as well as the difference in extraction and sample preparation methods. In order to completely comprehend the role of chemical changes in zein, it is crucial to understand the structure of zein, hence the well-established models of zein Argos et al. 1982 [13] and Matsushima et al. 1997 [17], as well as, the most recent study by Li et. al [18] were the basis for zein structure and nanocomposite formation discussion in this work.

2.3 Zein Films: Effect of Solvents, Plasticizers and Nanomaterial Addition

Zein's unique amphiphilic film forming property enables it to be utilized for various applications. As zein comes from a natural food source, FDA has declared zein to be generally recognized as safe (GRAS). Unfortunately, zein's insolubility in water and its shortage of

fundamental amino acids, for example, tryptophan and lysine makes zein unsuitable for human consumption. During the 1950s, zein had become largely well-known, and it was used in various coatings, as well as sold in a fiber form called 'Vicara', as a replacement of silk. In recent years zein has found application as animal feed, pharmaceutical coatings and packaging material [8]. Zein has also been the focus of many research projects, where its application varied from encapsulating nanoparticles [22] to colloidal suspensions [23] to research focusing on zein's film forming properties [24]. Zein needs to be dissolved in a suitable solvent for almost all of these applications, and for many of these applications a physical modification or chemical modification is required. Therefore, a thorough understanding of the changes in zein conformation in solution as well as in presence of different additives like plasticizers, nanofillers is necessary.

The effect of different types of solvents, solvent concentration, temperature and pH have been studied using FTIR, CD, AFM etc. [25]. In the secondary structure analysis of proteins, peaks between 1610–1640 cm^{-1} indicate β-sheets, peaks between 1640–1650 cm^{-1} indicate random coil, while α-helix and β-turns structures give characteristic peaks around 1650–1660 cm^{-1} and around 1660–1700 cm^{-1} respectively. When ethanol and isopropanol was used as solvents for zein, random coil structures decreased to zero, while α-helix increased. Higher %β-turn was observed for isopropanol compared to ethanol. As α-helix structures are linked through hydrophilic glutamine turns [13, 17], therefore increasing β-turns increases the surface hydrophilicity of the films [26, 27]. During zein film preparation, raising the concentration of alcohol up to 90% (v/v), resulted in optimized protein molecule electrostatic interaction, which increased tensile strength. However, increasing alcohol concentration over 90% (v/v) resulted in electrostatic repulsion, causing reduced tensile strength of films. Another study showed reducing alcohol concentration below 50% (v/v), could also cause electrostatic repulsion, evidenced by a −46.0 mV zeta potential [25]. Studies have also shown that, increasing alcohol concentration up to 90% caused increased water vapor barrier properties, as the up to this concentration

In another study by Bugs et al. [29], the CD results displayed when water content is increased to 72% in a water/ethanol solution for zein, α-helix content only showed slight change, owing to the main-chain hydrogen bonds in the secondary structure being protected from the solution, therefore preventing any alteration. Using CD, the researchers showed that when 70% ethanol is used as a solvent for Z19, at pH 6 or higher, a negative charge is observed which favors α-helix formation, but at lower pH from 3 to 6, α-helix decreased and β-tuns and random coils increased.

Guo et al. [30] studied the effect of zein concentration and the drying technique on the topography of the zein molecules and their orientation, by studying zein in 70% water-ethanol solution air dried over mica surface using AFM. They reported that, zein exhibited globular structures with 150 to 550 nm diameter range at higher concentration, whereas at lower conc. (1 μg/mL) they displayed more homogenous distribution of diameter, as shown in **Fig. 2.2**. Some rod like structure and doughnut like structure (which resulted from merging of rod like structures) were also observed, which increased with rapid drying and decreased when drying rate was slowed down. The mechanism of zein film formation can be explained through increased concentration of zein with solvent evaporation which leads to more hydrophobic interactions, disulfide bonding, and hydrogen bonding between zein molecules.

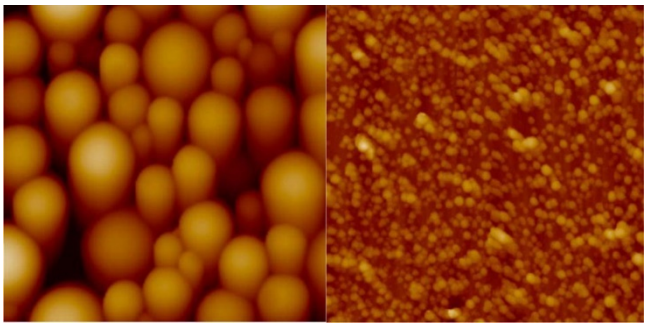

Fig. 2.2. Surface topography using AFM, for characterization of 70% ethanol solvent cast zein on mica substrate (left: concentrated, right: diluted). Reprinted from ref [30], Copyright 2005, with permission from Elsevier.

AFM was also used to investigate the effects of solvents on the surface morphology of zein films fabricated using the spin coating method [26]. When zein dissolved in acetic acid is spin coated, the positive charge of the glutamine turns cause the zein molecules to orient themselves horizontally on the negative silicon surface causing a smoother topography, as seen in **Fig. 2.3** (a). On the other hand, when zein is dissolved in 95% ethanol the overall charge of glutamine turns are negative, and zein molecules are oriented vertically on the negative silicon platform resulting in a rougher surface, as seen in **Fig. 2.3** (b). The higher surface roughness leads to a decreased water contact angle, making the surface more hydrophilic.

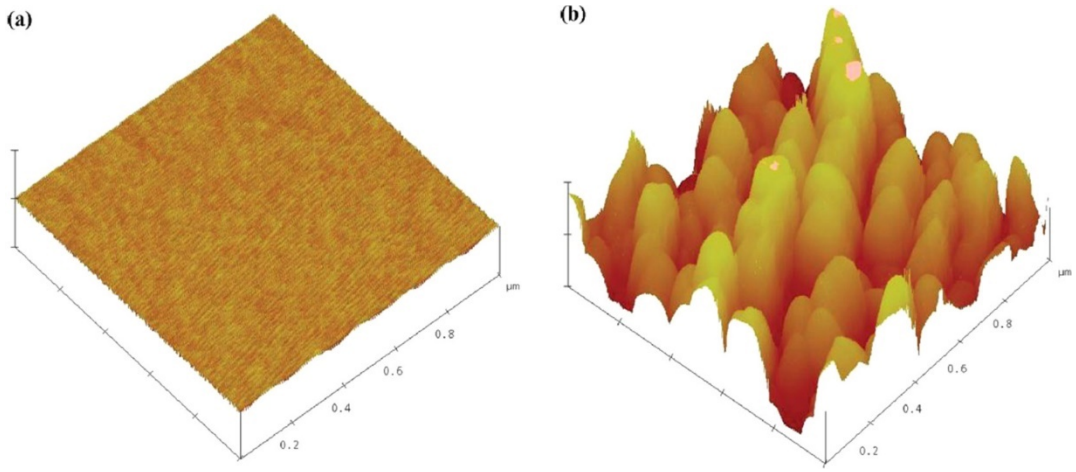

Fig. 2.3. Surface topography characterization using AFM (a) glacial acetic acid solvent cast zein films and (b) 95% aqueous ethanol solution cast zein films. Reprinted with permission from ref [26]. Copyright 2009 American Chemical Society.

Zein films are highly brittle and usually needs some form of plasticization in different applications, and thus understanding the molecular interaction between the plasticizer and zein can be of great use for zein application research. In a study that compared different plasticizers for zein [31], showed that in a glycerol plasticized zein film, hydrogen bonding takes place between the water and glycerol with the amide groups of zein, which can be detected through FTIR. On the other hand, when 2-mercaptoethanol is used, it breaks the disulfide bonds of zein to create a linkage which is undetectable in FTIR [31]. Another study showed that addition of glycerol plasticizer increases the free volume and random coil structure formation through significantly decreasing the β-turn fraction [25]. The study also showed up to 20% (w/w) addition of glycerol, increased % elongation at break by 20% and tensile strength increased by 40 MPa. This finding correlates with the free volume theory, as increased free volume allows more mobility in the polymer, granting higher degree of elongation under the same level of stress. However, above 20% loading, the tensile strength starts to drop, hence the 20% glycerol content can be considered as the critical plasticization point [32].

In the study by Athamneh et al., critical glycerol plasticization point for zein was found at around 16% w/w, when the secondary structure developed an opposite trend [32]. The study showed that, initially glycerol plasticization increases %β-sheet, until the critical plasticization point has been reached, then β-sheet decreases with increasing glycerol concentration. Glycerol

cluster formation at the binding sites of glycerol and zein, reinforces zein-glycerol linkage and improves the tensile strength of the films.

The combined and individual plasticization effect of glycerol and oleic acid on zein films' mechanical properties were explored by Xu et al. [33]. Zein secondary structure remained unaffected by the varying ratio of plasticizers as seen from the FTIR results. As the ductility of zein films was not related to increasing content of β-sheet and decreasing of α-helix, the authors proposed that a plasticization by glycerol and oleic acid took place through alteration of zein supramolecular structures.

Oleic acid plasticized zein films were studied using SAXS and WAXS to understand the plasticized zein structure [34] Inter-helices d-spacing were raised due to oleic acid, which was utilized to propose diverse structural models for zein-oleic acid resin films, that discussed either tetrameric zein aggregates or two layer zein aggregates separated by oleic acid bilayers.

To further improve the properties of plasticized zein films, and make them more competitive, researchers have explored addition of different nanomaterials like nanoparticles, nanotubes, nanoclay to zein films. The organization and dispersion of these additives in zein films is often relevant and needs in-depth study.

Luecha et al. have studied the addition of montmorillonite clay (MMT) to zein films through solvent casting and film blowing extrusion technique as shown in **Fig. 2.4** (a) [35]. TEM showed complete exfoliation of the nanoclay in both solvent cast and extruded films. Visual observation of the solvent cast films as shown in **Fig. 2.4** (b) and blown extrusion films in **Fig. 2.4** (c) shows that addition of MMT does not affect the translucency of the films and both types of films give a glossy yellowish appearance. The XRD showed that in both types of film preparation methods the MMT peaks disappeared when added to zein, which also is an indication of complete and uniform dispersion. Increasing the amount of MMT failed to enhance tensile strength and barrier properties of the films in a linear manner. However, MMT successfully improved the thermal stability of both types of films.

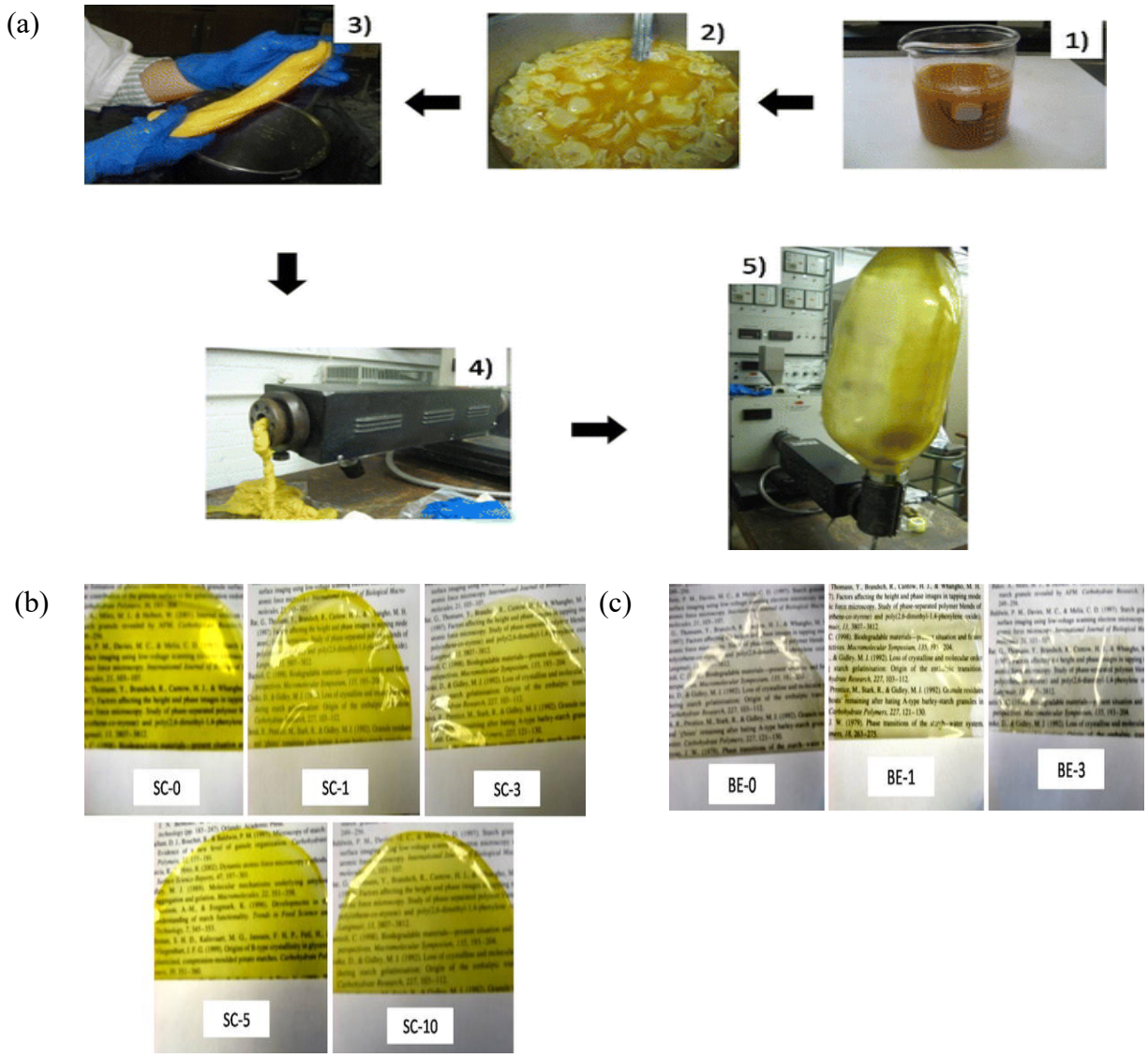

Fig. 2.4 (a) Film blowing extrusion technique steps showing solubilized zein containing MMT (step 1), precipitation of the solution (step 2), formation of zein-MMT resin (step 3), cold extrusion (step 4), and formation of zein-MMT balloon (step 5). (b) Visual observation of solvent cast (SC) zein MMT nanocomposite films with 0%, 1%, 3%, 5% and 10% MMT loading (c) Visual observation of blown extruded (BE) films with 0%, 1% and 3% MMT loading. Reprinted by permission from Springer Nature Customer Service Center, Springer, Journal of Materials Science, ref [35], Copyright 2010.

In a study investigating the effect of MMT nanoclay on zein nanofiber mats showed that, coexisting intercalated MMT layers as indicated by TEM and XRD, are responsible for the increase in thermal stability and hydrophilicity. Compared to the zein films contact angle of 74°, the contact angle of the nanofiber mats increased up to 133°, due to the nanofibrous network

structure. With further addition of MMT, the contact angle went down to 95° indicating a more wettable surface, widening the application fields for the zein-MMT nanofiber mats [36].

Manisara and Parichat, extracted cellulose microfibrils (CMF) from banana peels using acid hydrolysis, creating nanofibrils of 26nm diameter which was then used to functionalize zein films with glycerol plasticizer [37]. The addition of up to 4 wt% CMF gave the highest tensile strength and Young's modulus, but the films became rougher and elongation at break reduced.

In a similar study [38], magnetic iron oxide nanoplatelet loaded zein resin films were fabricated. The XRD results confirmed successful preparation and dispersion of nanofillers due to the observation of highly ordered and exfoliated nanocomposites. The variations in intensities between the XRD spectra of exfoliated and highly ordered nanocomposites demonstrated improved orientation of nanofillers within the zein matrix. The nanocomposites' gas permeability properties are lower than zein-only films, where highly ordered nanocomposite showed the lowest permeability. In addition, improved nanoplatelets orientation increased the nanocomposite elasticity as shown in **Fig. 2.5**.

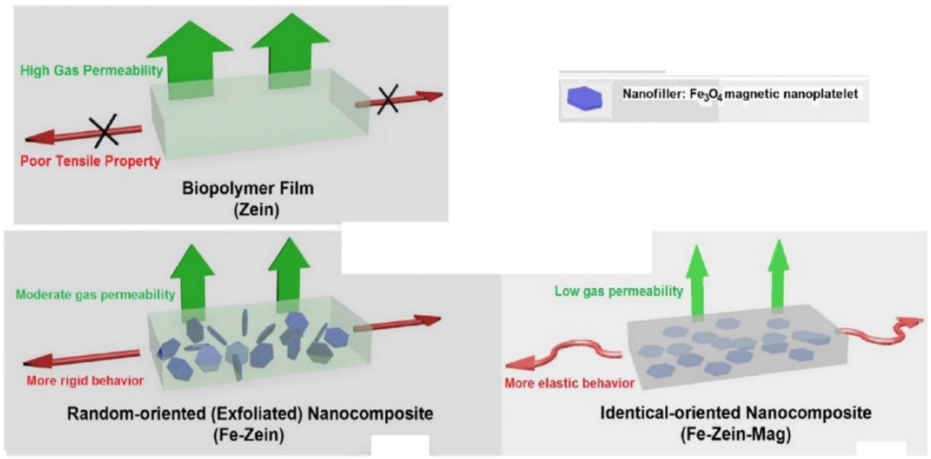

Fig. 2.5. Control and nanocomposite zein films. Reprinted with permission from ref [38]. Copyright 2012, American Chemical Society

The functional zein films produced from plasticization, as well as nanomaterial addition showed great potential for packaging due to increased barrier and tensile properties. Due to its biocompatibility, amphiphilic nature and adhesive film forming properties, zein nanocomposites and nanostructures can also be implemented in other application fields like biomedical and sensor research.

2.4 Zein Application: Scaffolding, Microfluidic Devices and Optical Sensors

In the biomedical field, wound dressing is a very critical component in the healing cycle because careful wound treatment will speed up wound recovery. Electrospun zein nanofibrous mats with diameters ranging from 350–500 nm were functionalized with silver (Ag) nanoparticles for wound dressing application, which showed excellent antibacterial performance against Escherichia coli (E. coli) and Staphylococcus aureus (S. aureus). The zein/Ag mats were characterized using FE-SEM, TEM and XPS, and exhibited uniform fibrous structure, effective adhesion of cells as well as good cytocompatibility. Hence the nanomats proved to be an excellent candidate for wound dressing applications for the synthesis of new bactericides. [39]

When biomaterials are used in artificial blood prostheses, blood compatible surfaces need to be engineered to reduce platelet surface interactions and enhance the foreign substance's thromboresistance. Electrospun zein-single wall carbon nanotubes (SWCNTs) fibrous nanocomposite scaffolds demonstrated hydrophilicity and antithrombogenicity [40]. SEM and TEM tests showed highly smooth uniform zein nanofibers with different loadings (0.2wt % -1 wt%) of SWCNTs. TGA showed increased thermal stability, while retention ability and water uptake of composite scaffolds decreased with increasing concentration of SWCNTs. The novel Zein-SWCNTs composite scaffolds showed potential application for a promising biomaterial and antithrombotic material for tissue engineering application, due to its platelet adhesion ability and hemolytic property.

Thin zein films with microfluidic chambers and channels using standard stereo lithography and soft lithography techniques were fabricated for the application of disposable green microfluidic device for biomedical and agriculture applications [24]. Ethanol vapor deposition technique was applied to create zein-zein and zein-glass adhesive surfaces with little to no trapped air and minimal shape deformation. A Rhodamine B solution concentration gradient through an interlinked letter stream (**Fig. 2.6** (a)), a microfluidic stream and chamber network (**Fig. 2.6** (b)), and a solved microfluidic maze with numerous false microfluidic network routes (**Fig. 2.6** (c)) can be seen. Zein's simplicity of procurement and bonding, as well as, flexibility and moldability grant great opportunities for design and manufacturing of microfluidic devices from eco-friendly materials that are non-dependent upon limited petroleum-based polymers.

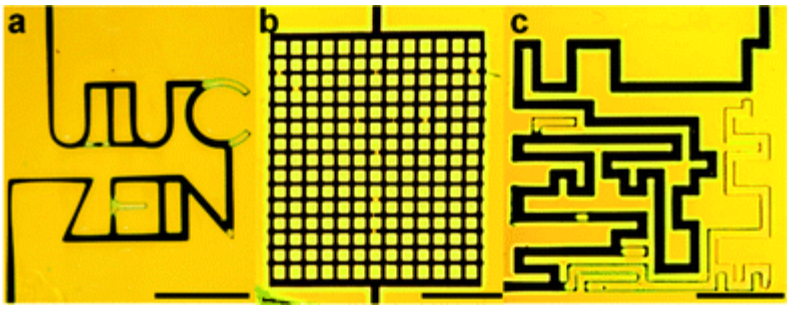

Fig. 2.6 (a) A Rhodamine B solution concentration gradient through an interlinked letter stream (b) a microfluidic stream and chamber network, and (c) an alleviated microfluidic maze with numerous false microfluidic network routes. Reproduced from Ref. [24] with permission from The Royal Society of Chemistry, Copyright 2011.

A nanophotonic gold coated platform made from zein was used to detect the main allergen protein, Ara h1 using surface enhanced Raman spectroscopy (SERS) [41]. The step-by-step manufacturing process schematics of zein-SERS detectors are shown in **Fig. 2.7**. Highly selective platforms were fabricated by functionalizing the zein SERS platform with monoclonal ara h1 antibody. Using a statistical clustering technique principal component analysis (PCA), the limit of detection was determined to be 0.14 mg/ml, which proved zein's feasibility as a platform for optical sensors using surface enhanced Raman spectroscopy. Biodegradable zein/gold SERS platform was also tested for the detection of acrylamide, by identifying a unique characteristic SERS peak at 1447 cm^{-1}[42].The detection range for acrylamide was between 10 mg/ml to 10 µg/ml, and limit of detection was 10 µg/ml, once again proving the applicability of zein as a biodegradable optical sensor platform for the detection of food toxins and pathogens found in food samples.

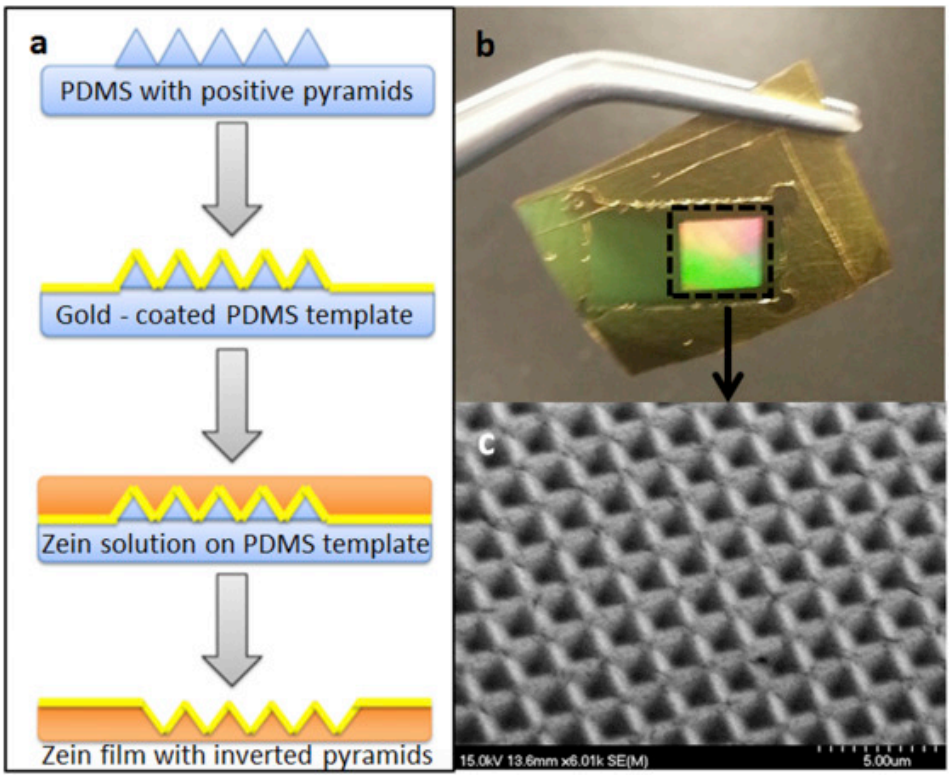

Fig. 2.7 (a) Manufacturing process schematics of zein-SERS detectors. PDMS has been used as a model for positive pyramid frameworks. Zein solution was poured on the structure after being gold coated with an e-beam evaporator. Upon drying at ambient temperature inside a desiccator, zein films are stripped to give inverted gold-coated pyramid structures. (b) Macroscopic image of zein-SERS sensor on gold-coated side, where the squared area shows location of nanophotonic patterns. (c) SEM images of the inverted pyramid structures. Reprinted from ref [42], Copyright 2016, with permission from Elsevier.

Although there are some notable studies on zein as a biodegradable platform for optical sensors and microfluidic devices, with its insulating properties, zein can act as an insulating layer in electrochemical biosensors and due to its various functional groups like $-CH_3$, -COOH and $-NH_3$ groups it can even play a bigger role as an immobilizing platform for capturing biorecognition elements in different electrochemical biosensors.

2.5 Electrochemical Biosensors

A biosensor is a diagnostic tool utilized for the recognition of an analyte, that consolidates a biological element capable of recognizing the target analyte and a physicochemical detector which generates a signal, proportion to the concentration of the target. The sensitive biological

component can be any biological material derivative that interacts, e.g. antibodies, cell, microorganisms, tissue etc. and recognizes the analyte being studied. Nano-biotechnology has been a significantly novel procedure to build straightforward and dependable monitoring frameworks for food safety. Because of the large variety of molecular species connected to food safety, the qualities of sensors must be constructed depending on the food source, target analyte concentration distribution, the particular response, and simplicity of application. Nanomaterials help in further improving the conventional benefits of electrochemical biosensors, for example, immediacy, simplicity of fabrication and field applicability. Moreover, nanomaterials enrich electrochemical biosensors with device miniaturization, as well as, increased specificity and sensitivity, giving them incredible potential to evaluate on-site food safety monitoring. With the advancement of present-day agriculture and the food industry, there is a drastic increase in food variety and quantity. Consequently, food safety holds extraordinary socioeconomic impact and pulls in worldwide consideration. There is a great variety and complexity of molecular species concerning food safety [43]. Particularly, food safety is threatened by use of illegal additives, pesticides, pathogens, organic compounds, heavy metals and toxins. These species can result in foodborne diseases, seriously affect human health, not to mention the income of various food companies. The expanding interest for rigorous monitoring and testing of hazardous materials in food prompts a boom in the food safety sensor research. Instrumental simplicity, portability and low cost are some of the benefits of modern electrochemical biosensors. Voltammetric techniques, encompassing cyclic voltammetry (CV) [45], square wave voltammetry (SWV) [46], differential pulse voltammetry (DPV) [45] and linear sweep voltammetry (LSV) [45] have been extensively implemented in food safety analysis. Another technique that has recently garnered attention is the electrochemical impedance spectroscopy (EIS).

One of the most common technique used in electrochemistry to routinely examine the electrode performance and identify transfers of electron related to biofilms or microbial cells, is cyclic voltammetry (CV) [44]. Usually in CV, the electrochemical cell consists of a three-electrode system, which are immersed in the electrolyte solution containing the molecule of interest as shown in **Fig. 2.8** (a). The anode or cathode can also be combined with the analyte and acts as the working electrode. The counter electrode observes the current change in the working electrode and passes the necessary current needed to restore balance (e.g., platinum wire); a reference electrode,

serves as a tool in quantifying the potential of working electrode (e.g., Ag/AgCl) and it does not pass any current [44].

Voltammetry is a sensitive analytical technique that informs us about a given analyte's thermodynamics and electron transfer kinetics. To understand the electrochemical process, we can consider that simplest possible voltammetric experiment which involves a simple redox reaction between the electrode and electrolyte solution (equation 1), and diffusion of electroactive substances:

$$Red_{sol} \rightleftarrows Ox_{sol} + ne^{-} \ldots\ldots\ldots (1)$$

Where, sol = dissolved species, n = stoichiometric number of electrons. The electron transfer results in the change of potential, if the change in the potential of the electrode is measured in one direction, then the experiment is referred to as linear sweep voltammogram, but if the electrode potential change is measured in forward and reverse direction (**Fig. 2.8** (b)), then after the potential reaches a certain value it stops and continues in reverse direction and returns to the starting potential, creating a cycle, hence the name cyclic voltammetry (CV) [45], and the resulting voltammograms are shown in **Fig. 2.8** (c).

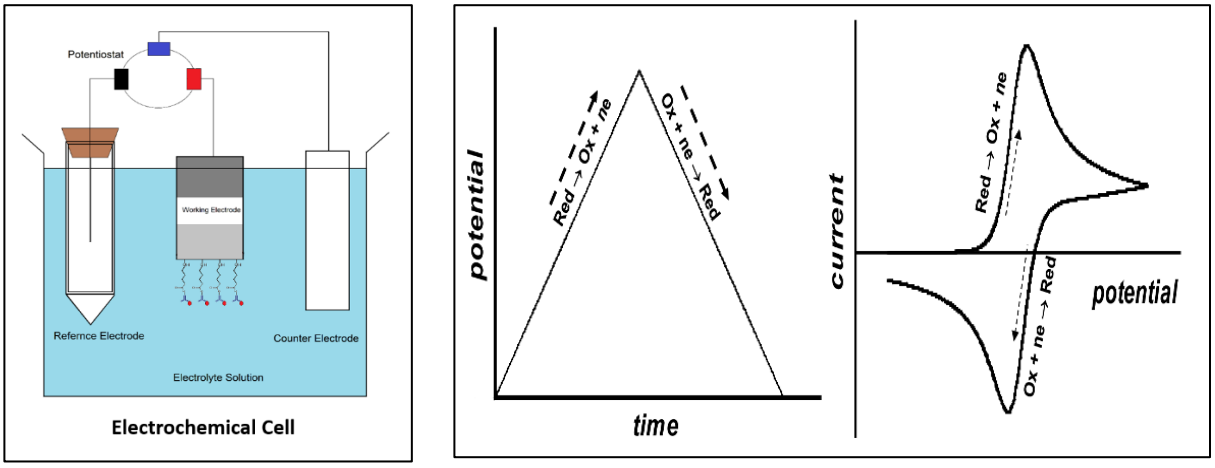

(a) (b) (c)

Fig. 2.8. (a) Typical three electrode electrochemical cell (b) Standard diagram for variation of potential and (c) Ideal model for I–E curve in the cyclic voltammetry technique. Reprinted by permission from Springer Nature Customer Service Center, Springer, ChemTexts, ref [45] Copyright 2018.

Cyclic voltammetry is a very useful technique for measuring electrochemical properties of different materials in solution or thin film where, the films are coated on the electrode. It is a fairly straightforward and simple technique that allows one to detect relative electrochemical potentials with an internal standard as long as the analytes show reversible redox behavior. Primarily CV is used to obtain information for battery applications and for organic electronics, CV can be used to obtain information on frontier orbital energy levels of various materials. [46]

To achieve a higher sensitivity, a continuous potential ramp in cyclic voltammetry (**Fig. 2.8**(b)) can be replaced with a potential-time staircase feature (**Fig. 2.9** (a)), where the current can be determined at the end of each potential phase, the input of charging current can be removed and the reliability and responsiveness of voltammetric data significantly enhanced [45]. At the end of each forward and reverse pulse, the current values are the forward (I_{for}) and reverse (I_{rev}) components of a voltammetric reaction (**Fig. 2.9** (b) and (c)), called the square wave voltammetry, which is an advanced form of cyclic voltammetry.

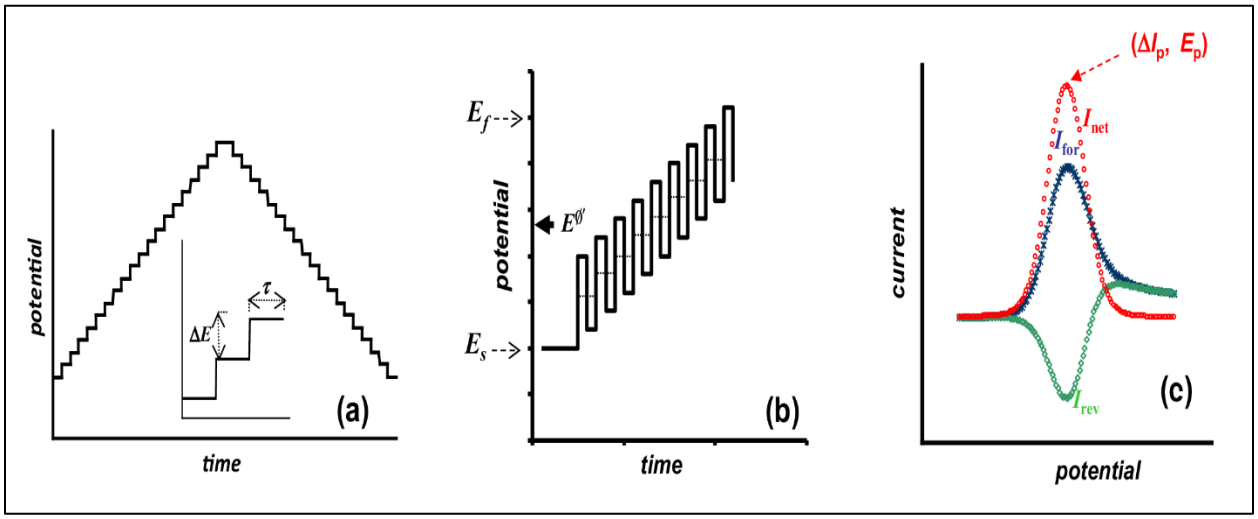

Fig. 2.9 (a) Cyclic staircase voltammetry producing a typical Potential wave-form. In inset τ = potential step duration and ΔE = staircase potential scan increment; (b) square-wave voltammetry potential modulation; (c) typical square-wave voltammogram. Reprinted by permission from Springer Nature Customer Service Center, Springer, ChemTexts, ref [45] Copyright 2018.

Recently, SWV has gained popularity as a suitable and inexpensive replacement to the time-consuming and costly techniques like spectrophotometry, or chromatography, for the detection of many significant biological and inorganic compounds. The simple set-up, quick response, the

variety of modes that can be applied, alongside its sensitivity, make the SWV the preferred technique for detection of significant classes of compounds for example pesticides, harmful additives, pathogens, drugs, heavy metals etc. as can be seen in **Table 2.2** .

Electrical impedance spectroscopy (EIS) is another impactful technique for investigating the electrical properties of a wide variety of materials. The basic principle is to apply to the sample analyte, a sinusoidal test voltage or current, and measure its impedance over an appropriate frequency range [47]. Using this method, we can gain insight into sample's behavior and properties, as the impedance spectra analyzed are fitted with an analogous electrical model reflecting the sample's electrical fingerprint. EIS can be applied to various field of science, due to its rapidity, simplicity in characterizing different samples like liquid, semiliquid, solid, inorganic as well as organic compounds [47]. **Fig. 2.10** (a) shows equivalent circuit, which acts as a model for the impedance generated in a three-electrode electrochemical cell, where Warburg impedance 'Z_W' is the impedance generated from the reactants' diffusion process, charge transfer resistance 'R_{ct}' is caused by electrolyte solution-working electrode redox reaction, electrical resistance 'Rs' experienced by the electrolyte; and double-layer capacitance 'C_{dl}' is the capacitance between the at the electrolyte-working electrode interface. **Fig. 2.10** (b) shows a Nyquist plot that describes the electrical circuit of **Fig. 2.10** (a). At high frequencies, the plot is a semicircle whose diameter is the same as charge transfer resistance R_{ct} and for low frequency, the plot is a straight line with slope 45°, due to dominant Warburg impedance.

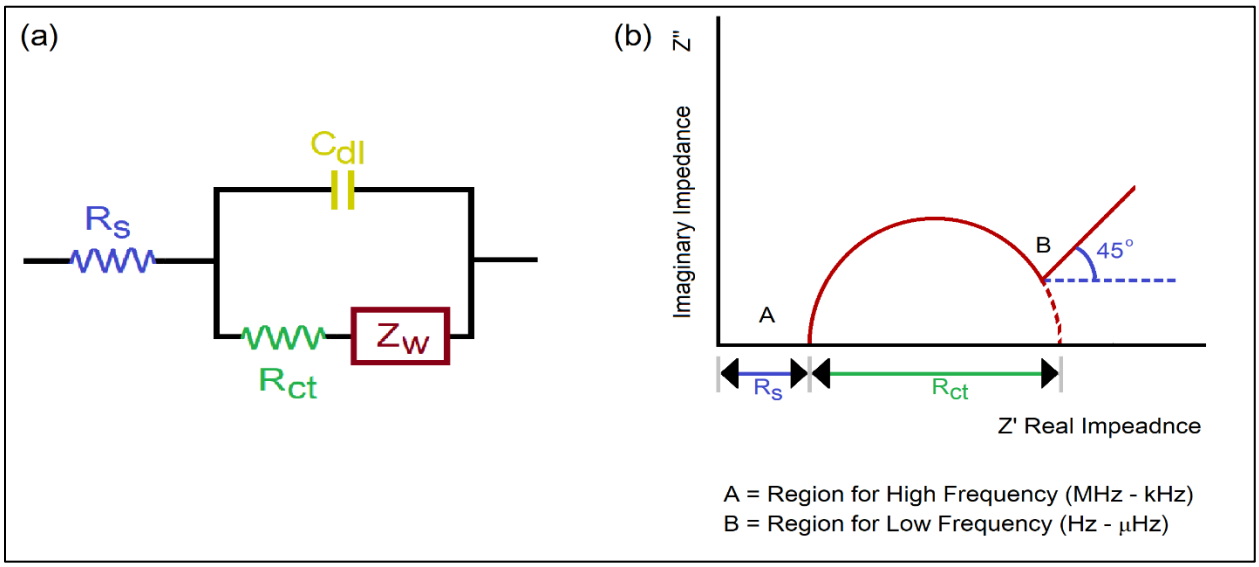

Fig. 2.10 (a) Equivalent electrical circuit of the biosensor; (b) Nyquist plot of the equivalent circuit.

2.6 Nanomaterial Based Electrochemical Sensors for Food Safety

Due to the unique chemical and electrical properties of nanomaterials, their incorporation in electrochemical biosensors can potentially improve reaction speed, selectivity and sensitivity to address the issue of contaminant identification in complex food materials. Novel functional nanomaterials are the key elements of numerous biological and chemical sensors, which are investigated to improve the competence of existing devices or bring new viewpoint in food safety [43]. Nanomaterials have two major functions in biosensors: to enhance the transducer response characteristics and as the bioreceptor immobilization matrix. Electrochemical biosensors designed for food safety have incorporated nanomaterials like magnetic nanoparticles, metal and metal oxide nanoparticles, carbon-based nanomaterials as well as, molecularly imprinted polymers.

Carbon nanotubes are classified into two types, based on the number of rolled layers 1. single walled carbon nanotubes (SWNTs), 2. multi-walled carbon nanotubes (MWNTs). SWNTs and MWNTs are essential resources for the manufacture of electrodes in biosensors because of their particular electrical, chemical and mechanical properties. To improve their functionality, CNTs can be combined with other materials, for example, ionic liquids, polymers or metal nanoparticles or to improve their biocompatibility and solubility they can be used with carboxyl or amino groups. Multiply nested graphene sheets are used to form MWNTs and their variable diameters can go up to 100 nm [43]. As MWNTs have the advantage of unique physical properties, large surface areas, moderate prices and adjustable lengths, they are strong contenders for implementation into biosensor. MWNTs are frequently the choice of material used to expedite transmission of electrons between the electroactive species and the electrode. In addition, MWNTs can be combined with various metal nanoparticles to generate supplementary electrocatalytic sites, enhance electrode sensitivity and improve detection limit.

Du et al. constructed an amperometric biosensor by multi-potential step technique for gold nanoparticle deposition on a MWNTs film for detection of methyl parathion [48]. A trace nitrite sensor for pickled food was constructed using an electrochemical layer-by-layer deposition of ZnO/Pt nanocomposite onto MWNTs modified GCE [49] for the detection of neotame, which is a non-caloric artificial sweetener. A copper nanoparticle (CuNP) decorated MWNTs was used for improving the performance of electrochemical sensor [50]. The CuNPs were anchored with ammonium piperidine dithiocarbamate (APDC) on the MWCNTs, and a platform material was

formed through weak hydrophobic and hydrogen bond interactions with β-cyclodextrin (β-CD) for the sensitive detection of neotame [50].

Graphene is a 2-D nanosheet, made of single carbon atoms are arranged in a honeycomb strucrue. Since its discovery by Geim and Novoselov [51], graphene, alongside its derivatives reduced graphene oxide and graphene oxide have drawn substantial technological and scientific interest. **Table 2.2** provides several examples of graphene-based nanomaterials in the design of food safety electrochemical sensors.

Due to graphene's unique electrochemical, physical and mechanical properties, it has extensively been applied to different types of biosensors, where various metal nanoparticles have been anchored to graphene (GR) in different ways to form nanocomposites. AuNPs/GR nanocomposites owing to its favorable electrochemical activity, robust functional property, provides an efficient highly sensitive electrochemical sensor platform in food safety. Zhang et al. has investigated the voltammetric response of AuNPs/GR in sensing caffeic acid and has reported a much stronger electron transfer kinetics compared to bare GCE [52]. Using electrostatic interaction, Zhu et al. built a Au nanorod (AuNRs) enhanced graphene nanocomposites (GR-AuNRs), for detection of methyl parathion [53]. Based on the specific covalent immobilization process between amino-attached DNA aptamer and its cognate protein lysozyme, a cheap, easy-to-use EIS sensor was manufactured using chitosan-graphene oxide modified pencil graphite electrode (PGE) [54]. The inexpensiveness of PGE endowed the potential to fabricate single use portable protein chip device. The limit of detection foe the sensor was 28.53 nM and the sensor remained highly specific to thrombin and bovine serum albumin in the presence of interfering molecules.

Biopolymers such as silk, gelatin, chitosan also play a very important role in these electrochemical sensors as they are used as a substrate molecule that facilitates the immobilization of antibody or other linker molecules due to the presence of a large number of functional groups in their structures. Bombyx mori silk fibroin (BMSF) retains superb physicochemical and biological properties such as biodegradability and biocompatibility. They can maintain their own properties required for sensing applications, even when they are molded into numerous forms of hydrogels, ultra-thin and dense films, etc., thus setting up versatile interfaces with biological detection systems such as enzymes, aptamers, antibodies, etc. [55].

Similar to silk, the unique structures of chitosan, multifaceted properties, and highly sophisticated functionality make it an appropriate matrix for biosensing element immobilization. The semi-synthetically derived chitosan is an amino-polysaccharide, with a large number of amino groups, strong biocompatibility and ability to coated as films on the transducer. Due to its non-conductive properties, it's often combined with different nanomaterials in sensor applications [54, 56].

Gelatin is yet another biopolymer that has potentially been used in different biosensors, either as an indicator for protease activity through measuring proteolytic digestion using EIS [57, 58], or used as an immobilizing platform based on ZnO nanocomposite for the detection of ascorbic acid using cyclic voltammetry [59]. Gelatin's significant affinity to proteins, nontoxicity, excellent biocompatibility, biodegradability, good film forming ability and inexpensive production makes it an excellent candidate for application in biosensors.

Table 2.2 Nanomaterial based sensors for food safety

Detection methods	Nanomaterials	Analytes	Detection limit	Ref.
CV	β-CD/MWNTs	Herbicide MCPA	0.99 μM	[60]
CV	MWNTs/ALB	Dichlorvos	0.68 ng mL^{-1}	[61]
SWV	Polypyrrole/SWNTs	Quinoline yellow	0.08 μM	[62]
SWV	NGR–NCNTs	Caffeine and vanillin	0.02 μM	[63]
SWV	AuNPs/MWCPE	Thiocyanate	0.005 μM	[64]
CV	CNTs@PNFs	Peroxydisulfate	0.09 pg mL^{-1}	[65]
SWV	AuNPs/MWCPE	Nitrite	0.01 μM	[66]
CV	COOH-SWNTs	Acrylamide	0.03 μM	[67]
SWV	GR-AuNRs	Methyl parathion	0.82 ng mL^{-1}	[53]
CV	P3MT/NGR	Phoxim	6.4 nM	[68]
CV	GO	Imidacloprid	0.3661 μM	[69]
CV	rGO-ATDT-Pt	Orange II	0.34 nM	[70]
CV	GR-ATDT	Sudan I	40 nM	[71]
CV	PANI/GQDs	Cr^{4+}	0.097 mg L^{-1}	[72]
SWV	GR-PANI	Anthracene	0.0044 μM	[73]
CV	GR/AuNPs	Aflatoxin B_1	1 fM	[74]
CV	GS-TH	Fumonisins B_1	1 pg mL^{-1}	[75]
EIS	CS–PB–MWNTs–H-PtCo	Glucose	0.47 μM	[76]
EIS	APTES-rGO	Staphylococcus aureus	—	[77]
EIS	GO/Au	aflatoxin B1	0.23 ng ml^{-1}	[78]
EIS	AuNPs/PB/CNTs-COOH	bisphenol A	—	[79]
EIS	c-MWCNT/CuNP/PANI	Acrylamide	0.2 nM	[80]

CV – cyclic voltammetry; β-CD – β-cyclodextrin; MWNT- multi walled carbon nanotube ; ALB – AChE liposomes bioreactor ;CNTs@PNFs – carbon nanotubes functionalized electrospun nanofiber; COOH-SWNTs – COOH functionalized single walled carbon nanotubesP3MT – poly(3-methylthiophene); NGR – nitrogen doped graphene; GO – graphene oxide;; rGO – reduced graphene oxide; ATDT – 5-amino-1,3,4-thiadiazole-2-thiol; GR – graphene; PANI – polyaniline; GQDs – graphene quantum dots; GS-TH – graphene sheet and thionine nanocomposite ;AuNPs – Au nanoparticles; SWV – square-wave voltammetry ; MWCPE - multi walled carbon nanotube/carbon paste electrode; AuNRs – Au nanorod; EIS – electrochemical Impedance spectroscopy; CS – Chitosan; H-PtCo –hollow PtCo nanochains; APTES – aminopropyltriethoxysilane; PB - Prussian Blue; CNTs – COOH – COOH functionalized carbon nanotubes; CuNP – Copper nanoparticles

2.7 References

1. Anderson TJ, Ilankovan P, Lamsal BP (2012) Two fraction extraction of α-zein from DDGS and its characterization. Industrial Crops and Products 37:466–472. https://doi.org/10.1016/j.indcrop.2011.07.022

2. Lawton JW (2002) Zein: A History of Processing and Use. Cereal Chemistry Journal 79:1–18. https://doi.org/10.1094/CCHEM.2002.79.1.1

3. Shukla R, Cheryan M (2001) Zein: the industrial protein from corn. Industrial crops and products 13:171–192

4. Core J (2002) Corn protein could reduce ethanol production costs. Agricultural Research Magazine 50:20–21

5. Teles FRR, Fonseca LP (2008) Applications of polymers for biomolecule immobilization in electrochemical biosensors. Materials Science and Engineering: C 28:1530–1543. https://doi.org/10.1016/j.msec.2008.04.010

6. Teles FRR, Fonseca LP (2008) Trends in DNA biosensors. Talanta 77:606–623

7. Holding DR, Larkins BA (2009) Zein storage proteins. In: Molecular Genetic Approaches to Maize Improvement. Springer, pp 269–286

8. Watson SA, Ramstad PE (1987) Corn: chemistry and technology

9. Smith CW, Betrán J (2004) Corn: origin, history, technology, and production. John Wiley & Sons

10. Ems-McClung SC, Benmoussa M, Hainline BE (2002) Mutational analysis of the maize gamma zein C-terminal cysteine residues. Plant Science 162:131–141. https://doi.org/10.1016/S0168-9452(01)00549-0

11. Nonthanum P, Lee Y, Padua GW (2012) Effect of γ-Zein on the Rheological Behavior of Concentrated Zein Solutions. J Agric Food Chem 60:1742–1747. https://doi.org/10.1021/jf2035302

12. Nonthanum P, Lee Y, Padua GW (2013) Effect of pH and ethanol content of solvent on rheology of zein solutions. Journal of cereal science 58:76–81

13. Argos P, Pedersen K, Marks MD, Larkins BA (1982) A structural model for maize zein proteins. J Biol Chem 257:9984–9990

14. Garratt R, Oliva G, Caracelli I, et al (1993) Studies of the zein-like α-prolamins based on an analysis of amino acid sequences: Implications for their evolution and three-dimensional structure. Proteins: Structure, Function, and Bioinformatics 15:88–99. https://doi.org/10.1002/prot.340150111

15. Tatham AS, Field JM, Morris VJ, et al (1993) Solution conformational analysis of the alpha-zein proteins of maize. J Biol Chem 268:26253–26259

16. Cabra V, Arreguin R, Galvez A, et al (2005) Characterization of a 19 kDa α-Zein of High Purity. J Agric Food Chem 53:725–729. https://doi.org/10.1021/jf048530s

17. Matsushima N, Danno G, Takezawa H, Izumi Y (1997) Three-dimensional structure of maize α-zein proteins studied by small-angle X-ray scattering. Biochimica et Biophysica Acta (BBA) - Protein Structure and Molecular Enzymology 1339:14–22. https://doi.org/10.1016/S0167-4838(96)00212-9

18. Li Y, Xia Q, Shi K, Huang Q (2011) Scaling behaviors of α-zein in acetic acid solutions. The Journal of Physical Chemistry B 115:9695–9702

19. Forato LA, Doriguetto AC, Fischer H, et al (2004) Conformation of the Z19 prolamin by FTIR, NMR, and SAXS. Journal of agricultural and food chemistry 52:2382–2385

20. Momany FA, Sessa DJ, Lawton JW, et al (2006) Structural Characterization of α-Zein. J Agric Food Chem 54:543–547. https://doi.org/10.1021/jf058135h

21. Turasan H, Kokini JL (2017) Advances in Understanding the Molecular Structures and Functionalities of Biodegradable Zein-Based Materials Using Spectroscopic Techniques: A Review. Biomacromolecules 18:331–354. https://doi.org/10.1021/acs.biomac.6b01455

22. Chen H, Zhong Q (2014) Processes improving the dispersibility of spray-dried zein nanoparticles using sodium caseinate. Food Hydrocolloids 35:358–366. https://doi.org/10.1016/j.foodhyd.2013.06.012

23. Folter JWJ de, Ruijven MWM van, P. Velikov K (2012) Oil-in- water Pickering emulsions stabilized by colloidal particles from the water-insoluble protein zein. Soft Matter 8:6807–6815. https://doi.org/10.1039/C2SM07417F

24. Luecha J, Hsiao A, Brodsky S, et al (2011) Green microfluidic devices made of corn proteins. Lab on a Chip 11:3419–3425

25. Chen Y, Ye R, Liu J (2014) Effects of different concentrations of ethanol and isopropanol on physicochemical properties of zein-based films. Industrial Crops and Products 53:140–147. https://doi.org/10.1016/j.indcrop.2013.12.034

26. Shi K, Kokini JL, Huang Q (2009) Engineering Zein Films with Controlled Surface Morphology and Hydrophilicity. J Agric Food Chem 57:2186–2192. https://doi.org/10.1021/jf803559v

27. Wang Q, Crofts AR, Padua GW (2003) Protein−Lipid Interactions in Zein Films Investigated by Surface Plasmon Resonance. J Agric Food Chem 51:7439–7444. https://doi.org/10.1021/jf0340658

28. Peñalva R, Esparza I, González-Navarro CJ, et al (2015) Zein nanoparticles for oral folic acid delivery. Journal of Drug Delivery Science and Technology 30:450–457. https://doi.org/10.1016/j.jddst.2015.06.012

29. Bugs MR, Forato LA, Bortoleto-Bugs RK, et al (2004) Spectroscopic characterization and structural modeling of prolamin from maize and pearl millet. Eur Biophys J 33:335–343. https://doi.org/10.1007/s00249-003-0354-3

30. Guo Y, Liu Z, An H, et al (2005) Nano-structure and properties of maize zein studied by atomic force microscopy. Journal of Cereal Science 41:277–281. https://doi.org/10.1016/j.jcs.2004.12.005

31. Gillgren T, Barker SA, Belton PS, et al (2009) Plasticization of Zein: A Thermomechanical, FTIR, and Dielectric Study. Biomacromolecules 10:1135–1139. https://doi.org/10.1021/bm801374q

32. Athamneh AI, Griffin M, Whaley M, Barone JR (2008) Conformational Changes and Molecular Mobility in Plasticized Proteins. Biomacromolecules 9:3181–3187. https://doi.org/10.1021/bm800759g

33. Xu H, Chai Y, Zhang G (2012) Synergistic Effect of Oleic Acid and Glycerol on Zein Film Plasticization. J Agric Food Chem 60:10075–10081. https://doi.org/10.1021/jf302940j

34. Lai H-M, Geil PH, Padua GW (1999) X-ray diffraction characterization of the structure of zein–Oleic acid films. Journal of Applied Polymer Science 71:1267–1281. https://doi.org/10.1002/(SICI)1097-4628(19990222)71:8<1267::AID-APP7>3.0.CO;2-O

35. Luecha J, Sozer N, Kokini JL (2010) Synthesis and properties of corn zein/montmorillonite nanocomposite films. J Mater Sci 45:3529–3537. https://doi.org/10.1007/s10853-010-4395-6

36. Park JH, Park SM, Kim YH, et al (2013) Effect of montmorillonite on wettability and microstructure properties of zein/montmorillonite nanocomposite nanofiber mats. Journal of Composite Materials 47:251–257. https://doi.org/10.1177/0021998312439221

37. Manisara P, Parichat M (2012) Cellulose Microfibril from Banana Peels as a Nanoreinforcing Fillers for Zein Films. Open Journal of Polymer Chemistry 2012:. https://doi.org/10.4236/ojpchem.2012.22007

38. Zhang B, Wang Q (2012) Development of Highly Ordered Nanofillers in Zein Nanocomposites for Improved Tensile and Barrier Properties. J Agric Food Chem 60:4162–4169. https://doi.org/10.1021/jf3005417

39. Dashdorj U, Reyes MK, Unnithan AR, et al (2015) Fabrication and characterization of electrospun zein/Ag nanocomposite mats for wound dressing applications. International Journal of Biological Macromolecules 80:1–7. https://doi.org/10.1016/j.ijbiomac.2015.06.026

40. Dhandayuthapani B, Varghese SH, Aswathy RG, et al (2012) Evaluation of Antithrombogenicity and Hydrophilicity on Zein-SWCNT Electrospun Fibrous Nanocomposite Scaffolds. International Journal of Biomaterials 2012:e345029. https://doi.org/10.1155/2012/345029

41. Gezer PG, Liu GL, Kokini JL (2016) Development of a biodegradable sensor platform from gold coated zein nanophotonic films to detect peanut allergen, Ara h1, using surface enhanced raman spectroscopy. Talanta 150:224–232. https://doi.org/10.1016/j.talanta.2015.12.034

42. Gezer PG, Liu GL, Kokini JL (2016) Detection of acrylamide using a biodegradable zein-based sensor with surface enhanced Raman spectroscopy. Food Control 68:7–13. https://doi.org/10.1016/j.foodcont.2016.03.002

43. Zeng Y, Zhu Z, Du D, Lin Y (2016) Nanomaterial-based electrochemical biosensors for food safety. Journal of Electroanalytical Chemistry 781:147–154. https://doi.org/10.1016/j.jelechem.2016.10.030

44. Li Y, Tremblay P-L, Zhang T (2018) Chapter 9 - Anode Catalysts and Biocatalysts for Microbial Fuel Cells. In: Kundu PP, Dutta K (eds) Progress and Recent Trends in Microbial Fuel Cells. Elsevier, pp 143–165

45. Mirceski V, Skrzypek S, Stojanov L (2018) Square-wave voltammetry. ChemTexts 4:17. https://doi.org/10.1007/s40828-018-0073-0

46. Boltalina OV (2017) 1 - Electronic Properties and Applications of Fluorofullerenes. In: Boltalina OV, Nakajima T (eds) New Fluorinated Carbons: Fundamentals and Applications. Elsevier, Boston, pp 1–34

47. Grossi M, Riccò B (2017) Electrical impedance spectroscopy (EIS) for biological analysis and food characterization: a review. J Sens Sens Syst 6:303–325. https://doi.org/10.5194/jsss-6-303-2017

48. Du D, Chen W, Zhang W, et al (2010) Covalent coupling of organophosphorus hydrolase loaded quantum dots to carbon nanotube/Au nanocomposite for enhanced detection of methyl parathion. Biosensors and Bioelectronics 25:1370–1375

49. Zhang M-L, Huang D-K, Cao Z, et al (2015) Determination of trace nitrite in pickled food with a nano-composite electrode by electrodepositing ZnO and Pt nanoparticles on MWCNTs substrate. LWT - Food Science and Technology 64:663–670. https://doi.org/10.1016/j.lwt.2015.06.025

50. Bathinapatla A, Kanchi S, Singh P, et al (2015) Fabrication of copper nanoparticles decorated multiwalled carbon nanotubes as a high performance electrochemical sensor for the detection of neotame. Biosensors and Bioelectronics 67:200–207. https://doi.org/10.1016/j.bios.2014.08.017

51. Geim AK, Novoselov KS (2007) The rise of graphene. Nature Materials 6:183–191. https://doi.org/10.1038/nmat1849

52. Zhang Y, Liu Y, He J, et al (2013) Electrochemical behavior of caffeic acid assayed with gold nanoparticles/graphene nanosheets modified glassy carbon electrode. Electroanalysis 25:1230–1236

53. Zhu W, Liu W, Li T, et al (2014) Facile green synthesis of graphene-Au nanorod nanoassembly for on-line extraction and sensitive stripping analysis of methyl parathion. Electrochimica Acta 146:419–428. https://doi.org/10.1016/j.electacta.2014.09.085

54. Erdem A, Eksin E, Muti M (2014) Chitosan–graphene oxide based aptasensor for the impedimetric detection of lysozyme. Colloids and Surfaces B: Biointerfaces 115:205–211. https://doi.org/10.1016/j.colsurfb.2013.11.037

55. Chakravarty S, Gogoi B, Mandal BB, et al (2018) Silk fibroin as a platform for dual sensing of vitamin B12 using photoluminescence and electrical techniques. Biosensors and Bioelectronics 112:18–22. https://doi.org/10.1016/j.bios.2018.03.057

56. Aydın EB, Aydın M, Sezgintürk MK (2018) Electrochemical immunosensor based on chitosan/conductive carbon black composite modified disposable ITO electrode: An analytical platform for p53 detection. Biosensors and Bioelectronics 121:80–89. https://doi.org/10.1016/j.bios.2018.09.008

57. Ionescu RE, Fillit C, Jaffrezic-Renault N, Cosnier S (2008) Urease–gelatin interdigitated microelectrodes for the conductometric determination of protease activity. Biosensors and Bioelectronics 24:489–492. https://doi.org/10.1016/j.bios.2008.06.021

58. Saum AGE, Cumming RH, Rowell FJ (2000) Detection of protease activity in the wetted surface of gelatin-coated electrodes in air by AC impedance spectroscopy. Biosensors and Bioelectronics 15:305–313. https://doi.org/10.1016/S0956-5663(00)00068-3

59. Rawat K, Sharma A, Solanki PR, Bohidar HB (2015) Potential of Gelatin-Zinc Oxide Nanocomposite as Ascorbic Acid Sensor. Electroanalysis 27:2448–2457

60. Rahemi V, Vandamme JJ, Garrido JMPJ, et al (2012) Enhanced host–guest electrochemical recognition of herbicide MCPA using a β-cyclodextrin carbon nanotube sensor. Talanta 99:288–293. https://doi.org/10.1016/j.talanta.2012.05.053

61. Yan J, Guan H, Yu J, Chi D (2013) Acetylcholinesterase biosensor based on assembly of multiwall carbon nanotubes onto liposome bioreactors for detection of organophosphates pesticides. Pesticide Biochemistry and Physiology 105:197–202. https://doi.org/10.1016/j.pestbp.2013.02.003

62. Gao Y, Wang M, Yang X, et al (2014) Rapid detection of quinoline yellow in soft drinks using polypyrrole/single-walled carbon nanotubes composites modified glass carbon electrode. Journal of Electroanalytical Chemistry 735:84–89

63. Jiang L, Ding Y, Jiang F, et al (2014) Electrodeposited nitrogen-doped graphene/carbon nanotubes nanocomposite as enhancer for simultaneous and sensitive voltammetric determination of caffeine and vanillin. Analytica chimica acta 833:22–28

64. Afkhami A, Soltani-Felehgari F, Madrakian T (2014) Highly sensitive and selective determination of thiocyanate using gold nanoparticles surface decorated multi-walled carbon nanotubes modified carbon paste electrode. Sensors and Actuators B: Chemical 196:467–474. https://doi.org/10.1016/j.snb.2014.01.115

65. Dai H, Xu G, Zhang S, et al (2014) Carbon nanotubes functionalized electrospun nanofibers formed 3D electrode enables highly strong ECL of peroxydisulfate and its application in immunoassay. Biosensors and Bioelectronics 61:575–578. https://doi.org/10.1016/j.bios.2014.05.061

66. Afkhami A, Soltani-Felehgari F, Madrakian T, Ghaedi H (2014) Surface decoration of multi-walled carbon nanotubes modified carbon paste electrode with gold nanoparticles for electro-oxidation and sensitive determination of nitrite. Biosensors and Bioelectronics 51:379–385. https://doi.org/10.1016/j.bios.2013.07.056

67. González-Fuentes FJ, Manríquez J, Godínez LA, et al (2014) Electrochemical Analysis of Acrylamide Using Screen-Printed Carboxylated Single-Walled Carbon Nanotube Electrodes. Electroanalysis 26:1039–1044. https://doi.org/10.1002/elan.201300636

68. Wu L, Lei W, Han Z, et al (2015) A novel non-enzyme amperometric platform based on poly(3-methylthiophene)/nitrogen doped graphene modified electrode for determination of trace amounts of pesticide phoxim. Sensors and Actuators B: Chemical 206:495–501. https://doi.org/10.1016/j.snb.2014.09.098

69. Lei W, Han Z, Si W, et al (2014) Sensitive and Selective Detection of Imidacloprid by Graphene-Oxide-Modified Glassy Carbon Electrode. ChemElectroChem 1:1063–1067. https://doi.org/10.1002/celc.201300244

70. Yun M, Choe JE, You J-M, et al (2015) High catalytic activity of electrochemically reduced graphene composite toward electrochemical sensing of Orange II. Food Chemistry 169:114–119. https://doi.org/10.1016/j.foodchem.2014.07.143

71. Ma X, Chao M, Wang Z (2013) Electrochemical determination of Sudan I in food samples at graphene modified glassy carbon electrode based on the enhancement effect of sodium dodecyl sulphonate. Food Chemistry 138:739–744. https://doi.org/10.1016/j.foodchem.2012.11.004

72. Punrat E, Maksuk C, Chuanuwatanakul S, et al (2016) Polyaniline/graphene quantum dot-modified screen-printed carbon electrode for the rapid determination of Cr(VI) using stopped-flow analysis coupled with voltammetric technique. Talanta 150:198–205. https://doi.org/10.1016/j.talanta.2015.12.016

73. Tovide O, Jahed N, Sunday CE, et al (2014) Electro-oxidation of anthracene on polyanilino-graphene composite electrode. Sensors and Actuators B: Chemical 205:184–192. https://doi.org/10.1016/j.snb.2014.07.116

74. Linting Z, Ruiyi L, Zaijun L, et al (2012) An immunosensor for ultrasensitive detection of aflatoxin B1 with an enhanced electrochemical performance based on graphene/conducting polymer/gold nanoparticles/the ionic liquid composite film on modified gold electrode with electrodeposition. Sensors and actuators B: chemical 174:359–365

75. Shi Z-Y, Zheng Y-T, Zhang H-B, et al (2015) DNA Electrochemical Aptasensor for Detecting Fumonisins B1 Based on Graphene and Thionine Nanocomposite. Electroanalysis 27:1097–1103. https://doi.org/10.1002/elan.201400504

76. Che X, Yuan R, Chai Y, et al (2011) A glucose biosensor based on chitosan–Prussian blue–multiwall carbon nanotubes–hollow PtCo nanochains formed by one-step electrodeposition. Colloids and Surfaces B: Biointerfaces 84:454–461. https://doi.org/10.1016/j.colsurfb.2011.01.041

77. Wang Z, Zhang J, Chen P, et al (2011) Label-free, electrochemical detection of methicillin-resistant staphylococcus aureus DNA with reduced graphene oxide-modified electrodes. Biosensors and Bioelectronics 26:3881–3886. https://doi.org/10.1016/j.bios.2011.03.002

78. Srivastava S, Ali MA, Umrao S, et al (2014) Graphene Oxide-Based Biosensor for Food Toxin Detection. Appl Biochem Biotechnol 174:960–970. https://doi.org/10.1007/s12010-014-0965-4

79. Azadbakht A, Roushani M, Abbasi AR, Derikvand Z (2016) A novel impedimetric aptasensor, based on functionalized carbon nanotubes and prussian blue as labels. Analytical biochemistry 512:58–69

80. Batra B, Lata S, Sharma M, Pundir CS (2013) An acrylamide biosensor based on immobilization of hemoglobin onto multiwalled carbon nanotube/copper nanoparticles/polyaniline hybrid film. Analytical Biochemistry 433:210–217. https://doi.org/10.1016/j.ab.2012.10.026

CHAPTER 3. BIODEGRADABLE BIOPOLYMER-GRAPHENE NANOCOMPOSITES: A REVIEW

Tahrima B. Rouf and Jozef L. Kokini

Department of Food Science, Purdue University, West Lafayette, IN 47907, USA

Reproduced with permission. Full citation:

Rouf, T. B., & Kokini, J. L. (2016). Biodegradable biopolymer–graphene nanocomposites. Journal of Materials Science, 51(22), 9915-9945.

3.1 Abstract

Graphene's invention has catalyzed many new material applications in different fields. It has been used in combination with different biopolymers to design nanocomposites with improved mechanical, thermal, electrical, as well as, gas and water vapor barrier properties. This review focuses on the chemistry and synthesis of Graphene Oxide (GO) and sheds some light on the different ecological pathways available for graphene oxide synthesis and reduction. The major pathways for graphene incorporation into biopolymers include; 1) solution intercalation, 2) melt intercalation and 3) in situ polymerization. The fabrication, application and mechanisms of bonding between biodegradable biopolymers, like poly (lactic acid), cellulose, starch, chitosan, alginates, polyamides, and other biodegradable materials, with different forms of graphene including graphene oxide (GO), reduced graphene oxide (RGO), graphene nanoplatelets (GNP) etc. are the focus of this review. The paper has been organized according to different methods of incorporating graphene derivatives into biopolymers, in order to highlight the mechanisms for chemical bonding-physical changes that biopolymers and graphene nanofillers undergo during the method of preparation and the impact of chemical changes on end use properties. The information has been assembled, so that new conclusions can be drawn from the available data. The mechanism of enhancement of functional properties are evaluated using techniques including Fourier Transform Infrared Spectroscopy (FTIR), X-ray Diffraction (XRD), Raman, Scanning Electron Microscopy (SEM), Transmission Electron Microscopy (TEM), Atomic Force Microscopy (AFM) and the synergy resulting from the use of different spectroscopic techniques is discussed beyond what the individual authors have been able to interpret often from a few techniques. Effectiveness

of solvents used and reaction conditions have also been focused, in order to offer mechanistic understanding for the improvement of mechanical properties. The new observations and findings by comparing all relevant literature will help the reader to look at the whole spectrum of available methods and materials, in addition to focusing on the original biopolymer-graphene work.

Keywords Graphene ·Biopolymer · Poly (lactic Acid)· Starch · Cellulose · Chitosan · Alginate

3.2 Introduction

Recent increase in interest towards more environmentally friendly materials have expanded the consideration of biopolymers and their nanocomposites with improved functional properties, as alternatives to synthetic polymers. Polymers that have been extracted from renewable resources are known as biopolymers, and these biopolymers can be classified into three main categories according to the production methods as shown in **Fig. 3.1.** Biopolymers require property enhancements for use in different applications, as they have traditionally higher costs and inferior property profiles compared to commercial thermoplastic polymers. Inclusion of a large variety of fillers like layered silicates, nanotubes etc. in conventional polymers lead to notable increase in their mechanical, thermal, rheological and gas-barrier properties [2–8]. Compared to all these fillers graphene appears to have a superior ability to result in substantial improvements in functional properties of polymers. The recent advances in the different fabrication techniques and modifications of graphene, as well as, the property improvements in poly (lactic acid) (PLA) - graphene nanocomposites have been reviewed [9]. The recent developments and the applications of graphene-polysaccharide nanocomposites, have also been reviewed [10]. These polysaccharides have different functional groups with distinct and divergent properties affecting the chemical mechanism of their interaction between graphene, resulting in different degrees of property changes as well as, diverse applications.

For polymer-nanocomposite fabrication, matching the polarity between the polymer and filler is of great importance for optimal interfacial interactions between the filler and the matrix. In addition, good geometrical and aspect ratio, large number of functional groups are some of the attributes that strongly influence the resultant property improvement. Therefore, high surface area, high aspect ratio, and high strength of graphene, enables it to outperform all other fillers in nanocomposites [10]. Sufficient interaction and interfacial bonding between the graphene/graphene derivative and the biopolymer; promotes uniform dispersion, which is of

utmost importance. The lower number of functional groups in graphene as compared to graphite oxide (such as carboxyl, epoxide, hydroxyl etc.) results in low surface energy, and lower compatibility with polar polymer matrices. Because of the higher compatibility with the functional groups of biopolymers, the oxidized form of graphene, GO has found more application in biopolymer graphene nanocomposite fabrication, compared to the other derivatives of graphene like RGO, GNP etc.

This review aims to organize much of the research done on biopolymer-graphene derivative nanocomposites, including the most recent findings, in more depth, by presenting quantitative information regarding different types of nanocomposite preparation methods, characterization and property enhancement in the biopolymer-graphene nanocomposite literature. The organization of information in this paper is according to manufacturing method, to show their correlation with the property improvement of biopolymer -graphene derivatives; emphasizing the properties of graphene and adding new information beyond other reviews, with more in depth interpretations consistent with this new organization. It is distinctly different from other reviews as it gives a new perspective on how the nanocomposite preparation method can have a major influence on the properties of biopolymers even using the same nanofiller, and we believe it will assist researchers at every stage of research in biopolymer nanocomposite.

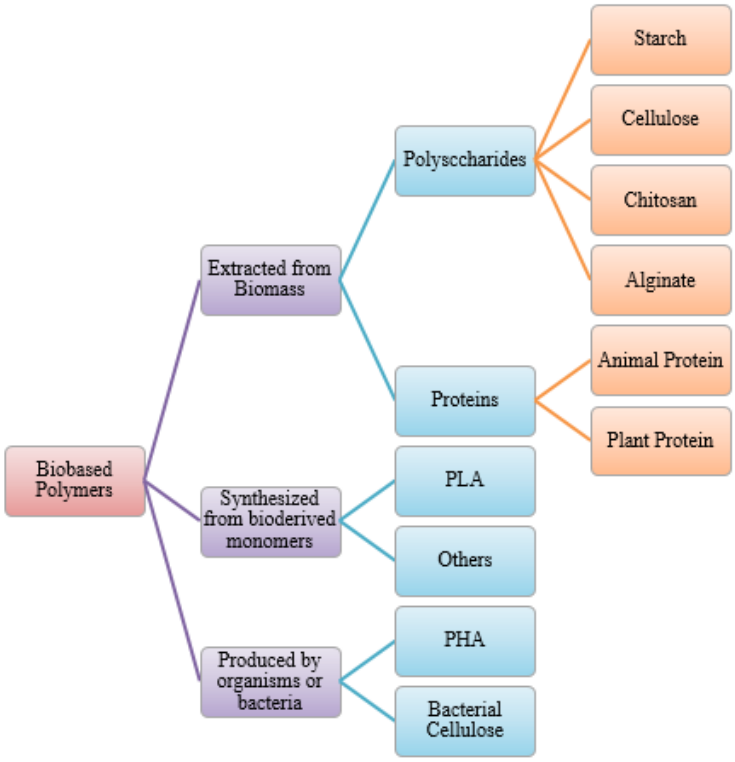

Fig. 3.1. Schematic overview of classification of biopolymers

3.3 Graphene

3.3.1 Structure of Graphene

Even though the history of graphene traces back to 1840 [11], room temperature stable graphene was not invented until 2004. Andre K. Geim and Konstantin S. Novoselov were the first to produce room temperature stable graphene [12] and received the highly prestigious Nobel Prize in 2010, for their innovative research with this amazing material. Graphene consists of a unit hexagonal cell, organized in a repeating honeycomb structure. In a unit cell of graphene, the subunits of carbon atoms are joined by sigma (σ) bonds (length 0.142 nm) [13] and the π-orbital from each carbon atom in the lattice, contribute to a network of delocalized electrons, ensuring enhanced stability of the nanosystems [14]. The original definition of graphene was of a single carbon layer [15], but now the definition has broadened. If the number of carbon layers is less than 10, it is still considered graphene, but if the layer number is 10 or more, it is then known as graphite nanoplatelet GNP, or exfoliated graphite nanoplatelet (xGnP) [16]. GNPs has also been defined as a graphite base nanofiller, whose thickness can vary between 30-80nm [17], depending on the

synthesis method. However, if the thickness is even lower than 30 nm, the form of graphene is then referred as graphene nanosheet (GNS)[17]. GNP or GNS contain a very small number of functional groups (carboxyl, epoxy, and hydroxyl). As a result, GNP and GNS do not go into polar interactions, or hydrogen bonding so they are considered hydrophobic. A useful derivative of graphene that has found application in nanocomposites, due to its numerous and diverse functional groups, is graphene oxide (GO). According to The Lerf-Klinowski model, the carbon plane in GO is enhanced with hydroxyl and epoxy (1,2-ether) functional groups enabling it to chemically interact with hydrophilic polymers through bonding with hydrogen [18]. This model, along with several other models for the structure of GO are depicted in **Fig. 3.2.** In addition to reinforcement, graphene nanocomposites find application in chemical adsorption and contaminant detection. GO has the ability to undergo hydrogen bonding or ionic interactions with heavy metals, which is the main reason behind its adsorption abilities. The π-π interactions of graphene with aromatic rings of dyes or drugs, are also why graphene can act as an adsorbent for these chemicals [19–21]. GO is polar in nature and bears a negative charge, due to many epoxy and hydroxyl groups on its surface and carboxyl (-COOH) group on the edges and as a result, it interacts better with polar polymers.

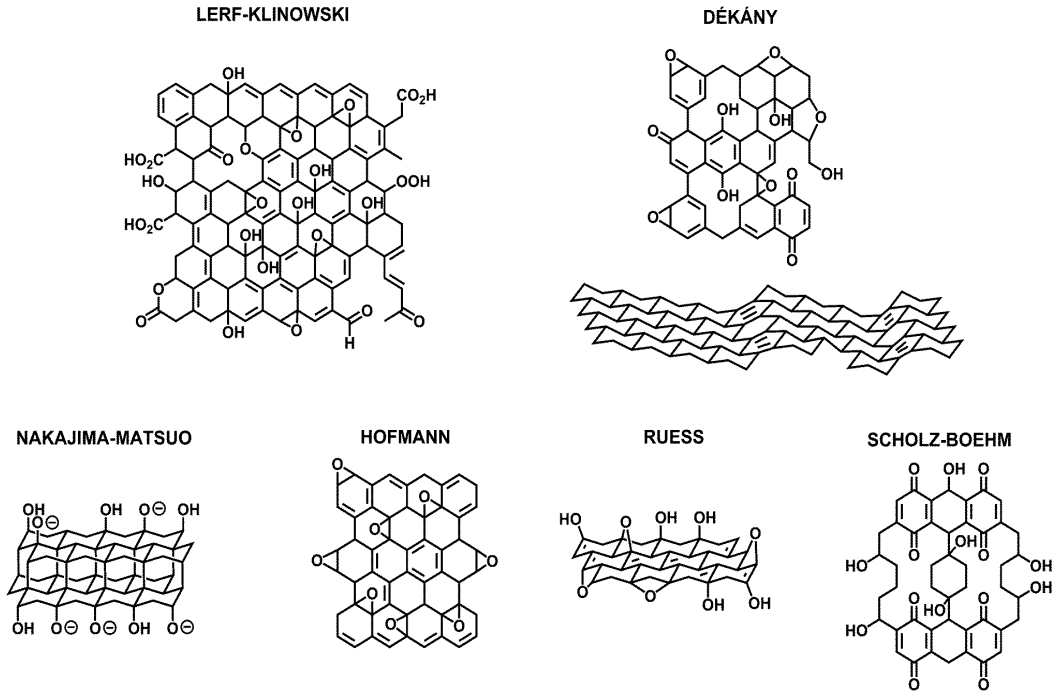

Fig. 3.2. Summary of proposed structural models of GO, including recent examples (top; Lerf–Klinowski and Dékány models) as well as earlier examples (bottom; Nakajima–Matsuo,

Hofmann, Ruess, and Scholz–Boehm models). Reprinted with permission from ref [181]. Copyright 2006, American Chemical Society.

3.3.2 Synthesis of Graphene Oxide and Derivatives

Pristine graphene can be synthesized using different fabrication methods. A well-known method for large scale production of monolayer or few layer graphene known as chemical vapor deposition (CVD) [22], includes extraction of carbon atoms from a carbon-rich source by reduction and consequent growth of graphene films on the surface of metal. On the other hand, for small sample preparation of single or few-layer graphene, a simple technique includes repeated peeling of graphene layers from graphite, using an adhesive tape [23]. Also unzipping of multiwall carbon nanotubes (MWCNTs), micro-mechanical exfoliation [24], mechanical assisted exfoliation followed by ultrasonication [25], growth on crystalline silicon carbide etc. are some popular graphene fabrication methods. There are mainly two routes through which graphite is processed, in order to obtain graphene-based materials; these are (i) Exfoliation of graphite (ii) Oxidation of Graphite [18].

Exfoliation of Graphite

Intercalation is the primary step of exfoliation and consists of treating graphite with a mixture of sulfuric and nitric acid, which causes the interlayer spacing to increase and produces Graphite Intercalated Compound (GIC). Then exfoliation of the GIC is undertaken by rapid heating or microwave treatment, producing expanded graphite (EG) [26]. The interlayer spacing of EG, is more than graphite and GIC, and it consists of loosely stacked thin platelets (30–80 nm) [26]. But the layered structure and relatively low specific surface area (below 40 m^2/g) [27] of EG hinders its performance as a composite filler [28–30]. So further exfoliation of EG is done using sonication; or re-intercalation with organic material followed by sonication, which produces GNP with thickness of 5nm or lower [31, 32]. These studies reported the thickness of GNP is in the range of 5-10 nm, whereas, another study reports that the thickness of GNPs are in the range of 30-80nm, and thickness of GNS is in the range of 3-30nm [17].

Oxidation of Graphite

The oxidation of graphite to produce graphite oxide, is mainly based on three methods: (i) Brodie's method [33]; (ii) Staudenmaier's method [34], and (iii) the method of Hummers which is a modification of Staudenmaier's method [19, 35]. Also there is a modified Hummers method, which requires shorter time and lower oxidation temperature, but produces GO with larger sheets and higher thermal stability, as compared to Hummers method [36]. The common thread for exfoliation of graphite, consists of using a chemical oxidant, like a combination of $KClO_4$ with HNO_3 [33, 34], or potassium permanganate [35]. The oxidation level of these reactions are very similar (C:O = 2:1 approximately) [19] and the oxidation process destroys the π-conjugation of the stacked graphene sheets resulting in the disappearance of delocalized electronic structure of graphite. In the oxidized graphite, there are nanoscale graphitic sp^2 domains, which are surrounded by highly disorganized oxidized domains (sp^3 C\C) [37]. As the electronic structure is destroyed, graphite losses its conductive properties but its surface become enriched with a variety of oxygen-based chemical functionalities. During further exfoliation, the phenol, hydroxyl and epoxy groups are formed at the basal plane and carboxylic acid groups are formed at the edges [23]. In order to use GO in biopolymer graphene-nanocomposites, many researchers have used the Hummers method [38–44] , modified Hummers method [43, 45–56], some researchers have also used the Staudenmaier's method [57–59] and Brodie's method [49] in order to fabricate the graphite oxide, which subsequently exfoliates to GO. Even though GO is structurally different from graphite oxide due to its quasi-infinite interlayer spacing; but chemically, the two materials are quite similar. GO retains the oxygen functionalities of its precursor, graphite oxide, but largely exists as mono-, bi- or few-layer graphene sheets. The exfoliation of graphite oxide to GO is usually achieved through mechanical stirring or ultrasonication methods in a polar organic solvent or aqueous media. Mechanical stirring produces graphene oxide of slow and low yield but has larger lateral dimension than the ones produced using sonication. On the other hand, the ultrasonication method may be time saving, but often involves structural damages and breaks off GO sheets into smaller fragments [60]. The vessel diameter and liquid height during sonication can play an important role for large-scale production of graphene. The cavitation, caused by sonication is the main factor behind exfoliation and in order to obtain, large scale few layer graphene (FLG), a large quantity of cavitation volume is required which can be achieved by, large vessel diameter D, liquid height H,

or D/H, or large sample volume [61]. **Fig. 3.3** summarizes the exfoliation and oxidation steps to obtain GO and GNP from graphite flakes.

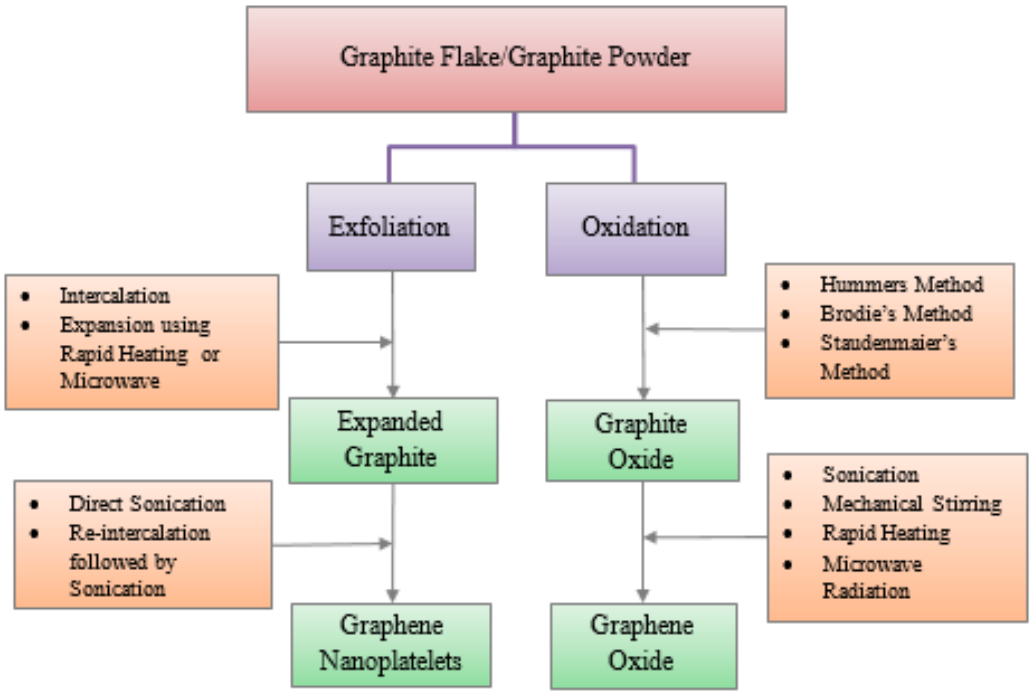

Fig. 3.3. Schematic representation of the steps for exfoliation of graphite to obtain GNP and oxidation of graphite to obtain GO.

Graphene is a highly conductive material with a conductance of 600,000 S/m. Since, the delocalized electronic structure of graphite is disrupted during formation of graphite oxide, GO is considered to have insulation properties. Therefore, GO platelets need to be reduced to generate a pristine graphene like material. GO has been chemically reduced, using hydrazine [42, 27, 30, 100] or glucose [73] or thermally reduced, using high temperature up to 1000^{o}C [88, 41, 90] to produce reduced graphene oxide (RGO). On the other hand, lower temperature (200^{o}-300^{o}C) reduction of graphene has also been reported [62]. Obtaining high temperature can be expensive and using toxic reducing agents like hydrazine can be harmful for graphene-based bio-related applications. In order to eradicate this problem, a great amount of research has been conducted to produce green reduction agents for graphene oxide. Nontoxic, pure natural, green reduction agents have been explored to synthesize graphene such as vitamin C (L-ascorbic acid) [63], amino acid [64], alcohol [65], reducing sugar [66–68], green tea polyphenols [69], wild carrot root [70], phytoextracts, [71], melatonin [72], bovine serum albumin [73] and bacteria [74]. Dong and co-workers demonstrated

the usage of glucose, fructose and sucrose in aqueous ammonia solution for the reduction of graphene oxide [66]. The ammonia contributed to a synergistic augmentation of the reaction rate and oxygen removal process. Fructose displayed reducing capability towards graphene oxide since it was capable of undergoing a keto–enol tautomerism under alkaline conditions. As for sucrose, despite being a non-reducing sugar, it could readily break down into fructose and glucose upon hydrolysis in an alkaline environment, to affect the reduction of graphene oxide. However, the reducing capability was lower than that of glucose and fructose. The resulting graphene obtained from glucose treatment showed good electrocatalytic activity towards dopamine, epinephrine and norepinephrine. In another work by Min and co-workers. [75], dextran (polysaccharide) in aqueous ammonia solution was applied. Due to the synergistic effect of ammonia, the reduction step was shortened to 3 h instead of 3 days. The mechanism of the reduction was postulated to go through a similar route as that of glucose. Moreover, the obtained graphene showed a measured conductivity of 1.1 S/m. The conjugation of bovine serum albumin (BSA) with GO [73] showed that, a change in conjugation conditions (temperature and pH) could provide two different types of complexes, mainly BSA-GO and graphene conjugates. The amino acid group tyrosine present in BSA was the main reducing agent. The phenolic groups of tyrosine were ionized at a high pH, which promoted the electron transfer to GO, resulting in successful reduction.

3.4 Biopolymer-Graphene Based Nanocomposites

The discussion of different biopolymer-graphene nanocomposites will be based according to their manufacturing method. A good distribution of the nanomaterials in polymers depends on the preparation of polymer-based nanocomposites, which ultimately can influence the mechanical, thermal, electrical, water vapor and gas barrier properties of nanocomposites. Other than graphene or graphene oxide, carbon nanotubes (CNT) have shown great promise in reinforcement of nanocomposite, but CNTs require chemical modification for good distribution, as they have a tendency to aggregate [76]. In the case of GO, even though aggregate formation is not regarded as a major issue, incomplete exfoliation and restacking is commonly observed [77]. Polarity, molecular weight, hydrophobicity, nature of the reactive groups that have been added to graphene, or which are present in the polymer, graphene, and solvent; are the main governing factors behind the mechanism for interaction in polymer-graphene nanocomposites [78]. There are mainly three pathways for incorporation of graphitic nanofiller into polymer matrices; i) Solution Intercalation, ii) Melt Intercalation, and iii) In situ intercalative polymerization. There are also other methods like wet spinning, electro spinning, freeze-drying, drop casting etc. Examples of different studies of biopolymer-graphene nanocomposites that have used these methods have been shown in **Fig. 3.4**

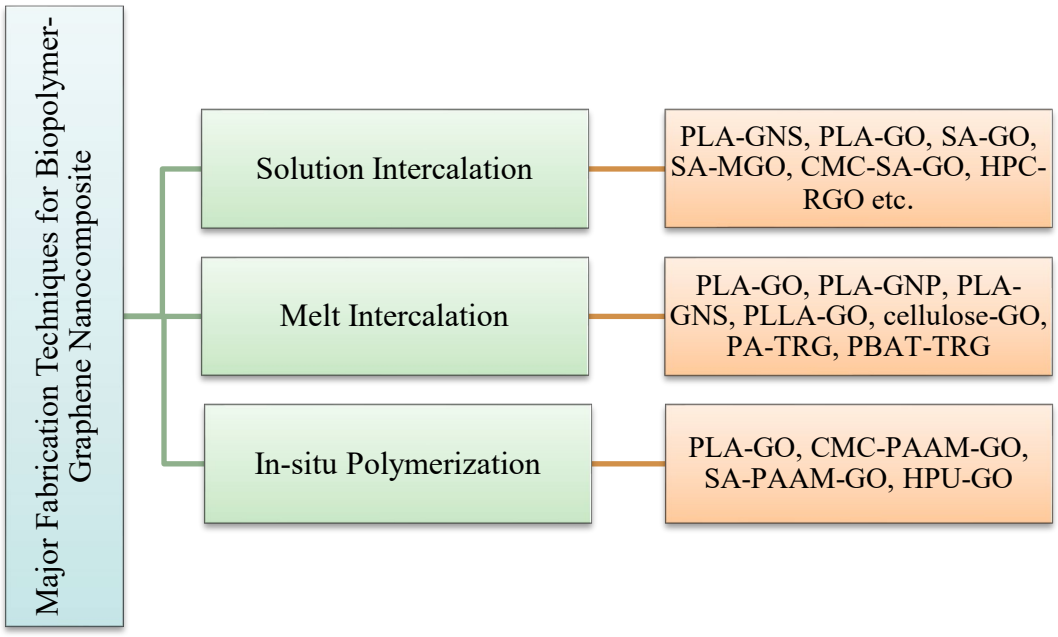

Fig. 3.4. Three major fabrication techniques for synthesis of biodegradable biopolymer-graphene nanocomposites and the examples in literature that have used the techniques.

3.4.1 Solution Intercalation

Solution Intercalation is the most popular fabrication technique out of all other techniques and involves the "simple stirring or shear mixing of colloidal suspensions of graphene" [32] with the desired biopolymer, followed by evaporation of solvent, which causes the adsorbed polymer to reassemble and form a sandwich between polymer and graphene, resulting in formation of nanocomposites. There have been numerous publications focusing on solution intercalation for incorporating graphene in different biopolymers like starch, chitosan, PLA, cellulose, alginate, gelatin, poly (hydroxyalkanoates) etc. In most of these cases, chemical structure of the biopolymer in the composite films barely changes with the increasing content of graphene, indicating that there may be moderate chemical reaction but mainly physical interaction, like hydrogen bonding, between biopolymers and graphene derivatives. Different researches that use solution intercalation method to incorporate graphene and its derivative into biopolymers for improving their properties have been discussed briefly in this section.

Starch

Starch based materials have garnered a lot of attention due to its biodegradability, low cost, abundance, renewability, and therefore it has the most potential to replace synthetic plastic. Starch based materials have been used in different fields like agriculture, medicine and packaging industries. However, due to its poor mechanical strength and hydrophilic nature it has been combined with different forms of graphene like GO, RGO nanomaterials to improve its mechanical, thermal and electrical properties. Different reaction conditions like dispersibility in solvents, temperature, and use of plasticizers play a significant role in the performance of graphene nanofiller in the bio-nanocomposites. There is a correlation between the dispersibility of GO and RGO, with a combination of polar component δ_P, Hydrogen Component δ_H (Hansen Solubility Parameter, HSP) and polar surface energy γ_s^p of the solvent [79]. The larger the HSP of polar aprotic solvents (Chloroform, Acetone etc.), the higher the dispersibility of graphene based materials in that solvent. On the other hand, samples with more polar groups on the surface can be dispersed more stably in polar protic solvents (water, acetic acid) [79]. Since GO has more polar groups compared to RGO, the order of dispersion stability in solvents like water, is GO> RGO.

A comparative study of the effects of GO and RGO, on the overall properties of starch has been conducted [48], where nanocomposites of glycerol plasticized starch (PS), with GO and RGO fillers were prepared using solution casting methods where water was used as a solvent. The study showed better overall property improvement for starch-GO nanocomposites, as compared to starch-RGO nanocomposites. The comparatively larger number of polar groups rendered GO with better compatibility with PS, which led to better mechanical properties compared with RGO. In addition to that, the better dispersibility of GO in water, compared to RGO, ensured better distribution of the nanofiller, throughout the starch matrix. Hence, tensile strength increase for starch-GO nanocomposite was 66% at 2wt% GO loading and for starch-RGO nanocomposite was 67% for 6 wt% addition of RGO. Water vapor permeability tests showed, improved water vapor barrier properties for PS-4wt% GO nanocomposite, but noticeable improvement for PS-RGO was not achieved even at 8wt% RGO loading. Because GO formed better interactions with the PS matrix than RGO and produced a denser network, which provided hindrance in the path of the escaping water molecules.

Effect of plasticizer on starch-graphene nanocomposites were studied, where glycerol was used as a plasticizer for starch, and starch grafted graphene (GN-Starch) was used as a nanofiller, to prepare PS-graphene nanocomposites [80]. For this study, GO was reduced by hydrazine in the presence of starch, which resulted in starch grafted graphene (GN-Starch). The purpose of using starch was to prevent restacking of graphene during reduction. In **Fig. 3.5**, TEM images of graphene and GN-Starch shows that, when graphite sheets are oxidized, it becomes flat and transparent with wrinkled structure, while GN-Starch has a darker appearance due to the presence of starch. In **Fig. 3.6.** FTIR spectra of starch shows that, in the fingerprint region, there are three peaks; 1156 cm^{-1} from C–O bond stretching of the C–O–H group, and the two peaks at 1080 and 980 cm^{-1}, from C–O bond stretching of the C–O–C group. These main characteristic peaks are also visible in in FTIR spectrum of GN-starch components, which indicates that starch components are present in the GN-starch nanofiller. The Raman spectra of GO and GN-starch are shown in **Fig. 3.6**, where for GO, peaks are observed at about 1350 cm^{-1} for the disordered structure (D mode) and at about 1590 cm^{-1} for the graphite structure (G mode), due to the sp^2 domain. For GN-Starch, the increased intensity at D mode compared G mode, indicates that it has reduced sp^2 domains and higher degree of disorder, resulting from the creation of new graphitic domains in the GN-Starch. Mechanical, WVP and electrical tests proved the efficacy of the nanofiller by

displaying significant improvement at a loading as low as 0.28-1.7 wt%, as shown in **Table 3.1, 3.3** and **3.4**.

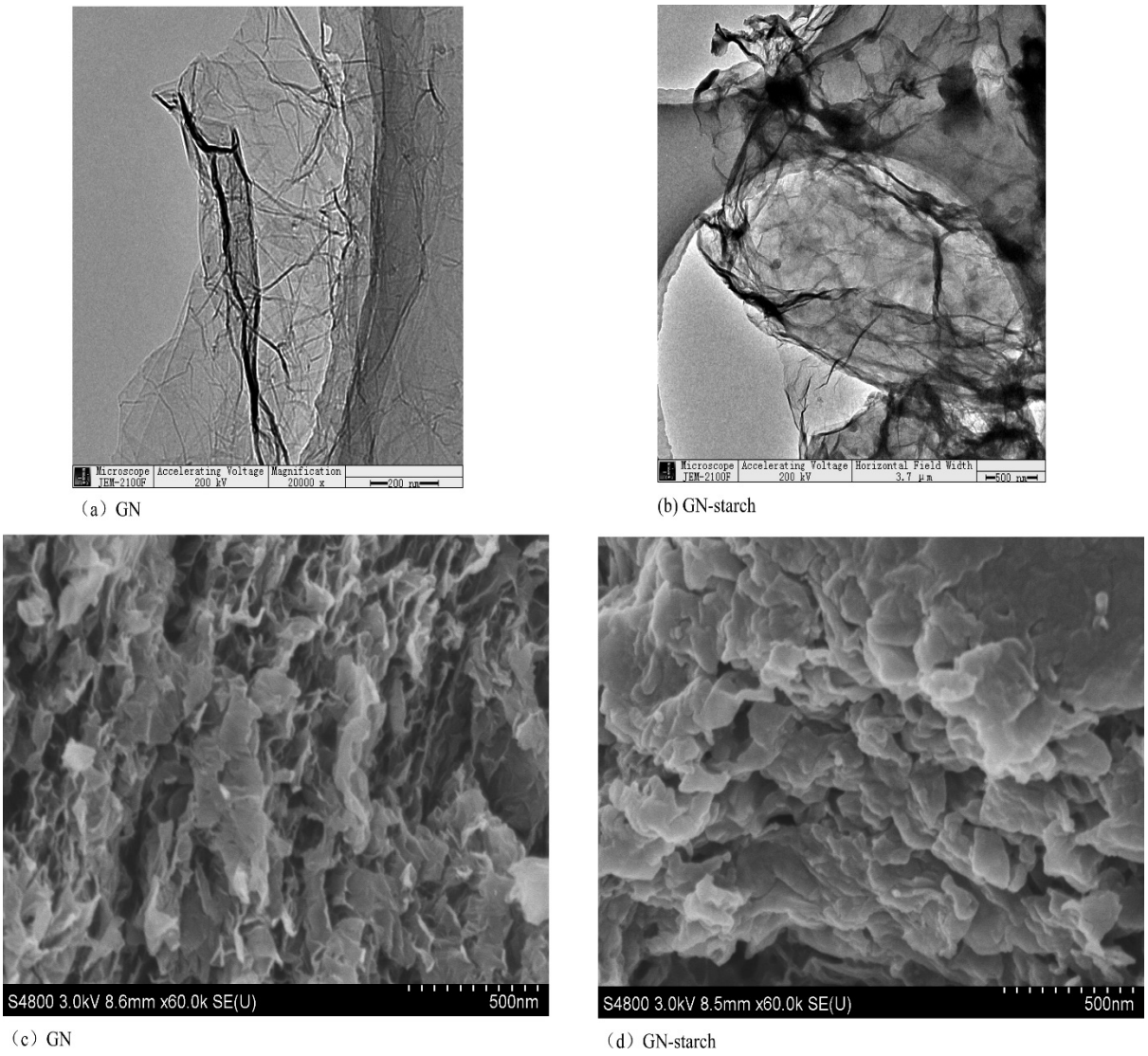

（a）GN　　(b) GN-starch

（c）GN　　（d）GN-starch

Fig. 3.5. TEM images of (a) Graphene (b) GN-Starch; SEM images of (c) Graphene, and (d) GN-Starch. Reprinted with permission from ref [80]. Copyright 2013, American Chemical Society.

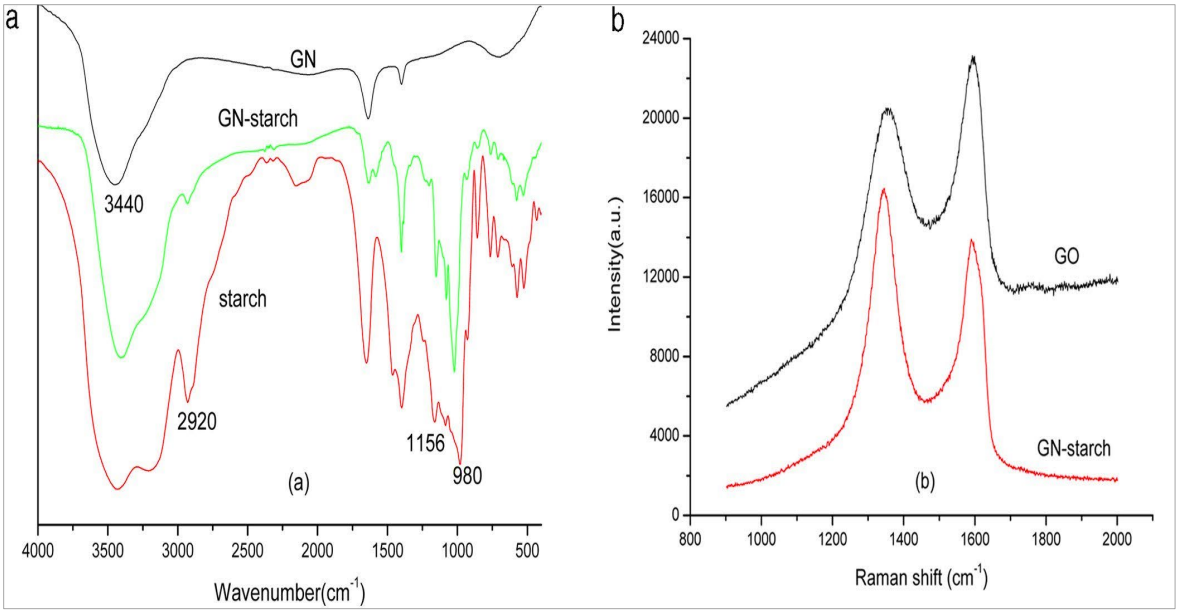

Fig. 3.6. (a) FTIR spectra of starch, GO, and GN-starch. (b) Raman spectra of GO and GN-starch. Reprinted with permission from ref [80]. Copyright 2013, American Chemical Society.

The effect of GO on Glycerol-plasticized pea starch (Pea starch-GO) were studied, with different loading levels of GO (0, 0.4, 0.8, 1.0, 1.5 and 2.0 wt%) were prepared by solution casting method, using water as a solvent. Morphology tests of the bio-nanocomposite films showed that, in the FTIR spectra of pea starch-GO nanocomposite, with increasing concentration of GO, the characteristic starch FTIR peaks move to a lower wave number, and similarly the characteristic XRD diffraction peaks of starch, decreased in intensity, indicating hydrogen bonding between starch and GO. In **Fig. 3.7**, AFM images show that plasticized pea starch with no GO, has a mean roughness of R_a = 8.068 nm, and root mean square roughness R_q = 10.500 nm, but the roughness decreases for pea starch-1% GO nanocomposite (R_a = 7.330, R_q = 10.082 nm), indicating the good compatibility between GO and starch [81]. However, after addition of 2wt% GO, blisters and depressions were visible, indicating aggregations at higher loading. The tensile strength increased form 4.56 MPa to 13.79 MPa, and the young's modulus increased from 0.11GPa to 1.05 GPa, indicating the excellent mechanical reinforcement of starch on addition of only 2wt% GO.

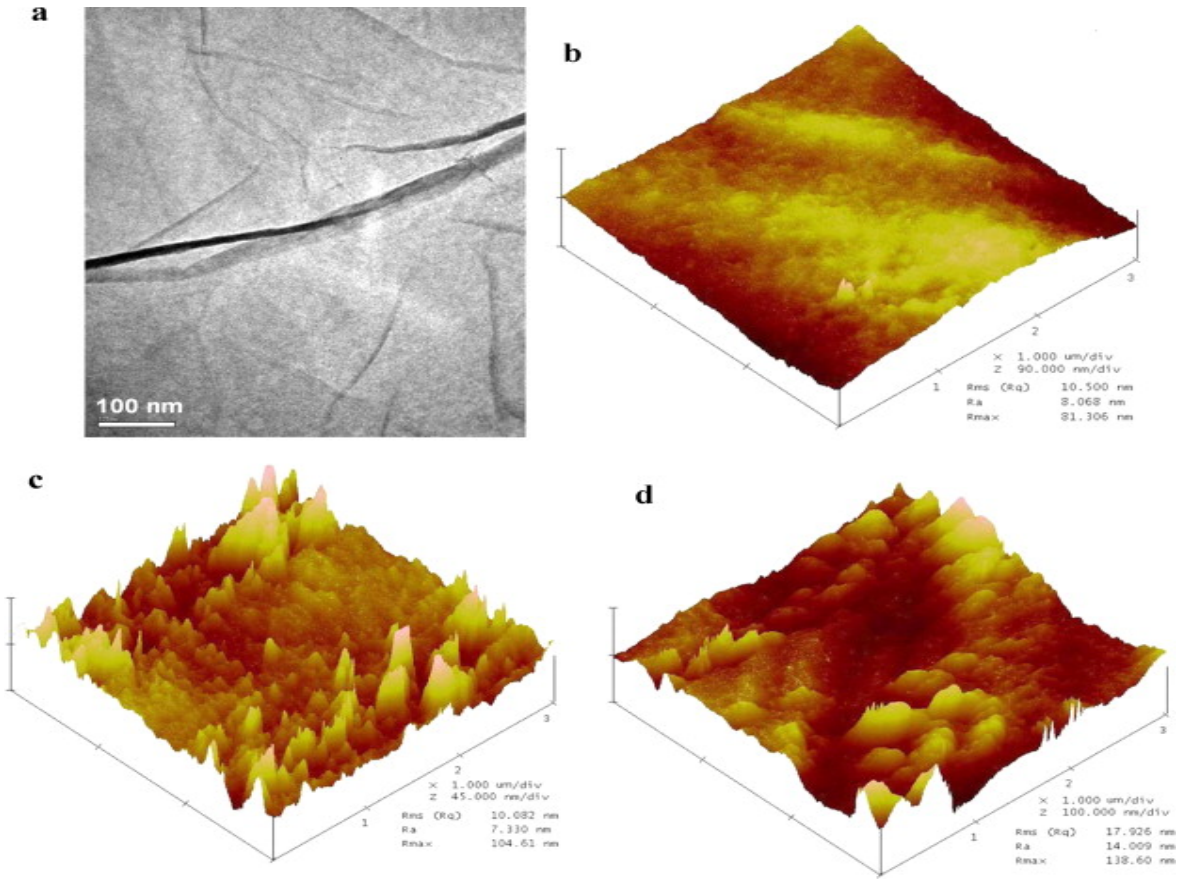

Fig. 3.7. (a) TEM images of Pea starch-GO nanocomposite; AFM images of (b) pea starch, (c) pea starch-1 wt% GO nanocomposite (d) pea starch-2wt% GO nanocomposites. Reprinted with permission from ref [81]. Copyright 2011, Elsevier.

Following the study on pea starch-GO, a study comparing starch-GNS and chitosan-GNS nanocomposites were conducted [82]. The SEM images showed that both pristine chitosan and starch displayed a smooth surface, with chitosan having a smoother surface than starch, but the nanocomposite with 3% graphene loading showed significant roughness, phase separation, with starch showing higher percentage of agglomeration. Mechanical testing on chitosan-graphene and starch graphene composites showed that, the tensile strength first started to increase on addition of graphene, and for chitosan it increased up to 45% on addition of 1.5 wt%, but after that the graphene platelets started to aggregate, the tensile strength began to drop. With 3 wt% graphene loading, the WVTR of chitosan dropped from 53.1 to 40.3 g/m^{2}h and for starch it dropped from 47.8 to 39.7 g/m^2 h. Another study where blend of Chitosan-Starch with Graphene nanofillers, showed that chitosan-starch blend has a higher tensile strength increase compared to starch and chitosan individually [82]. This phenomenon could be attributed to a much stronger formation of

intermolecular hydrogen bonding between NH_3 of the chitosan backbone and OH of the starch. The blend also showed improved water vapor barrier properties, over the previous study[82] , with a WVTR drop from 44.3 to 38.7 g/m^{2}h, at only 2.5 wt% graphene addition.

Chitosan

Among different biodegradable polymer materials, chitosan has received significant consideration as a result of its remarkable properties, for example, biocompatibility, biodegradability, antibacterial properties etc. Biosensor, biological engineering, controlled drug release, packaging, pervaporation etc. are some of the field where the application of chitosan has been investigated. Nonetheless, its usage has been limited due to its poor mechanical properties. Solution casting of graphene had positive effects on the mechanical, thermal, water vapor barrier as well as electrical properties, as evident from the different studies that have been conducted on chitosan-graphene nanocomposites.

Chitosan-RGO nanocomposites [83] were fabricated by dissolving chitosan in an aqueous solution of acetic acid, then addition of 1-7% modified RGO, followed by sonication for 30 min. The XRD pattern of the composite is similar to that of chitosan, hence, it was assumed that, chitosan peaks at $2\theta = 21.3^0$, overlapped the weak peaks of aggregated RGO sheets, indicating RGO did not affect the crystalline structure of chitosan. Young's modulus and tensile strength of CS-6 wt% RGO composite film were measured to be 2.7 and 2.3 times greater than those of chitosan, and exhibited an increase in elongation at break from 1% to 6%. RGO formed a network with conductive properties, across the insulating polymer matrix, caused the conductivity of the composite film to increase in 5 orders of magnitude and the CS-6 wt% RGO composite film exhibited the maximum conductivity of 1.28 S/m, mainly due to its high RGO content and uniform layered structures. However, RGO fillers aggregated at higher weight content (7 wt%), which partly destroyed the electron transport network, leading to the decrease of conductivity. In another study, the high specific surface area and excellent conductivity of RGO, had been combined with the dispersion and film-forming abilities of chitosan, to form a chitosan-graphene film modified Glassy Carbon Electrode (GCE), for the development of a simplified reliable analytical method for the determination of 4-Aminophenol (4-AP) [84]. Graphene enhanced the redox peak currents of 4-AP, lowered the oxidation over potential and decreased the peak-to-peak separation of redox peaks, proving its great potential application of 4-AP detection. In addition to, electrical

conductivity, RGO also has been used to improve the adsorption abilities of chitosan [85]. Large specific surface area CS-RGO mesoporous nanocomposites have been fabricated, for bio-adsorption and removal of anionic azo dye Reactive Black 5 (RB5), where the nanocomposite achieved a removal efficiency of to 97.5%, at initial RB5 concentrations of 1 mg/L, which means, that the solution can be decolorized to nearly colorless using the nanocomposite. This indicated that RGO had significantly improved the dye adsorption properties of chitosan.

Other than RGO, strong interactions between GO and Chitosan (CS) have also been reported [86], where CS-GO nanocomposites were synthesized via solution casting, with adding GO in 6, 12, 18 wt% into chitosan in acetic acid solvent and mixed via magnetic stirring for an hour. The FTIR spectrum of the CS-GO nanocomposite displayed amine stretch from the chitosan and the OH groups from the GO, indicating that the nanocomposite has characteristics similar to both pristine chitosan and GO. The peak representing COOH groups and the C=C groups from GO, shifts to a lower wave number due to hydrogen bonding between the GO and hexatomic ring of the chitosan. The XRD patterns of the films with different content of GO, showed that diffraction angles of the composite films were similar to the pure CS, and the diffraction peaks corresponding to GO were absent even at the highest graphene concentration, indicating their complete exfoliation. Chitosan displayed a prominent diffraction intensity as compared to CS-GO, which indicated that degree of crystallinity of chitosan decrease after adding GO. Strong hydrogen bonding and uniform distribution of GO can be attributed to the increase in tensile strength on the content of graphene oxide. The elongations at break of the composite films decreases compared with the pure chitosan film. Tensile strength of wet state CS-GO film, compared to pristine wet state CS and pristine dry state CS, is 1.7 times and 3 times greater respectively. On the other hand, a study on chitosan GO nanofillers with acetic acid solvent and 24 hr stirring reported 2.23 times increase in tensile strength at only 1 wt% addition of GO [87]. This improvement over the previous study could be attributed to the prolonged mixing time that allowed better dispersion of the filler. This study reported, hydrogen bonding and electrostatic interaction were supported by the FTIR spectra of CS-GO nanocomposites that showed complete disappearance of the characteristic peak for GO at 1730 cm^{-1}, attributed to C=O stretch, and characteristic peak for CS at 1596 cm^{-1} attributed to NH_2 absorbance. In **Fig. 3.8,** XRD peaks of pristine chitosan and CS-GO showed that adding GO contributes to a relatively ordered arrangement of the attached CS chains, resulting in

first two prominent crystalline peaks at 2θ = 18.2 and 23°, as compared to the more amorphous peaks of pristine CS. These findings are very different than the previous study, which reports addition of GO reduced the crystallinity of CS [86]. This once again can be attributed to the prolonged mixing time. The XPS spectra in **Fig. 3.9** shows the N1s spectra of CS and CS-GO nanocomposite. The peak at 401.7eV, which is representative of binding energy for protonated amine, increases in intensity from 7% for pristine CS, to 13% for CS-1% GO. which supports the electrostatic interaction between the negative charge on the surface of GO and N groups of CS[44].

CS nanocomposites with small area GO and RGO, as well as, large area GO and RGO with filler amounts 0.3%–0.9 wt% have also been studied for the purpose of understanding the effect of surface area of GO on property improvements of CS [88]. Field emission scanning electron microscopy (FESEM) showed that, the GO prepared from graphite powder (average lateral size100 μm) and using Hummers method, had a small area of less than 50 μm^2. On the other hand, GO prepared from graphite flakes (average lateral size 400 μm) and using simplified Hummers method, had a large area of about 7000 μm^2. After reduction by sodium hydroxide, drop casting technique was used to produce thin films of small area

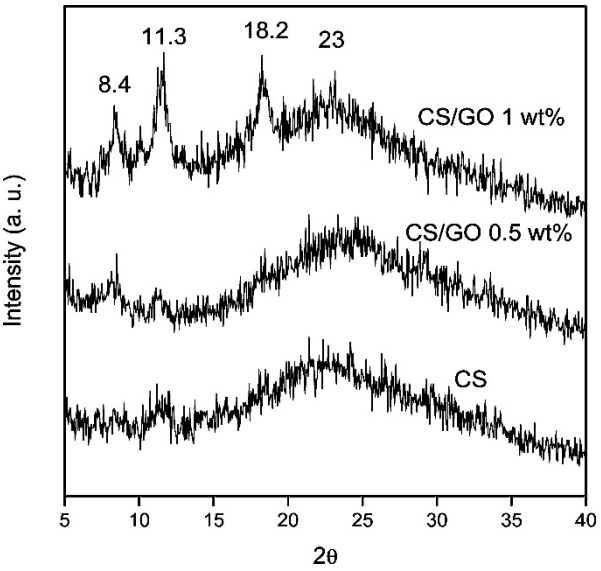

Fig. 3.8. XRD patterns of CS and CS-GO nanocomposite. Reprinted with permission from ref [86]. Copyright 2010, American Chemical Society.

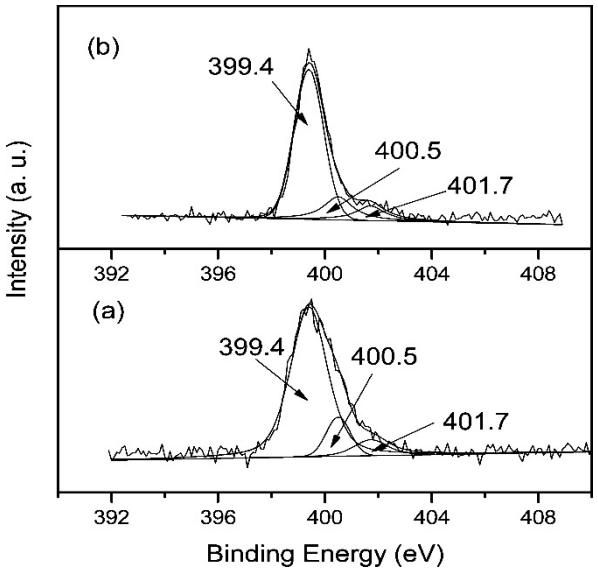

Fig. 3.9. XPS N 1s core-level spectra of (a) CS and (b) the CS-1wt%GO nanocomposite. Reprinted with permission from ref [86]. Copyright 2010, American Chemical Society.

CS-RGO and large area CS-RGO nanocomposite. XRD studies showed that, small area GO and large area GO have diffraction peaks at 10.3° and 9.1°, corresponding to an increased interlayer distance compared to graphite flake and powders. **Table 3.1** and **3.2** shows, the large area GO and RGO composites showed better, glass transition temperature (T_g) and mechanical strength compared to the small area GO and RGO nanocomposites, indicating that increased surface area aided better interaction between biopolymer and resulted in better improvement. CS-small area GO composites had better thermal and tensile properties than CS-small area RGO, which is similar to the findings on starch-GO and starch-RGO study as before [48].

Table 3.1. Effect of Graphene on the mechanical properties of Different Biopolymers

Matrix	Graphene	Preparation	Young's Modulus (%)	Tensile Strength (%)	Ref.
Pea Starch	2 wt% GO	SC	↑854	↑202	[81]
PS	2 wt% GO	SC	—	↑92	[48]
PS	6 wt% RGO	SC	—	↑54	[48]
CS	6 wt% RGO	SC	↑170	↑130	[83]
CS	1 wt% GO	SC	↑51	↑93	[56]
CS	1 wt% GO	SC	↑64	↑122	[87]
CS-Tap-S	3 wt% GNS	SC	—	↑37.5	[89]
CS-OST	2 wt% GO	SC	↑367.9	↑42.9	[90]
Cellulose	0.75 wt% GO	SC	↑31	↑19	[91]
Cellulose	0.27 vol% GO	SC	—	↑20	[92]
RC	3wt%GNP	SC	↑56	↑34	[93]
RC	1.6 wt% GNP	SC	↑111	↑66	[94]
RC	1.6 vol% GONS	SC	↑68	↑67	[39]
BC	5 wt% GO	SC	↑10	↑20	[95]
CMC	1 wt% GO	SC	↑148 ± 5	↑67 ± 6	[40]
CEA	.25 wt% RGO	SC	—	↑31.8	[51]
PLA	0.3wt%GO	SC	↑115	↑95 (YS)	[54]
SA	6 wt% GO	SC	↑391.8	↑59	[96]
SA	1 wt% GO	SC	↑19.6	↑44	[41]
SA	1 WT% MGO	SC	↑37.8	↑68.4	[41]
CC	2 wt% GO	SC	↑280	↑180	[97]
SA-CMC	1 wt% GO	SC	↑1128	↑40	[42]
PLA	0.4wt%GNP	SC	↑156	↑129 (YS)	[54]
PLLA	0.5 wt% GO-g-PLA	MP+ SC	—	↑105.7	[98]
PLA	0.2wt%LGNS	SC	↑18	↑26	[57]

Table 3.1 continued

Matrix	%Graphene	Preparation	Young's Modulus (%)	Tensile Strength (%)	Ref.
PPC	0.1wt%GO	SC	↑1800	↑1000	[99]
PHO	2.5 wt% TRG	SC	↑590	↑9	[100]
PHD	2.5 wt% TRG	SC	↑200	↑16	[100]
PHOe	2.5 wt% TRG	SC	↑280	↑2	[100]
PLA	1wt%PFG	AP+MB	↑22	↑8.6	[101]
PLA	2wt%EG	MB	↑33 approx.	↑10 approx.	[58]
PLA	4 wt% EG	MB	↑55.5	↑18	[102]
PLA	0.3 wt% RGO	MB	—	↑3.4	[103]
PLA-EPO	0.3 wt% RGO	MB	—	↓32	[103]
PLA-PEG	0.3 wt% RGO	MB	—	↓43	[103]
PLA	0.3 wt% GNP	MB	—	↑1.7	[103]
PLA-EPO	0.3 wt% xGNP	MB	—	↓34	[103]
PLA-PEG	0.3 wt% xGNP	MB	—	↓49	[103]
PLA-PEG	0.3 wt% xGNP	MB	↑69.5	↑32.7	[104]
PBAT	5wt%GO	MB	↑41.02	—	[105]
PA	5wt%GO	MB	↑26.9	—	[105]
HPU	0.4wt% GO	IP	—	↓25	[53]
PU	0.8wt%GO	IP	↓80	↓51	[106]
BC	0.48wt% GO	IB	↑120	↑38	[50]
PLGA	2wt%GO	ES	↑205	—	[46]
RC	0.2 wt% GO	WS	↑25	↑50	[49]
SA	4 wt% GO	WS	↑126	↑95	[52]

AP= Admicellar Polymerization; BC = Bacterial Cellulose; C= Cellulose; CC = Cellulose Carbamate; CEA = Cellulose Acetate; CMC = Carboxy Methyl Cellulose; CS = Chitosan; EG = Exfoliated Graphite; EPO = Epoxide; ES = Electrospinning; GNP = Graphene nanoplatelet; GNS = Graphene nanosheet; GO = Graphene Oxide; GO-g-PLA = GO grafted PLA, PLLA = Poly-L-Lactic Acid= ;HPU = Bio-based Hyper-branched Polyurethane; IB = In situ Biosynthesis; IP = In situ Polymerization; LGNS = Lyophilized Graphene nanosheet; MB = Melt Blending; MP = Melt Polycondensation; OST = Oxidized starch; PA = Poly Amide; PBAT = Poly(butylene-adipate-coterephthalate); PEG = Poly ethylene Glycol; PFG = PMMA Functionalized Graphene; PHO = poly (hydroxyoctanoate); PHD = poly (hydroxydecanoate); PHOe = poly (hydroxyoctenoate); PLA = Poly (lactic acid); PLGA = Poly (D, L-lactic-*co*-glycolic acid); PLLA = Poly-L-Lactic Acid; PMMA = poly (methyl methacrylate) PPC = Polypropylene Carbonate; PS = Plasticized starch; PU = Bio-Based Polyurethane; RC = Regenerated Cellulose; RGO = Reduced Graphene Oxide; SA = Sodium Alginate; SC= Solution Casting Tap-S= Tapioca starch; TT = Thermal Treatment; VGNS= Vacuum Filtered Graphene nanosheet; WS = Wet Spinning, YS = Yield Strength

Cellulose

Cellulose is a well-known industrial biopolymer with a wide variety of application like bioadsorption, detergent, paper, packaging etc. In order to overcome its main disadvantage of poor mechanical property and thermal stability, it has been combined with different graphene

nanofillers. Cellulose has a similar structure to starch which has repeating glucose units. However, in cellulose the glucose units are roughly parallel and point slightly up, which is known as beta linkage. This slight difference in structure ultimately results in starch being soluble, but cellulose being insoluble in water. Therefore different solvents have been used for solution casting of, cellulose and cellulose derivatives with graphene, such as, *N*-methylmorpholine-*N*-oxide (NMMO), 1-ethyl-3-methylimidazolium acetate (EMIMAc) monohydrate, *N*,*N*-dimethylacetamide-lithium chloride (DMAC-LiCl) etc.

For solution blending of Cellulose-GO nanocomposite, NMMO [91] had hydrogen bonding capabilities among matrix (cellulose) and filler (GO), so it proved to be a good model system for dispersing and exfoliating the GO in the composite, as well as, an excellent ecofriendly solvent for cellulose. Cellulose-GO nanocomposite were prepared, with GO loadings of 0.2, 0.5, 1, 3, 5wt% and ultra-sonication of 6h at high temperature of 95^{o} C. Improved thermal and electrical properties were observed as shown in **Table 3.2** and **3.3**. Annealing the composite film at a 230^{o} C caused removal of the oxygen-containing groups of the GO, resulting in improved electrical conductivity, from 1×10^{-4} S/m to 1×10^{-2}S/m. Interactions between GO and cellulose through hydrogen bonding, resulted in a step-wise increase in viscosity, and an improved Young's modulus from 73.1 to 97.8 MPa with addition of 0.75 wt % GO. Another efficient as a dispersing agent of GO in cellulose, was LiOH-Urea [92], as tensile strength increased up to 20% at addition of only 0.27 vol%, increased the elongation at break by 335%. For this study, freeze-dried sponge like GO and cellulose, were dispersed in to aqueous LiOH-urea (7wt%-12wt%) solution followed by, freezing and thawing and casting on glass plate [92]. Based on the nearly identical images of cellulose-GO and pristine cellulose found in Raman and XRD results, the study concluded that, there were no chemical interactions between cellulose and GO nanosheets, only physical interactions took place.

Following the research on Cellulose-GO nanocomposite, Regenerated Cellulose (RC)-RGO nanocomposites were investigated [39]. When natural cellulose is solubilized and regenerated, typically forming either a fiber (via electrospinning) or a film (via solution casting), the resultant material is called Regenerated cellulose (RC). For RC-RGO nanocomposite, aqueous NaOH-Urea served as a solvent, dispersing GO uniformly throughout the matrix, supported by TEM images of RC-1.64 vol% GONS nanocomposite (RC 1.64), which showed complete exfoliation into individual nanosheets and homogeneous dispersion. Two-dimensional wide-angle X-ray diffraction (2D-WAXD) shows the characteristic diffraction ring of GONSs is absent in the

cellulose nanocomposite, signifying disappearance of the regular and periodic structure of graphite oxide. On addition of up to 1.64 vol% GONS, increase in mechanical strength is evident from 67% increase in the tensile strength and 68% in Young's modulus, relative to the pristine RC, as shown in **Fig. 3.10.** The authors used the well-known Halpin-Tsai model [107], which is a simulation model for predicting modulus of randomly or unidirectionally distributed nanofiller, and their studies found that the GONSs were more parallel aligned to the film surface, which the authors concluded was due to the gravitational forces and hot pressing during fabrication. **Table 3.3** shows, three times decrease in O_2 permeability coefficient, as the result of improved barrier properties.

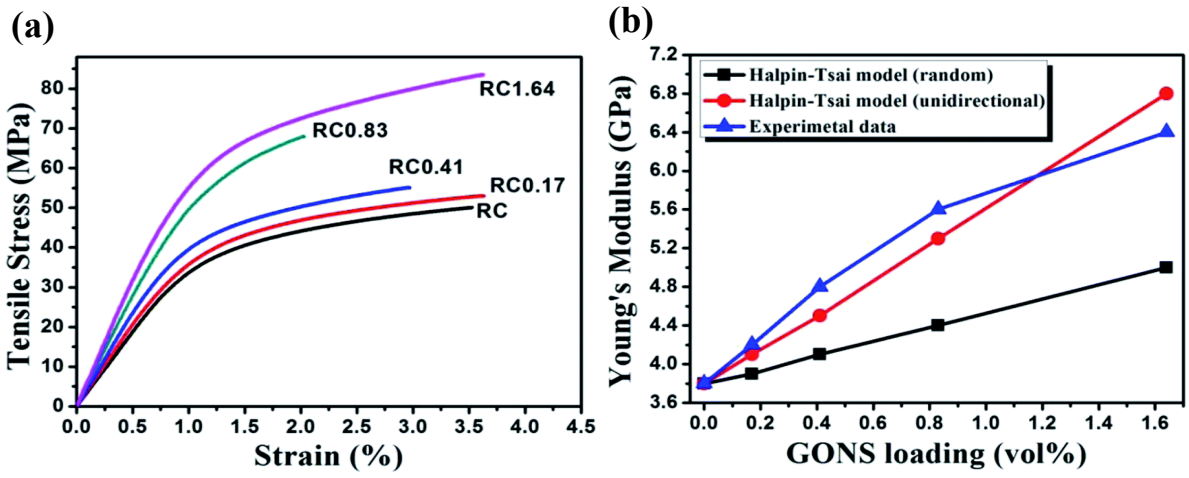

Fig. 3.10. (a) Typical stress–strain curves of RC and the cellulose nanocomposite films with different GONS loadings (b) Young's modulus of the samples as determined experimentally and the theoretical values obtained by Halpin–Tsai models based on the hypothesis that GONSs are randomly or unidirectionally distributed in the cellulose matrix. Reprinted with the permission from ref [39]. Copyright 2014, Royal Society of Chemistry.

For fabrication of RC-GNP nanocomposites, two different types of solvents have been reported which are, EMIMAc [93] and DMAC-LiCl [94]. The study involving EMIMAC solvent involved dissolving of cellulose and GNP at 80ºC, and sonication for 90min, and finally solution casting. SEM and XRD showed homogenous dispersion, so the ionic liquid was an effective dispersing agent for the GNPs. Increase in hydrophobicity with the presence of GNPs was observed using contact angle measurements. FTIR studies showed no significant shifts or changes in the peaks, indicating the incorporation of graphene did not result in any change in the chemical structures of RC. The 3% GNP added to cellulose showed an increase in the tensile strength by 34%. The temperature for 20% weight loss ($T_{20\%}$) of RC improved about 20ºC from 294.95ºC to

314ºC with 5 wt% GNPs content. Gas barrier property of the nanocomposites were also improved, evidenced by lower O_2 and CO_2 permeability. The improvement of thermal properties and gas barrier properties of cellulose-graphene nanocomposites have been shown in **Table 3.2** and **3.3**. The strong interaction between cellulose and GNP, resulted in an impermeable GNP network and lower water affinity of GNP. However, later DMAC-LiCl proved to be a better solvent for efficiently dispersing GNP in RC matrix, as tensile strength improved 67% at 1.6 wt% and 50% thermal decomposition temperature increased 18ºC, at only 0.2 wt% addition of GNP.

Other notable cellulosic derivatives are Hydroxypropyl Cellulose (HPC) and Bacterial cellulose (BC). Hydroxypropyl Cellulose (HPC)-RGO [108] nanocomposites were fabricated by solution mixing at 80°C, followed by dropwise addition of reducing agent hydrazine. Finally, compression molding was applied to obtain the HPC-RGO composite films. Any temperature below 80°C is considered the lower critical solution temperature (LCST) of HPC. Metastable nanospheres of HPC are observed above the LCST, which can clamp GO sheets and finely disperse them, avoiding the possibility of aggregation [108]. The results showed that, nanocomposites prepared by LCST method, compared to conventional solution casting method had improved electrical properties. The electrical conductivity of HPC-graphene composites improved by 2–3 orders of magnitude and percolation threshold value reduced as low as 0.11 vol%. The RGO surface can enhance the electron transfer (ET) rate, which is the fundamental process in electrochemical reactions between enzymes and electrodes, thus, graphene-modified electrodes can be used as electrochemical sensors. Bacterial Cellulose (BC)-GO nanocomposites were prepared [95], by mixing aqueous suspensions of GO and BC, using DI water as the solvent followed by in situ reduction of GO. AFM and TEM measurements indicated the complete exfoliation of GO. Also, the more compact morphology observed with SEM, the prominent change in the C=O peak and the relative intensity change of the C–O stretching vibration peak for FTIR, as well as the weakened peaks in the XRD spectra of BC on different loadings of GO, all indicate good dispersion of GO in the BC matrix. The addition of 5 wt% GO increased Young's modulus and tensile strength by 10% and 20% respectively relative to pristine BC. The composite film with 1 wt% RGO exhibited, a major increase in electrical conductivity by 6 orders of magnitude relative to pristine BC.

A cellulose derivative that has higher solubility than cellulose alone is Carboxymethyl Cellulose (CMC), which is a methylated cellulose derivative. CMC-RGO nanocomposites were

also prepared for sensor applications, where solutions of CMC and GO (50:50 weight) were mixed and reduced with $NaBH_4$ to manufacture a modified electrode for hemoglobin immobilization [109]. CMC has an amphiphilic characteristic, which made it possible to expose the electrical activity center of protein to the solution and the presence of RGO enhanced the electron transfer. RGO-CMC film combines the electron transfer acceleration capabilities of graphene and the biocompatibility offered by CMC. In another study, CMC-GO nanocomposite films with improved properties were investigated [40]. In the case of BC-GO [95] and CMC-GO nanocomposites [40], DI water was not very effective at the intercalation of GO in the matrix, as the tensile strength only increased 22% on addition of 5wt% GO. In contrast, for a derivative of cellulose, Cellulose Carbamate (CC), ultrapure water, functioned as an excellent solvent for CC and GO as, at only an addition of 0.25% addition of GO, the tensile strength increased to 182% [97]. Moreover, the use of Magnetic cellulose (MC)-GO (MCGO) nanocomposite as adsorbent for dye wastewater disposal were explored [110], where cellulose was mixed and dispersed with Fe_3O_4 nanoparticles and GO, by ultrasonication and cross-linking. MCGO nanocomposite was very stable and can easily be recycled and the adsorption efficiency of MCGO was still over 89% after recycling for five times.

Table 3.2. The effects of Graphene on the Thermal Properties of different Biopolymers

Matrix-Graphene	**Preparation**	**Thermal Property**	**Ref.**
PLLA-TRG	IP	T_m (↑)11^{0}C at 2wt% TGA T_g (↑) 9^{0}C at 0.01 wt% DSC	[38]
PAAm-CMC-GO	IP	$T_{50\%}$ (↑) 15^{0}C at 1.6wt%	[111]
PLLA-GO	SC	$t_{0.5}$ ↓ 58% for 2wt% GO at 123°C T_{cc}	[59]
PLA- LGNS; PLA-VGNS	SC	$T_{5\%}$ (↑)10^{0}C at 0.2wt% for LGNS	[57]
PHBV-GNS	SC	T_m (↑)11^{0}C at 6wt% T_g (↑) 2^{0}C at 4wt%	[112]
PLA-RGO; PLA-GNP	SC	T_g (↑) 5^{0}C at 0.4 wt% RGO T_g (↑) 7^{0}C at 0.4 wt% GNP	[54]
Cellulose-GO	SC	$T_{50\%}$ (↑)20^{0}C at 0.25wt%	[91]
RC-GNP	SC	$T_{20\%}$ (↑)20^{0}C at 0.25wt%	[93]
RC-Graphene	SC	$T_{10\%}$ (↑) 20^{0}C at 0.4wt%	[94]
CMC-GO	SC	T_{max} (↑) 10^{0}C at 2wt%	[40]
CEA-RGO	SC	T_{max} (↑) 2^{0}C at 1wt%	[51]

Table 3.2 continued

Matrix-Graphene	Preparation	Thermal Property	Ref.
SA-GO	SC	$T_{3\%}$ (↑) 30^0C at 6wt%	[96]
SA-GO; SA-MGO	SC	T_{end} (↑) 12^0C at 1wt% GO T_{end} (↑)12^0C at 1wt% MGO	[41]
Pea Starch-GO	SC	T_{onset} (↑) 10.2^0C at 2wt% T_{end} (↑) 7.4^0C at 2wt%	[81]
PPC-GO	SC	T_g (↑) 10.5^0C	[99]
PLA-EG	MB	$T_{5\%}$ (↑) 12^0C at 12 wt% $T_{50\%}$ (↑) 11^0C at 12wt%	[102]
PLA-EG	MB	$T_{50\%}$ (↑) 7^0C at 3wt%	[113]
PLLA-GO-g-PLLA	MP	T_m (↑)5^0C at 0.5wt% T_g (↑) 7^0C at 0.5wt%	[98]
PBAT -TRG	MB	T_m (↓) 2^0C at 5wt% T_{cc} (↑) 17^0C at 5wt%	[105]
PA- TRG	MB	T_m (↑) 2^0C at 5wt% T_{cc} (↑) 1^0C at 5wt%	[105]
PLA-TRG	MB	T_m (↓) 1^0C at 5wt% T_{cc} (↑) 19^0C at 5wt%	[105]
Jatropha Curcas Oil based alkyd-epoxy resin-EG		T_{onset} (↑) 38^0C at 5wt% T_{end} (↑) 51^0C at 5wt%	[114]
PLA- CO_3O_4 -f-Graphene	MB	T_{onset} (↑) 14^0C at 1wt%	[115]
PLA-EG; PLA-NG	MB	NG: No Improvements EG: $T_{5\%}$ (↑)14^0C at 3wt%	[58]
CAP-EG	MB	$T_{50\%}$ (↑) 29^0C at 10wt%	[116]
RC-RGO	WS	$T_{50\%}$ (↑)25^0C at 0.2wt%	[49]
DSC= Differential Scanning Calorimetry, PHBV= biodegradable poly (3-hydroxybutyrate-co-4-hydroxybutyrate), TGA= Thermogravimetric Analysis, T_m= Melting Temperature, T_{onset}= Onset Temperature for Thermal Decomposition, T_{max}= Maximum Decomposition Temperature, T_{end}= End Temperature for Thermal Decomposition, T_g= Glass Transition Temperature, T_{cc}= Crystallization Temperature, T_{50}= 50% decomposition Temperature, CO_3O_4 -f-Graphene = Tricobalt tetroxide-functionalized graphene			

Alginate

For solution casting of Alginate-graphene biopolymer nanocomposites, the primary solvents used were double distilled water and tetraethylenepentamine (TEP). [96] Sodium alginate (SA)-GO nanocomposite films were prepared by, preparing GO aqueous suspension using double distilled (DD) water as solvent and then solution mixing at 0 to 6% GO contents. In the FTIR study

of SA and SA-GO, dominant peaks of pristine SA, corresponding to -OH stretching, -COO stretching and of -C-O-C- stretching vibration were visible. The FTIR of SA-GO nanocomposite new peaks are visible, in addition, existing peaks move to a smaller wavelength, indicating strong electrostatic interaction and hydrogen bonds between SA and GO. The XRD images did not show any significant peak changes, which means the SA structure was not significantly affected by GO, so only physical interaction was present. Because of the bonding between SA and GO, thermal and mechanical stability of SA increased, evident from the 59% tensile strength increase at 6% GO. The TG analysis of SA-GO composite films shows higher initial decomposition temperature around 100 °C and temperature for 3% weight loss ($T_{3\%}$) increased by about 30 °C with addition of 6 wt% GO.

To understand the effect of solvents other than DD water, sodium alginate were studied as (SA)-GO and SA-Modified GO (MGO→ surface functionalized with active N sites) nanocomposite films, with tetraethylenepentamine (TEP) as the solvent [41]. For solution casting of SA with GO, tetraethylenepentamine (TEP) was an excellent dispersing agent, compared to DD water [96]. This is evident from the results, when TEP used as a solvent, it promotes the efficient blending of GO in the SA matrix, enabling better interaction of SA and GO, which increases the tensile strength of SA 44% with only 1wt% GO, and 68% with only 1wt% MGO. This could be due to the fact that TEP has a higher polar surface area $88A^{o2}$, which had a much higher compatibility with polar GO, as compared to water which has a polar surface area of $25A^{o2}$ [117]. In addition, FTIR and XRD results of the SA-MGO nanocomposites confirmed interactions between active N sites on MGO and -COO groups of SA, which could have attributed to the positive improvement in mechanical property. The two nanocomposites showed a $5^{o}C$ increase in thermal degradation temperature at 1.5 wt% addition, but at 2 wt% addition, aggregation occurred, and thermal degradation temperature started to decrease. Even though water proved to be an inferior solvent for SA as compared to TEP, the weaker performance of water as a solvent can be compensated by using blend of SA instead of pristine SA. For SA-CMC blend [42] for example, only adding deionized (DI) water as a solvent during the solution casting, aided homogenous dispersion of GO, which helped to increase the tensile strength up to 120% with only the addition of 1 wt% GO. Here, GO also has acted as a crosslinker to the CMC-SA blend, where it forms hydrogen bonding with the OH groups of CMC and SA, promoting their miscibility. Contact angle measurement showed that the hydrophilicity of the films increased with increasing GO content

and was highest for 4 wt% GO. The presence of a number of hydrophilic functional groups in the graphene oxide, caused decrease in water contact angle measurement with increasing GO content with 4% CMC-SA-GO having the lowest contact angle, meaning highest hydrophilic characteristics. The nearly identical XRD pattern of the GO-CMC-SA nanocomposite and the CMC-SA blend indicated that GO sheets were efficiently exfoliated.

Poly (lactic Acid)

PLA is considered biodegradable and biocompatible, which has made it possible to be used in short term packaging, tissue scaffolds, internal sutures, implant devices etc. Different studies have incorporated graphene nanofiller into the PLA matrix, in order to overcome its shortcomings like poor mechanical property, low crystallization rate and thermal resistance. In the case of solution casting of PLA-graphene nanocomposites, a similar trend is observed as the previous studies where, using the same percentage of nanofiller, with different solvents has yielded significantly different property enhancement in the nanocomposites. Solvents like N,N-dimethyl-formamide (DMF), chloroform, acetone were used in dispersing graphene derivative in PLA matrices. The dispersibility of graphene varies depending on the solvents Hydrogen Component δ_H, also known as Hansen Solubility Parameter HSP, and polar surface energy γ_s^p [79]. The HSP of DMF, acetone and chloroform are 25 $MPa^{0.5}$, 17.4 $MPa^{0.5}$ and 8.8 $MPa^{0.5}$ respectively, so the order of HSP is DMF> acetone> chloroform. As DMF has the highest HSP, so graphene derivatives should be most dispersible in DMF, resulting in better performance enhancement like improved mechanical property and thermal property.

This coincided with the study on PLA- graphene nanosheets (GNS) nanocomposites, where lyophilized GNS was dispersed in DMF with 2h mixing and sonication [57]. The effectiveness of dispersion between PLA-lyophilized GNS (LGNS) and PLA-vacuum-filtered GNS nanosheets (VGNS) were compared, where LGNS showed superior properties in producing organically dispersible GNS powders, which enhanced PLA's thermal and mechanical properties. The FESEM showed that the GNSs displayed flake-like morphology, resulting in a good interaction, whereas, Tapping-mode AFM images, revealed a lower thickness of LGNSs compared to single layer GO nanosheets, which was the result of the removal of oxide groups. XRD measurements of pristine PLA and PLA-GNS showed, similar XRD patterns for the PLA-0.2wt% GNS and pristine PLA, with no graphite layer structure peak or graphite oxide peak, indicating that the GNS was dispersed

in single sheets. The tortuous path created by the GNS prevented escape of volatile thermally decomposed products, as a result, the onset temperature for 5% weight loss of PLA, increased by 10 °C, at only 0.2wt% GNS addition. DMF was also used as a solvent for Poly-L-lactic acid (PLLA), with GO at 0.5, 1 and 2wt% loading and a similar ultrasonication time of 2h, to prepare P L L A - G O nanocomposites [45]. The study showed that crystallization temperature of PLLA decreased at higher loading of GO. Similar to the XRD results of PLA-GNS nanocomposites as shown before [57], the XRD results showed, identical patterns for pristine PLLA and the PLLA-GO nanocomposites, indicating that crystal structure of PLLA remains unchanged despite the addition of GO in the PLLA-GO nanocomposites. However, the shift to lower temperatures in the DSC crystallization peak temperature of PLLA-GO nanocomposites with increasing GO loading indicates that the non-isothermal cold crystallization behavior of PLLA has been facilitated by the influence of GO loading.

Another solvent used for solution intercalation of graphene and PLA, is acetone, which has a lower dispersibility parameter compared to DMF, but has more environment friendly impact [79]. PLA-GO and PLA-GNP nanocomposite were fabricated using acetone solvent with sonication for 5 h, for the purpose of comparing the biocompatibility, topography, roughness and wettability of the two composites [47]. XPS results showed that, both graphite and GNP had a low degree of oxidation, as both are mainly constituted by carbon, but after the oxidation of graphite to GO, the oxygen percentage increased from 9 to15%. GNP having less group with oxygen compared GO, proved less compatible with the polymer matrix and more hydrophobic, with 2.3^{o} increase in the water contact angle of PLA-GNP film compared to pristine PLA films.

In another study, to understand the effect of plasticization, plasticized and unplasticized PLA-GO and PLA-GNP nanocomposite films [54] were prepared using chloroform solvent. The plasticized nanocomposite films exhibited 100% higher tensile strength and Young's modulus than pristine PLA and for unplasticized nanocomposite films at the same concentration of graphene, the tensile strength was only 15% higher and Young modulus was 85% higher than control. Increase in glass transition temperature with increasing filler loading in PLA was observed, and a maximum at PLA-0.4 wt% GO and PLA-0.4wt%GNP nanocomposite was observed, as shown in **Fig. 3.11**. The T_g for PLA-GNP is 2^{o}C higher than that for PLA-GO, probably owing to the more planar geometry of the filler resulting in confined chain segment mobility. In order to prevent

stacking of GO sheets in situ melt polycondensation method was used to graft GO onto the surface of PLA, producing GO grafted PLA (GO-g-PLA) and this was used as a nanofiller for poly-L-lactic acid (PLLA) [98]. Successful prevention of aggregation and efficient dispersion by chloroform solvent, resulted in increase in flexural and tensile strength by 114.3% and 105.7%, respectively.

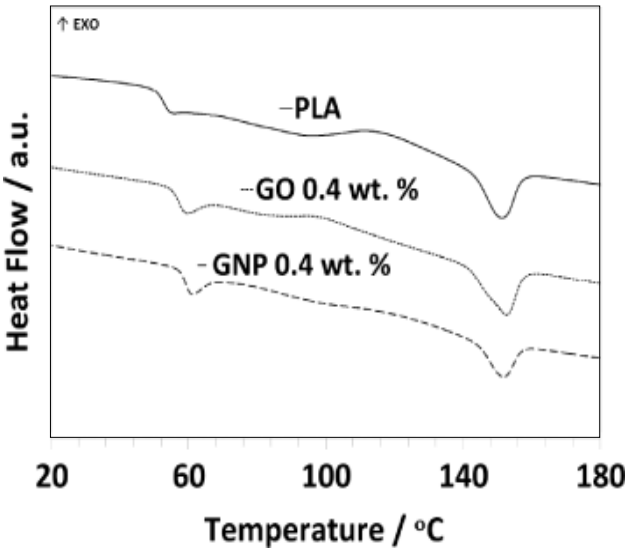

Fig. 3.11. Representative DSC curves for PLA films dried in a vacuum oven. Reprinted with permission from [54]. Copyright 2013, John Wiley and Sons.

The solvents most frequently used for solution casting of PLA and graphene are chloroform [54, 98], acetone [47] and DMF [45, 57, 59]. Comparing PLA-GNP [54] and PLA-LGNS [57], DMF has been shown to be the better solvent compared to Chloroform. When DMF is used as a efficient dispersion occurs and it takes only 0.2 wt% nanofiller to increase the tensile strength by 26%, but when Chloroform is used, it takes twice the amount of nanofiller to increase the tensile strength by 20%. However, considering environmental impact of the biopolymer nanocomposite, chloroform is a better option, as DMF has been linked to serious toxic effects.

Poly (hydroxyalkanoate)

Another class of biodegradable and renewable biopolymers with elastomeric qualities are the medium-chain-length poly (hydroxyalkanoate)s (PHA_{mcl}). Three different types of PHA_{mcl} polymers; poly (hrydroxyoctanoate) (PHO), poly (hydroxydecanoate), PHD and poly (hydroxyoctenoate) (PHOe) were functionalized with thermally reduced graphene (TRG) nanoparticles, using solution casting technique with chloroform solvent and characterized, for the purpose of producing biodegradable packaging sensors and charge dissipating applications [100, 118]. Length of chain packing, ability of non-covalent interaction with TRG and covalent crosslinking greatly affected the matrices under study. The results showed that the addition of up to 2.5 vol % TRG to PHA_{mcl} increases the Young's modulus of PHO by 590%, PHD by 200% and PHOe by 280%. Due to the presence of long aliphatic extension from the polyester backbone in

the PHA_{mcl} polymers, it caused some steric hindrance and reduced the intensity of hydrogen bonding between, the PHA_{mcl} and TRG. Hence the shorter chain PHA_{mcl} polymer, PHO has the least hindrance to hydrogen bonding and therefore the highest modulus enhancement. TEM images of the PHA_{mcl} shows best dispersion is observed in PHO, while the worst dispersion is seen in PHOe. On the other hand, the SEM images show that for PHO at only 0.5% loading of TRG result in entanglement, while entanglement in PHOe composite does not occur until 2.5% loading of TRG. The melting temperature increased by 1−3 °C, and the electrical conductivity increased over 7 orders of magnitude. On the other hand, rheology data indicated that percolation of a pseudo-solid network based on graphene-polymer entanglements occurred at a distinctly lower graphene loading close to zero vol%. In another study, iron nanoparticle embedded Fe_3O_4-RGO grafted Poly (3-hydroxybutyrate-*co*-3-hydroxyvalerate) (Fe_3O_4/RGO-g-PHBV) using solution casting method had been investigated [119], which displayed excellent improvement of mechanical strength, magnetic properties over control, as well as, its proliferation into micro-porous 3D scaffold, indicated the biocompatibility of the Fe_3O_4/RGO-g-PHBV nanocomposite based supporting biomaterials.

Other Biopolymers

Panzavolta et al. [120] also utilized solution casting, to obtain nanocomposites of type 'A' gelatin from pig skin and GO amounts (0.5, 1, 1.5, 2 wt%). The different GO were added to aqueous gelatin solution in acetic acid- double distilled water 60-40 (v-v) at 50^0C. Addiiton of 1% GO efficiently improved the Young's modulus upto 50%. Stainer et al. [43] and Zhan et al. [121] used solution casting for incorporation of exfoliated graphite into biodegradable natural rubber [122]. Also Hyper branched polyurethane (HPU)-GO nanocomposite, using solution intercalation has also been explored by Thakur and Karak [53].

In summary, solution intercalation is a simple, yet highly efficient graphene-biopolymer nanocomposite fabrication technique, as it involves simplified and effective dispersion of graphite in polymer matrix. Due to its simplicity and lack of need for heavy equipment is the main reason for its frequent use in fabrication of many different biopolymer-graphene nanocomposites. It also enables the synthesis of intercalated nanocomposites based on polymers with low polarity, by preparing a homogenous dispersion of the filler. However, the removal of solvents sometimes adds

a disadvantage, as it can occasionally be costly and time consuming. Therefore, this technique is not applicable for large-scale industrial productions.

Table 3.3. The Effects of graphene on gas and vapor barrier properties of different biopolymers

Matrix- Graphene Derivative	Permeability	Ref
1. RC-GNP	P_{CO_2} ↓ 35% at 3wt% P_{O_2} ↓ 27% at 3wt%	[93]
2. RC- GONS*	P_{O2} ↓ 98% at 1.64vol%	[39]
3. PLA- GNP; PLA -GO	P_{O_2} ↓ 67.3% at 0.4wt% for GO P_{O_2} ↓ 68.1% at 0.4wt% for GNP P_{N_2} ↓ 75.4% at 0.2wt% for GO P_{N_2} ↓ 78.5% at 0.6wt% for GNP	[54]
4. PS -GO, PS-RGO	WVP ↓ 43.7% at 4wt% GO WVP ↓ 34.9% at 8wt% RGO	[48]
5. Pea Starch-GO	WVP ↓ 39.4% at 1.5wt% GO at 98% RH	[81]
*GONS= Graphene Oxide Nano-sheets		

3.4.2 Melt Intercalation

The method of mixing and shearing of graphene into the molten state of polymer, to produce graphene-biopolymer nanocomposites, is called melt intercalation. During melt intercalation, chemical functionalization with oxygen causes some defects in the matrix; restricting electron flow and reducing the electric conductivity. So, melt intercalated nanocomposites find application in electrical energy storage devices. Nevertheless, graphene functionalized with oxygen groups is widely used in polymer research, and is preferred for melt intercalation [123]. In the literature, melt blending has been used for incorporating different forms of graphene with biopolymers like PLA, cellulose, bio-polyamide (PA), Poly (butylene adipate-co-terephthalate) (PBAT) etc. The different reaction conditions, like rotor speed, reaction temperature, residence time, post extrusion processing conditions have been varied, to study the effect on the end product. Increased rotor speed demonstrated better mechanical and thermal property improvement, but addition of

plasticizer was able to compensate for reduced speed. The morphological characterization and resultant property change have been discussed briefly in this section.

Thermal and mechanical properties of PLA-Exfoliated Graphite (EG) and PLA-Natural Graphite (NG), produced through twin screw extrusion was studied [58]. The nanocomposites were fabricated using 180 rpm screw speed, at 200ºC temperature and 0.1%, 0.5%. 1%, 3%, 5% and 7% EG and NG were incorporated in the PLA-graphite nanocomposite. SEM images confirmed the homogeneous dispersion of EG in the PLA-EG nanocomposite and aggregate formation of NG in the PLA-NG nanocomposite. The XRD patterns of NG shows a sharp diffraction peak at 2θ = 26.5ºand EG shows a very weak and broad diffraction at 2θ = 25.0º. On the other hand, in **Fig. 3.12,** for PLA-EG nanocomposites, peaks of EG at 2θ = 25.0º were not visible, even at a percentage as high as 7%, but for PLA-NG nanocomposites, a clear diffraction peak at 2θ = 26.5º, was detected at a very small NG loading of 0.5%. This indicated EG is homogenously dispersed in the PLA matrix and NG indicating aggregate crystalline nature in the PLA-NG nanocomposite, which agrees with the SEM images. The poor dispersion of NG, lead to very low improvement of thermal degradation temperature and only a slight improvement of mechanical strength in the PLA-NG nanocomposite. On the other hand since EG dispersed homogeneously in the PLA matrix it successfully increased thermal decomposition temperature, electrical conductivity and Young's moduli in the PLA-EG nanocomposites, as shown in **Table 3.1**, **3.2** and **3.4**. A similar study with PLA-EG

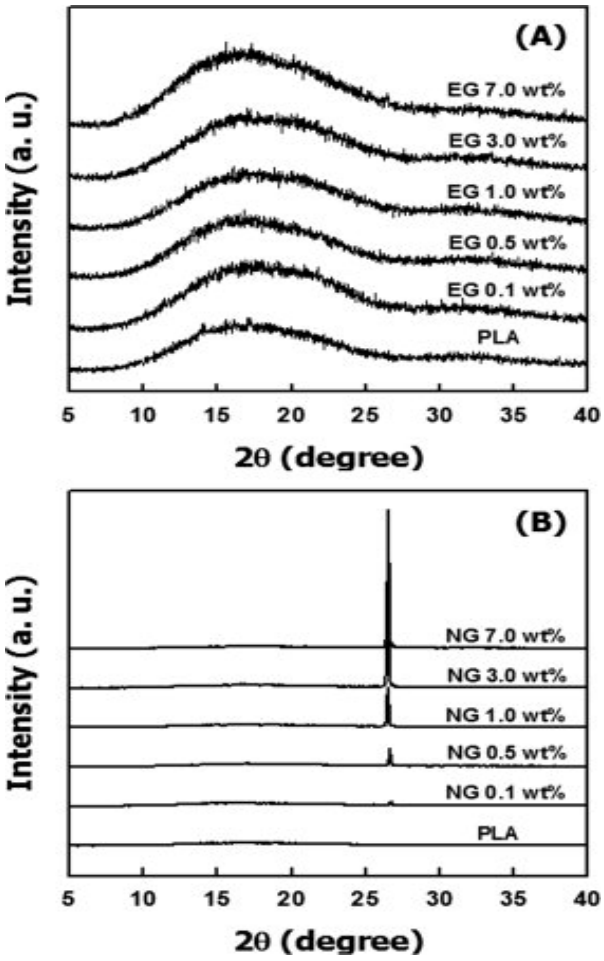

Fig. 3.12. XRD Images of (a) PLA-EG and (b) PLA-NG nanocomposites showing various concentrations of graphite. Reprinted with permission from ref [58]. Copyright 2010, John Wiley and Sons.

nanocomposite using melt blending [102] showed, decrease in average molecular weight (M_n) of PLA can be prevented by increasing the EG loading from 2 to 6 wt%. Purification and pre-dispersion of EG nanofiller, where a two-step mixing of 3 min premixing at 30 rpm-speed, followed by 7 min mixing at 70 rpm, helped to avoid excessive increase of the torque during melting of PLA, and ensured preservation of PLA and enhanced mechanical performance. This showed even better performance than compared to PLA-EG nanocomposite with one step mixing in the previous study [58].

Other studies were conducted where different conditions for melt intercalation, as well as different forms of graphene was applied. The effects of different rotor speeds and time of melt blending, were studied [113], where pristine PLA at rotor speed of 100 and 150 rpm for 10 min; and PLA-3% EG for 50, 100, 150 rpm at 10 min were studied. The study showed that increase in screw speed and residence time, significantly improved EG dispersion and ultimately lead to better thermal stability. However, when plasticizer is used with PLA, lower rotor speed can result in reasonable increase in mechanical property as evidenced by the study of PLA- xGnP and PLA-rGO nanocomposites, plasticized with Polyethylene Glycol (PEG) and epoxy (EPO). The study used melt blending, with a rotor speed of 50 rpm, at 170 °C for 10 min. RGO showed higher aspect ratio, better dispersion and interfacial stress transfer, compared to xGnP, proven by higher tensile strength increase in PLA/RGO, as compared to PLA/xGNP [103]. In another study, effect of cooling rate on melt intercalated-compression molded PLA graphene nanocomposites were investigated [124]. PLA-GNP nanocomposite films using two different routes were fabricated, where the one route for making nanocomposite included melt compounding followed by compression molding and the second route consists of solution casting (SC) GNP filler into the PLA matrix. The higher crystallinity and broader glass transition region for solution cast films compared to the other two types of films indicate that the chloroform solvent, which was used in solution casting, acts as a plasticizer. Micro-porosity and dispersion-distribution of GNP coupled with the excluded volume effect, contributed in the higher percolation threshold of SC films compared to slow cooled films. Conductive PLA with PMMA-functionalized graphene (PFG) was prepared using, admicellar polymerization was used to functionalize GO with PMMA, and the resultant PFG, improved the interfacial adhesion between PLA and PFG [101] . Similarly, Tricobalt tetroxide was adsorbed on graphene via in situ reduction process, which was then used to melt processing with PLA, to successfully reduce fire hazards of aliphatic polyesters. [115]. The

findings in these researches of PLA-graphene nanocomposite have been have been summarized in **Table 3.1, 3.2, 3.3** and **3.4**.

Other polymers that have been used to make nanocomposite with graphene, using the process of melt blending include poly-L-lactide (PLA), bio-polyamide (PA), (butylene adipate-co-terephthalate) (PBAT). 1-5% amounts of TRG was added to PBAT, PA and PLA [105], to study their improvement in properties. FTIR and Nuclear Magnetic Resonance (NMR) spectra confirmed that, PLA and PBAT did not go through any structural change but the free amide bonds in PA underwent chemical changes in the presence of graphene. In **Fig. 3.13,** the TEM images of the nanocomposites with 5% graphene shows that PBAT and PA had uniform dispersion, with large number of exfoliated single graphene platelet. However, PLA showed large aggregates present in the matrix. The researchers concluded that in addition to the shear in the extruder, the varying extent of interaction of biopolymer with graphene resulted in varying amount of filler distribution. Strong hydrogen bonding and Van der Waals force, between PA and TRG resulted in 8.6 times shear modulus increase in PA at 5% loading compared to 2.2 and 1.8 times in PLA and PBAT. In addition, there was 1.8 times increase in tensile modulus of PA, compared to 1.4 times for PLA and 1.1 times for PBAT.

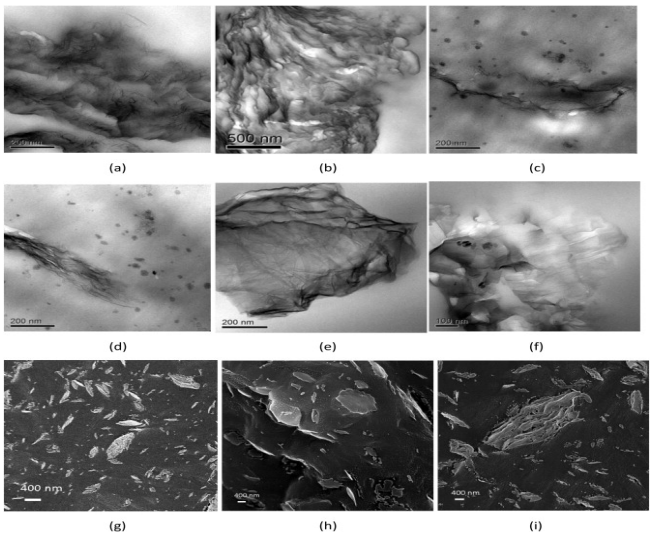

Fig. 3.13. TEM micrographs of nanocomposites containing; (a), (b) PBAT-5% TRG, (c), (d) PA-5% TRG and (e), (f) PLA-5% TRG nanocomposites; (g)–(i) shows the SEM micrographs of fracture surface of 5% filler nanocomposites of PBAT, PA and PLA respectively. Reprinted with permission from ref [105]. Copyright 2014, Elsevier.

Table 3.4. The effects of graphene on the electrical properties of different biopolymers

Biopolymer-Graphene	Electrical Property	Ref
PLA- EG	Resistivity ↓ 100% at 3wt%	[58]
PLLA- TRG	Conductivity ↑ 1.63×10^{-2} S/m from 7.16 $\times10^{-14}$ S/m at 2wt%	[38]
PP-GO	Conductivity ↑ 1.10 wt% 9.25×10^{-9} to 9.33×10^{-4} S/m	[125]
PS-RGO	Conductivity ↑ 500% at 2wt%	[48]
HPC-RGO	Percolation threshold ↓ 0.11vol%	[108]
BC -RGO	Conductivity ↑ 1.1×10^{-4} S/m from 1.1×10^{-12} S/m at 1wt%	[95]
Cellulose-GO	Conductivity ↑ 1×10^{-4} S/m from 1×10^{-6} to S/m at 5wt%	[91]
RC-Graphene	Conductivity ↑ 9.25×10^{-8} S/m at 1wt%	[94]
CAP-EG	Electrical Volume Resistivity ↓ 10^6 Ωcm from 10^{15} Ωcm	[116]

Melt blending has also been used, for the property improvements of Cellulose acetate propionate (CAP) after reinforcement with expanded graphite nanoplatelets [116]. Thermal stability of the CAP-EG nanocomposite increased due to graphene forming an interlocking network with the polymer matrix and preventing oxygen permeation. An electrical conduction path was created at 5 and 7 wt% EG, which decreased The electrical volume resistivity of CAP-EG composites were reduced from 10^{15} to 10^6 Ωcm, as shown in **Table 3.4**. In addition, graphene improved the dynamic storage modulus of CAP.

The advantage of using melt intercalation process, over solution intercalation is that, it does not require any noxious solvents and offers large-scale manufacturing, using twin-screw extruder, two roll mills or internal mixer. However, in melt intercalation, the stacking of pristine graphene occurs due to the large aspect ratio of graphene sheets and involves Van der Waals forces and strong interactions between single sheets of graphene, which ultimately leads to inferior mechanical property compared to in solution intercalation and situ polymerization.

3.4.3 In Situ Polymerization

In situ polymerization is another notable method for fabrication of graphene-biopolymer nanocomposites, and this method consists of dispersing the nanofiller in monomer solution, followed by polymerization of monomers to achieve the nanocomposites. As the monomer reacts with itself to form the polymer, it binds to the nanoparticles and helps them intercalate and disperse, resulting in increased interlayer spacing and exfoliation of the layered structure of graphite. So as a result, a prior exfoliation step is not required for good dispersion of graphene-based filler [9]. In this process, polymer matrices can undergo covalent bonding with functionalized GO sheets through various condensation reactions. Nevertheless, this technique can also be applied for non-covalent bonded composites, for example, Polypropylene (PP)-GO [125], Polyethylene (PE)-graphite [126] and Polymethyl-methacrylate (PMMA)-GO [127]. Different researches that use in-situ polymerization to incorporate graphene and its derivative into biopolymers like PLA, Cellulose, Alginate, hyperbranched polyurethane (HPU), Bio-based thermosetting polyurethane (PU) etc. for the purpose of improving their properties have been discussed briefly in this section.

In situ ring-opening polymerization of lactide, in the presence of different concentrations of thermally reduced graphene (TRG), was studied [38]. Poly (l-lactic acid) (PLLA)-thermally reduced graphene oxide composites were formed using TRG in different concentrations of 0.01, 0.1, 1.0, 1.5 and 2.0 wt% and heating the mixture at 170ºC for 4h. TEM images of the nanocomposite formed suggested that the graphene sheets consist of only a few layers. In XRD, FTIR and Raman techniques were used to prove successful conversion of lactide into PLLA and successful reduction of GO into TRG. The maximum thermal decomposition temperature was for PLLA-1.5% TRG (GLLA-1.5) was increased 16ºC. The percolation threshold for PLLA was between 1-1.5% TRG, which means only addition of 1% TRG, developed conductive behavior in PLLA. In addition, the electrical conductivity increased 12 orders of magnitude for GLLA-2.00, which is shown in **Table 3.4.**

In situ polymerization was applied [111] to reinforce a Polyacrylamide PAAm- Carboxy Methyl Cellulose (CMC) matrix, by adding GO and CMC to the polymerization mixture of Acrylamide (AAm), followed by ionic cross-linking with Al^{3+}. This is attributed to the stronger hydrogen-bonding interaction between oxygen-containing groups of GO and polar functional groups of the PAAm side chains. The XRD pattern for pure GO showed a peak at $2\theta = 10.6^0$, disappeared in the XRD image of PAAm-CMC-GO nanocomposites, suggesting uniform

dispersion without aggregation. FTIR characterization confirmed hydrogen bond formation between the oxygen-containing groups of the GO sheets and the N–H bond of PAAM, observed through a decrease in intensity and in some cases disappearance of the characteristic GO peaks in the FTIR spectra of PAAm-CMC-GO nanocomposites. The compressive strength of the 1.6 wt% PAAm-CMC-GO, increased by approximately 260% compared with the 0.4wt% PAAm-CMC-GO hydrogel, indicating a significant mechanical strength improvement at a small GO loading. Another study that used in situ polymerization with PAAm [120] in order to fabricate an excellent water soluble dye. The study combined the effective bio-adsorption abilities of alginate and GO [128, 129] by preparing SA-PAAm-GO nanocomposite hydrogels. The synthesis of the ternary nanocomposite included adding SA and GO, to the free radical polymerization of acrylamide (AAm), followed by cross-linking of Ca^{2+}. The compressive strength of SA-PAAm-5% GO nanocomposite hydrogel increased 270 times, and deformation to rupture increased from 35% to ~70.5%. The tensile strength of PAAm increased from 8.4 MPa to 201.7 MPa for the three component cross-linked nanocomposite. The bond formation of GO with cationic dyes through the amino and azo groups, and strong π-π interactions, causes GO nanocomposite hydrogel to exhibit excellent adsorbent capabilities.

In other studies, in-situ polymerization in bio-based thermosetting polyurethane (PU)-GO nanocomposites, showed a slight decrease in tensile strength and Young's Modulus [106]. However, chemical interaction between PU and GO, improved the elongation at break 1.3 times, toughness 0.8 times and storage modulus increased up to 21% at 0.4 wt% GO loading. Even though PU-GO nanocomposites did not display increase in tensile strength, a study on castor oil-modified hyperbranched polyurethane (HPU)-GO nanocomposites [53] reported high toughness (4267 MJ m^{-3}), 128% increase in tensile strength and 115% increased elongation at break. This improvement over the PU-GO study could be due to the strong hydrogen bonding and polar-polar interaction present in the HU interface, which offered a more stable interface with lesser number of defects. The different property changes that has been observed in the biopolymer nanocomposite fabricated through in-situ polymerization have been summarized in **Table 3.1, 3.2, 3.3** and **3.4**..

The advantage of this process is that, the good dispersion of graphene-based filler is not dependent upon prior exfoliation step, but in order to perform the polymerization procedure, monomer units and large amounts of reagents are required. Hence, this process does not find application in naturally existing biopolymers.

3.5 Applications, Future Perspective and Challenges

In situ biosynthesis [50], is also a nanocomposite fabrication method used to prepare bacterial cellulose -graphene nanocomposites, in a graphene-dispersed culture medium. Besides this, wet spinning [52, 130, 131], electrospinning [46], freeze drying [132–136] are methods that have also been applied to produce biopolymer graphene nanocomposites that result in products in the form of beads, hydrogels, nanofibers etc., used in various applications. A notable application of nanocomposites prepared from biopolymer-graphene derivatives, are bioadsorbents for heavy metal ions [135, 137–144] and different types of industrial dye [85, 110, 131, 145–152]. The nanocomposites have also been used in the biomedical field, for drug removal [130], drug encapsulation [153, 154], drug delivery [155] scaffolding materials [136, 156–158], post operation anticancer implants [159], fibers with wound healing capabilities [160], for immobilization of hemoglobin [109, 161], immobilization of myoglobin [162], bilirubin adsorbent [163] etc. Also the nanocomposites have been used to make solar cells [164], as well as, in the field of electrochemistry as glassy carbon electrodes for the detection of 4-Aminophenol [84], Bisphenol A [165], Dopamine [166], Urea [167], Ascorbic Acid [167], as binder for Li-ion Battery [168] and so on. In addition to already existing applications, different biopolymer graphene nanocomposites can be applied in a variety of fields. Smart biodegradable packaging with built in sensor for food and pharmaceuticals quality control and storage, can be synthesized using different biopolymers, utilizing different forms of graphene, like reduced graphene or CVD graphene in biopolymer-graphene sandwich structure. Nanocomposites can also be used as substrate for, antibody-antigen based Field effect transistor (FET) biosensor, [169, 170] as well as synthetic detecting element (liposome, aptamer, and peptide) based FET biosensors [171]. In addition, different nanocomposites can be used as gate dielectrics for different types of biosensor, for enhanced current modulation throughout the biosensor, for improved detection of different food toxins, allergen, as well as pathogenic bacteria.

The inherent biodegradability of biopolymers poses a great challenge in the nanocomposites study as, controlled environment is required to prevent premature degradation. Control of environment is achieved through control of moisture, nutrients or microorganisms, although in some environments, such as the tropics, this becomes a more difficult challenge. Another limitation is the temperature stability of most biopolymers, so handling during high temperature experimentations also becomes a hindrance [172]. In addition, the weaker performance of

biopolymers compared to synthetic polymers when graphene is added is also another shortcoming. The weaker performance of the biopolymer nanocomposites can be attributed to the more random configuration of the repeating units in biopolymers and the resulting steric hindrance compared to the more controlled and organized configurations of synthetic polymers. **Table 3.5.** shows, comparison of the young's modulus of biopolymer-graphene nanocomposite with synthetic polymer-graphene nanocomposites which provides a clear difference between biopolymer and synthetic polymer- graphene nanocomposites.

Table 3.5. Comparison of highest reported young's modulus increase of some common biopolymer-graphene and synthetic polymer-graphene nanocomposites

Biopolymer				Synthetic Polymer			
Polymer	Graphene	YM (%)	Ref.	Polymer	Graphene	YM (%)	Ref.
Starch	2 wt% GO	854	[81]	PVA	2.5vol% GO	128	[173]
CS	6 wt% RGO	170	[83]	SF	0.12 vol% GO	200	[174]
CC	2 wt% GO	280	[97]	PCL	2.4 vol% GO	108	[175]
SA-CMC	1 wt% GO	1128	[42]	NR	1.2vol% TRG	750	[176]
PLA	0.4wt%GNP	156	[54]	PDMS	2.2 vol% TRG	1100	[176]
PHO	2.5 wt% TRG	590	[100]	TPU	2.4 vol% GO	900	[177]
PLGA	2wt%GO	205	[46]	SBR	0.8% TRG	390	[176]
NR = Natural Rubber; PCL = poly (ε-caprolactone); PDMS = polydimethylsiloxane; PVA = Poly (vinyl alcohol); SBR = Styrene-butadiene rubber; SF = Silicone foam; TPU = Tetra polyurethane; YM = Young's Modulus							

3.6 Conclusion

The discovery of graphene as nanofiller has led to the production of low cost, light weight, and high-reinforcement nanocomposites, leading the way to a wide range of innovative applications. The presence of carboxyl, amino or hydroxyl groups in the biopolymers lead to a very efficient interaction with the functional groups on graphene and GO. These materials have environment-friendly impact in the various novel applications that emerge because the amount of graphene in the film is usually very small <5%. The property improvement is not only due to the nanofiller but also, is the consequence of the reaction condition and an optimal graphene percentage, which is evident from the comparison of the mechanical property enhancement of all

the biopolymer nanocomposite. Most of the papers used hydrazine for graphene reduction, which is detrimental for the environment, even though nanocomposites were prepared for bio-based application, hence the eco-friendly route to reduce graphene also need to be explored. This paper has attempted to highlight the routes for more bio-based material available for the reduction of graphene. There has been extensive research on polysaccharides, PLAs and other biopolymers as discussed above but the field of proteins is yet to be explored. Unlike synthetic polymers [178, 179], the grafting synthesis techniques for incorporating graphene derivatives to biopolymers have not been extensively explored. This area also needs to be explored as it may produce better performing nanocomposites compared to the solution blending and melt blending techniques. Also there has been some report of release of nanomaterials like silver (Ag), Cu, Ag-zeolites, montmorillonite nanoclay, from its host polymer matrix in some applications [180]. There has not been enough research on graphene release from its polymer /biopolymer host matrix, so more research needs to be conducted in this field, to ensure safe and efficient application of graphene and its derivatives.

- Conflicts of interest: The authors declare no conflict of interest

3.7 References

1. Petersen K, Væggemose Nielsen P, Bertelsen G, et al (1999) Potential of biobased materials for food packaging. Trends in Food Science & Technology 10:52–68. doi: 10.1016/S0924-2244(99)00019-9

2. Mark JE (1996) Ceramic-reinforced polymers and polymer-modified ceramics. Polymer Engineering & Science 36:2905–2920.

3. Mittal V (2007) Polypropylene-layered silicate nanocomposites: filler matrix interactions and mechanical properties. Journal of Thermoplastic Composite Materials 20:575–599.

4. Mittal V (2008) Mechanical and gas permeation properties of compatibilized polypropylene–layered silicate nanocomposites. Journal of applied polymer science 107:1350–1361.

5. Ray SS, Yamada K, Okamoto M, Ueda K (2003) New polylactide-layered silicate nanocomposites. 2. Concurrent improvements of material properties, biodegradability and melt rheology. Polymer 44:857–866.

6. Ray SS, Bandyopadhyay J, Bousmina M (2007) Thermal and thermomechanical properties of poly [(butylene succinate)-co-adipate] nanocomposite. Polymer degradation and stability 92:802–812.

7. Favier V, Cavaille JY, Canova GR, Shrivastava SC (1997) Mechanical percolation in cellulose whisker nanocomposites. Polymer Engineering & Science 37:1732–1739.

8. Luecha J, Sozer N, Kokini JL (2010) Synthesis and properties of corn zein/montmorillonite nanocomposite films. Journal of Materials Science 45:3529–3537. doi: 10.1007/s10853-010-4395-6

9. Norazlina H, Kamal Y (2015) Graphene modifications in polylactic acid nanocomposites: a review. Polymer Bulletin 72:931–961.

10. Terzopoulou Z, Kyzas GZ, Bikiaris DN (2015) Recent advances in nanocomposite materials of graphene derivatives with polysaccharides. Materials 8:652–683.

11. Dreyer DR, Ruoff RS, Bielawski CW (2010) From conception to realization: an historial account of graphene and some perspectives for its future. Angewandte Chemie International Edition 49:9336–9344.

12. Novoselov KS, Geim AK, Morozov SV, et al (2004) Electric field effect in atomically thin carbon films. science 306:666–669.

13. Avouris P, Dimitrakopoulos C (2012) Graphene: synthesis and applications. Materials today 15:86–97.

14. Zhu Y, Murali S, Cai W, et al (2010) Graphene and graphene oxide: synthesis, properties, and applications. Advanced materials 22:3906–3924.

15. Boehm H-P (2010) Graphene—how a laboratory curiosity suddenly became extremely interesting. Angewandte Chemie International Edition 49:9332–9335.

16. Chung DDL (2016) A review of exfoliated graphite. Journal of Materials Science 51:554–568.

17. Shokrieh MM, Esmkhani M, Shahverdi HR, Vahedi F (2013) Effect of graphene nanosheets (GNS) and graphite nanoplatelets (GNP) on the Mechanical properties of epoxy nanocomposites. Science of Advanced Materials 5:260–266.

18. Lerf A, He H, Forster M, Klinowski J (1998) Structure of graphite oxide revisited‖. The Journal of Physical Chemistry B 102:4477–4482.

19. Dreyer DR, Park S, Bielawski CW, Ruoff RS (2010) The chemistry of graphene oxide. Chemical Society Reviews 39:228–240.

20. Depan D, Girase B, Shah JS, Misra RDK (2011) Structure–process–property relationship of the polar graphene oxide-mediated cellular response and stimulated growth of osteoblasts on hybrid chitosan network structure nanocomposite scaffolds. Acta biomaterialia 7:3432–3445.

21. Kim H, Abdala AA, Macosko CW (2010) Graphene/polymer nanocomposites. Macromolecules 43:6515–6530.

22. Dervishi E, Biris AR, Watanabe F, et al (2011) Few-layer nano-graphene structures with large surface areas synthesized on a multifunctional Fe:Mo:MgO catalyst system. Journal of Materials Science 47:1910–1919. doi: 10.1007/s10853-011-5980-z

23. Singh V, Joung D, Zhai L, et al (2011) Graphene based materials: past, present and future. Progress in materials science 56:1178–1271.

24. Jayasena B, Reddy CD, Subbiah S (2013) Separation, folding and shearing of graphene layers during wedge-based mechanical exfoliation. Nanotechnology 24:205301. doi: 10.1088/0957-4484/24/20/205301

25. Guan G, Lu J, Jiang H (2016) Preparation, characterization, and physical properties of graphene nanosheets and films obtained from low-temperature expandable graphite. Journal of Materials Science 51:926–936.

26. Chen G, Weng W, Wu D, et al (2004) Preparation and characterization of graphite nanosheets from ultrasonic powdering technique. Carbon 42:753–759.

27. Celzard A, Mareche JF, Furdin G, Puricelli S (2000) Electrical conductivity of anisotropic expanded graphite-based monoliths. Journal of Physics D: Applied Physics 33:3094.

28. Pötschke P, Abdel-Goad* M, Pegel S, et al (2009) Comparisons among electrical and rheological properties of melt-mixed composites containing various carbon nanostructures. Journal of Macromolecular Science, Part A 47:12–19.

29. Yasmin A, Luo J-J, Daniel IM (2006) Processing of expanded graphite reinforced polymer nanocomposites. Composites Science and Technology 66:1182–1189.

30. Zheng W, Lu X, Wong S-C (2004) Electrical and mechanical properties of expanded graphite-reinforced high-density polyethylene. Journal of Applied Polymer Science 91:2781–2788.

31. Jang BZ, Zhamu A (2008) Processing of nanographene platelets (NGPs) and NGP nanocomposites: a review. Journal of Materials Science 43:5092–5101.

32. Potts JR, Dreyer DR, Bielawski CW, Ruoff RS (2011) Graphene-based polymer nanocomposites. Polymer 52:5–25.

33. Brodie BC (1859) On the atomic weight of graphite. Philosophical Transactions of the Royal Society of London 149:249–259.

34. Staudenmaier L (1898) Verfahren zur darstellung der graphitsäure. Berichte der deutschen chemischen Gesellschaft 31:1481–1487.

35. William S, Hummers JR, Offeman RE, others (1958) Preparation of graphitic oxide. J Am Chem Soc 80:1339.

36. Shao G, Lu Y, Wu F, et al (2012) Graphene oxide: the mechanisms of oxidation and exfoliation. Journal of Materials Science 47:4400–4409. doi: 10.1007/s10853-012-6294-5

37. Krishnan D, Kim F, Luo J, et al (2012) Energetic graphene oxide: challenges and opportunities. Nano today 7:137–152.

38. Yang J-H, Lin S-H, Lee Y-D (2012) Preparation and characterization of poly (l-lactide)–graphene composites using the in situ ring-opening polymerization of PLLA with graphene as the initiator. Journal of Materials Chemistry 22:10805–10815.

39. Huang H-D, Liu C-Y, Li D, et al (2014) Ultra-low gas permeability and efficient reinforcement of cellulose nanocomposite films by well-aligned graphene oxide nanosheets. Journal of Materials Chemistry A 2:15853–15863.

40. Yadav M, Rhee KY, Jung IH, Park SJ (2013) Eco-friendly synthesis, characterization and properties of a sodium carboxymethyl cellulose/graphene oxide nanocomposite film. Cellulose 20:687–698.

41. Nie L, Liu C, Wang J, et al (2015) Effects of surface functionalized graphene oxide on the behavior of sodium alginate. Carbohydrate polymers 117:616–623.

42. Yadav M, Rhee KY, Park SJ (2014) Synthesis and characterization of graphene oxide/carboxymethylcellulose/alginate composite blend films. Carbohydrate polymers 110:18–25.

43. Stanier DC, Patil AJ, Sriwong C, et al (2014) The reinforcement effect of exfoliated graphene oxide nanoplatelets on the mechanical and viscoelastic properties of natural rubber. Composites Science and Technology 95:59–66.

44. He L, Wang H, Xia G, et al (2014) Chitosan/graphene oxide nanocomposite films with enhanced interfacial interaction and their electrochemical applications. Applied Surface Science 314:510–515.

45. Wang H, Qiu Z (2011) Crystallization behaviors of biodegradable poly (l-lactic acid)/graphene oxide nanocomposites from the amorphous state. Thermochimica Acta 526:229–236.

46. Yoon OJ, Jung CY, Sohn IY, et al (2011) Nanocomposite nanofibers of poly (d, l-lactic-co-glycolic acid) and graphene oxide nanosheets. Composites Part A: Applied Science and Manufacturing 42:1978–1984.

47. Pinto AM, Moreira S, Gonçalves IC, et al (2013) Biocompatibility of poly (lactic acid) with incorporated graphene-based materials. Colloids and Surfaces B: Biointerfaces 104:229–238.

48. Ma T, Chang PR, Zheng P, Ma X (2013) The composites based on plasticized starch and graphene oxide/reduced graphene oxide. Carbohydrate polymers 94:63–70.

49. Tian M, Qu L, Zhang X, et al (2014) Enhanced mechanical and thermal properties of regenerated cellulose/graphene composite fibers. Carbohydrate polymers 111:456–462.

50. Si H, Luo H, Xiong G, et al (2014) One-Step In Situ Biosynthesis of Graphene Oxide–Bacterial Cellulose Nanocomposite Hydrogels. Macromolecular rapid communications 35:1706–1711.

51. Liu L, Shen Z, Liang S, et al (2014) Graphene for reducing bubble defects and enhancing mechanical properties of graphene/cellulose acetate composite films. Journal of Materials Science 49:321–328.

52. He Y, Zhang N, Gong Q, et al (2012) Alginate/graphene oxide fibers with enhanced mechanical strength prepared by wet spinning. Carbohydrate Polymers 88:1100–1108.

53. Thakur S, Karak N (2013) Bio-based tough hyperbranched polyurethane–graphene oxide nanocomposites as advanced shape memory materials. RSC Advances 3:9476–9482.

54. Pinto AM, Cabral J, Tanaka DAP, et al (2013) Effect of incorporation of graphene oxide and graphene nanoplatelets on mechanical and gas permeability properties of poly (lactic acid) films. Polymer International 62:33–40.

55. Faghihi S, Gheysour M, Karimi A, Salarian R (2014) Fabrication and mechanical characterization of graphene oxide-reinforced poly (acrylic acid)/gelatin composite hydrogels. Journal of Applied Physics 115:83513.

56. Pan Y, Wu T, Bao H, Li L (2011) Green fabrication of chitosan films reinforced with parallel aligned graphene oxide. Carbohydrate polymers 83:1908–1915.

57. Cao Y, Feng J, Wu P (2010) Preparation of organically dispersible graphene nanosheet powders through a lyophilization method and their poly (lactic acid) composites. Carbon 48:3834–3839.

58. Kim I-H, Jeong YG (2010) Polylactide/exfoliated graphite nanocomposites with enhanced thermal stability, mechanical modulus, and electrical conductivity. Journal of Polymer Science Part B: Polymer Physics 48:850–858.

59. Wang H, Qiu Z (2012) Crystallization kinetics and morphology of biodegradable poly (l-lactic acid)/graphene oxide nanocomposites: Influences of graphene oxide loading and crystallization temperature. Thermochimica Acta 527:40–46.

60. Park S, Ruoff RS (2009) Chemical methods for the production of graphenes. Nature nanotechnology 4:217–224.

61. Yi M, Shen Z, Zhang X, Ma S (2012) Vessel diameter and liquid height dependent sonication-assisted production of few-layer graphene. Journal of Materials Science 47:8234–8244. doi: 10.1007/s10853-012-6720-8

62. Wan L, Liu P, Zhang T, et al (2014) Exfoliation and reduction of graphene oxide at low temperature and its resulting electrocapacitive properties. Journal of Materials Science 49:4989–4997.

63. Lehtola J, Hakala M, Hamalainen K (2010) Structure of liquid linear alcohols. The Journal of Physical Chemistry B 114:6426–6436.

64. Gao J, Liu F, Liu Y, et al (2010) Environment-friendly method to produce graphene that employs vitamin C and amino acid. Chemistry of Materials 22:2213–2218.

65. Dreyer DR, Murali S, Zhu Y, et al (2011) Reduction of graphite oxide using alcohols. Journal of Materials Chemistry 21:3443–3447.

66. Zhu C, Guo S, Fang Y, Dong S (2010) Reducing sugar: new functional molecules for the green synthesis of graphene nanosheets. ACS nano 4:2429–2437.

67. Akhavan O, Ghaderi E, Aghayee S, et al (2012) The use of a glucose-reduced graphene oxide suspension for photothermal cancer therapy. Journal of Materials Chemistry 22:13773–13781.

68. Feng Y, Feng N, Du G (2013) A green reduction of graphene oxide via starch-based materials. RSC Advances 3:21466–21474.

69. Akhavan O, Kalaee M, Alavi ZS, et al (2012) Increasing the antioxidant activity of green tea polyphenols in the presence of iron for the reduction of graphene oxide. Carbon 50:3015–3025.

70. Kuila T, Bose S, Khanra P, et al (2012) A green approach for the reduction of graphene oxide by wild carrot root. Carbon 50:914–921.

71. Thakur S, Karak N (2012) Green reduction of graphene oxide by aqueous phytoextracts. Carbon 50:5331–5339.

72. Esfandiar A, Akhavan O, Irajizad A (2011) Melatonin as a powerful bio-antioxidant for reduction of graphene oxide. Journal of Materials Chemistry 21:10907–10914.

73. Liu J, Fu S, Yuan B, et al (2010) Toward a universal “adhesive nanosheet” for the assembly of multiple nanoparticles based on a protein-induced reduction/decoration of graphene oxide. Journal of the American Chemical Society 132:7279–7281.

74. Salas EC, Sun Z, Luttge A, Tour JM (2010) Reduction of graphene oxide via bacterial respiration. AcS Nano 4:4852–4856.

75. Kim Y-K, Kim M-H, Min D-H (2011) Biocompatible reduced graphene oxide prepared by using dextran as a multifunctional reducing agent. Chemical communications 47:3195–3197.

76. Roy N, Sengupta R, Bhowmick AK (2012) Modifications of carbon for polymer composites and nanocomposites. Progress in Polymer Science 37:781–819.

77. Young RJ, Kinloch IA, Gong L, Novoselov KS (2012) The mechanics of graphene nanocomposites: a review. Composites Science and Technology 72:1459–1476.

78. Zhang H-B, Zheng W-G, Yan Q, et al (2010) Electrically conductive polyethylene terephthalate/graphene nanocomposites prepared by melt compounding. Polymer 51:1191–1196.

79. Dai J, Wang G, Ma L, Wu C (2015) Study on the surface energies and dispersibility of graphene oxide and its derivatives. Journal of Materials Science 50:3895–3907.

80. Zheng P, Ma T, Ma X (2013) Fabrication and properties of starch-grafted graphene nanosheet/plasticized-starch composites. Industrial & Engineering Chemistry Research 52:14201–14207.

81. Li R, Liu C, Ma J (2011) Studies on the properties of graphene oxide-reinforced starch biocomposites. Carbohydrate Polymers 84:631–637.

82. Ashori A (2014) Effects of graphene on the behavior of chitosan and starch nanocomposite films. Polymer Engineering & Science 54:2258–2263.

83. Wang X, Bai H, Yao Z, et al (2010) Electrically conductive and mechanically strong biomimetic chitosan/reduced graphene oxide composite films. Journal of Materials Chemistry 20:9032–9036.

84. Yin H, Ma Q, Zhou Y, et al (2010) Electrochemical behavior and voltammetric determination of 4-aminophenol based on graphene–chitosan composite film modified glassy carbon electrode. Electrochimica Acta 55:7102–7108.

85. Cheng J-S, Du J, Zhu W (2012) Facile synthesis of three-dimensional chitosan–graphene mesostructures for reactive black 5 removal. Carbohydrate Polymers 88:61–67.

86. Han D, Yan L, Chen W, Li W (2011) Preparation of chitosan/graphene oxide composite film with enhanced mechanical strength in the wet state. Carbohydrate Polymers 83:653–658.

87. Yang X, Tu Y, Li L, et al (2010) Well-Dispersed Chitosan/Graphene Oxide Nanocomposites. ACS Appl Mater Interfaces 2:1707–1713. doi: 10.1021/am100222m

88. Lim HN, Huang NM, Loo CH (2012) Facile preparation of graphene-based chitosan films: Enhanced thermal, mechanical and antibacterial properties. Journal of Non-Crystalline Solids 358:525–530.

89. Ashori A, Bahrami R (2014) Modification of physico-mechanical properties of chitosan-tapioca starch blend films using nano graphene. Polymer-Plastics Technology and Engineering 53:312–318.

90. Ma J, Liu C, Li R, Wang J (2012) Properties and structural characterization of oxide starch/chitosan/graphene oxide biodegradable nanocomposites. Journal of Applied Polymer Science 123:2933–2944.

91. Kim C-J, Khan W, Kim D-H, et al (2011) Graphene oxide/cellulose composite using NMMO monohydrate. Carbohydrate Polymers 86:903–909.

92. Wu Y, Li W, Zhang X, et al (2014) Clarification of go acted as a barrier against the crack propagation of the cellulose composite films. Composites Science and Technology 104:52–58.

93. Mahmoudian S, Wahit MU, Imran M, et al (2012) A facile approach to prepare regenerated cellulose/graphene nanoplatelets nanocomposite using room-temperature ionic liquid. Journal of nanoscience and nanotechnology 12:5233–5239.

94. Zhang X, Liu X, Zheng W, Zhu J (2012) Regenerated cellulose/graphene nanocomposite films prepared in DMAC/LiCl solution. Carbohydrate Polymers 88:26–30.

95. Feng Y, Zhang X, Shen Y, et al (2012) A mechanically strong, flexible and conductive film based on bacterial cellulose/graphene nanocomposite. Carbohydrate polymers 87:644–649.

96. Ionita M, Pandele MA, Iovu H (2013) Sodium alginate/graphene oxide composite films with enhanced thermal and mechanical properties. Carbohydrate polymers 94:339–344.

97. Yao L, Lu Y, Wang Y, Hu L (2014) Effect of graphene oxide on the solution rheology and the film structure and properties of cellulose carbamate. Carbon 69:552–562.

78. Li W, Xu Z, Chen L, et al (2014) A facile method to produce graphene oxide-g-poly (L-lactic acid) as an promising reinforcement for PLLA nanocomposites. Chemical Engineering Journal 237:291–299.

99. Gao J, Chen F, Wang K, et al (2011) A promising alternative to conventional polyethylene with poly (propylene carbonate) reinforced by graphene oxide nanosheets. Journal of Materials Chemistry 21:17627–17630.

100. Barrett JSF, Abdala AA, Srienc F (2014) Poly(hydroxyalkanoate) Elastomers and Their Graphene Nanocomposites. Macromolecules 47:3926–3941. doi: 10.1021/ma500022x

101. Lei L, Qiu J, Sakai E (2012) Preparing conductive poly (lactic acid)(PLA) with poly (methyl methacrylate)(PMMA) functionalized graphene (PFG) by admicellar polymerization. Chemical engineering journal 209:20–27.

102. Murariu M, Dechief AL, Bonnaud L, et al (2010) The production and properties of polylactide composites filled with expanded graphite. Polymer Degradation and Stability 95:889–900.

103. Chieng BW, Ibrahim NA, Yunus WMZW, et al (2014) Effects of Graphene Nanoplatelets and Reduced Graphene Oxide on Poly (lactic acid) and Plasticized Poly (lactic acid): A Comparative Study. Polymers 6:2232–2246.

104. Chieng BW, Ibrahim NA, Yunus WMZW, Hussein MZ (2013) Poly (lactic acid)/poly (ethylene glycol) polymer nanocomposites: effects of graphene nanoplatelets. Polymers 6:93–104.

105. Mittal V, Chaudhry AU, Luckachan GE (2014) Biopolymer–Thermally reduced graphene nanocomposites: Structural characterization and properties. Materials Chemistry and Physics 147:319–332.

106. Zhang J, Zhang C, Madbouly SA (2015) In situ polymerization of bio-based thermosetting polyurethane/graphene oxide nanocomposites. Journal of Applied Polymer Science 132:

107. Affdl JCH, Kardos JL (1976) The Halpin-Tsai equations: A review. Polym Eng Sci 16:344–352. doi: 10.1002/pen.760160512

108. Liao R, Lei Y, Wan J, et al (2012) Dispersing graphene in hydroxypropyl cellulose by utilizing its LCST behavior. Macromolecular Chemistry and Physics 213:1370–1377.

109. Cheng Y, Feng B, Yang X, et al (2013) Electrochemical biosensing platform based on carboxymethyl cellulose functionalized reduced graphene oxide and hemoglobin hybrid nanocomposite film. Sensors and Actuators B: Chemical 182:288–293.

110. Shi H, Li W, Zhong L, Xu C (2014) Methylene blue adsorption from aqueous solution by magnetic cellulose/graphene oxide composite: Equilibrium, kinetics, and thermodynamics. Industrial & Engineering Chemistry Research 53:1108–1118.

111. Zhang H, Zhai D, He Y (2014) Graphene oxide/polyacrylamide/carboxymethyl cellulose sodium nanocomposite hydrogel with enhanced mechanical strength: preparation, characterization and the swelling behavior. RSC Advances 4:44600–44609.

112. Sridhar V, Lee I, Chun HH, Park H (2013) Graphene reinforced biodegradable poly (3-hydroxybutyrate-co-4-hydroxybutyrate) nano-composites. Express Polymer Letters 7:320–328.

113. Hassouna F, Laachachi A, Chapron D, et al (2011) Development of new approach based on Raman spectroscopy to study the dispersion of expanded graphite in poly (lactide). Polymer Degradation and Stability 96:2040–2047.

114. Gogoi P, Boruah M, Bora C, Dolui SK (2014) Jatropha curcas oil based alkyd/epoxy resin/expanded graphite (EG) reinforced bio-composite: Evaluation of the thermal, mechanical and flame retardancy properties. Progress in Organic Coatings 77:87–93.

115. Wang X, Song L, Yang H, et al (2012) Cobalt oxide/graphene composite for highly efficient CO oxidation and its application in reducing the fire hazards of aliphatic polyesters. Journal of Materials Chemistry 22:3426–3431.

116. Jeon GW, An J-E, Jeong YG (2012) High performance cellulose acetate propionate composites reinforced with exfoliated graphene. Composites Part B: Engineering 43:3412–3418.

117. Pubchem TETRAETHYLENEPENTAMINE | C8H23N5 - PubChem. https://pubchem.ncbi.nlm.nih.gov/compound/tetraethylenepentamine#section=Top. Accessed 9 Mar 2016

118. Barrett J (2014) Physical and Biochemical Strategies for Improving the Yield and Material Properties of Polyhydroxyalkanoate Biopolymers.

119. Pramanik N, De J, Basu RK, et al (2016) Fabrication of magnetite nanoparticle doped reduced graphene oxide grafted polyhydroxyalkanoate nanocomposites for tissue engineering application. RSC Adv 6:46116–46133. doi: 10.1039/C6RA03233H

120. Panzavolta S, Bracci B, Gualandi C, et al (2014) Structural reinforcement and failure analysis in composite nanofibers of graphene oxide and gelatin. Carbon 78:566–577.

121. Zhan Y, Lavorgna M, Buonocore G, Xia H (2012) Enhancing electrical conductivity of rubber composites by constructing interconnected network of self-assembled graphene with latex mixing. Journal of Materials Chemistry 22:10464–10468.

122. Rose K, Steinbüchel A (2005) Biodegradation of natural rubber and related compounds: recent insights into a hardly understood catabolic capability of microorganisms. Applied and Environmental Microbiology 71:2803–2812.

123. Hu Y, Su X (2013) Chemically Functionalized Graphene and Their Applications in Electrochemical Energy Conversion and Storage. Advances in Graphene Science

124. Sullivan EM, Gerhardt RA, Wang B, Kalaitzidou K (2016) Effect of compounding method and processing conditions on the electrical response of exfoliated graphite nanoplatelet/polylactic acid nanocomposite films. Journal of Materials Science 51:2980–2990.

125. Huang Y, Qin Y, Zhou Y, et al (2010) Polypropylene/graphene oxide nanocomposites prepared by in situ Ziegler- Natta polymerization. Chemistry of Materials 22:4096–4102.

126. Fim F de C, Guterres JM, Basso NR, Galland GB (2010) Polyethylene/graphite nanocomposites obtained by in situ polymerization. Journal of Polymer Science Part A: Polymer Chemistry 48:692–698.

127. Jang JY, Kim MS, Jeong HM, Shin CM (2009) Graphite oxide/poly (methyl methacrylate) nanocomposites prepared by a novel method utilizing macroazoinitiator. Composites Science and Technology 69:186–191.

128. Xue Z, Zhao S, Zhao Z, et al (2016) Thermodynamics of dye adsorption on electrochemically exfoliated graphene. Journal of Materials Science 51:4928–4941. doi: 10.1007/s10853-016-9798-6

129. Duru İ, Ege D, Kamali AR (2016) Graphene oxides for removal of heavy and precious metals from wastewater. Journal of Materials Science 51:6097–6116. doi: 10.1007/s10853-016-9913-8

130. Wu S, Zhao X, Li Y, et al (2013) Adsorption of ciprofloxacin onto biocomposite fibers of graphene oxide/calcium alginate. Chemical engineering journal 230:389–395.

131. Li Y, Sun J, Du Q, et al (2014) Mechanical and dye adsorption properties of graphene oxide/chitosan composite fibers prepared by wet spinning. Carbohydrate polymers 102:755–761.

132. Wan Y, Chen X, Xiong G, et al (2014) Synthesis and characterization of three-dimensional porous graphene oxide/sodium alginate scaffolds with enhanced mechanical properties. Materials Express 4:429–434.

133. Zhang J, Cao Y, Feng J, Wu P (2012) Graphene-oxide-sheet-induced gelation of cellulose and promoted mechanical properties of composite aerogels. The Journal of Physical Chemistry C 116:8063–8068.

134. Wang Y, Yadav S, Heinlein T, et al (2014) Ultra-light nanocomposite aerogels of bacterial cellulose and reduced graphene oxide for specific absorption and separation of organic liquids. RSC Advances 4:21553–21558.

135. Zhang Y, Liu Y, Wang X, et al (2014) Porous graphene oxide/carboxymethyl cellulose monoliths, with high metal ion adsorption. Carbohydrate polymers 101:392–400.

136. Mohandes F, Salavati-Niasari M (2014) Freeze-drying synthesis, characterization and in vitro bioactivity of chitosan/graphene oxide/hydroxyapatite nanocomposite. RSC Advances 4:25993–26001.

137. Algothmi WM, Bandaru NM, Yu Y, et al (2013) Alginate–graphene oxide hybrid gel beads: an efficient copper adsorbent material. Journal of colloid and interface science 397:32–38.

138. Yang H, Li H, Zhai J, et al (2014) Magnetic prussian blue/graphene oxide nanocomposites caged in calcium alginate microbeads for elimination of cesium ions from water and soil. Chemical Engineering Journal 246:10–19.

139. Debnath S, Maity A, Pillay K (2014) Magnetic chitosan–GO nanocomposite: Synthesis, characterization and batch adsorber design for Cr (VI) removal. Journal of Environmental Chemical Engineering 2:963–973.

140. Li L, Luo C, Li X, et al (2014) Preparation of magnetic ionic liquid/chitosan/graphene oxide composite and application for water treatment. International journal of biological macromolecules 66:172–178.

141. Li L, Fan L, Sun M, et al (2013) Adsorbent for chromium removal based on graphene oxide functionalized with magnetic cyclodextrin–chitosan. Colloids and Surfaces B: Biointerfaces 107:76–83.

142. Liu L, Li C, Bao C, et al (2012) Preparation and characterization of chitosan/graphene oxide composites for the adsorption of Au (III) and Pd (II). Talanta 93:350–357.

143. Jiao C, Xiong J, Tao J, et al (2016) Sodium alginate/graphene oxide aerogel with enhanced strength–toughness and its heavy metal adsorption study. International journal of biological macromolecules 83:133–141.

144. Najafabadi HH, Irani M, Rad LR, et al (2015) Removal of Cu2+, Pb2+ and Cr6+ from aqueous solutions using a chitosan/graphene oxide composite nanofibrous adsorbent. RSC Adv 5:16532–16539.

145. Li Y, Du Q, Liu T, et al (2013) Methylene blue adsorption on graphene oxide/calcium alginate composites. Carbohydrate polymers 95:501–507.

146. Ma T, Chang PR, Zheng P, et al (2014) Fabrication of ultra-light graphene-based gels and their adsorption of methylene blue. Chemical Engineering Journal 240:595–600.

147. Fan L, Luo C, Sun M, et al (2012) Preparation of novel magnetic chitosan/graphene oxide composite as effective adsorbents toward methylene blue. Bioresource technology 114:703–706.

148. Liu X, Zhou Y, Nie W, et al (2015) Fabrication of hydrogel of hydroxypropyl cellulose (HPC) composited with graphene oxide and its application for methylene blue removal. Journal of Materials Science 50:6113–6123. doi: 10.1007/s10853-015-9166-y

149. Sun L, Fugetsu B (2014) Graphene oxide captured for green use: Influence on the structures of calcium alginate and macroporous alginic beads and their application to aqueous removal of acridine orange. Chemical Engineering Journal 240:565–573.

150. Fan J, Shi Z, Lian M, et al (2013) Mechanically strong graphene oxide/sodium alginate/polyacrylamide nanocomposite hydrogel with improved dye adsorption capacity. Journal of Materials Chemistry A 1:7433–7443.

151. Li L, Fan L, Luo C, et al (2014) Study of fuchsine adsorption on magnetic chitosan/graphene oxide. RSC Advances 4:24679–24685.

152. Sheshmani S, Ashori A, Hasanzadeh S (2014) Removal of Acid Orange 7 from aqueous solution using magnetic graphene/chitosan: A promising nano-adsorbent. International journal of biological macromolecules 68:218–224.

153. Wang J, Liu C, Shuai Y, et al (2014) Controlled release of anticancer drug using graphene oxide as a drug-binding effector in konjac glucomannan/sodium alginate hydrogels. Colloids and Surfaces B: Biointerfaces 113:223–229.

154. Pourjavadi A, Shakerpoor A, Tehrani ZM, Bumajdad A (2015) Magnetic graphene oxide mesoporous silica hybrid nanoparticles with dendritic pH sensitive moieties coated by PEGylated alginate-co-poly (acrylic acid) for targeted and controlled drug delivery purposes. Journal of Polymer Research 22:1–13.

155. Lee J, Lee K, Park SS (2016) Environmentally friendly preparation of nanoparticle-decorated carbon nanotube or graphene hybrid structures and their potential applications. Journal of Materials Science 51:2761–2770.

156. Nandgaonkar AG, Wang Q, Fu K, et al (2014) A one-pot biosynthesis of reduced graphene oxide (RGO)/bacterial cellulose (BC) nanocomposites. Green Chemistry 16:3195–3201.

157. Li M, Wang Y, Liu Q, et al (2013) In situ synthesis and biocompatibility of nano hydroxyapatite on pristine and chitosan functionalized graphene oxide. Journal of Materials Chemistry B 1:475–484.

158. Xiong G, Luo H, Zuo G, et al (2015) Novel porous graphene oxide and hydroxyapatite nanosheets-reinforced sodium alginate hybrid nanocomposites for medical applications. Materials Characterization 107:419–425.

159. Chen Y, Qi Y, Yan X, et al (2014) Green fabrication of porous chitosan/graphene oxide composite xerogels for drug delivery. Journal of Applied Polymer Science 131:

160. Lu B, Li T, Zhao H, et al (2012) Graphene-based composite materials beneficial to wound healing. Nanoscale 4:2978–2982.

161. Xu H, Dai H, Chen G (2010) Direct electrochemistry and electrocatalysis of hemoglobin protein entrapped in graphene and chitosan composite film. Talanta 81:334–338.

162. Ma Q, Sun H, Hou S (2013) Application of graphene oxide sheets incorporated in the porous calcium alginate films on the glassy carbon electrode for biosensor construction based on myoglobin. Journal of Applied Electrochemistry 43:975–984.

163. Wei H, Han L, Tang Y, et al (2015) Highly flexible heparin-modified chitosan/graphene oxide hybrid hydrogel as a super bilirubin adsorbent with excellent hemocompatibility. Journal of Materials Chemistry B 3:1646–1654.

164. Valentini L, Bon SB, Fortunati E, Kenny JM (2014) Preparation of transparent and conductive cellulose nanocrystals/graphene nanoplatelets films. Journal of Materials Science 49:1009–1013.

165. Wang Q, Wang Y, Liu S, et al (2012) Voltammetric detection of bisphenol a by a chitosan–graphene composite modified carbon ionic liquid electrode. Thin Solid Films 520:4459–4464.

166. Liu B, Lian HT, Yin JF, Sun XY (2012) Dopamine molecularly imprinted electrochemical sensor based on graphene–chitosan composite. Electrochimica Acta 75:108–114.

167. Han D, Han T, Shan C, et al (2010) Simultaneous Determination of Ascorbic Acid, Dopamine and Uric Acid with Chitosan-Graphene Modified Electrode. Electroanalysis 22:2001–2008.

168. Li J, Zhao Y, Wang N, et al (2012) Enhanced performance of a MnO 2–graphene sheet cathode for lithium ion batteries using sodium alginate as a binder. Journal of Materials Chemistry 22:13002–13004.

169. Guo J, Liu J, Yang B, et al (2015) Biodegradable Junctionless Transistors With Extremely Simple Structure. Electron Device Letters, IEEE 36:908–910.

170. Qian C, Sun J, Yang J, Gao Y (2015) Flexible organic field-effect transistors on biodegradable cellulose paper with efficient reusable ion gel dielectrics. RSC Advances 5:14567–14574.

171. Chen H, Huang J, Palaniappan A, et al (2016) A review on electronic bio-sensing approaches based on non-antibody recognition elements. Analyst 141:2335–2346. doi: 10.1039/C5AN02623G

172. Kaplan DL (1998) Introduction to Biopolymers from Renewable Resources. In: Kaplan DDL (ed) Biopolymers from Renewable Resources. Springer Berlin Heidelberg, pp 1–29

173. Xu Y, Hong W, Bai H, et al (2009) Strong and ductile poly(vinyl alcohol)/graphene oxide composite films with a layered structure. Carbon 47:3538–3543. doi: 10.1016/j.carbon.2009.08.022

174. Verdejo R, Barroso-Bujans F, Rodriguez-Perez MA, et al (2008) Functionalized graphene sheet filled silicone foam nanocomposites. J Mater Chem 18:2221–2226. doi: 10.1039/B718289A

175. Kai W, Hirota Y, Hua L, Inoue Y (2008) Thermal and mechanical properties of a poly(ϵ-caprolactone)/graphite oxide composite. J Appl Polym Sci 107:1395–1400. doi: 10.1002/app.27210

176. Prud'Homme R, Ozbas B, Aksay I, et al (2010) Functional graphene-rubber nanocomposites.

177. Kim H, Miura Y, Macosko CW (2010) Graphene/Polyurethane Nanocomposites for Improved Gas Barrier and Electrical Conductivity. Chem Mater 22:3441–3450. doi: 10.1021/cm100477v

178. Fang M, Wang K, Lu H, et al (2010) Single-layer graphene nanosheets with controlled grafting of polymer chains. Journal of Materials Chemistry 20:1982–1992.

179. Song K, Zhao X, Xu Y, Liu H (2013) Modification of graphene oxide via photo-initiated grafting polymerization. Journal of Materials Science 48:5750–5755.

180. Duncan TV, Pillai K (2014) Release of engineered nanomaterials from polymer nanocomposites: diffusion, dissolution, and desorption. ACS applied materials & interfaces 7:2–19.

181. Szabó T, Berkesi O, Forgó P, et al (2006) Evolution of Surface Functional Groups in a Series of Progressively Oxidized Graphite Oxides. Chem Mater 18:2740–2749. https://doi.org/10.1021/cm060258+

CHAPTER 4. ZEIN/LAPONITE® NANOCOMPOSITES WITH IMPROVED MECHANICAL, THERMAL AND BARRIER PROPERTIES

Tahrima B. Rouf, Gudrun Schmidt, and Jozef L. Kokini

Purdue University, 745 Agriculture Mall Drive, West Lafayette, IN 47907, USA

Reproduced with permission. Full citation:

Rouf TB, Schmidt G, Kokini JL (2018) Zein–Laponite nanocomposites with improved mechanical, thermal and barrier properties. J Mater Sci 1–16. https://doi.org/10.1007/s10853-018-2061-6

4.1 Abstract

Zein, a prolamine of corn, is a bio-renewable resource that can potentially offer alternatives for petroleum-based polymers in many applications. Nanocomposite formation with addition of silicate nanoparticles (Laponite®) to zein films, cast from 70% ethanol solutions, significantly improved the mechanical, thermal and barrier properties. Based on FTIR findings, a mechanism for zein-Laponite® nanocomposite formation is proposed, which suggests Laponite® nanoparticles bind to zein molecules through Si-N bond formation. Structural characteristics investigated using AFM and TEM confirmed exfoliation of the nanoparticle. The changes in the surface energy of the films were evaluated using water contact angle measurements and showed increase in surface hydrophobicity. The Young's modulus and tensile strength increased with nanoparticle concentration. The glass transition temperature increased, and water vapor permeability decreased with only a small amount of Laponite®.

Keywords: Zein, Laponite®, TEM, FTIR, AFM, Water Vapor Permeability, DSC

4.2 Introduction

Petroleum-based polymers have exceptional physical and chemical properties including endurance and resistance to biological degradation. Unfortunately these polymers are causing significant pollution and global environmental concerns [1]. For example, large plastic trash

islands are floating on the oceans in many parts of the world [2] and plastic materials pollute pristine islands, lands and seas [3]. Therefore, biodegradable alternatives for plastics can solve some of these problems and improve environmental sustainability[4, 5].

The biopolymer zein is a major storage prolamin protein of corn, and an abundant by-product of the ethanol industry. Zein is generally recognized as a safe (GRAS) material, by the Food and Drug Administration, and has unique amphiphilic, antioxidant, antibacterial and adhesive film forming properties. Zein is considered a highly suitable candidate for designing environmentally friendly polymers [6–8]. The polymer chains of zein, are able to change their conformation, and the mechanical and rheological properties can be tailored to give a range of properties from flexible to tough polymer, while maintaining a glossy appearance [9, 10]. Zein's versatile properties are useful for various applications in packaging, biomedical, agricultural areas, and add value to an abundant by-product of ethanol production. Zein has found applications in several industries including adhesives, coatings, printing, fibers, packaging films and plastics [11, 12].

Zein is an attractive alternative to synthetic polymers and animal derived proteins, as zein has no allergenic compounds, it is a much less expensive and safe alternative for biomaterial research. When modified with different types of nanofillers, the resulting zein films showed significant improvements in mechanical, thermal, barrier and antimicrobial properties [7, 13–17]. Maximum improvement of zein properties is contingent upon optimum filler-matrix interaction, but the interaction between filler and zein matrix and the chemistry behind the property improvement of the matrices is not yet fully understood. In previous studies, where plasticized zein is reinforced with different nanomaterials [16, 18], proposed mechanisms suggested the supramolecular interaction between protein and reinforcing nanomaterials could result in physical crosslinking and reduce local mobility of the protein molecules. This would result in higher stiffness and glass transition temperature.

As efficient nanofillers, nanoclays have received a great deal of attention, as they are cost efficient, chemically and thermally stable, and property enhancing due to their platelet-like structure. Laponite®, $Na_{+0.7}[(Si_8Mg_{5.5}Li_{0.3}).O_{20}(OH)_4]^{-0.7}$, is a synthetic layered silicate nanoclay, which is hydrophilic and biocompatible [19]. Its well-defined nano-size disk shape, has been used as a model in fundamental studies of polymer nanocomposites, to improve the mechanical and barrier properties [20–25]. These nanoparticles have also been studied for fabrication of sensors [26–28] and nanocomposite hydrogels [29, 30].

In our previous studies [8, 31, 32], zein has shown potential to be used in biodegradable packaging films, as well as microfluidic device and sensor platforms. Therefore, the aim of this paper is focused on the changes in mechanical, thermal, barrier and surface properties of zein, by addition of Laponite®. To investigate the effects of Laponite® on zein, the changes in the physical properties and structural characteristics of the zein-Laponite® (Z-L) nanocomposites were examined by changing the nanofiller concentration. Atomic Force Microscopy (AFM), Transmission Electron Microscopy (TEM), Water Contact Angle (WCA) measurements and Fourier Transform Infrared (FTIR) spectroscopy were used to observe the structural changes occurring within the films when nanofillers were added. The effects of nanocomposite formation on mechanical, water vapor permeability and thermal properties are also presented. These experiments offer mechanistic insights for changes in physical properties of zein and show desirable results for use as a platform for biodegradable packaging, microfluidic devices, biosensor platforms, and other functional film research.

4.3 Experimental

4.3.1 Materials

70% Ethanol (140 proof (70%), Decon™ Labs), and oleic acid were obtained from Fisher Scientific, monoglyceride was purchased from Alfa Aeser, Ward Hill, MA, USA, zein (90% crude protein dry weight basis) from Sigma-Aldrich, Milwaukee, WI, USA, and Laponite® RD Clay was obtained from Byk Chemicals. Drierites were purchased from W.A. Hammond Drierite Company. Polydimethylsiloxane (PDMS) kits were purchased from Sylgard, Dow Corning (Midland, MI).

4.3.2 Fabrication of zein –Laponite® nanocomposite films

A solvent casting technique was applied for preparation of the nanocomposite films, as it ensures optimal dispersion of the nanofillers, therefore ensures maximum interaction of the filler and matrix and use of environmentally preferred solvents [33]. Nanocomposite films (Z-L) were prepared with 0, 1, 3, 5, and 10 wt% Laponite®, designated as Z-0L, Z-1L, Z-3L, Z-5L and Z-10L respectively. First the Laponite® was dispersed in 25 mL of 70% ethanol / 30% water and heated up to 60-65^{o}C. Then 5g of zein were added to the solution, (a 1:5 weight (g)/volume (ml) ratio was maintained) and stirred vigorously until the zein dissolved. In a separate beaker, 6.25g of oleic

acid plasticizer and 0.15 g of monoglyceride emulsifier were mixed and heated, until the monoglyceride dissolved in the oleic acid. The oleic acid-monoglyceride solution was added to the zein-Laponite® solution and the resulting mixture was stirred for another hour. The ratio of zein/plasticizer/emulsifier (1 / 1 / 0.15) was maintained constant throughout this study because previous results showed that this formulation improved overall physical properties [7]. Prior to solvent casting each mixture was sonicated for at least 5 minutes with the sonicator amplitude set to 39% of total 500 watts. 10 ml of nanocomposite solution was pipetted into polystyrene petri dishes lined with PDMS, which allowed the zein film to be removed easily after solvent evaporation. The films were dried inside desiccators over calcium sulfate Drierite. The thicknesses of the dried films were fairly similar, and they were : Z-0L= 0.52 ± 0.18mm, Z-1L= 0.75 ± 0.05 mm, Z-3L= 0.71 ± 0.11 mm, Z-5 L= 0.71 ± 0.14mm, Z-10 L= 0.67 ± 0.11 mm.

4.3.3 Characterization of Nanocomposite films

Transmission Electron Microscopy

Transmission Electron Microscopy (TEM) was used to examine the structure of the Laponite® nanoparticles, as well as, investigate the dispersion of the nanoparticles in the nanocomposite films. For nanocomposite sample preparation, the films were treated with fixative agents, followed by dehydration in an ethanol gradient. The films were embedded in epoxy resin and then they were cut into ultra-thin sections using microtome diamond and mounted on holey copper grids. The microtomed samples were characterized with a Tecnai T20 TEM at 200 kV.

Atomic Force Microscopy

The surface morphologies and roughness of the nanocomposite films were investigated using a Veeco Multimode Atomic Force Microscope (AFM) (Veeco Instruments, Inc., New York). AFM tips used for characterization included a Si-Ni Tip (Spring Constant: 37 N/m, Frequency: 300 kHz), with a pyramidal shape and a height of 15 μm (App Nano, Inc). The film surfaces were imaged in the tapping mode and in scans of 500 nm×500 nm according to procedures published in the literature [34]. Data evaluation of images included calculating the average roughness (Ra) and the root mean square roughness (Rq).

Fourier Transform Infrared Spectroscopy

Fourier Transform Infrared Spectroscopy (FTIR) was performed for quantitative and qualitative analysis, and for identifying specific chemical bonding within nanocomposites. Experiments were done using a nitrogen cooled Attenuated Total Reflectance FTIR (Nicolet Nexus 470 FTIR), with 64 scans at a resolution of 4 cm^{-1}. The spectra were recorded between 800 - 4000 cm^{-1}. For the secondary structure analysis of zein, deconvolution of each spectrum was done using the Omnic FTIR software according to the methods of Fourier self-deconvolution (FSD). Three prominent and characteristic bands important for protein data evaluation are the amide I, II, and III bands. The amide I band, is a sharp peak that is usually seen between 1600 - 1700 cm^{-1} in protein spectra. This band is caused by the stretching of the C=O double bond and gives information about the secondary structures. The amide II and III bands are not analyzed here as they give peaks of weak intensity and can be easily overlooked [35]. The amide I regions (1600-1700 cm^{-1}) of the spectra were analyzed by Gaussian curve fitting. The secondary structural content was calculated from the relative areas of the individual assigned bands in the amide I region. The details of the curve fitting has been included in the supplementary information.

Differential Scanning Calorimetry

DSC experiments were performed using a Discovery Nano Series DSC instrument. Calibration was based on pure indium and sapphire. An empty Aluminum pan was used as reference. Samples of 10-14 mg were subjected to analysis using a heating rate of 10°C/min per heating cycle, under continuous purging of nitrogen at 50ml/min. Glass transition temperatures were determined from resulting thermograms as the midpoint between onset and end temperatures of step changes in heat flow observed during heating. In all DSC traces, positive upward peaks correspond to exothermic processes, and downward peaks correspond to endothermic processes.

Water Vapor Permeability

The barrier properties of the nanocomposite films were analyzed using water vapor permeability (WVP) experiments. WVP cups were purchased from the Paul N. Gardner Company Inc. and measurements were done using an American Society for Testing and Materials, ASTM E 96 (1996) standard [36]. The zein-Laponite® (Z-L) films were attached to the permeability cups

containing 8 mL of distilled water. Then the cups were placed in desiccators containing a saturated salt solution of $MgCl_2$, while a temperature of 22°C and a relative humidity (RH) gradient of 64% was maintained. The sample cups were weighed every 24 hours until steady state vapor flow was reached. At least three sets were tested for each formulation. The water vapor transmission rate was calculated from the weight loss of the permeation cup. The water vapor transmission rate (WVTR) was defined as the slope (g/hr) divided by the transfer area (m^2). After the permeation tests were completed, the water vapor permeability, WVP, ($g\ Pa^{-1}\ hr^{-1}\ m^{-1}$) was calculated as follows:

$$WVP = \frac{WVTR}{P(R_1 - R_2)} \times x \quad \ldots\ldots\ldots(1)$$

P is the saturation vapor pressure of water (Pa) at the test temperature (25 °C); R_1 is RH in the permeation cell; R_2, the RH in the $MgCl_2$ solution; and x is the film thickness (m).

Water Contact Angle Measurements

Water contact angle measurements were performed with an Attension Theta Auto 1 Optical Tensiometer. All measurements were done on the sides of the zein-Laponite® films that were previously in contact with PDMS. 2µL droplets of deionized water were dispensed onto the surface of the film and images were collected for 10 seconds at a rate of 12 frames per second. The images were taken as soon as the water droplet touched the designated baseline. Then the stable contact angle at the water zein film interface was measured and the change in hydrophobic/hydrophilic balance on film surfaces was evaluated. Water contact angle measurements were conducted in triplicate for the contact side, following the method described in literature [37].

Mechanical Properties

The tensile strength (TS), Young's modulus (YM) and percentage of elongation at break (% EAB) of films were determined using a TA. XT Plus Texture Analyzer with a 30g load cell. The films were cut into 20 mm × 70 mm strips and the samples were kept for 48hrs at 50% relative humidity and 25 °C before analysis. Three thickness measurements were taken across the gauge length of the films and averaged. The pre-test and post-test speed was 1 mm/min.

Statistical Analysis

For each of the five-different zein nanocomposite formulations, the experiments were repeated three times. Data were statistically analyzed and compared using Minitab. One-way ANOVA was used to evaluate the differences, and Tukey's pairwise comparison tests were applied with 95% confidence interval. The letter system was used throughout the paper to show significant difference; such that different letters indicate significant difference between the adjacent values.

4.4 Results and Discussion

4.4.1 Transmission Electron Microscopy

An important prerequisite for the improvement of the physical and mechanical properties is the uniform nanoparticle dispersion within the nanocomposite. TEM provides information about the dispersion of the Laponite® and, therefore helps explain the physical changes as result of the nanoparticle-matrix interactions. In order to baseline the organization of Laponite®, 1 g Laponite® powder has been mixed with 10 mL of 70% aqueous ethanol solution, stained with 1% uranyl acetate and have been imaged with TEM and can be seen in **Fig. 4.1.** (a) . Light colored streaks that are prevalent throughout the image are on average 1 nm thick and 25 nm long. These streaks represent the side view of individual Laponite® nanoparticles. As Laponite® is disk shaped, the appearance of these streaks means that some Laponite® nanoparticles are arranged perpendicularly to the surface so that only the side view of the disks can be seen. The top view of nanoparticles that may lie flat on the surface cannot be seen here due to low contrast. The top view of individual Laponite® nanoparticles can be seen in published work for example by Guimarães et al. [38]. In this paper, formation of Laponite® covered latexes, allow the nanoparticles to be imaged from the top so that the coin like shapes can be seen. However, in the case of solution casting presented here, the nanoparticles align sideways; therefore, only streaks are observed in the TEM (**Fig. 4.1** (a), (c) and (d)).

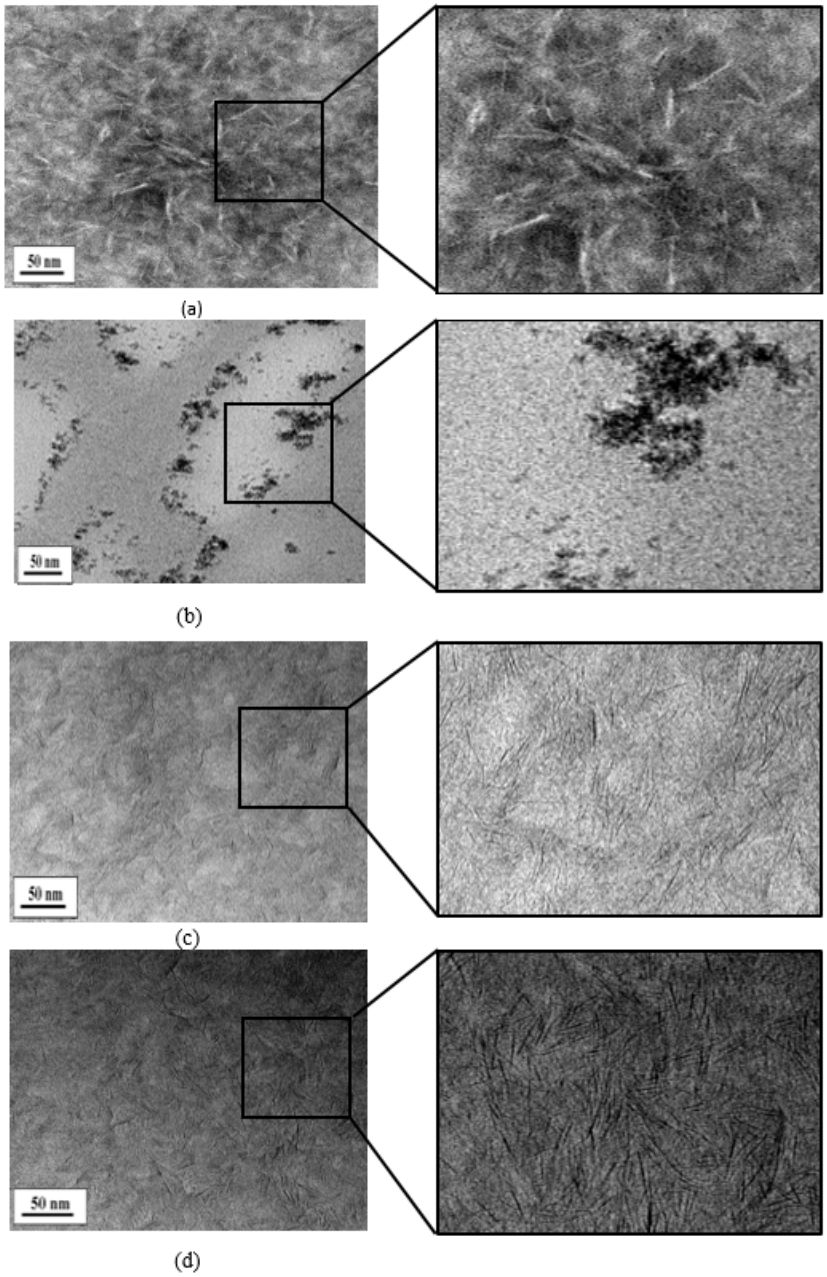

Fig. 4.1. TEM images: (a) Pristine Laponite® nanoparticles can be recognized as white streaks against the dark background (stain: uranyl acetate). The magnified areas show more details. (b) Plasticized zein film showing dark areas of phase separated oleic acid. (c) Z-5L nanocomposite film, showing intercalated, exfoliated Laponite® platelets dispersed throughout the zein matrix. (d) Z-10L nanocomposite film, showing intercalated, exfoliated Laponite® platelets and some degree of aggregation. The magnified areas show individual nanoparticles as seen from the side

Fig. 4.1 (b) shows the TEM image of a zein film containing oleic acid plasticizer. The dark spots seen within the polymer matrix come from phase-separated oleic acid. **Fig. 4.1** (c and d)

show images from zein-Laponite® nanocomposites. The dark streaks represent Laponite® nanoparticles as seen from the side. The Laponite® is homogeneously dispersed but visible throughout the zein matrix. Single platelets can be observed together with stacked and multilayered nanostructures within the zein matrix. The images suggest that Laponite® is exfoliated (individual platelets fully separated) to some degree but also intercalated (partially separated individual platelets) areas are visible. As the concentration of Laponite® increases to 10% (**Fig. 4.1**(d)) intercalated areas are more frequent and aggregation becomes more pronounced. Within small aggregates or domains, the nanoparticles appear to align parallel to each other. This parallel orientation or intercalation is more prominent at higher Laponite® concentrations where polymer space decreases and a house of cards structure is not feasible any more. Intercalation and orientation of Laponite® within smaller domains further increases barrier properties and thus water vapor permeability decreases (see below). The structural characteristics observed here can be related to the sample preparation and film casting techniques used.

Fig. 4.2, shows photographs of the three different nanocomposite films taken over a Purdue Pete cartoon, to examine the optical appearance of the films. The zein control (Z-0L) is yellow but transparent to the eye. With increasing Laponite® content the cartoon is still visible through films (Z-5L) and (Z-10L) even at the highest loading of (10 wt %) Laponite®. However, the yellow (Z-10L) film appears to be darker and perhaps not as clear as the zein control when examined by the eyes. This means that Laponite® may have some influence on the optical appearance of the films. We assume that at the concentrations used here, most of the nanoparticles are exfoliated or intercalated (see **Fig. 4.1**), however micron sized heterogeneities in the films or density fluctuations of Laponite® within the polymer matrix (see, TEM, **Fig. 4.1**) may lead to darker and translucent films.

(a) (b) (c)

Fig. 4.2. Photographs of zein control and zein-Laponite® films over the Purdue Pete cartoon as they appear to the eye. (a) Z-0L film (b) Z-5L film and (c) Z-10L nanocomposite film.

4.4.2 Atomic Force Microscopy

Atomic Force Microscopy (AFM) is another technique that helps visualize and understand the dispersion of the nanoparticles, as uniform dispersion can lead to smoother surfaces compared to the original polymer matrix [39]. Non-uniform dispersion can lead to rough and irregular surface properties [25]. As uniform dispersion leads to better interactions between polymer and nanoparticles, the AFM technique also helps optimize the fabrication of better nanocomposite films with improved properties. Surface topography of Laponite® nanoparticles using AFM have been investigated in different studies [40–42] and in those studies, the nanoparticles have shown characteristic rag-like surface with domains of ridges and valleys. Topographies of the zein control (only plasticized) and zein-Laponite® nanocomposite surfaces are shown in **Fig. 4.3**. The images shown in **Fig. 4.3** (a), (b) suggest that pristine zein surfaces have high surface roughness which is in agreement with findings from the literature [34, 43]. **Fig. 4.3** (c), (d) display the surface topology of a representative zein-Laponite® nanocomposite (Z-5L). Comparison of **Fig. 4.3** (a) and (c), shows that the control zein film has large features and bumpy areas with cavities, whereas the Z-5L nanocomposite films have isolated small granular like domains [44]. The surface topography of the nanocomposite resembles the surface topographies of pristine Laponite® nanoparticles [42], as the nanocomposite films also seem to have a rag-like structure.

'Roughness Analysis' for the control zein films, yields an average roughness of Ra = 5.83 nm and a root mean square roughness of Rq = 7.11 nm. Analysis of Z-5L, the 5% Laponite® containing nanocomposite, gives Ra = 0.567 nm and Rq = 0.799 nm. These results indicate that, Laponite® disperses well within the zein matrix, thus creating a smoother surface. The dispersion

of the Laponite®® and the nanoparticle interactions with the zein polymer influence the arrangement of the polymer chains near to the Laponite® surfaces, which results in a more compact structure. With increasing Laponite® concentration (Z-5L), the amount of zein in the matrix decreases which leads to a change in the surface roughness when compared to the zein only control. This change in surface roughness is influenced by the degree of exfoliation and intercalation of the Laponite®, throughout the zein matrix.

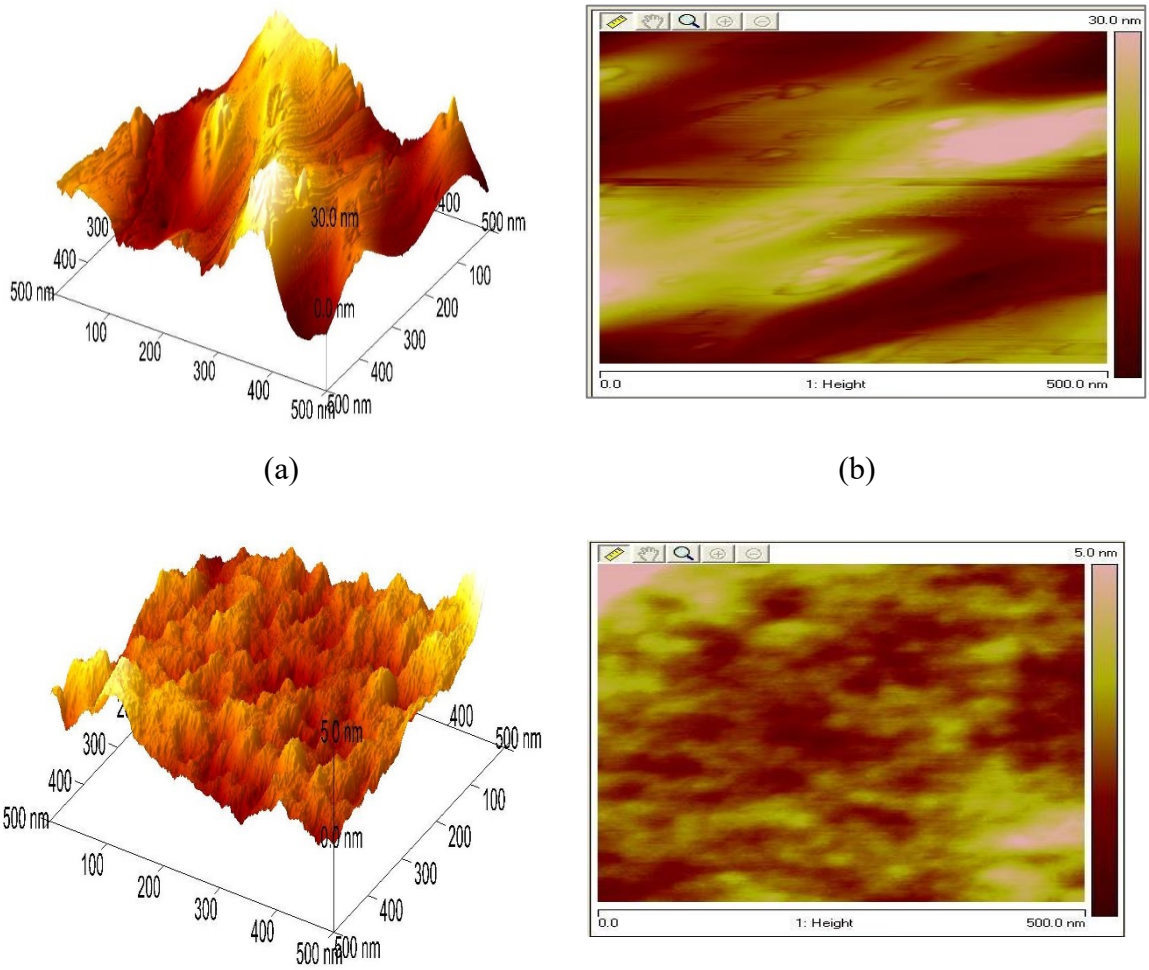

Fig. 4.3. (a) Three-dimensional AFM image of a control zein film on a 500 nm×500 nm scale, showing large features as high as 30 nm. (b) Top view of the control zein-film section. (c) Three-dimensional image of a Z-5L film on a 500 nm×500 nm scale, showing smaller granular areas. The height of the features is as high as 5 nm. (d) Top view of the Z-5L film section.

Other studies investigating Laponite® nanocomposite surfaces have reported slight increases in roughness [25], mostly due to irregular or non-uniform dispersion of the nanoparticle in the polymer matrix. Publications on different polymer-clay nanocomposites such as chitosan-Montmorillonite [39], or poly(3-hydroxybutyrate-co-3-hydroxyvalerate)-Cloisite30B [45] have reported significant decreases in surface roughness after addition and dispersion of clay.

4.4.3 Fourier Transform Infrared Spectroscopy

In Fourier transform infrared spectroscopy (FTIR), the rise of new peaks or the shift in original peaks may give information about the physicochemical environment of functional groups within the nanocomposite. The changes may confirm specific interactions between the polymer matrix and the nanoparticles, which in turn helps understand and improve nanocomposite material design. **Fig. 4.4** summarizes FTIR data from pristine zein powder, plasticized control zein films and plasticized nanocomposite films containing 1, 3, 5, 10% Laponite®. FTIR data of pristine zein powder and the zein control and nanocomposite films show the typical characteristics of proteins including the amide I, II and III bands or peaks. The peaks observed between 2800-3000 cm^{-1} come from $-CH_3$ and $-CH_2$ side chain vibrations in aliphatic groups of amino acids. The broad peak at 3000-3500 cm^{-1} is related to the N-H stretching in amide structures [46]. The amide I band at 1643 cm^{-1}, which comes from C=O and C-C vibrations, and the amide II band at 1536 cm^{-1}, related to CN stretching and NH bending are visible [46].

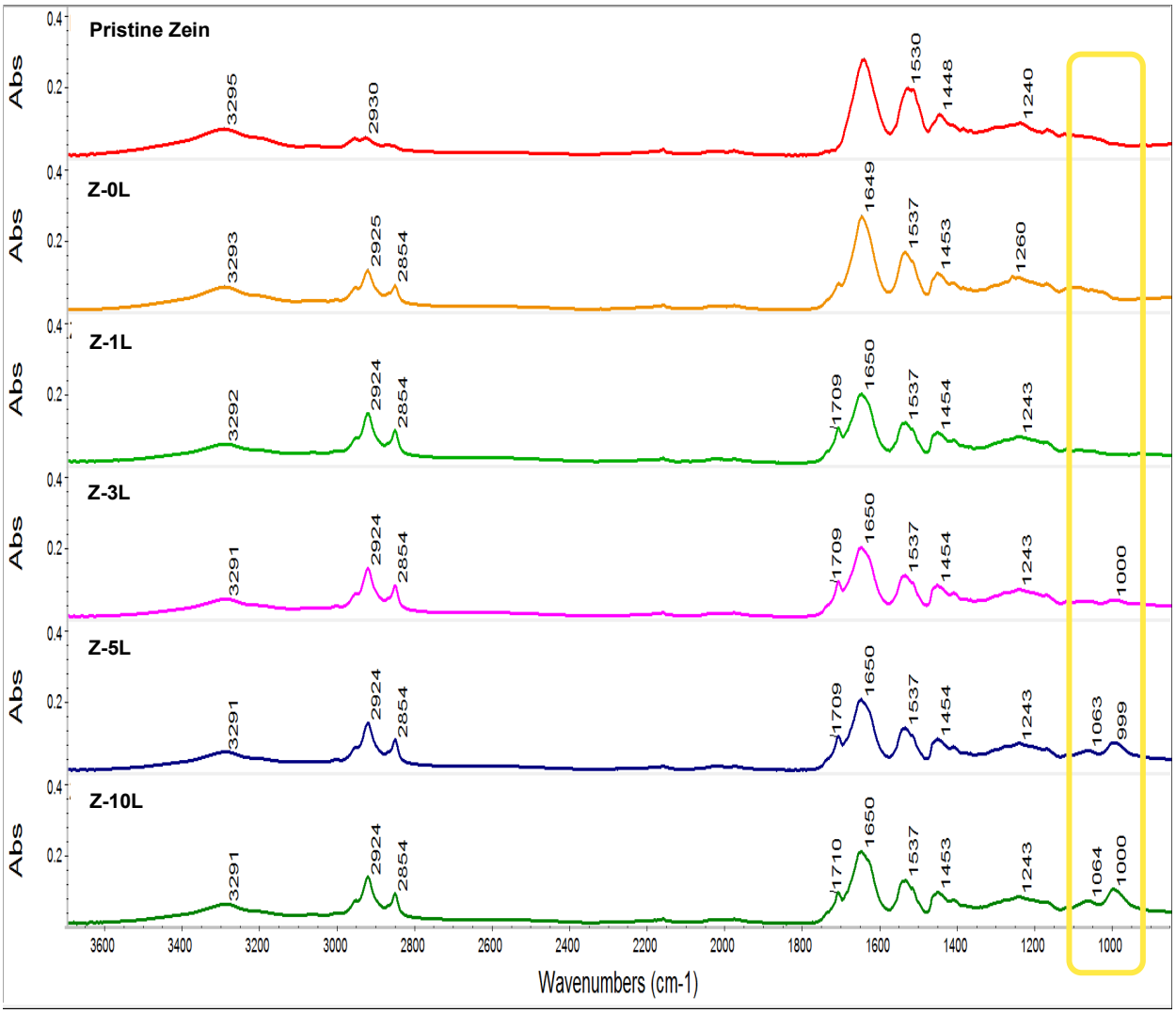

Fig. 4.4. Comparison of the FTIR spectra of pristine zein powder, control zein with oleic acid, and zein-Laponite® nanocomposites (1%, 3%, 5%, 10%), within the 3700cm^{-1}-800cm^{-1} range. Addition of oleic acid results in increases in the intensity of new peaks at 1709cm^{-1} due to the carboxylic acid C=O stretch, and 2854 cm^{-1} due to alkyl C-H stretch, and further addition of Laponite® result in new peaks at 1064 cm^{-1}which can be attributed to Si-O stretching. The peak at 1000 cm^{-1} can be attributed to Si-N stretching.

When pristine zein is compared to the control zein plasticized with oleic acid, an increase in intensity is visible at 2924 cm^{-1} and 2854 cm^{-1}. The oleic acid increases the number of alkyl groups in the matrix, these alkyl groups show C-H stretching vibrations in the FTIR. Therefore, the presence of additional alkyl groups from the oleic acid plasticizer resulted in increased C-H stretching [46] and ultimately increased the intensities of the peaks at 2924 cm^{-1} and 2854 cm^{-1} . A new peak at 1709cm^{-1} comes from the carboxylic C=O stretching of the oleic acid.

Typical FTIR spectra of pristine Laponite® show a prominent peak from Si-O stretching, located at 1080 cm^{-1} [47]. The Si-O peak has also been located at 1011 cm^{-1} [48], and at 1090 cm^{-1} [37]. A comparison of the FTIR spectra in Fig. 4 shows the rise of new peaks at 1000 cm^{-1} for Z-3L, Z-5L and Z-10L and at 1064cm^{-1} for Z-5L and Z-10L, which is similar to the peak found in Laponite® at 1080 cm^{-1} (Si-O). The multiple spectra obtained for each concentration of Laponite® were averaged over multiple locations. They are reproducible and superimpose nicely indicating that on average, the Laponite® has been distributed uniformly throughout the zein matrix. This is consistent with our observations with TEM. The gradual increase in intensity of the new peaks indicates a gradual increase in nanoparticle concentration.

The chemical changes observed in FTIR, are related to the addition of Si-O groups and may affect the secondary structures of zein. Within the amide I band, the α-helix structures give characteristic peaks around 1653- 1658 cm^{-1}, the β-sheets give characteristic peaks around 1632-1636 cm^{-1} and the β-turn structures show characteristic peaks around 1680-1686 cm^{-1} [49] . Another study [50] has reported that, β turns appear around 1671 cm^{-1}, and intermolecular β sheets appear around 1610 cm^{-1}. Pristine Zein, Z-0L to Z-10L nanocomposites show, β turns, α helices, as well as intramolecular and intermolecular β sheets. The nanocomposite formation affected the area and height intensities of all the characteristic amide I peaks. From **Fig. 4.5**, we can conclude that the area under the peak that is related to β-sheets increases relative to the control. The area under the peak related to α-helices decreases with increasing Laponite® concentration and the β-turns remain the same. The formation of new bonds between Si-O and zein eliminates some of the degree of freedom that the conformation of zein had before being absorbed to the Laponite® surfaces. The change in degree of freedom explains why the zein molecules become more rigid with an increase in β-sheet conformation and this transformation occurs at the expense of α-helices.

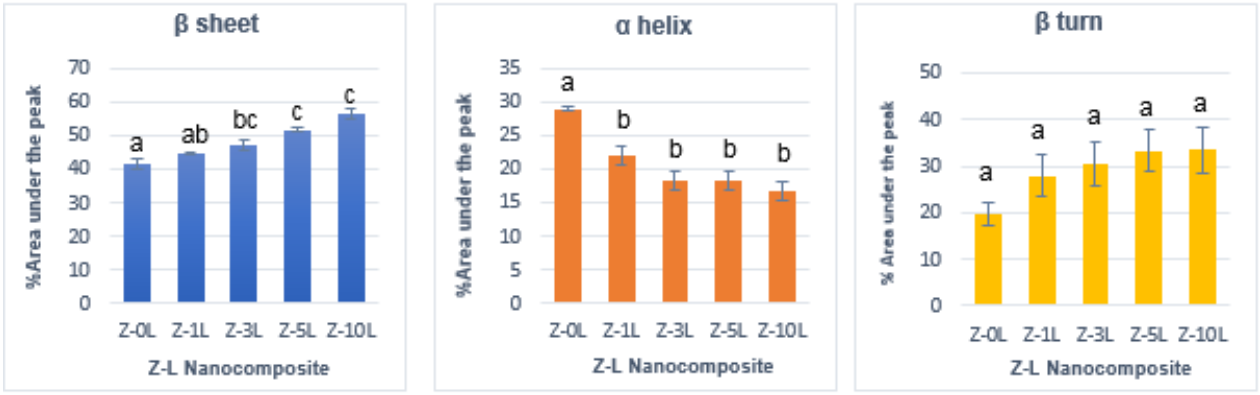

Fig. 4.5. Comparison of change in secondary structure distribution, in the amide I region, with addition of Laponite®. (a) β-sheet shows increase, (b) α-helix shows decrease and (c) β-turns show increasing trend, indicating that addition of Laponite® to zein, promotes the decrease in ordered structure and gives rise to more disordered structure. Different letters above error bars signify statistically significant differences according to Tukey's pairwise comparison ($p<0.05$). Although the area under the peak shows an increasing trend for β turns, the standard deviation is high. Therefore, these data points are not considered significantly different by Tukey's pairwise comparison. Therefore, the columns for β turns have the same letter above them.

Zein organizes itself in mostly compact capsule-like structures which are bonded to each other through glutamine residues [51]. β-turns are largely associated with the glutamines at the end of the capsule-like bodies and since their ratio remains the same, the glutamines are not affected by the bonding processes through Si-O.

It is reasonable to expect that, Laponite® can interact with zein in two ways; either through glutamine ends of zein, or the Si-O interacts with the N atom in the hydrophobic alpha helices and forms a bond. Since β-turns show no change with addition of Laponite® in **Fig. 4.5**, it can be assumed that Laponite® does not bond with zein through glutamine turns. A mechanistic figure depicting the possible interaction sites between zein and Laponite® is shown in the **Fig. 4.6**.

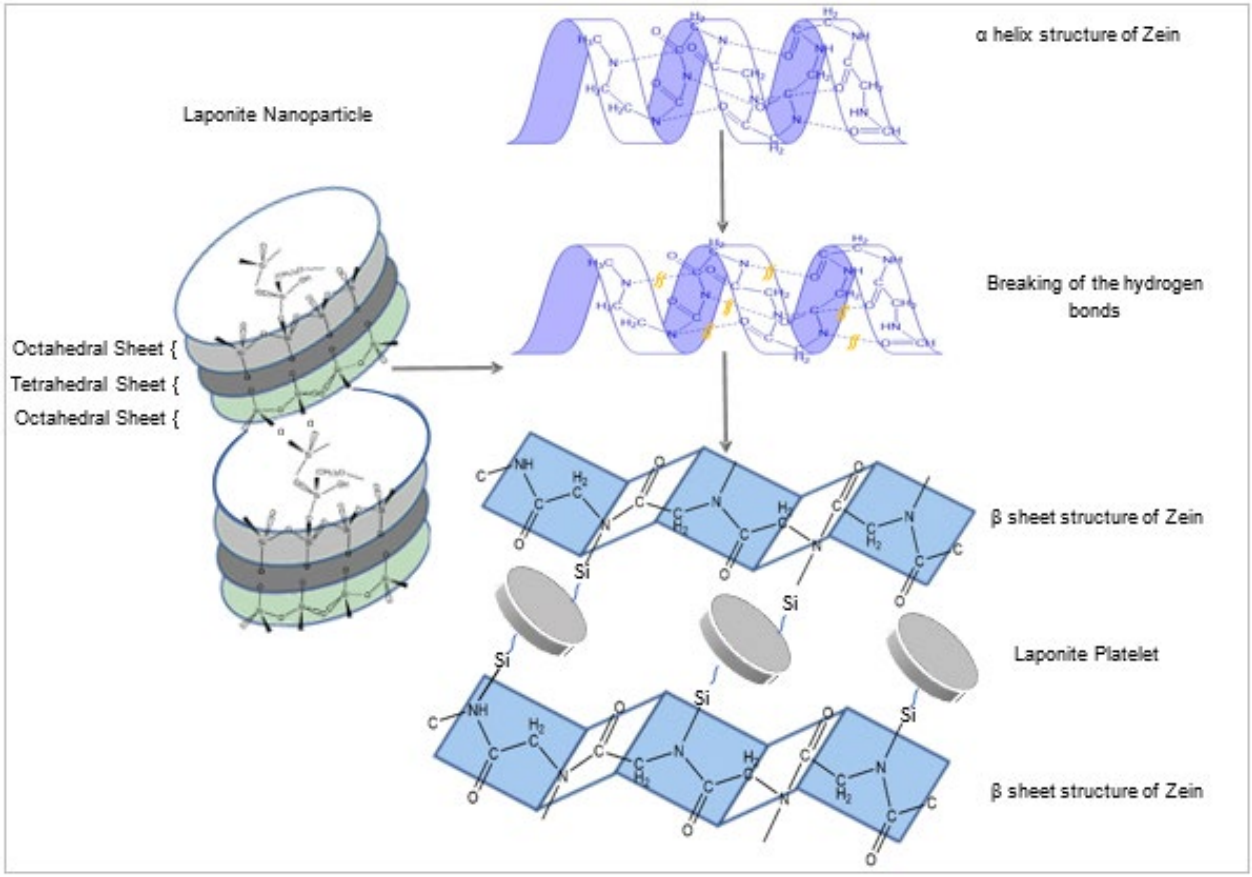

Fig. 4.6. Proposed mechanism of interaction between zein and Laponite®

As suggested in the Fig. 6, a logical way is that the Si-O groups of Laponite® breaks up the H bond in the α-helix and forms either Si-C or Si-N bonds, which results in changing of the α-helix into β-sheets, or β-turns. The rise of a new peak at 1000 cm^{-1} as seen in Fig. 4, can be attributed to Si-N stretching [52–54]. The characteristic peak at 800cm^{-1} for Si-C [55] is not observed leading to the conclusion that no Si-C bonds were formed.

4.4.4 Differential Scanning Calorimetry

The Differential Scanning Calorimetry (DSC), gives information of the changes in the thermal properties of the nanocomposites, which can be a direct result of the interaction and physical or chemical bond formation between the polymer matrix and nanoparticles. In **Fig. 4.7** (a), the DSC thermograms of the zein-Laponite® nanocomposites shifted (right) to higher temperatures with increasing Laponite® content, and the glass transition temperature T_g showed

increase with increasing Laponite® content. This can also clearly be seen from the histograms in **Fig. 4.7** (b). The increase in T_g is probably due to the higher restricted chain mobility resulting from the interactions of Laponite® and the zein polymer chains. This result confirms the FTIR findings, which show that the formation of new bonds between Laponite® Si-O and zein eliminates some of the degrees of freedom of the conformation of zein. Interactions with Laponite® make zein more rigid, resulting in an increase in β-sheet conformation, and decrease in α-helices. This result is also, in good agreement to mechanical properties, which show higher tensile strength with increasing Laponite® content.

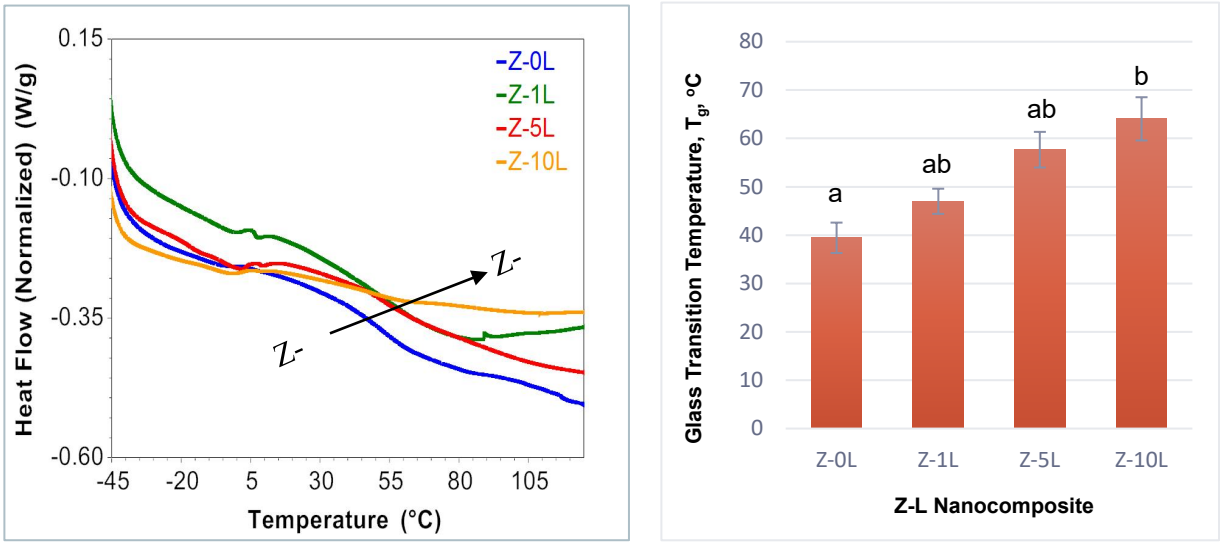

(a) **(b)**

Fig. 4.7. (a) DSC thermograms of Zein-Laponite® Nanocomposites. (b) DSC histograms of Zein-Laponite® Nanocomposites. Addition of Laponite® increases the glass transition temperature, indicating that Laponite® forms a bond with zein polymer chains and increases rigidity, hence raises Tg. Different letters above error bars signify a statistically significant difference ($p<0.05$)

Other studies showed that addition of Laponite® as well as other clays like Montmorillonite, increase the T_g of PMMA [56]. Similar results were reported by Manisara and Pancheri, where they found that addition of cellulose microfibrils to zein increased the T_g of Zein films [15]. Other biopolymer-nanocomposite studies show a similar trend of nanofillers bonding with polymeric chains thereby creating a more compact and rigid structure, which increase the T_g. This increase correlates with the tensile strength and Young's modulus and with a decrease in the % elongation at break [57].

4.4.5 Water Vapor Permeability

The Water Vapor Permeability (WVP) is an important property that guides the application of the biopolymer. An increase in permeability is sometimes desired, e.g. for wound dressings [58], whereas, in some cases a decrease in WVP is crucial for applications such as biosensors and packaging materials. WVP of zein-Laponite® nanocomposite films are summarized in **Fig. 4.8**. The data suggest that the WVP decreased as the Laponite® content increased up to Z-10L. The WVP decreased the most (about 40%) for Z-10L. It appears that the influence on barrier properties has a linear relationship with Laponite® content. The improvement of water vapor barrier properties of Z-L nanocomposite films is due to the presence of impermeable Laponite® platelets that are distributed in the polymer matrix in a manner that increases the effective diffusion path length. The level of improvement depends not only on the nanocomposite structure (intercalated, exfoliated or some intermediate), but also upon the relative orientation of the sheets or nanoplatelets in the matrix. The Laponite® orientation can result in highest tortuosity when the nanoplatelets arrange perpendicular to the direction of diffusion. Any kind of deviation from such arrangement results in an increase in WVP. From the TEM images shown in Figure 1, we can see that on average the nanoplatelets are randomly oriented. However, within small aggregates or domains the nanoplatelets are not exfoliated but remain intercalated. Parallel orientation or intercalation of Laponite® within small domains further increases barrier properties through creating a tortuous path for small water molecules. This effect can be observed when comparing water vapor permeability data of Z-5L and Z-10L in **Fig. 4.8**.

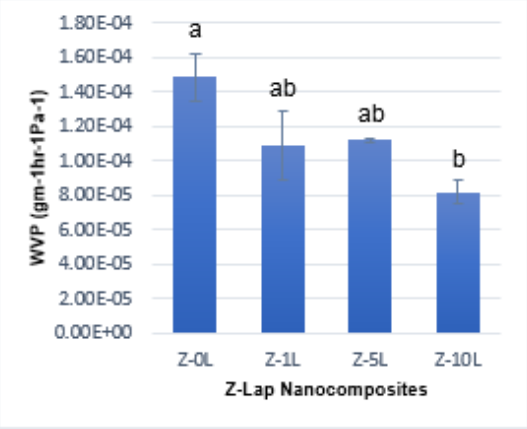

Fig. 4.8. Water vapor permeability decreased with increasing Laponite® concentration, indicating that the presence of Laponite® in the zein polymer matrix creates a tortuous path for the water molecules to escape. Different letters above error bars signifies a statistically significant difference ($p<0.05$)

4.4.6 Water Contact Angle Measurements

Several studies from the literature report a relationship between water contact angle measurements and water vapor permeability [59–62]. The authors usually find that an increase in hydrophobicity leads to an increase in water vapor barrier properties. One explanation for such behavior is that polar H_2O molecules cannot be readily adsorbed to non-polar film surfaces or hydrophobic surfaces, which ultimately results in a reduction of water vapor permeability. Since Laponite® is hygroscopic as well as hydrophilic, we would assume that addition of Laponite® will increase the hydrophilicity of a polymer nanocomposite, which in turn may reduce the barrier properties of the film. Here we investigate the surface hydrophilicity by presenting water contact angle measurements (WCA) on zein-Laponite® surfaces. We then determine how the changes in WCA are correlated to the WVP findings presented above.

Water Contact Angle, WCA measurements were done from the zein-PDMS contact side. **Fig. 4.9** shows the average WCA values for films with different Laponite® concentrations. The control zein as well as the Z-L nanocomposites showed hydrophilic properties, as their WCA were lower than 90º. Control Zein had a contact angle of 54º which is consistent with the findings from the literature[37]. However, as Laponite® was added to zein, the WCA started to increase; with the highest WCA recorded was 64.77±1.76 º for Z-5L nanocomposite. Surprisingly Laponite® addition slightly increased the hydrophobicity, by increasing the WCA. The change in the WCA with different concentrations of Laponite®, can be the function of surface morphology of the films, coating of the Laponite® with zein polymer and orientation of the nanoparticle in the nanocomposite. Similar results were found for Montmorillonite clay, MMT, which increased the water contact angle of methyl cellulose [63] and regenerated cellulose [64] nanocomposites. Another study on Cloisite-10A a hydrophilic nanoclay and zein also showed an increase in WCA [17]. Our data suggest that the increasing amount of zein covered Laponite® surfaces prevented the spreading of the water droplets and increased the WCA. This may be correlated to the formation of hydrophobic Si-N groups (Si from Laponite®, N from amide) on the surface, which is supported by the FTIR results (**Fig. 4.4**). As the degree of surface hydrophobicity increased, the WVP of nanocomposite films decreased. This trend may indicate a relationship between contact angle changes and water vapor barrier due to presence of Laponite® in the polymer matrix.

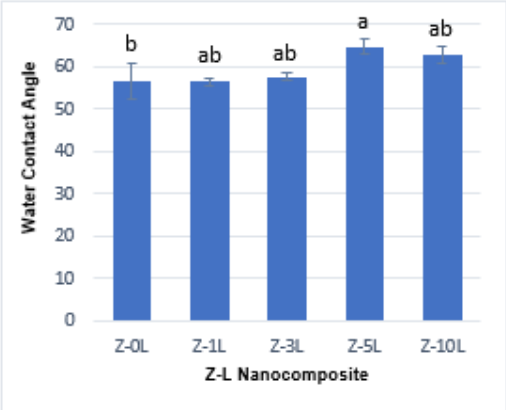

Fig. 4.9. Water contact angle of zein-Laponite® nanocomposites, show increase with increasing Laponite® concentration. The presence of Laponite® slightly increases the hydrophobic properties of zein. However, the WCA of the nanocomposite films are still within hydrophilic range. Different letters above error bars show statistically significant differences ($p<0.05$)

4.4.7 Mechanical Property

Mechanical properties of nanocomposites constitute an important factor in its various biomaterial applications. Nanocomposites should withstand different stresses, whether used as microfluidic substrates, as scaffolding materials or in food packaging. The mechanical properties of zein-Laponite® nanocomposites including tensile strength (TS), Young's modulus (YM) and % elongation at break (EAB) are summarized in **Fig. 4.10**. With increasing Laponite® concentration the tensile strength and the Young's modulus increased, while the elongation at break decreased. The Z-L nanocomposite films had greater Young's modulus and tensile strength than the pristine zein films. The tensile strength which is the maximum tensile stress that the sample can carry before rupture, improved the most for Z-10L. The tensile strength of the pristine zein control was 2.26 ± 0.48 MPa and increased to, 5.53 ± 0.17 MPa when 10 % Laponite® were added (Z-10L). This corresponds to a 150% increase in tensile strength. The Young's Modulus, YM increased from 41 ± 1.9 MPa (Z-0L), to 114 ± 7.8 MPa (Z-10L) which corresponds to a 180% increase. The elongation at break, EAB, decreased with increasing Laponite® concentration. The reason behind the decrease in EAB with increasing Laponite® concentration can be attributed to the Si-N and Si-O bond formation (as seen in FTIR results), due to the interaction between the zein polymer and Laponite® nanoparticles. Increasing Laponite® particles increased the number of bond formation; as a result, the polymer chain experiences restricted mobility and % elongation at break decreased.

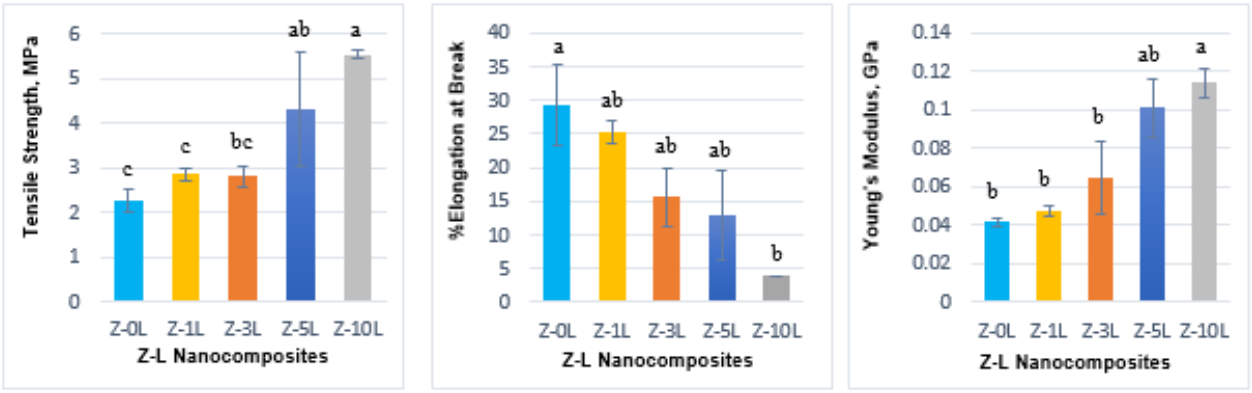

(a) (b) (c)

Fig. 4.10. Comparison of the different mechanical properties of the zein-Laponite® nanocomposites (a) Tensile Strength (b) %Elongation at Break (c) Young's Modulus. Different letters above error bars signifies a statistically significant difference ($p<0.05$)

Table 4.1. Comparison of Mechanical Property modification of different Zein-nanocomposites (with similar %nanomaterial loading) from literature

Zein Treatment	Plasticizer	% Nanofiller	Tensile Strength		Young's Modulus		Ref.
			% Increase	Value (MPa)	% Increase	Value (MPa)	
L	Oleic Acid	5	↑90%	4.3	↑146%,	101	Current Study
MMT	PEG	5	↑127%	6.48	↑ 315%,	3.36	[7]
CMF	Glycerol	4	↑28%	15.05	↑62%,	14.75	[15]
AL	Polyethylene Glycol	5 (1) *	↑153% *	3.8 (4.53) *	NA	NA	[16]

L Laponite®, *MMT* Montmorillonite, *CMF* Cellulose Micro fibrils, *AL* Alkaline Lignin

* Zein-AL nanocomposite showed highest tensile strength at 1% loading, but then it started to deteriorate, so tensile strength results for both 1% and 5% loading is reported.

Table 4.1 shows comparison with property modification of other zein nanocomposite films from the literature shows, the Z-L nanocomposites had the highest Young's modulus improvement compared to the other nanocomposites of zein.

4.5 Conclusion

For this study, novel biodegradable zein-Laponite® nanocomposites were successfully engineered, aiming at understanding the chemistry behind zein-Laponite® interaction, for advanced material design. Different fractions of Laponite® was incorporated into the zein biopolymer matrix using solvent casting technique and their investigation focused on the effects of Laponite® concentration on the mechanical, thermal, barrier and other physical properties, using the AFM, TEM, FTIR, Water vapor permeability, DSC and texture analyzer. The experimental findings show that Laponite® has been dispersed uniformly throughout the zein matrix, which is evident from the TEM images, FTIR spectra inspection as well as from the AFM roughness measurement. Films that were functionalized with the Laponite® nanoparticles were found to be superior combining a relatively high resistance to tearing (150% increase in tensile strength) and stiffness (180% increase in Young's Modulus). The WVP of the films decreased 40% on addition of 10% nanoparticle. The findings in this study can benefit advanced materials research in many aspects as it thoroughly explores the underlying chemistry between zein and nanoparticles interaction and explains in detail, the effect on their properties. This new and improved knowledge can lead to several innovative research opportunities related to enhancement of biodegradable packaging, designing of high-performance sensor materials and other biomaterials research with broad applications.

Supporting Information

Detailed description of characterization methods

Disclosure

The authors would like to disclose that there are no conflicts of interests.

Acknowledgements

The authors would like to thank, Dr. Christopher Gilpin and Laurie Mueller, for their assistance with TEM experiments, Dr. Patricia Bishop and Dr. Hartmut Hedderich, for their assistance with AFM and FTIR experiments. We would like to acknowledge USDA Hatch funds and the Scholle Endowment for financial support of this work.

4.6 References

1. Netravali AN, Chabba S (2003) Composites get greener. Materials Today 6:22–29 . doi: 10.1016/S1369-7021(03)00427-9

2. MacArthur E (2017) Beyond plastic waste. Science 358:843–843 . doi: 10.1126/science.aao6749

3. Law KL, Morét-Ferguson S, Maximenko NA, et al (2010) Plastic Accumulation in the North Atlantic Subtropical Gyre. Science 329:1185–1188 . doi: 10.1126/science.1192321

4. Chen G-G, Qi X-M, Guan Y, et al (2016) High Strength Hemicellulose-Based Nanocomposite Film for Food Packaging Applications. ACS Sustainable Chem Eng 4:1985–1993 . doi: 10.1021/acssuschemeng.5b01252

5. Rouf TB, Kokini JL (2018) Natural Biopolymer-Based Nanocomposite Films for Packaging Applications. In: Bionanocomposites for Packaging Applications. Springer, Cham, pp 149–177

6. Lai H-M, Padua GW (1997) Properties and Microstructure of Plasticized Zein Films. Cereal Chemistry Journal 74:771–775 . doi: 10.1094/CCHEM.1997.74.6.771

7. Luecha J, Sozer N, Kokini JL (2010) Synthesis and properties of corn zein/montmorillonite nanocomposite films. J Mater Sci 45:3529–3537 . doi: 10.1007/s10853-010-4395-6

8. Luecha J, Hsiao A, Brodsky S, et al (2011) Green microfluidic devices made of corn proteins. Lab on a Chip 11:3419–3425

9. Shukla R, Cheryan M (2001) Zein: the industrial protein from corn. Industrial crops and products 13:171–192

10. Lawton JW (2002) Zein: A History of Processing and Use. Cereal Chemistry Journal 79:1–18 . doi: 10.1094/CCHEM.2002.79.1.1

11. Anderson TJ, Ilankovan P, Lamsal BP (2012) Two fraction extraction of α-zein from DDGS and its characterization. Industrial Crops and Products 37:466–472 . doi: 10.1016/j.indcrop.2011.07.022

12. Shi W, Dumont M-J (2013) Review: bio-based films from zein, keratin, pea, and rapeseed protein feedstocks. J Mater Sci 49:1915–1930 . doi: 10.1007/s10853-013-7933-1

13. Dashdorj U, Reyes MK, Unnithan AR, et al (2015) Fabrication and characterization of electrospun zein/Ag nanocomposite mats for wound dressing applications. International Journal of Biological Macromolecules 80:1–7 . doi: 10.1016/j.ijbiomac.2015.06.026

14. Li J, Li Y, Lee T-C, Huang Q (2013) Structure and Physical Properties of Zein/Pluronic F127 Composite Films. J Agric Food Chem 61:1309–1318 . doi: 10.1021/jf3043055

15. Manisara P, Parichat M (2012) Cellulose Microfibril from Banana Peels as a Nanoreinforcing Fillers for Zein Films. Open Journal of Polymer Chemistry 2012: . doi: 10.4236/ojpchem.2012.22007

16. Oliviero M, Verdolotti L, Di Maio E, et al (2011) Effect of Supramolecular Structures on Thermoplastic Zein–Lignin Bionanocomposites. J Agric Food Chem 59:10062–10070 . doi: 10.1021/jf201728p

17. Ozcalik O, Tihminlioglu F (2013) Barrier properties of corn zein nanocomposite coated polypropylene films for food packaging applications. Journal of Food Engineering 114:505–513 . doi: 10.1016/j.jfoodeng.2012.09.005

18. Nedi I, Di Maio E, Iannace S (2012) The role of protein–plasticizer–clay interactions on processing and properties of thermoplastic zein bionanocomposites. J Appl Polym Sci 125:E314–E323 . doi: 10.1002/app.36860

19. Gaharwar AK, Rivera CP, Wu C-J, Schmidt G (2011) Transparent, elastomeric and tough hydrogels from poly(ethylene glycol) and silicate nanoparticles. Acta Biomaterialia 7:4139–4148 . doi: 10.1016/j.actbio.2011.07.023

20. Utech S, Boccaccini AR (2016) A review of hydrogel-based composites for biomedical applications: enhancement of hydrogel properties by addition of rigid inorganic fillers. J Mater Sci 51:271–310 . doi: 10.1007/s10853-015-9382-5

21. Kvien I, Sugiyama J, Votrubec M, Oksman K (2007) Characterization of starch based nanocomposites. J Mater Sci 42:8163–8171 . doi: 10.1007/s10853-007-1699-2

22. Liu F, Jiang G-C, Wang K, Wang J (2017) Laponite nanoparticle as a multi-functional additive in water-based drilling fluids. J Mater Sci 52:12266–12278 . doi: 10.1007/s10853-017-1375-0

23. Chouhan DK, Rath SK, Kumar A, et al (2015) Structure-reinforcement correlation and chain dynamics in graphene oxide and Laponite-filled epoxy nanocomposites. J Mater Sci 50:7458–7472 . doi: 10.1007/s10853-015-9305-5

24. Li X, Zhou M, Xu H, et al (2014) Synthesis and electrochemical performances of a novel two-dimensional nanocomposite: polyaniline-coated Laponite nanosheets. J Mater Sci 49:6830–6837 . doi: 10.1007/s10853-014-8385-y

25. Wu W, Dong Z, He J, et al (2016) Transparent cellulose/Laponite nanocomposite films. J Mater Sci 51:4125–4133 . doi: 10.1007/s10853-016-9735-8

26. Shan D, Li Q-B, Ding S-N, et al (2010) Reagentless biosensor for hydrogen peroxide based on self-assembled films of horseradish peroxidase/Laponite/chitosan and the primary investigation on the inhibitory effect by sulfide. Biosensors and Bioelectronics 26:536–541 . doi: 10.1016/j.bios.2010.07.051

27. Zanini VP, López de Mishima B, Solís V (2011) An amperometric biosensor based on lactate oxidase immobilized in Laponite–chitosan hydrogel on a glassy carbon electrode. Application to the analysis of l-lactate in food samples. Sensors and Actuators B: Chemical 155:75–80 . doi: 10.1016/j.snb.2010.11.026

28. Barbieri M, Cellini F, Cacciotti I, et al (2017) In situ temperature sensing with fluorescent chitosan-coated PNIPAAm/alginate beads. J Mater Sci 52:12506–12512 . doi: 10.1007/s10853-017-1345-6

29. Schmidt G, Nakatani AI, Butler PD, Han CC (2002) Small-Angle Neutron Scattering from Viscoelastic Polymer−Clay Solutions. Macromolecules 35:4725–4732 . doi: 10.1021/ma0115141

30. Schmidt G, Nakatani AI, Butler PD, et al (2000) Shear Orientation of Viscoelastic Polymer−Clay Solutions Probed by Flow Birefringence and SANS. Macromolecules 33:7219–7222 . doi: 10.1021/ma9918811

31. Gezer PG, Liu GL, Kokini JL (2016) Development of a biodegradable sensor platform from gold coated zein nanophotonic films to detect peanut allergen, Ara h1, using surface enhanced raman spectroscopy. Talanta 150:224–232 . doi: 10.1016/j.talanta.2015.12.034

32. Gezer PG, Hsiao A, Kokini JL, Liu GL (2016) Simultaneous transfer of noble metals and three-dimensional micro- and nanopatterns onto zein for fabrication of nanophotonic platforms. J Mater Sci 51:3806–3816 . doi: 10.1007/s10853-015-9699-0

33. Capello C, Fischer U, Hungerbühler K (2007) What is a green solvent? A comprehensive framework for the environmental assessment of solvents. Green Chemistry 9:927–934 . doi: 10.1039/B617536H

34. Panchapakesan C, Sozer N, Dogan H, et al (2012) Effect of different fractions of zein on the mechanical and phase properties of zein films at nano-scale. Journal of Cereal Science 55:174–182 . doi: 10.1016/j.jcs.2011.11.004

35. Bal Ram Singh (1999) Basic Aspects of the Technique and Applications of Infrared Spectroscopy of Peptides and Proteins. In: Infrared Analysis of Peptides and Proteins. American Chemical Society, pp 2–37

36. ASTM E (96) Standard test methods for water vapor transmission of materials. Foundation drainage rate: Hydraulic Gradient 1:18

37. Gezer PG, Brodsky S, Hsiao A, et al (2015) Modification of the hydrophilic/hydrophobic characteristic of zein film surfaces by contact with oxygen plasma treated PDMS and oleic acid content. Colloids and Surfaces B: Biointerfaces 135:433–440 . doi: 10.1016/j.colsurfb.2015.07.006

38. Guimarães TR, Chaparro T de C, D'Agosto F, et al (2014) Synthesis of multi-hollow clay-armored latexes by surfactant-free emulsion polymerization of styrene mediated by poly(ethylene oxide)-based macroRAFT/Laponite complexes. Polym Chem 5:6611–6622 . doi: 10.1039/C4PY00362D

39. Lewandowska K, Sionkowska A, Kaczmarek B, Furtos G (2014) Mechanical and Morphological Studies of Chitosan/Clay Composites. Molecular Crystals and Liquid Crystals 590:193–198 . doi: 10.1080/15421406.2013.874718

40. Fatnassi M, Solterbeck C-H, Es-Souni M (2014) Clay nanomaterial thin film electrodes for electrochemical energy storage applications. RSC Advances 4:46976–46979 . doi: 10.1039/C4RA04330H

41. Hodges CS, Ding Y, Biggs S (2010) The influence of nanoparticle shape on the drying of colloidal suspensions. Journal of Colloid and Interface Science 352:99–106 . doi: 10.1016/j.jcis.2010.08.044

42. Shan D, Wang Y-N, Xue H-G, et al (2009) Xanthine oxidase/Laponite nanoparticles immobilized on glassy carbon electrode: Direct electron transfer and multielectrocatalysis. Biosensors and Bioelectronics 24:3556–3561 . doi: 10.1016/j.bios.2009.05.009

43. Shi K, Kokini JL, Huang Q (2009) Engineering Zein Films with Controlled Surface Morphology and Hydrophilicity. J Agric Food Chem 57:2186–2192 . doi: 10.1021/jf803559v

44. Lee H-T, Lin L-H (2006) Waterborne Polyurethane/Clay Nanocomposites: Novel Effects of the Clay and Its Interlayer Ions on the Morphology and Physical and Electrical Properties. Macromolecules 39:6133–6141 . doi: 10.1021/ma060621y

45. Farmahini-Farahani M, Khan A, Lu P, et al (2017) Surface morphological analysis and water vapor barrier properties of modified Cloisite 30B/poly(3-hydroxybutyrate-co-3-hydroxyvalerate) composites. Applied Clay Science 135:27–34 . doi: 10.1016/j.clay.2016.08.033

46. Lin-Vien D, Colthup NB, Fateley WG, Grasselli JG (1991) The handbook of infrared and Raman characteristic frequencies of organic molecules. Elsevier

47. Yamazaki H, Ishikawa Y, Fujii M, et al (2014) The Influence of Fluorinated Silicon Nitride Gate Insulator on Positive Bias Stability toward Highly Reliable Amorphous InGaZnO Thin-Film Transistors. ECS J Solid State Sci Technol 3:Q20–Q23 . doi: 10.1149/2.014402jss

48. Reza Mahdavinia G, Ettehadi S, Amini M, Sabzi M (2015) Synthesis and characterization of hydroxypropyl methylcellulose- g -poly(acrylamide)/LAPONITE® RD nanocomposites as novel magnetic- and pH-sensitive carriers for controlled drug release. RSC Advances 5:44516–44523 . doi: 10.1039/C5RA03731J

49. Krimm S, Bandekar J (1986) Vibrational Spectroscopy and Conformation of Peptides, Polypeptides, and Proteins. Advances in Protein Chemistry 38:181–364 . doi: 10.1016/S0065-3233(08)60528-8

50. Mizutani Y, Matsumura Y, Imamura K, et al (2003) Effects of Water Activity and Lipid Addition on Secondary Structure of Zein in Powder Systems. J Agric Food Chem 51:229–235 . doi: 10.1021/jf0205007

51. Matsushima N, Danno G, Takezawa H, Izumi Y (1997) Three-dimensional structure of maize alpha-zein proteins studied by small-angle X-ray scattering. Biochim Biophys Acta-Protein Struct Molec Enzym 1339:14–22 . doi: 10.1016/S0167-4838(96)00212-9

52. Benami A, Santana G, Ortiz A, et al (2007) Strong white and blue photoluminescence from silicon nanocrystals in SiN x grown by remote PECVD using SiCl 4 /NH 3. Nanotechnology 18:155704 . doi: 10.1088/0957-4484/18/15/155704

53. Li Y, Wang L, Yin S, et al (2011) Rapid Crystallization Process of Amorphous Silicon Nitride. J Am Ceram Soc 94:4169–4173 . doi: 10.1111/j.1551-2916.2011.04914.x

54. Kopani M, Mikula M, Pinčík E, et al (2014) FT IR spectroscopy of nitric acid oxidation of silicon with hafnium oxide very thin layer. Applied Surface Science 301:24–27 . doi: 10.1016/j.apsusc.2014.01.124

55. Pluchery O, Costantini J-M (2012) Infrared spectroscopy characterization of 3C–SiC epitaxial layers on silicon. J Phys D: Appl Phys 45:495101 . doi: 10.1088/0022-3727/45/49/495101

56. Huang X, Brittain WJ (2001) Synthesis and Characterization of PMMA Nanocomposites by Suspension and Emulsion Polymerization. Macromolecules 34:3255–3260 . doi: 10.1021/ma001670s

57. Rouf TB, Kokini JL (2016) Biodegradable biopolymer–graphene nanocomposites. Journal of Materials Science 51:9915–9945

58. Peles Z, Zilberman M (2012) Novel soy protein wound dressings with controlled antibiotic release: Mechanical and physical properties. Acta Biomaterialia 8:209–217 . doi: 10.1016/j.actbio.2011.08.022

59. Martin-Polo M, Mauguin C, Voilley A (1992) Hydrophobic films and their efficiency against moisture transfer. 1. Influence of the film preparation technique. Journal of agricultural and food chemistry 40:407–412

60. Martin-Polo M, Voilley A, Blond G, et al (1992) Hydrophobic films and their efficiency against moisture transfer. 2. Influence of the physical state. Journal of agricultural and food chemistry 40:413–418

61. Bras J, Vaca-Garcia C, Borredon M-E, Glasser W (2007) Oxygen and water vapor permeability of fully substituted long chain cellulose esters (LCCE). Cellulose 14:367–374 . doi: 10.1007/s10570-007-9123-2

62. Hirvikorpi T, Vähä-Nissi M, Harlin A, et al (2011) Enhanced water vapor barrier properties for biopolymer films by polyelectrolyte multilayer and atomic layer deposited Al2O3 double-coating. Applied Surface Science 257:9451–9454 . doi: 10.1016/j.apsusc.2011.06.031

63. Tunç S, Duman O, Polat TG (2016) Effects of montmorillonite on properties of methyl cellulose/carvacrol based active antimicrobial nanocomposites. Carbohydrate Polymers 150:259–268 . doi: 10.1016/j.carbpol.2016.05.019

64. Mahmoudian S, Wahit MU, Ismail AF, Yussuf AA (2012) Preparation of regenerated cellulose/montmorillonite nanocomposite films via ionic liquids. Carbohydrate Polymers 88:1251–1257 . doi: 10.1016/j.carbpol.2012.01.088

CHAPTER 5. DESIGN AND MECHANISTIC UNDERSTANDING OF GRAPHENE OXIDE REINFORCED ZEIN NANOCOMPOSITES WITH IMPROVED MECHANICAL, BARRIER AND THERMAL PROPERTIES

Tahrima B. Rouf [1], Gudrun Schmidt [2], Mukerrem Cakmak [3], Jozef L. Kokini [1]

1. Department of Food Science, Purdue University, West Lafayette, IN-47907, USA
2. Department of Chemistry, Purdue University, West Lafayette, IN-47907, USA
3. School of Materials and Mechanical Engineering, Purdue University, West Lafayette, IN-47907, USA

Reproduced with permission. Full citation:

Rouf TB, Schmidt G, Cakmak M, Kokini JL (2019) Design and mechanistic understanding of graphene oxide reinforced zein nanocomposites with improved mechanical, barrier and thermal properties. J Mater Sci 54:12533–12552. https://doi.org/10.1007/s10853-019-03817-w

5.1 Abstract

Graphene oxide (GO)-based zein nanocomposite films with superior mechanical, barrier and thermal properties were fabricated by incorporating GO nanoparticles into corn protein zein (Z), through the solvent casting process. The study offers a mechanistic understanding of the effect of graphene oxide nanofiller on the physico-chemical properties of zein. TEM of the zein/graphene oxide (Z-GO) nanocomposites showed uniform dispersion of GO sheets up to 1%GO loading. Mechanisms for Z-GO nanocomposite formation through covalent and non-covalent bonding are developed based on FTIR, FT-Raman and DSC results. At only 3% loading, the Young's Modulus of a nanocomposite film increased by 300% and Tensile strength increased by 80%. The increases in mechanical property improvements are accompanied by surface roughness increases as indicated by AFM studies. Even though GO is hydrophilic, the Z-GO nanocomposite films showed hydrophobic tendencies. The amount and degree of exfoliation of GO as well as the relative orientation of GO nanoparticles within the zein film all play an important role in the physical property changes of the film. The films became less permeable with increasing amounts of GO

addition, as shown by water vapor permeability tests. GO increased thermal stability as shown by TGA.

Keywords: Zein, GO, Packaging, TEM, FTIR, AFM, Water Vapor Permeability

5.2 Introduction

Synthetic polymers are polluting the environment at an alarming rate. The "Great pacific ocean garbage patch", has grown in size from double the span of Texas [1], to three times the span of France [2]. Biopolymers have received significant consideration as eco-friendly alternatives with nontoxicity, biocompatibility, low cost, non-dependence on petroleum sources, and availability from renewable resources. Moreover, natural bio-based polymers are easily biodegradable within a short period, which solves the waste-disposal problems generated by synthetic non-biodegradable polymers. Unfortunately, many biopolymers do not have good mechanical strength and barrier properties. As a result many research groups are exploring how various performance properties of biodegradable biopolymers can be improved [3].

Plant and animal proteins including wheat gluten, sorghum kafirin, peanut proteins, corn zein, gelatin, fish myofibrillar protein, keratin, casein and whey protein [4–7] have been studied for their film formation properties and the associated applications. Zein, an amphiphilic protein from corn, has shown potential for use as biodegradable packaging material [8, 9], encapsulating agent [10], sensor platform [11]. Zein films can be formed using solution casting and thermoplastic processing [8, 9]. Although pristine zein films have poor mechanical properties and are brittle, plasticizers including oleic acid, palmitic acid, linoleic acid, chemical cross-linking, and laminating with other protein films can reduce brittleness and increase ductility [12]. However, none of these techniques have been able to improve zein's thermal and mechanical properties so as to compete with commercial synthetic polymer films. A potential solution and impactful avenue to explore is to improve zein properties using a combination of nanofillers and film forming techniques [8, 13, 14].

Carbon nanotubes, nano clays, and graphene nano sheets have been successfully used to improve the properties of polymers and biopolymers[13, 15–17]. For example, PLA from starch, showed excellent mechanical and barrier properties after incorporating thermally reduced graphene (TRG) [18], graphene oxide (GO) [19] and reduced graphene oxide (RGO), mainly using

in situ polymerization, melt blending and solution casting [20]. Nanocomposites of polysaccharides including starch, chitosan, alginate and cellulose have been manufactured using different forms of graphene, with different preparation methods [13, 21–23]. Results have shown that graphene increases mechanical, thermal, barrier and electrical properties of many of these biopolymers [20, 24]. Graphene and its derivatives have also been used in biosensors for the purpose of protein detection [25]. The level of enhancement of mechanical and barrier properties depends on the nature of polymer-nanoparticle interactions and the uniform dispersion of nanoparticle in polymer matrix [26].

There have been some recent studies on the fabrication of nanocomposite hydrogels using GO and different polysaccharides and proteins. Zhao et al. 2019 [21] fabricated GO-maize amylopectin (MA) (GO: MA ratio = 20:1, 30:1) composite gels to study their adsorption capacities for different organic chemicals like p-aminophenol (PAP), p-nitrophenol (PNP) and inorganic substances like Pb^{2+}, Mn^{2+}, $Cr_2O_7^{2-}$, Cd^{2+} etc. FTIR comparison of GO-$MA_{30:1}$ and GO-$MA_{20:1}$ before and after adsorption of PAP, Pb^{2+} and Nd^{3+} indicated peak shift due to adsorption, XPS peaks indicate formation of metal-oxygen coordination bonds (O-Pb, O-Nd) that greatly improved the adsorption process. In the study by Xu et al. 2019 [23], three-dimensional (3D) egg-white (EW)-GO nanocomposite gels (GO: EW = 1:1, CEG1:1) were studied for their adsorption abilities of rare earth elements. FTIR studies indicated hydrogen-bonding interactions between GO and EW, while XPS spectrum further verified successful fabrication of CEG nanocomposites.

Three-dimensional porous graphene oxide-zein hydrogels have been produced with GO to zein ratio of 3: 1, 5:1, 9:1 using a hydrothermal process, where zein acts as a strengthening agent for the GO hydrogel, for the purposes of selectively adsorbing and harvesting rare earth elements [27]. Maximization of the adsorption and harvesting capacities of these rare earth elements for enrichment purposes were the main focus of the paper and they reported the maximum adsorption capacities of GO-$Z_{9:1}$ for lanthanum (La), yttrium (Y), ytterbium (Yb), neodymium (Nd) and erbium (Er) were 17.29, 14.2, 10.08, 9.68 and 11.72 mg/g, respectively.

The role of zein as a strengthening agent for GO hydrogels for the purposes of selectively adsorbing rare earth elements have been studied [27], but the role of GO nanoparticles as a reinforcing agent for zein nanocomposite films for packaging application has never been investigated. In fact, there are very few studies on protein-GO nanocomposites films in general. A study by Panzavolta et al. [28] utilized solution casting to fabricate nanocomposites from pig

gelatin and graphene oxide and reported a 50% increase in Young's modulus at 1% GO loading. While another group studied bioactive gelatin-GO nanocomposites, where addition of 1 wt% GO improved Young's modulus by 65% and acted as a biological activator [29].

According to our knowledge, zein protein has never been functionalized or reinforced with GO nanoparticles, in order to form nanocomposite films for packaging and other functional film applications. Many studies lack mechanistic understanding for specific interactions of the biopolymer and the nanofiller. The effects of the plasticizer on the interactions between the polymer and the nanoparticle are not clear. Earlier research primarily focused on the combined effects of the nanoparticles and plasticizers, by studying macroscopic property changes [13]. The underlying chemistry of nanocomposite formation, in the presence, and absence of plasticizers needs further understanding.

This paper focuses on the property enhancements of zein films with the addition of graphene oxide. We provide mechanistic understanding of the synergistic effects involved in zein-GO nanocomposites by studying 1) the conformational changes in zein secondary structure during nanocomposite formation and 2) The changes in FTIR and FT-Raman spectra leading to understanding chemical interactions between zein, the plasticizer oleic acid and GO. The mechanism proposed between zein and GO in the presence of the plasticizer, is based on interpretation of these results. The effects of nanocomposite formation on zein surface topography through AFM and water contact angle measurements, are particularly significant for the development of tunable hydrophilic/hydrophobic properties relevant to biomedical, industrial and functional film research. We present detailed understanding related to the changes in surface topography and surface wettability.

5.3 Experimental Methods

5.3.1 Materials

70% ethanol (140 proof (70%)) was purchased from Decon™ Labs). Monoglyceride was purchased from Alfa Aeser (Ward Hill, MA, USA). Zein (90% crude protein dry weight basis) and oleic acid were obtained from Sigma-Aldrich (Milwaukee, WI, USA)). Graphite flakes, potassium permanganate ($KMnO_4$), 96% sulfuric acid (H_2SO_4), phosphoric acid (H_3PO_4), 30% hydrogen peroxide (H_2O_2) were purchased from Fisher Scientific.

5.3.2 Preparation of GO using Tour's Method

Graphene Oxide (GO) was prepared using Tour's method [30]. An aliquot consisting of 3g of graphite flake, 18g $KMnO_4$, 360 mL H_2SO_4, 40 mL H_3PO_4 was added into a beaker to form a dark green color. The mixture was stirred vigorously at 50°C. After 12 h, the mixture was poured over 400mL of ice (DI water) while stirring. This step caused the color of the mixture to turn brown. Then H_2O_2 was added dropwise until the mixture turned bright yellow. Centrifuging at 10,000 rpm speed for 30min, caused separating of GO from the supernatant. The graphene oxide was washed/centrifuged three times with 1 M of HCl aqueous solution and deionized water. After several washing steps, GO turned black. Afterwards the GO was dried in a desiccator, over $CaSO_4$ drierites, and then re-dispersed in 70% aqueous solution with sonication.

5.3.3 Fabrication of Zein-GO Nanocomposite Films

Zein films were prepared according to Rouf et al. 2018 [8]. A beaker was filled with 50 mL of 70% ethanol, then GO was added in amounts of 0.1wt%, 0.3wt%, 0.5wt%, 0.7wt%, 1wt%, 1.5wt%, 2wt%, 3wt%. This mixture was sonicated for 1 minute at 39% amplitude, stirred and heated to 65^0C. Zein powder in amounts of 10g was poured slowly into each GO-ethanol mixture and stirred for one hour. The zein to 70% ethanol ratio was maintained at 1:5 weight/volume. In a separate beaker, 10 g of oleic acid plasticizer and 1.5 g of monoglyceride emulsifier were mixed and heated, until the monoglyceride dissolved in the oleic acid. The oleic acid-monoglyceride solution was added to the zein-GO solutions and the resulting mixtures were stirred for 24 hours and then sonicated for 30 seconds. Afterwards, 10 ml of each solution was pipetted onto a polystyrene petri dish lined with PDMS, which allowed the zein film to be removed easily after solvent evaporation. The petri dishes were placed in desiccators and dried over $CaSO_4$ drierites for 3 weeks.

5.3.4 Characterization Methods

GO samples for Transmission Electron Microscopy (TEM), were prepared by dispersing the GO in ethanol, sonicating for 5 minutes and then placing the dispersion on holey carbon TEM grids. A Tecnai T20 TEM (FEI Company) with an acceleration voltage of 200 kV was used. Z-

GO nanocomposite samples for TEM were prepared following a procedure published previously [8].

The surface morphologies and roughness of the nanocomposite films were investigated using a Veeco Multimode Atomic Force Microscope (AFM) (Veeco Instruments, Inc., New York). Si-Ni Tips (Spring Constant: 37 N/m, Frequency: 300 kHz), had a pyramidal shape with a height of 15 μm, from Ted Pella, Inc. Roughness data was presented in the forms of root mean square roughness, 'Rq' and average roughness 'Ra'. Details about Rq and Ra are discussed in the supplementary information. Other specifics of these measurements are reported in the literature [8].

Fourier Transform Infrared Spectroscopy (FTIR) was performed for both quantitative and qualitative analysis, specifically for identifying chemical bond formation within the nanocomposites. Experiments were done using a nitrogen cooled Attenuated Total Reflectance FTIR (Nicolet Nexus 470 FTIR, Thermo Fisher Scientific, Waltham MA), with 64 scans at a resolution of 4 cm^{-1}. The FTIR analysis and secondary structural analysis was done using a method described before [8]. Within the amide I band, the α-helix conformation gives characteristic peaks around 1653- 1658 cm^{-1}, β-sheets give characteristic peaks around 1632-1636 cm^{-1} and β-turn structures show characteristic peaks around 1680-1686 cm^{-1} [31]. The amide I region may also display the presence of β-turns around 1671 cm^{-1}, and intermolecular β sheets around 1610 cm^{-1} [32].

FT-Raman spectroscopy using a NXR FT-Raman Spectrometer (Thermo Fisher Scientific, Waltham, MA) provided fingerprint identification of molecules through vibrational information specific to the chemical bonds and symmetry of molecules. FT-Raman tests were conducted for the GO sheets and Z-GO nanocomposites, following a method described in literature [33].

Differential scanning calorimetry (DSC) was performed using a Discovery Nano Series DSC instrument (TA instruments, Delaware, USA). Calibration was based on pure indium and sapphire. An empty aluminum pan was used as reference. Samples of 4-5 mg were subjected to analysis using an initial heating cycle starting from 20 ºC to 300 ºC and then cooling back to 20 ºC at a rate of 10 ºC/min per cycle, and under continuous purging of nitrogen at 50 ml/min. In all DSC traces, positive upward peaks correspond to exothermic processes and downward peaks correspond to endothermic processes.

Water contact angle (WCA) measurements were performed with an Attension Theta Auto Optical Tensiometer (Biolin Scientific). All measurements were done on the sides of the zein-GO films that were previously in contact with PDMS. Other specifics of these measurements are reported in the literature [8].

The water vapor barrier properties of the nanocomposite films were analyzed through measuring water vapor permeability (WVP) using Gardco® permeability cups (Paul N. Gardner Company, Inc., FL, USA) by following ASTME 96 (1996) method [34]. Other aspects of these measurements have been described before [8].

Thermogravimetric analysis (TGA) was used to monitor the effect of GO content on thermal properties of zein-GO nanocomposite films. TGA was performed on a TGA 55 instrument (TA instruments, Delaware, USA) in nitrogen atmosphere. The samples were heated from room temperature to 600 °C at a heating rate of 10 °C/min.

The tensile strength (TS), Young's Modulus (YM) and percentage of elongation at break (%EAB) were determined using a TA.XT Plus Texture Analyzer (Texture Technologies Corp, South Hamilton, MA) with a 30 g load cell following a well-known procedure [8].

For each of the zein nanocomposites, the experiments were repeated three times. Data were statistically analyzed and compared using Minitab 18 (one-way ANOVA) with 95% confidence level. Tukey's comparison tests were applied ($p < 0.05$) and lettering system was used throughout the paper to show significant difference, such that different letters indicate significant difference between the adjacent values [8].

5.4 Results and Discussion

We first present the results from FTIR, FT-Raman and DSC. These chemical interaction experiments help establish the nature of chemical bonding between zein and GO. Then we present and discuss the TEM experiments providing microscopic insights into interactions between GO and zein. Surface properties, permeability, thermal and mechanical measurements present evidence for the changes and improvements in physical properties of zein GO nanocomposite films.

5.4.1 FTIR

In **Fig. 5.1**, FTIR data from pristine GO sheets showed characteristic peaks at 1067 cm^{-1} due to C-OH bending oscillations, 1390 cm^{-1} due to epoxide (C–O–C) vibrations, and 1623 cm^{-1}due to vibrations from ketonic species (C=O). Weaker peaks were observed at 1738 cm^{-1} from C=O stretching vibrations of carboxyl and carbonyl moieties [35]. A broad prominent peak at 3358 cm^{-1} comes from –OH stretching vibrations of hydroxyl groups. All these peaks are in agreement with earlier studies with pristine GO [35]. The pH of GO solution in water was reproduced at pH 2-2.50, suggesting that the C=O and C-OH groups are responsible for the carboxylic acid character of GO in solution. This is important because GO may interact with the $-NH_2$ groups on proteins to form covalent peptide-like bonds.

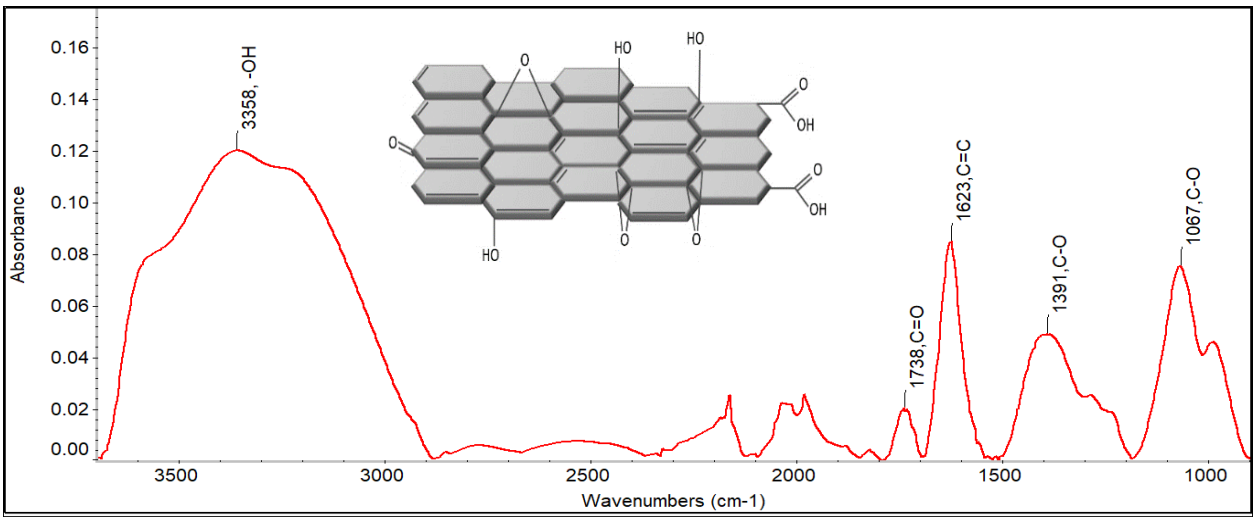

Fig. 5.1. FTIR Spectra of GO showing all the characteristic peaks (Inset image shows surface of GO decorated with possible oxygen containing functional groups)

Fig. 5.2 shows comparison of FTIR data of plasticized zein control films (zein + oleic acid), as well as plasticized zein nanocomposite films containing 0.1%, 0.3%, 0.5%, 0.7%, and 1% GO. FTIR data of the zein nanocomposite films show typical protein peaks with amide I (1600 -1700 cm^{-1}), amide II (1480-1575 cm^{-1}) and amide III (1230-1330 cm^{-1}) bands. The amide I band, is caused by the stretching of the C=O double bonds and gives information about the secondary structures in proteins. The peaks between 2800 to 3000 cm^{-1} come from $-CH_3$ and $-CH_2$ side chain aliphatic groups of amino acids. The broad peak at 3000-3500 cm^{-1} is well known and comes from the N-H stretching of amide structures. In FTIR spectroscopy, the rise of new peaks in the zein nanocomposite films or shift in original zein peaks in the spectra gives information about zein-

graphene oxide interactions. These peaks help understand and ultimately tune these interactions for an improved nanocomposite design. The interactions of zein with C-O groups from graphene oxide are derived from the peaks shown in Fig. 2, where a new peak 1050 cm^{-1} in the zein GO nanocomposite films is attributed to increased C-C-O stretching vibrations [36]. The inset expansion of this peak in **Fig. 5.2**, shows this increase in intensity with concentration of GO.

The spectra for each concentration of GO obtained over multiple locations on the zein-GO films are highly reproducible and superimpose perfectly. This suggest that GO is dispersed uniformly throughout the matrix. If the sample would be heterogeneous, the peak intensities would differ within the samples of the same formulation. Other studies found in the literature have used this technique to confirm uniform distribution of particles in a matrix [13].

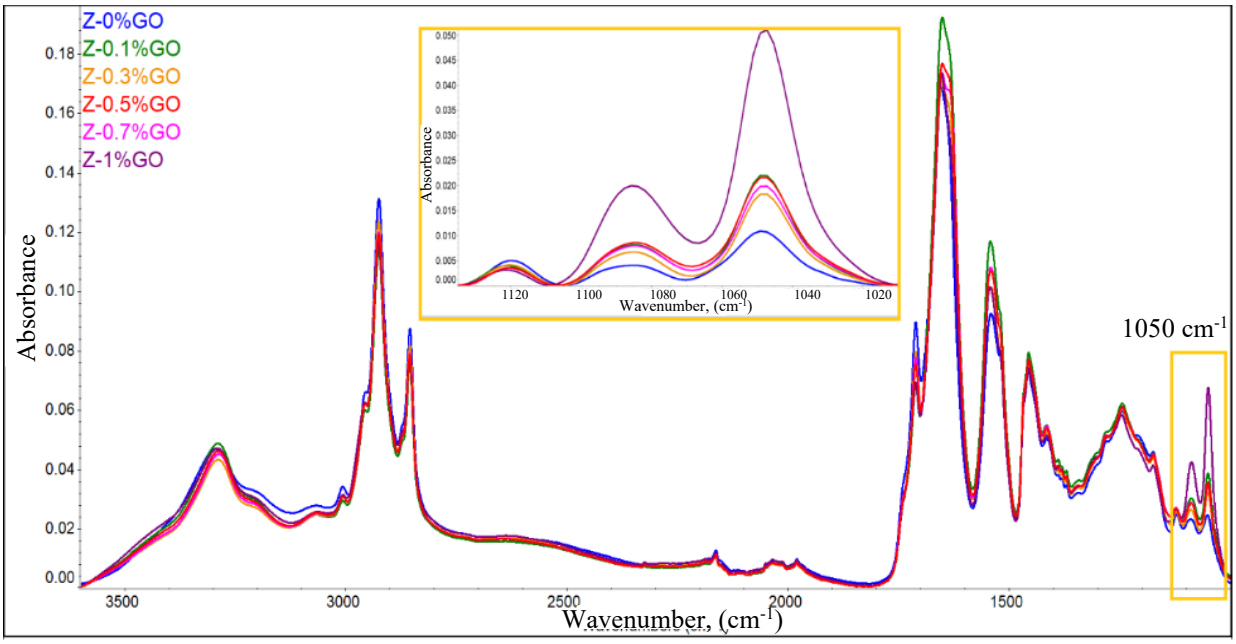

Fig. 5.2. Superimposition of full FTIR spectra of Z-GO nanocomposites, showing how the peak at 1050 cm^{-1} increases in intensity with increasing concentration of GO

There are possibilities of hydrogen bonding between oxygen containing groups (-OH, -COOH) from GO and –NH and -C=O groups of zein, as can be seen in previous studies of GO with other polymers [37–40]. Hydrogen bonding between GO and zein amino acids changes the native secondary structure of zein. Nanocomposites films containing Z-0% to Z-3% GO show different ratios of β turns, α helices, and β sheets (**Fig. 5.3**). The nanocomposite formation affected the area and height of the characteristic amide I peaks. For example, β-sheet conformation increases relative to the zein control up to Z-0.7% GO. Above a concentration of 0.7% GO, the β-

sheet conformation decreases. Changes observed in α-helix and β-turns are the result of changes in % β-sheet conformation. The decrease in % β sheets can be attributed to hydrogen bond formation between zein molecule and graphene oxide.

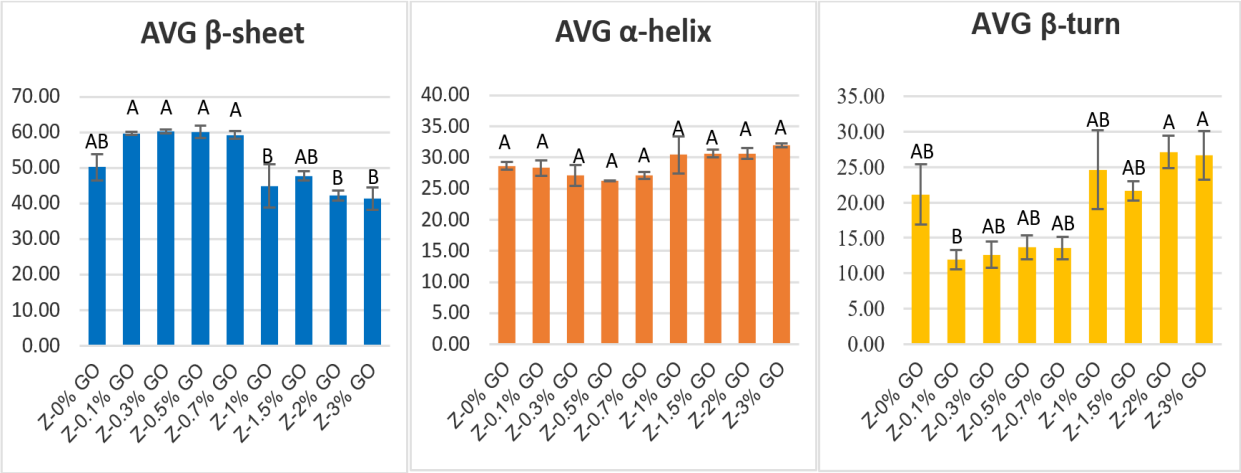

Fig. 5.3. Zein-GO nanocomposites show a decrease in β sheets, while α-helix data do not show significant difference with increasing GO concentrations, β-turns do show some increase, but it is statistically insignificant. Different letters above error bars signifies a statistically significant difference ($p < 0.05$)

GO showed greater propensity to form hydrogen bonds with β-sheets as opposed to α-helices. The H-bond forming functional groups in β-sheets are exposed due to the sheet like orientation which can more easily accommodate the C=O groups from GO, resulting in H-bond formation. The hydrogen bonding groups are buried in the interior of the α-helices and thus not easily available to GO sheets. β-sheet structures were bonded to each other through intermolecular hydrogen bonds, before being broken in favor of hydrogen bonds to GO. This may have caused reduction of β sheet peaks in the Z-GO nanocomposites in the presence of GO.

5.4.2 FT-Raman

The FT-Raman spectrum of GO in **Fig. 5.4** (a) showed two prominent and characteristic peaks at 1309 and 1590 cm^{-1}, corresponding to the D band and G band [10]. These are Raman active bands that are not detected using FTIR. The G band is caused by in plane C=C bond stretching vibrations of sp^2 bonded carbon atoms and the D band is due to vibrations of the carbon atoms of disordered graphite. The prominent D peak in the FT-Raman spectra is an indication of the presence of disorder in the GO sheets. Structural disorder is induced by tears and folding over

of the GO sheets as well as the presence of residual oxygen coming from graphene oxidation and point defects [41].The intensity ratio of D to G bands (I_D/I_G) indicates the ratio of C=O to C=C. The degree of disorder caused by defects, ripples and edges is approximately 0.86 in this study compared to 0.64 [42] and 0.76 [41] reported in earlier studies. Highly ordered graphite displays a G band at 1575 cm^{-1}, which is caused by in-phase vibration of the graphite lattice and a very weak disorder band at approximately 1355 cm^{-1}[42]. During GO fabrication, amorphization of graphite causes significant changes in both G and D bands. A common understanding is that, higher disorder in graphite results in broader G and D bands, where the D band is of higher intensity compared to the G band [43]. As the graphite is oxidized during GO preparation method, the D/G ratio increases, and approaches 1 (D band peak height, 0.55/ G band peak height, 0.64 = 0.86) (**Fig. 5.4** (a)).

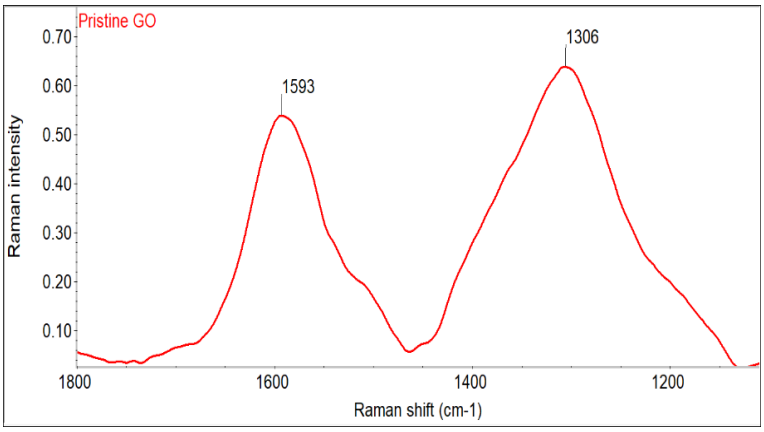

(a)

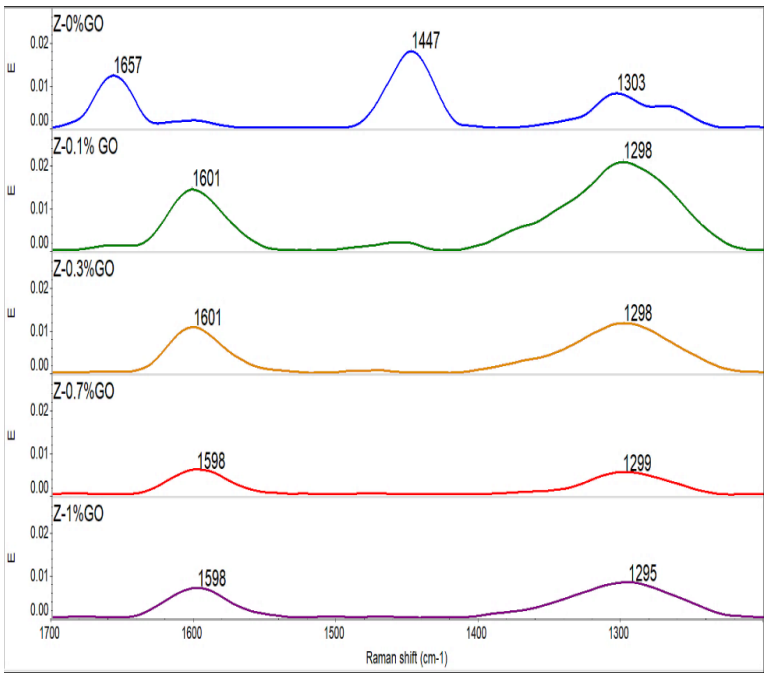

(b)

Fig. 5.4. FT-Raman of (a) GO only sample, (b) Control Zein film, Z-0.1%GO, Z-0.3%GO, Z-0.7% GO and Z-1% GO nanocomposites

The average FT-Raman spectra of Z-GO nanocomposite films containing 0%, 0.1%, 0.3%, 0.7% and 1% GO are shown in **Fig. 5.4** (b). FT-Raman spectra of control zein films shows the amide I band (1600–1700 cm^{-1}), which is caused by the C=O and C=C groups. The amide III peaks (1220–1300 cm^{-1}) are caused by C-N and N-H groups. The peak observed between 1400 and 1480 cm^{-1} is typically caused by aliphatic $–CH_2$ and $–CH_3$ vibrations, and partially in plane OH bending in carboxylic acids [44, 45], which comes from oleic acid [46]. When the zein control is compared with the Z-GO nanocomposites spectra, two major changes are observed. The first

change is the disappearance of the peak at 1450 cm^{-1} with only small amounts of GO addition (Z-0.1%GO). The peak at 1450 cm^{-1} is attributed to -CH_2 bond vibrations and in plane OH bending in carboxylic acids coming from oleic acid and is only visible for zein control samples. This peak disappears in all of the Z-GO nanocomposites, which might be correlated with a reduction in the interaction between zein and oleic acid during nanocomposite formation, which reduces the intensity of the 1450cm^{-1} peak.

Another significant difference between the spectra of the zein control and the Z-GO film, is the shift in peaks at 1657 to 1595 cm^{-1}. The zein control peak at 1650cm^{-1} is the amide I band, but after nanocomposite formation, this peak shifted to 1600-1595 cm^{-1}. This shift can be the result of secondary structure changes through hydrogen bond formation, discussed in the FTIR section.

5.4.3 Differential Scanning Calorimetry (DSC)

Fig. 5.5 shows the DSC thermograms obtained from pristine graphene oxide, and zein-GO nanocomposites films. For pristine GO, a strong exothermic peak from 150^{o}C to 200^{o}C and an endothermic peak between 200 to 250 ^{o}C are observed, which can be attributed to the decomposition of the labile oxygen-containing functional groups, –COOH, –OH, –C=O etc. [47]. For lower loadings of GO in Z-GO films the thermograms look similar to each other but at loadings higher than 1%, two significant changes occur. First, for Z-2%GO and Z-3%GO a strong endothermic peak between 260-290^{o}C is observed which is the melting peak of the Z-GO nanocomposite films. With higher loading of GO, (from 2% GO to 3%GO), the endothermic melting peak shifts by 20^{o}C lower temperature. This is a clear indication of hydrogen bond formation between zein and graphene oxide molecules [48]. On the other hand, for both Z-2%GO and Z-3%GO nanocomposite film thermograms, there are two exothermic peaks between 150-160^{o}C and between 170-200^{o}C (highlighted with dashed lines). The exothermic peaks for Z-3%GO nanocomposite compared to that of Z-2%GO is broader and has higher intensity. The broadening and the shift in the peak for Z-3%GO indicates covalent bond formation between zein and GO molecules [49]. From the DSC images, we can see that control plasticized zein film did not show any strong peaks indicating hydrogen or covalent bonds, whereas for the zein-GO nanocomposites, strong peaks indicating covalent and hydrogen bonds were clearly visible at 2 and 3% GO loading. The DSC results of the Z-GO nanocomposites support both hydrogen bonding as well as covalent bonding, with exothermic covalent bonding interactions visible only at higher loadings of GO.

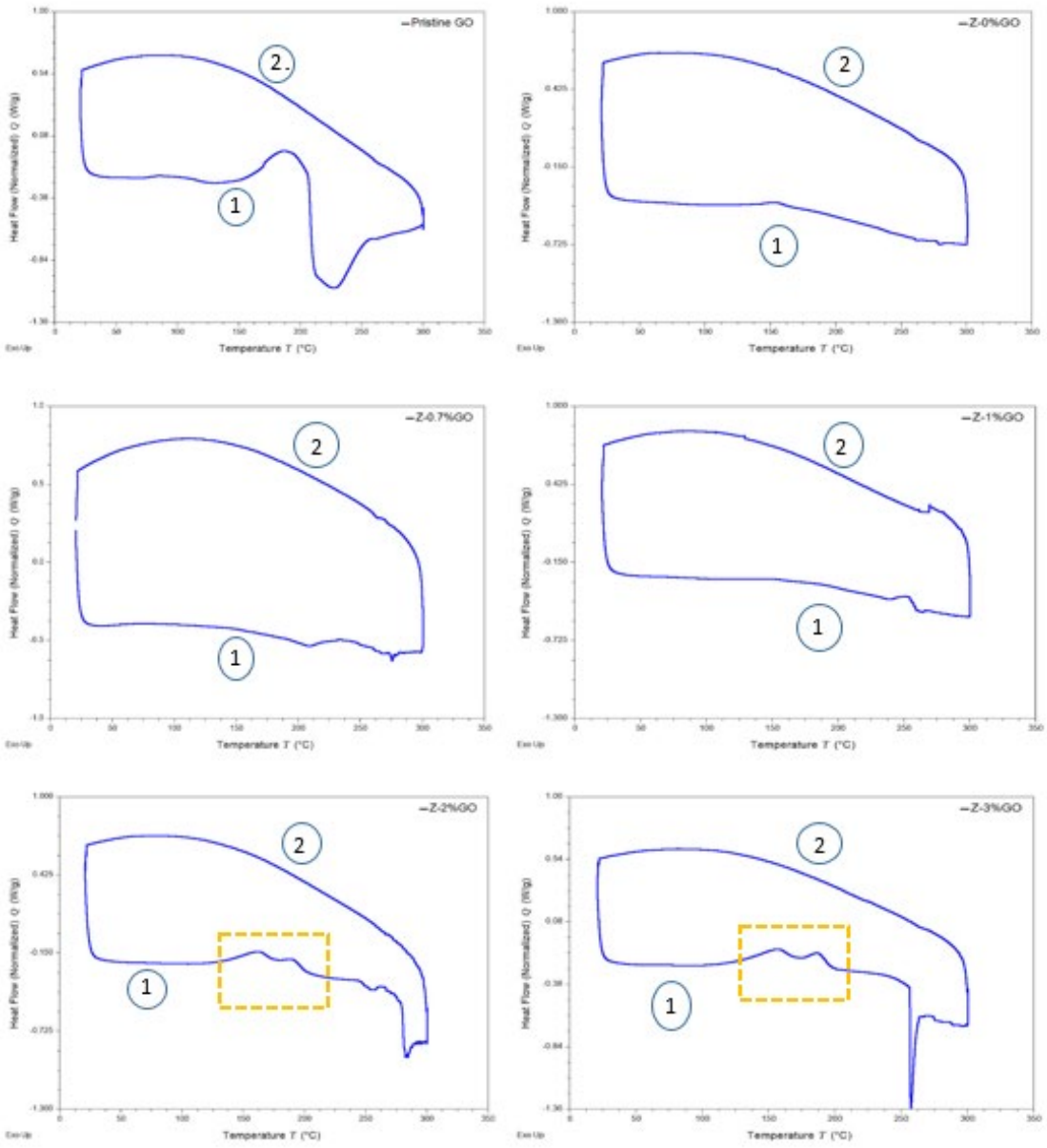

Fig. 5.5. DSC curves for Pristine GO, Z-0%GO, Z-0.7%GO, Z-1%GO, Z-2%GO and Z-3%GO. (1) Heating Cycle from 20ºC to 300ºC (2) Cooling cycle from 300ºC to 20ºC

All three characterization techniques, FTIR, FT-Raman, and DSC suggest that both hydrogen and covalent bonding interactions are present. For FTIR, the new peak at 1050 cm^{-1} is an indication of increased C-C-O stretching vibrations possibly formed through bonding between zein and GO molecules. This observation is also supported by the decrease in β-sheets within the matrix suggesting that the -NH groups in β-sheets participate in hydrogen bonding. For FT-Raman data, the disappearance of the 1450 cm^{-1} peak, responsible for $–CH_2$ and –OH vibrations from oleic acid, indicates reduced covalent interaction between oleic acid and zein molecules. The lower shift of

the amide I peak can be related to hydrogen bond forming between zein and GO molecules. The DSC results support the observations and interpretations resulting from FTIR and FT-Raman data. The reduction in melting point with higher concentration of GO indicates hydrogen bonding, whereas, two exothermic peaks of Z-GO nanocomposite films indicate covalent bonding. Taken together there is complimentary evidence of two types of bonding; hydrogen bonding and covalent bonding. Hydrogen bonding can take place when 1)the -NH groups in the β-sheet structure of zein hydrogen bonds with the -C=O groups of graphene oxide 2) Hydrogen bonding between amine groups of glutamine turns in zein and hydroxyl groups on GO is possible, which was also proposed in the previous literature [50]. Possible routes for hydrogen bonding are shown below:

$$\text{Zein-NH} + \text{CO-GO} \rightarrow \text{Zein-NH----OC-GO} \quad \ldots\ldots\ldots\ldots\ldots\ldots\ldots\ldots \quad (1)$$

$$\text{Zein-NH}_2 + \text{OH-GO} \rightarrow \text{Zein-NH}_2\text{----OH-GO} \quad \ldots\ldots\ldots\ldots\ldots\ldots\ldots\ldots \quad (2)$$

When zein is introduced into the heated 70% ethanol solution, the zein molecules undergo a solubilization process, which breaks some of the intermolecular hydrogen bonds in β-pleated sheets. When GO molecules come near the β-pleated sheets in solution, the lone pair electrons of oxygen in the GO may also induce the breakage of intermolecular hydrogen bonds in the β-pleated sheets of zein. This results in hydrogen bound to electronegative N atoms in the amine group of zein experiencing an attraction to the lone pair electrons in carbonyl groups of graphene oxide generating a dipole-dipole interaction among the amine groups of zein and carbonyl groups of graphene oxide, resulting in hydrogen bonding, as shown in equation 1. Zein molecules also have an abundance of hydrophilic amine groups in their glutamine turns, and since GO is hydrophilic, when it is mixed with zein, the -OH groups of GO interact with the amine groups of zein through forming hydrogen bonds as seen from equation 2. Similar bonding mechanism has been proposed previously [37, 38, 50].

Based on data from the literature and our own findings, we propose that, covalent bonding between GO and zein molecules are possible through amidation reaction between the amine groups, in the glutamine turns of zein, with carboxylic acid (-COOH) groups at the edges of GO [51]. Previous studies reported reactions of proteins in acidic solutions with imine or amide bond formation [33]. When GO is added first to the zein solution in 70% ethanol at 65 °C and left for the reaction between zein and GO to proceed for one hour. This facilitates the -COOH groups located at the edges of GO sheets to interact with the -NH_2 groups of glutamine ends in zein, in

amidation reaction. The oleic acid is then added to the zein/GO solution in 70% ethanol and serves as a plasticizer and binds to zein through the amine groups in glutamine turns, which results in C-N bond formation [33]. Once covalent bonds are formed between zein and GO, it is anticipated that they remain stable when the oleic acid is added even though there is a large amount of oleic acid added compared to the amount of GO.

It is possible that additional covalent bonds will form with the COOH groups of oleic acid, but this is not at the expense of the covalent bonds formed with zein. It is well known from prior mechanistic work that oleic acid will also form hydrophobic bonds through its aliphatic groups and the aliphatic side chains of hydrophobic amino acids in zein [52]. When zein is dissolved in 70% ethanol, a hydrophilic solvent, the hydrophobic side chains in the α-helix conformation will be buried inside the helices and become unavailable to interact with oleic acid. In the β-turns, leucine offers a potential site for hydrophobic interaction with aliphatic end of oleic acid molecules. The hydrophobic amino acids in β-sheets can also use the hydrophobic side chains to interact with hydrophobic tail of oleic acid. From the DSC images, we can see that control plasticized zein film did not show any strong peaks indicating hydrogen or covalent bonds, whereas for the zein-GO nanocomposites strong peaks indicating covalent and hydrogen bonds were clearly visible at 2 and 3% GO loading.

Since both GO and oleic acid covalently bind to zein through C-N bonds, as shown in **Fig. 5.6**, new C-N bonds are formed between zein and GO. The number of C-N bonds appear to remain the same in the matrix, and no new FTIR peak attributed to increased C-N bonds can be seen as a result of this amidation reaction. The disappearance of the 1450cm^{-1} in FT-Raman also supports this hypothesis, as the peak is an indication of $–CH_2$ stretching vibrations and partial in plane –OH vibrations from the –COOH group of oleic acid and its disappearance indicates reduced interaction between oleic acid and zein molecules.

The replacement of oleic acid by GO results in crosslinking or tighter linkage formation between zein layers, which can be seen through stronger mechanical properties. More free oleic acid molecules in the zein-GO matrix can travel to the material's surface and effect the surface hydrophobicity, which we will see in water contact angle measurement section.

Ring-opening amination of epoxy on the surface of GO [51] is another possibility for covalent bonding route for Z and GO, however the temperature for ring opening reactions is much higher (90 ^{o}C) than that used in our study (65 ^{o}C), thus we assume the route to be unlikely.

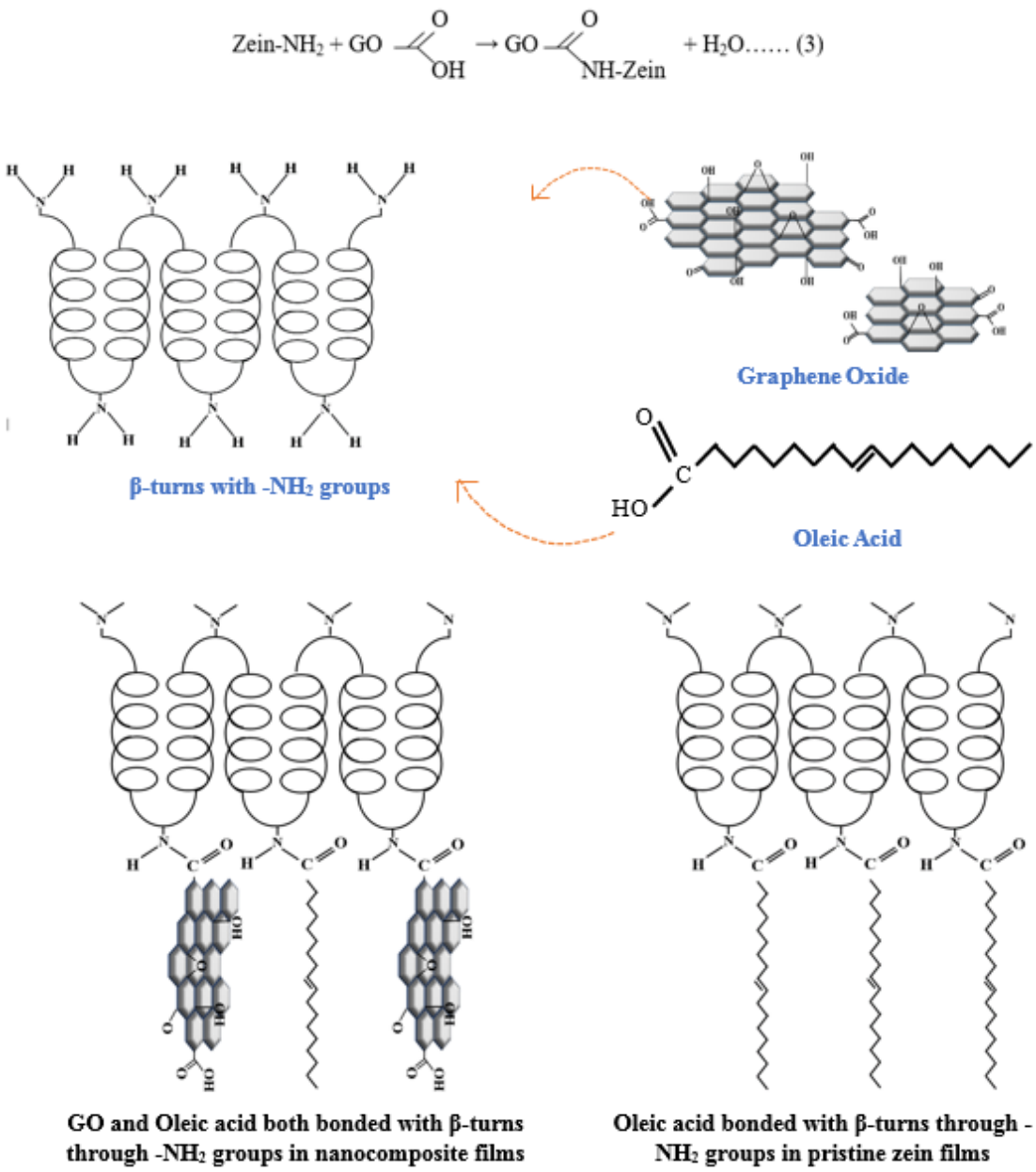

Fig. 5.6. Model showing possible covalent bonding between zein and GO sheets, through interaction between –NH_2 groups of β-turn and –COOH groups of GO

5.4.4 Transmission Electron Microscopy (TEM)

TEM experiments were used to visualize individual GO sheets alone and within the zein matrix in Z-GO nanocomposite films. TEM images shown in **Fig. 5.7** (a, b), show a wrinkled morphology of GO. The presence of numerous wrinkles is similar to what has been observed in the literature [53]. The GO sheets appear translucent enabling the observation of stacked layers. Light colored wrinkles are an indication of single or few layers of GO, which is consistent with

other studies [54]. The exfoliation of GO layers help achieve extensive biopolymer/filler interfaces resulting in multiple interactions between Z and GO. Similar results were reported by Ghobadi et al. 2015 [53], who suggested that transparent GO sheets in the TEM images were indicative of few layers of graphene oxide and good exfoliation.

Figures **Fig. 5.7** (c, d), (e, f) and (g, h), show TEM images of Z-0.5%GO, Z-1%GO and Z-3%GO respectively. The dark spots seen in the images come from phase-separated oleic acid [8]. In these images the wrinkled morphology is no longer seen directly. The GO sheets distributed throughout zein matrix are either fully exfoliated, intercalated or dispersed within tactoid structures. The figures suggest there is uneven distribution of the GO nanosheets within the zein matrix creating a non-uniform particle density.

The samples appear heterogeneous with sub-micrometer regions void of particles, and areas of high particle density, as indicated by darker regions. The figures show stacked layers of GO closely located to each other. This arrangement is referred to as "tactoids". Significant concentration of tactoids are visible in the micrographs (**Fig. 5.7** (c, d)). These structures are formed by restacking of the nanosheets during the nanocomposite fabrication process. In **Fig. 5.7** (e, f), the GO sheets roll up and form aggregates that looks similar to aggregated GO liquid crystal lamella [55]. The light-colored streaks seen in the image are GO sheets stacked together with a thickness of 14-17 nm. Considering a single layer graphene oxide has a thickness of 0.78 nm and interplanar GO spacing d_{GO} = 0.65−0.75 nm [56], there would be approximately 9-11 layers of GO sheets that constitute the white streaks. It is evident from the rolled-up morphology at concentrations higher than 1% of GO, the compatibility between zein, and GO declines and aggregates start to form which may become sites for crack propagation as suggested by permeability measurements discussed later. In **Fig. 5.7** (g, h), thicker tactoids are more prevalent than at 1 and 0.5% GO, suggesting that the higher the ratio of GO sheets, the greater the likelihood of restacking.

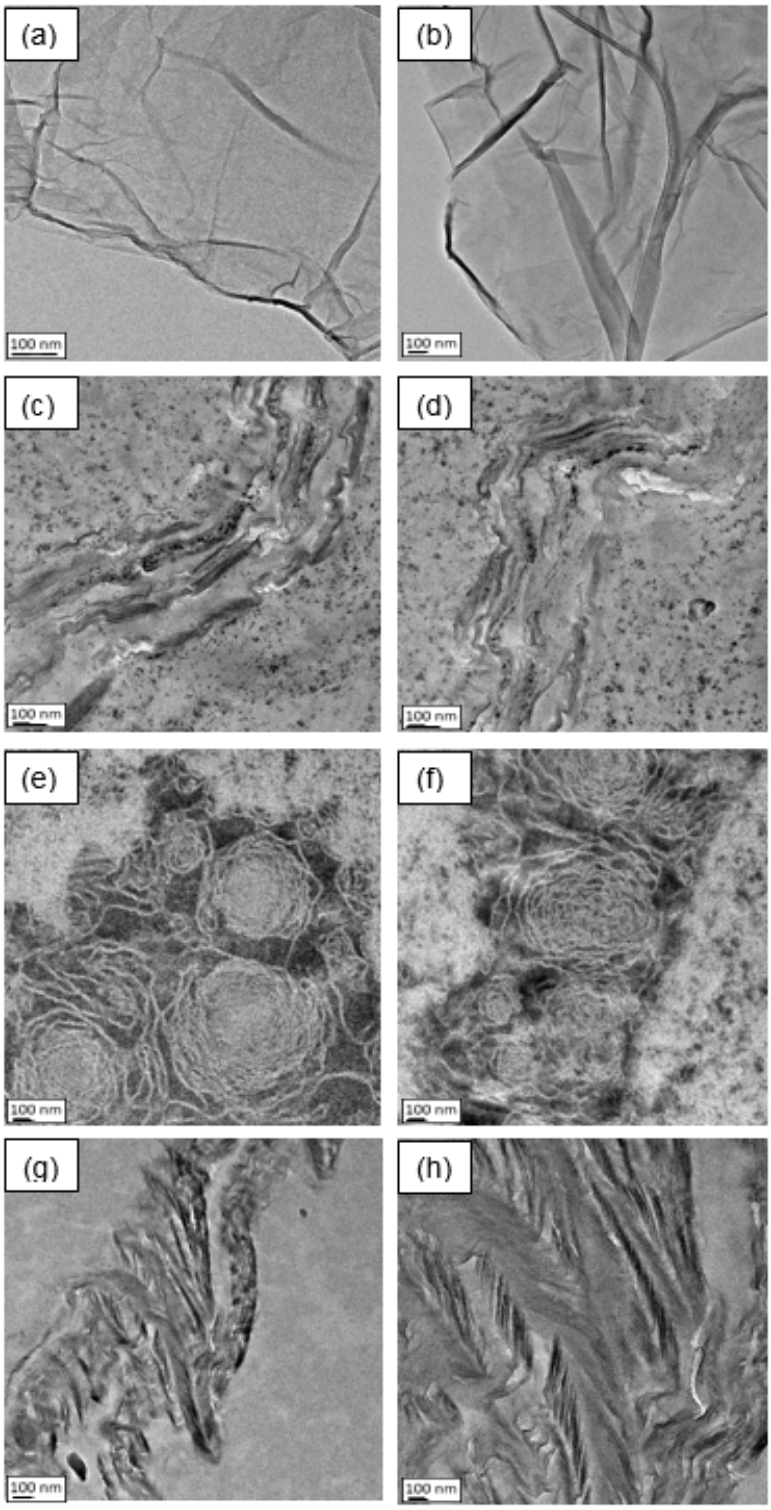

Fig. 5.7. TEM micrograph of (a, b) Wrinkled morphology of GO sheets seen from the top, (c, d) Z-0.5%GO nanocomposite seen from the side, (e, f) Z-1% GO seen from the side, where multi layers of GO sheets are rolled up and (g, h) Z-3% GO nanocomposite seen from the side

5.4.5 Atomic Force Microscopy (AFM)

Fig. 5.8 summarizes the effects of GO sheets on the surface morphology of plasticized zein films. AFM is used here to image the changes in the topography of films and as a complementary method to TEM. Prior studies have reported that uniform dispersion can sometimes lead to smoother surfaces than the original matrix alone [57], whereas, non-uniform dispersion can lead to rough and irregular surfaces [58]. While TEM offers a direct visualization of the dispersion of GO, AFM links the quality of the GO dispersion to the surface roughness of the films. AFM also offers hints related to the efficient fabrication of nanocomposite films.

The topographies of the zein control (0% GO) and surfaces from samples containing 0.5%, 1% and 3% GO are shown in **Fig. 5.8**. 'Roughness Analysis' indicates that the control zein films have the smoothest surface with a root mean square roughness, Rq = 0.963±0.13 nm and average roughness of Ra = 0.755±0.435 nm. Analysis of Z-0.5% GO gives a surface roughness of Rq = 1.68±0.1 nm and Ra = 1.32±1.07 nm showing a slight increase in surface roughness. The roughness significantly increases to Rq=2.45nm±0.75 and Ra=2.00±0.762 nm, at 1% GO concentration. At Z-3%GO the roughness is Rq = 3.09 ±1.3 nm and Ra = 2.53±1.32 nm. These results indicate that, at concentrations of 0.5%, GO disperses well within the zein matrix, but above 0.5% GO, aggregates start to form, and rougher surface is created. The dispersion of GO in zein influences the arrangement of the polymer chains near to the surfaces. With increasing GO concentration (Z-3%GO), the amount of zein in the matrix decreases and a change in the surface roughness is observed. This change in surface roughness can potentially be influenced by the degree of exfoliation and intercalation of the GO within the zein matrix.

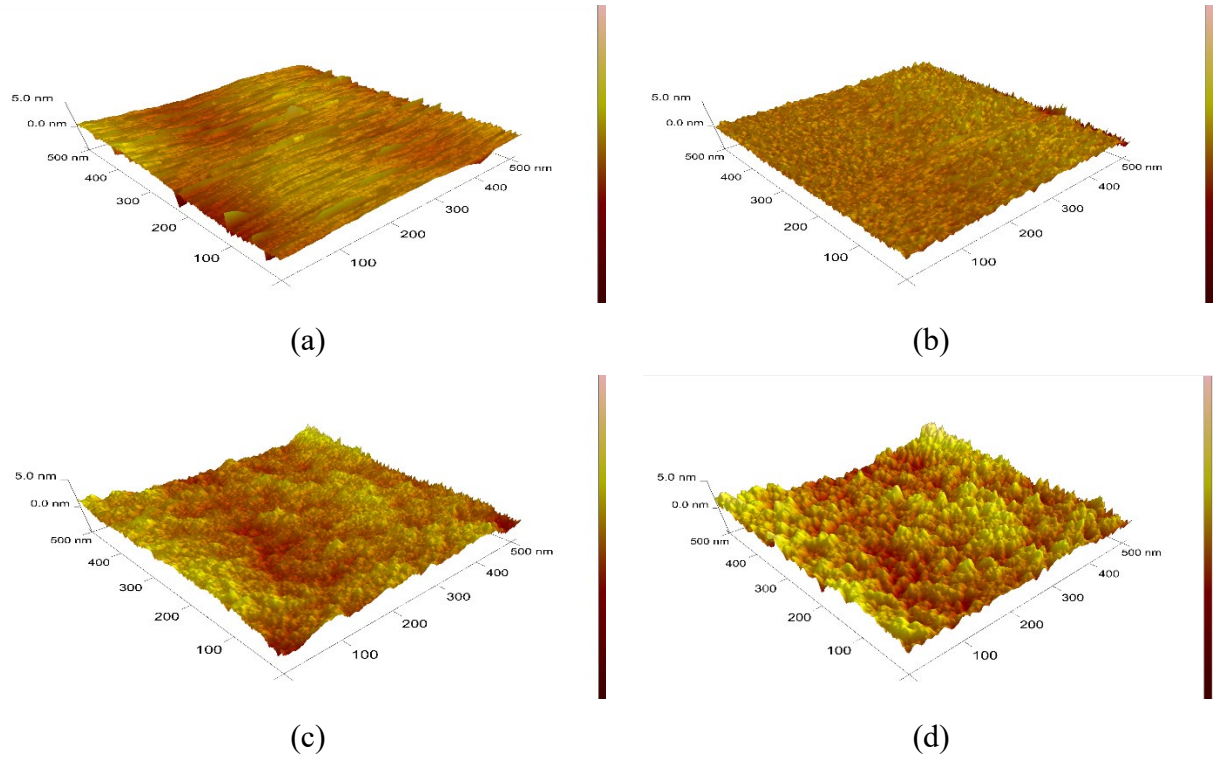

Fig. 5.8. Three-dimensional AFM images of zein films on a 500 nm×500 nm scale, (a) Z-0% GO. (b)Z-0.5% GO. (c) Z-1% GO and (d) Z-3% GO

5.4.6 Water Contact Angle (WCA)

The surface properties of biodegradable films are important, especially the ability to repel water in biodegradable packaging applications and applications where the film is in contact to other surfaces. We first present WCA measurements on zein-GO surfaces and then determine how the changes in WCA are correlated to the water vapor permeability properties (section 5.4.7). Contact angles for the Z-GO films were generated using a tensiometer. **Fig. 5.9** summarizes the average WCA values for films with different GO concentrations.

All films had water contact angles lower than 90º, suggesting hydrophilic properties. The contact angle of zein control was 50º, which is consistent with findings from the literature [59]. With addition of GO to zein, the WCA started to increase; with the highest WCA recorded at 64.77±1.76 º for Z-0.7%GO. Other studies have reported that GO displays mostly hydrophilic properties with WCA ≈ 30–60°, which thus can be successfully dispersed in solution [60]. Surprisingly, GO addition to zein, slightly increased the hydrophobicity, by increasing the WCA. Addition of GO, impacts the surface morphology of the films by making the GO added films

progressively rougher. Increasing surface roughness at the nanoscale, increases the surface area, which is one of the important mechanisms for increasing hydrophobicity [61].

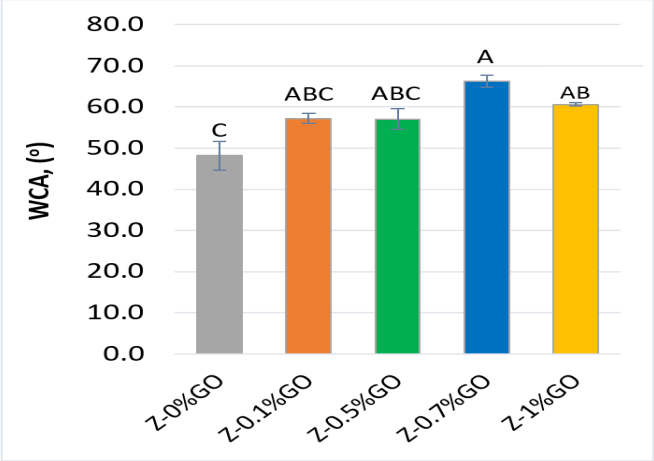

Fig. 5.9. WCA Analysis of Z-GO nanocomposites. Different letters (A, B) above error bars signifies a statistically significant difference ($p < 0.05$)

Orientation of the aliphatic groups of oleic acid towards the surface can be another possible factor that affect the change in WCA. In pristine zein, oleic acid using its –COOH group binds to zein through NH_2 sites. In the Z-GO nanocomposites, GO has the first shot at forming covalent bonds with NH_2 sites because the oleic acid is only added later. When the oleic acid (OA) is added, since GO used up a considerable number of the NH_2 sites, this prevents the oleic acid from binding with zein molecule and therefore OA remains free within the zein solution. Since the films are cast on hydrophobic PDMS coated petri dishes, the free OA molecules in the zein matrix travels to the PDMS side and orient its aliphatic tail towards the hydrophobic PDMS. After the films are dried and peeled from the PDMS, the WCA is measured from the side of the films that were previously in contact with the PDMS. This explains why the Z-GO nanocomposites become more and more hydrophobic as GO is added to zein, even though GO is a hydrophilic compound. As more GO is added to zein, more NH_2 sites are occupied by forming bonds with GO, and more OA molecules become free to travel within the zein matrix and orient its hydrophobic tail towards the surface. Similar results were reported for Montmorillonite, a hydrophilic nanoclay, which increased the water contact angle of methyl cellulose [62] and regenerated cellulose [63]. As the degree of surface hydrophobicity increased, the water vapor permeability (WVP) of nanocomposite films decreased (as will be seen in section 5.4.7). Our data indicates a relationship between contact angle changes and water vapor barrier similar to results reported in the literature [64, 65]. As polar H_2O

molecules cannot be readily adsorbed to non-polar film surfaces or hydrophobic surfaces, a reduction of water vapor permeability is expected.

5.4.7 Water Vapor Permeability (WVP)

Average WVP data of zein-GO nanocomposite films are summarized in **Fig. 5.10**. The data show that the WVP begins to decrease with the addition of small amounts of GO to zein at levels of 0.1% GO. The WVP continues to decrease up to 1% GO and begins to increase at 1%GO.

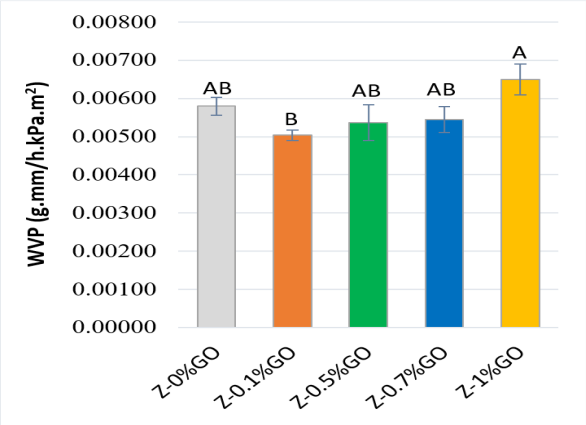

Fig. 5.10. WVP of Z-GO nanocomposites. Different letters (A, B) above error bars signifies a statistically significant difference ($p < 0.05$)

It appears that GO content has a non-linear relationship with barrier properties. The improvement of water vapor barrier properties of Z-GO nanocomposite films may be due to the presence of impermeable GO sheets that are distributed in the zein polymer matrix in a manner that increases tortuosity and the effective diffusion path length. The degree of enhancement however depends on the type of nanoparticle dispersion (intercalated, exfoliated or some intermediate), as well as the orientation of the GO sheets in the polymer. The GO sheet orientation can result in the highest tortuosity when they arrange themselves perpendicular to the direction of diffusion. Any kind of deviation from such an orientation appears to result in an increase in WVP. As we concluded from the TEM analysis (section 5.4.4), above 0.5% the GO starts to aggregate, forming tactoids and other structures. For Z-1%GO nanocomposite films, we can see GO aggregates forming a rolled-up structure, which deviates from the perpendicular orientation GO sheets, favorable for increasing water vapor barrier properties. WVP results are consistent with the WCA data (section 5.4.6), as lower contact angles at 1%GO coincide with lower water vapor barrier properties, suggesting a more hydrophilic behavior leads to increasing WVP.

5.4.8 Thermogravimetric Analysis (TGA)

The effect of GO on the thermal stability of zein-GO nanocomposite films was investigated by thermogravimetric analysis. The TGA curves as shown in **Fig. 5.11** (a), display two stages of thermal decomposition under nitrogen atmosphere. The first stage which ranges from 70 to 200 °C and is associated with the loss of low molecular mass compounds, i.e., plasticizers and solvent. The second stage is between 250 to 600 °C and corresponds to the breakdown of the amino acid residues and cleavage of the peptide bonds in the protein [9]. The two stages of molecular mass loss can be understood from the derivative thermogravimetric analysis (DTG) curves as shown in **Fig. 5.11** (b). Broad weight loss peaks are observed for Z-0%GO to Z-0.7%GO at temperatures around 200-260 ºC. For higher concentrations of GO, sharp weight loss peaks appear at temperatures 280-320 ºC. The temperature at which the polymer begins to degrade is the most important parameter to assess the thermal stability of the polymer [9]. Our data show that, the temperature at which 50% weight loss (T_{50}) occurred, increased with the GO content. The T_{50} for the control zein film was 273±1 ºC and the 90% decomposition temperature (T_{90}) was 398±19 ºC. The equivalent temperatures for Zein-3%GO, were 296±2 ºC (T_{50}), and 482±1 º C (T_{90}). These results indicate that 2wt% addition of GO, increased T_{50} by 23ºC. This shift in temperature in nanocomposites was also in agreement with gelatin/GO nanocomposite, wheat PLA/GO nanocomposites and cellulose/GO nanocomposites [13]. According to published work, the enhancement of thermal stability in polymer nanocomposites is caused by the expansion of combustion gas diffusion pathways generated from the dispersed GO layers which act as insulators as was discussed previously [9]. The thermal property improvements are an indication for strong interaction within the Z-GO nanocomposites. Compared to other studies in the literature [66–68] Z-GO nanocomposites show the highest 50% decomposition temperature at a very low loading.

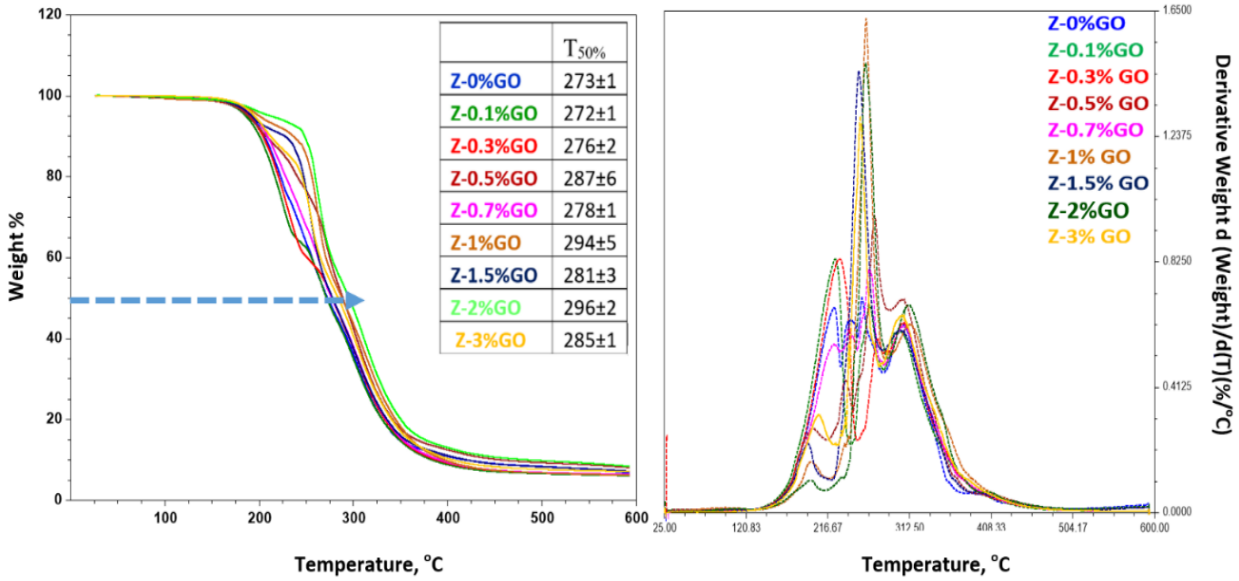

Fig. 5.11. (a) Comparison of TGA Curves for zein control, Z-0.1%, 0.3%, 0.5%, 0.7%, 1%, 1.5%, 2% and Z-3% GO nanocomposites (b) DTG curves for zein-GO nanocomposites showing decomposition rate

5.4.9 Mechanical Properties

Mechanical properties of nanocomposites are important in various biomaterial applications. For example, nanocomposites are subjected to considerable stresses, when used in microfluidic applications, for scaffolding materials or in food packaging. The mechanical properties of zein-GO nanocomposites including tensile strength (TS), Young's modulus (YM) and % elongation at break (EAB) are summarized in **Table 5.1**. The stress-strain curves from the tensile tests performed on the zein-GO nanocomposites have been shown in appendix B. The data show that with increasing GO concentration, the tensile strength and the Young's modulus increased, while the elongation at break decreased. The Z-GO films had larger Young's moduli and tensile strength than the zein control films. The Z-3%GO nanocomposite film showed the highest Young's modulus at 145 MPa, which is a 300% increase compared to the zein control (35MPa). The tensile strength increased 82% at Z-3%GO nanocomposite film, compared to the zein control film. %EAB decreased with increasing GO concentration in the films. The control zein films had the highest elongation with 65%, while the Z-3%GO nanocomposite films had the lowest elongation with 5.8%. From **Table 5.1**, we can see there is clear indication of an increasing trend of YM and TS with increasing %GO, however, the trend does not follow a specific order. This can be explained

using the TEM images, which shows that at higher concentration the GO forms aggregates and rolls up into bundles of different sizes indicating a non-uniform distribution of the GO filler. The mechanical property trends can be further explained using the proposed covalent bonding mechanism. When more GO is introduced in the film, the number of interactions between GO and zein will increase. At the same time, the presence of GO hinders the interactions between zein molecules and the oleic acid molecules. This may result in restricted polymer mobility and formation of tighter junctions. Therefore, the flexibility of the films decreased with increasing concentrations of GO in this study. Compared to other studies in the literature, Z-GO nanocomposites presented here show the highest Young's moduli at a very low loadings [8, 9, 69] (Table S2).

Table 5.1. Comparison of Young's Modulus, Tensile strength and % elongation at break for Z-0%, 0.1%, 0.3%, 0.5%, 0.7%, 1%, 2% and 3% GO nanocomposite films.

	YM (MPa)	**% ↑**	**TS (MPa)**	**% ↑**	**%EAB**	**% ↓**
Z-0%GO	35.0±1.8 ^{e}	—	1.7±0.1 ^{c}	—	64.8±8.6 ^{a}	—
Z-0.1%GO	48.0±11.4 ^{de}	37	1.8±0.1 ^{bc}	6	49.3±8.2 ^{ab}	24
Z-0.3%GO	77.8±16.1 ^{bcde}	123	2.7±0.4 ^{ab}	59	44.3±21.8 ^{ab}	32
Z-0.5%GO	103.0±4.8 ^{abc}	194	2.6±0.3 ^{ab}	53	23.1±13.8 ^{b}	64
Z-0.7%GO	94.8±1.2 ^{bcd}	171	2.7±0.1 ^{a}	59	17.2±6.0 ^{b}	73
Z-1%GO	79.0±4.4 ^{bcde}	126	2.3±0.0 ^{abc}	35	35.0±12.4 ^{ab}	46
Z-2%GO	123.7±21.2 ^{ab}	251	2.3±0.1 ^{abc}	35	14.4±11.9 ^{b}	78
Z-3%GO	145.9±2.8 ^{a}	317	3.1±0.1 ^{a}	82	6.4±0.6 ^{b}	90

* Different letters indicate statistically significant difference at $p < 0.05$.

5.5 Conclusion

A novel nanocomposite formation mechanism is proposed for plasticized Z-GO nanocomposite films. FTIR, FT-Raman and DSC findings indicates strong interaction including hydrogen and covalent bond formation. The -NH_2 groups in glutamine turns of zein participates in covalent bonding with -COOH sites of GO, resulting in replacement of some of the OA molecules bound to zein. This results in free OA in the matrix and tighter junction forming between zein

molecules, which is later reflected through 300% increase in Young's modulus and 80% increase in tensile strength and 90% decrease in %elongation at break, as well as through the 10^{o} increase in hydrophobicity of zein nanocomposites influenced by the freely roaming hydrophobic OA molecules. TEM, AFM images show that GO has been dispersed uniformly throughout the zein matrix. Our study demonstrates how the physical, mechanical and surface properties of zein films can be modified with nanocomposite formation with GO. Such advancements in the properties of zein films are significantly fundamental since the industrial uses of zein are extremely constrained because of the shortcomings of unmodified zein products. Outcome of this research will increase understanding of zein and benefit the application of zein-GO nanocomposite for packaging materials, sensor platforms and microfluidic device platforms that can compete with the performance standards offered by synthetic polymers.

Acknowledgements

The authors would like to thank Dr. Christopher Gilpin and Laurie Mueller for their assistance with TEM experiments. We would like to acknowledge USDA Hatch funds and the Scholle Endowment for financial support of this work.

Conflicts of interest

The authors declare no conflict of interest.

5.6 References

1. Sigler M (2014) The Effects of Plastic Pollution on Aquatic Wildlife: Current Situations and Future Solutions. Water Air Soil Pollut 225:2184. https://doi.org/10.1007/s11270-014-2184-6

2. Lebreton L, Slat B, Ferrari F, et al (2018) Evidence that the Great Pacific Garbage Patch is rapidly accumulating plastic. Scientific Reports 8:4666. https://doi.org/10.1038/s41598-018-22939-w

3. Rouf TB, Kokini JL (2018) Natural Biopolymer-Based Nanocomposite Films for Packaging Applications. In: Bionanocomposites for Packaging Applications. Springer, Cham, pp 149–177

4. Cuq B, Gontard N, Guilbert S (1998) Proteins as Agricultural Polymers for Packaging Production. Cereal Chemistry Journal 75:1–9. https://doi.org/10.1094/CCHEM.1998.75.1.1

5. Hernandez-Izquierdo VM, Krochta JM (2008) Thermoplastic processing of proteins for film formation—a review. Journal of food science 73:

6. Rhim J-W, Ng PKW (2007) Natural Biopolymer-Based Nanocomposite Films for Packaging Applications. Critical Reviews in Food Science and Nutrition 47:411–433. https://doi.org/10.1080/10408390600846366

7. Yang K, Wang X, Wang Y, others (2007) Progress in nanocomposite of biodegradable polymer. JOURNAL OF INDUSTRIAL AND ENGINEERING CHEMISTRY-SEOUL-13:485

8. Rouf TB, Schmidt G, Kokini JL (2018) Zein–Laponite nanocomposites with improved mechanical, thermal and barrier properties. J Mater Sci 1–16. https://doi.org/10.1007/s10853-018-2061-6

9. Luecha J, Sozer N, Kokini JL (2010) Synthesis and properties of corn zein/montmorillonite nanocomposite films. J Mater Sci 45:3529–3537. https://doi.org/10.1007/s10853-010-4395-6

10. Pan Y, Tikekar RV, Wang MS, et al (2015) Effect of barrier properties of zein colloidal particles and oil-in-water emulsions on oxidative stability of encapsulated bioactive compounds. Food Hydrocolloids 43:82–90. https://doi.org/10.1016/j.foodhyd.2014.05.002

11. Gezer PG, Liu GL, Kokini JL (2016) Development of a biodegradable sensor platform from gold coated zein nanophotonic films to detect peanut allergen, Ara h1, using surface enhanced raman spectroscopy. Talanta 150:224–232. https://doi.org/10.1016/j.talanta.2015.12.034

12. Turasan H, Kokini JL (2017) Advances in Understanding the Molecular Structures and Functionalities of Biodegradable Zein-Based Materials Using Spectroscopic Techniques: A Review. Biomacromolecules 18:331–354. https://doi.org/10.1021/acs.biomac.6b01455

13. Rouf TB, Kokini JL (2016) Biodegradable biopolymer–graphene nanocomposites. Journal of Materials Science 51:9915–9945

14. Maftoonazad N, Ramaswamy H (2018) Novel techniques in food processing: bionanocomposites. Current Opinion in Food Science 23:49–56. https://doi.org/10.1016/j.cofs.2018.05.010

15. Hou W, Gao Y, Wang J, et al (2018) Nanodiamond decorated graphene oxide and the reinforcement to epoxy. Composites Science and Technology 165:9–17. https://doi.org/10.1016/j.compscitech.2018.06.008

16. Pramanik C, Nepal D, Nathanson M, et al (2018) Molecular engineering of interphases in polymer/carbon nanotube composites to reach the limits of mechanical performance. Composites Science and Technology 166:86–94. https://doi.org/10.1016/j.compscitech.2018.04.013

17. Xing W, Li H, Huang G, et al (2017) Graphene oxide induced crosslinking and reinforcement of elastomers. Composites Science and Technology 144:223–229. https://doi.org/10.1016/j.compscitech.2017.03.006

18. Yang J-H, Lin S-H, Lee Y-D (2012) Preparation and characterization of poly (l-lactide)–graphene composites using the in situ ring-opening polymerization of PLLA with graphene as the initiator. Journal of Materials Chemistry 22:10805–10815

19. Wang H, Qiu Z (2012) Crystallization kinetics and morphology of biodegradable poly (l-lactic acid)/graphene oxide nanocomposites: Influences of graphene oxide loading and crystallization temperature. Thermochimica Acta 527:40–46

20. Norazlina H, Kamal Y (2015) Graphene modifications in polylactic acid nanocomposites: a review. Polymer Bulletin 72:931–961

21. Zhao X-R, Xu X, Teng J, et al (2019) Three-dimensional porous graphene oxide-maize amylopectin composites with controllable pore-sizes and good adsorption-desorption properties: Facile fabrication and reutilization, and the adsorption mechanism. Ecotoxicology and Environmental Safety 176:11–19. https://doi.org/10.1016/j.ecoenv.2019.03.069

22. Wang R, Shou D, Lv O, et al (2017) pH-Controlled drug delivery with hybrid aerogel of chitosan, carboxymethyl cellulose and graphene oxide as the carrier. International Journal of Biological Macromolecules 103:248–253. https://doi.org/10.1016/j.ijbiomac.2017.05.064

23. Xu X, Zou J, Zhao X-R, et al (2019) Facile assembly of three-dimensional cylindrical egg white embedded graphene oxide composite with good reusability for aqueous adsorption of rare earth elements. Colloids and Surfaces A: Physicochemical and Engineering Aspects 570:127–140. https://doi.org/10.1016/j.colsurfa.2019.03.022

24. Terzopoulou Z, Kyzas GZ, Bikiaris DN (2015) Recent advances in nanocomposite materials of graphene derivatives with polysaccharides. Materials 8:652–683

25. He L, Wang Q, Mandler D, et al (2016) Detection of folic acid protein in human serum using reduced graphene oxide electrodes modified by folic-acid. Biosensors and Bioelectronics 75:389–395

26. Hussain F, Hojjati M, Okamoto M, Gorga RE (2006) Polymer-matrix nanocomposites, processing, manufacturing, and application: an overview. Journal of composite materials 40:1511–1575

27. Xu X, Jiang X-Y, Jiao F-P, et al (2018) Tunable assembly of porous three-dimensional graphene oxide-corn zein composites with strong mechanical properties for adsorption of rare earth elements. Journal of the Taiwan Institute of Chemical Engineers 85:106–114. https://doi.org/10.1016/j.jtice.2017.12.024

28. Panzavolta S, Bracci B, Gualandi C, et al (2014) Structural reinforcement and failure analysis in composite nanofibers of graphene oxide and gelatin. Carbon 78:566–577

29. Wan C, Frydrych M, Chen B (2011) Strong and bioactive gelatin–graphene oxide nanocomposites. Soft Matter 7:6159–6166. https://doi.org/10.1039/C1SM05321C

30. Marcano DC, Kosynkin DV, Berlin JM, et al (2010) Improved synthesis of graphene oxide. ACS nano 4:4806–4814

31. Krimm S, Bandekar J (1986) Vibrational Spectroscopy and Conformation of Peptides, Polypeptides, and Proteins. Advances in Protein Chemistry 38:181–364. https://doi.org/10.1016/S0065-3233(08)60528-8

32. Mizutani Y, Matsumura Y, Imamura K, et al (2003) Effects of Water Activity and Lipid Addition on Secondary Structure of Zein in Powder Systems. J Agric Food Chem 51:229–235. https://doi.org/10.1021/jf0205007

33. Turasan H, Barber EA, Malm M, Kokini JL (2018) Mechanical and spectroscopic characterization of crosslinked zein films cast from solutions of acetic acid leading to a new mechanism for the crosslinking of oleic acid plasticized zein films. Food Research International 108:357–367. https://doi.org/10.1016/j.foodres.2018.03.063

34. ASTM E (96) Standard test methods for water vapor transmission of materials. Foundation drainage rate: Hydraulic Gradient 1:18

35. Kumar N, Das S, Bernhard C, Varma GD (2013) Effect of graphene oxide doping on superconducting properties of bulk MgB2. Superconductor Science and Technology 26:095008

36. Lin-Vien D, Colthup NB, Fateley WG, Grasselli JG (1991) Alcohols and Phenols. In: The Handbook of Infrared and Raman Characteristic Frequencies of Organic Molecules. Elsevier, pp 45–60

37. Akhtar FH, Kumar M, Peinemann K-V (2017) Pebax®1657/Graphene oxide composite membranes for improved water vapor separation. Journal of Membrane Science 525:187–194. https://doi.org/10.1016/j.memsci.2016.10.045

38. Ammar A, Al-Enizi AM, AlMaadeed MA, Karim A (2016) Influence of graphene oxide on mechanical, morphological, barrier, and electrical properties of polymer membranes. Arabian Journal of Chemistry 9:274–286. https://doi.org/10.1016/j.arabjc.2015.07.006

39. Duan J, Gong S, Gao Y, et al (2016) Bioinspired Ternary Artificial Nacre Nanocomposites Based on Reduced Graphene Oxide and Nanofibrillar Cellulose. ACS Appl Mater Interfaces 8:10545–10550. https://doi.org/10.1021/acsami.6b02156

40. Kabiri R, Namazi H (2014) Nanocrystalline cellulose acetate (NCCA)/graphene oxide (GO) nanocomposites with enhanced mechanical properties and barrier against water vapor. Cellulose 21:3527–3539. https://doi.org/10.1007/s10570-014-0366-4

41. Somanathan T, Prasad K, Ostrikov KK, et al (2015) Graphene oxide synthesis from agro waste. Nanomaterials 5:826–834

42. Zhuo Q, Tang J, Sun J, et al (2018) High Efficient Reduction of Graphene Oxide via Nascent Hydrogen at Room Temperature. Materials 11:340. https://doi.org/10.3390/ma11030340

43. Kudin KN, Ozbas B, Schniepp HC, et al (2008) Raman Spectra of Graphite Oxide and Functionalized Graphene Sheets. Nano Lett 8:36–41. https://doi.org/10.1021/nl071822y

44. Lambert JB, Shurvell HF, Lightner DA, Cooks RG (1998) Organic Structural Spectroscopy Prentice-Hall. Inc New Jersey

45. Larkin P (2017) Infrared and Raman spectroscopy: principles and spectral interpretation. Elsevier

46. Reitzenstein S, Rösch P, Strehle MA, et al (2007) Nondestructive analysis of single rapeseeds by means of Raman spectroscopy. Journal of Raman Spectroscopy 38:301–308. https://doi.org/10.1002/jrs.1643

47. Ji Z, Zhu G, Shen X, et al (2012) Reduced graphene oxide supported FePt alloy nanoparticles with high electrocatalytic performance for methanol oxidation. New J Chem 36:1774–1780. https://doi.org/10.1039/C2NJ40133A

48. Painter PC, Shenoy SL, Bhagwagar DE, et al (1991) Effect of hydrogen bonding on the melting point depression in polymer blends where one component crystallizes. Macromolecules 24:5623–5629. https://doi.org/10.1021/ma00020a022

49. Koch-Schmidt AC, Mosbach K (1977) Studies on conformation of soluble and immobilized enzymes using differential scanning calorimetry. 2. Specific activity and thermal stability of enzymes bound weakly and strongly to Sepharose CL 4B. Biochemistry 16:2105–2109. https://doi.org/10.1021/bi00629a009

50. Matsuo Y, Miyabe T, Fukutsuka T, Sugie Y (2007) Preparation and characterization of alkylamine-intercalated graphite oxides. Carbon 45:1005–1012. https://doi.org/10.1016/j.carbon.2006.12.023

51. Piao Y, Chen B (2016) One-pot synthesis and characterization of reduced graphene oxide–gelatin nanocomposite hydrogels. RSC Adv 6:6171–6181. https://doi.org/10.1039/C5RA20674J

52. Barber EA (2018) Optimization of Zein Based Surface Enhanced Raman Spectroscopy Biosensor for the Detection of Gliadin as a Marker for Celiac Disease. Theses and Dissertations Available from ProQuest 1–173

53. Ghobadi S, Sadighikia S, Papila M, et al (2015) Graphene-reinforced poly (vinyl alcohol) electrospun fibers as building blocks for high performance nanocomposites. RSC Advances 5:85009–85018

54. Li M, Wu Z, Ren W, et al (2012) The doping of reduced graphene oxide with nitrogen and its effect on the quenching of the material's photoluminescence. Carbon 50:5286–5291. https://doi.org/10.1016/j.carbon.2012.07.015

55. Xu Z, Gao C (2011) Graphene chiral liquid crystals and macroscopic assembled fibres. Nature Communications 2:571. https://doi.org/10.1038/ncomms1583

56. Schniepp HC, Li J-L, McAllister MJ, et al (2006) Functionalized Single Graphene Sheets Derived from Splitting Graphite Oxide. J Phys Chem B 110:8535–8539. https://doi.org/10.1021/jp060936f

57. Lewandowska K, Sionkowska A, Kaczmarek B, Furtos G (2014) Mechanical and Morphological Studies of Chitosan/Clay Composites. Molecular Crystals and Liquid Crystals 590:193–198. https://doi.org/10.1080/15421406.2013.874718

58. Wu W, Dong Z, He J, et al (2016) Transparent cellulose/Laponite nanocomposite films. J Mater Sci 51:4125–4133. https://doi.org/10.1007/s10853-016-9735-8

59. Gezer PG, Brodsky S, Hsiao A, et al (2015) Modification of the hydrophilic/hydrophobic characteristic of zein film surfaces by contact with oxygen plasma treated PDMS and oleic acid content. Colloids and Surfaces B: Biointerfaces 135:433–440. https://doi.org/10.1016/j.colsurfb.2015.07.006

60. Wei N, Lv C, Xu Z (2014) Wetting of graphene oxide: A molecular dynamics study. Langmuir 30:3572–3578

61. Bhushan B, Chae Jung Y (2007) Wetting study of patterned surfaces for superhydrophobicity. Ultramicroscopy 107:1033–1041. https://doi.org/10.1016/j.ultramic.2007.05.002

62. Tunç S, Duman O, Polat TG (2016) Effects of montmorillonite on properties of methyl cellulose/carvacrol based active antimicrobial nanocomposites. Carbohydrate Polymers 150:259–268. https://doi.org/10.1016/j.carbpol.2016.05.019

63. Mahmoudian S, Wahit MU, Ismail AF, Yussuf AA (2012) Preparation of regenerated cellulose/montmorillonite nanocomposite films via ionic liquids. Carbohydrate Polymers 88:1251–1257. https://doi.org/10.1016/j.carbpol.2012.01.088

64. Martin-Polo M, Mauguin C, Voilley A (1992) Hydrophobic films and their efficiency against moisture transfer. 1. Influence of the film preparation technique. Journal of agricultural and food chemistry 40:407–412

65. Martin-Polo M, Voilley A, Blond G, et al (1992) Hydrophobic films and their efficiency against moisture transfer. 2. Influence of the physical state. Journal of agricultural and food chemistry 40:413–418

66. Hassouna F, Laachachi A, Chapron D, et al (2011) Development of new approach based on Raman spectroscopy to study the dispersion of expanded graphite in poly (lactide). Polymer Degradation and Stability 96:2040–2047

67. Zhang H, Zhai D, He Y (2014) Graphene oxide/polyacrylamide/carboxymethyl cellulose sodium nanocomposite hydrogel with enhanced mechanical strength: preparation, characterization and the swelling behavior. RSC Advances 4:44600–44609

68. Jeon GW, An J-E, Jeong YG (2012) High performance cellulose acetate propionate composites reinforced with exfoliated graphene. Composites Part B: Engineering 43:3412–3418

69. Manisara P, Parichat M (2012) Cellulose Microfibril from Banana Peels as a Nanoreinforcing Fillers for Zein Films. Open Journal of Polymer Chemistry 2012:. https://doi.org/10.4236/ojpchem.2012.22007

CHAPTER 6. APPLICATION OF ZEIN AS AN ANCHORING MOLECULE IN A CARBON NANOTUBE ENHANCED ELECTROCHEMICAL SENSORS FOR DETECTION OF GLIADIN

Tahrima Binte Rouf [1], Lia Stanciu [2], Susana Diaz[2], Jozef Kokini [1]

1. Department of Food Science, Purdue University, West Lafayette, IN-47907, USA
2. Department of Material Engineering, Purdue University, West Lafayette, IN-47907, USA

In preparation for review with Talanta

6.1 Abstract

This research focused on the fabrication of an electrochemical sensor capable of detecting the protein 'gliadin', which is responsible for the allergic reaction with people having celiac disease. The fabrication process involves the replacement of toxic synthetic chemicals that are used for anchoring of the capture antibody in the working electrode, by the natural polymer zein coupled with several nanoparticles including, carbon nanotubes, graphene oxide and Laponite®. Novel biodegradable coatings made from zein nanocomposites: zein-graphene oxide (Z-GO), zein-Laponite® (Z-LAP) and zein-multiwalled carbon nanotubes (Z-CNT) using drop casting nanocomposite technique were tested for fabricating the electrochemical sensors using cyclic voltammetry (CV), square wave voltammetry (SWV) and electrochemical impedance spectroscopy (EIS). Pristine zein coated electrode did not generate any oxidation/reduction peaks in the cyclic voltammograms and showed high degree of impedance in the EIS curves. While addition of the three nanoparticles (MWCNT, LAP, GO) considerably improved the electrical signal, Z-CNT gave highest and strongest signals compared to other nanomaterials. The active tip of the electrochemical sensor was functionalized through a sequence of layer by layer deposition of Z-CNT nanocomposite, and other linker molecules, where Z-CNT acts as a natural linker molecule with large number of functional groups, that offers immobilization of capture antibody and target, and ensures high performance. Both CV curves and SWV curves indicated successful sequential immobilization of gliadin antibody onto the Z-CNT coated electrode. The Z-CNT biosensor was successfully able to give CV signals for gliadin toxins for as low as 0.5 ppm, and

was highly specific for gliadin, when tested against other food toxins like acrylamide, and formamide and remained stable over a 30-day period.

Graphical Abstract

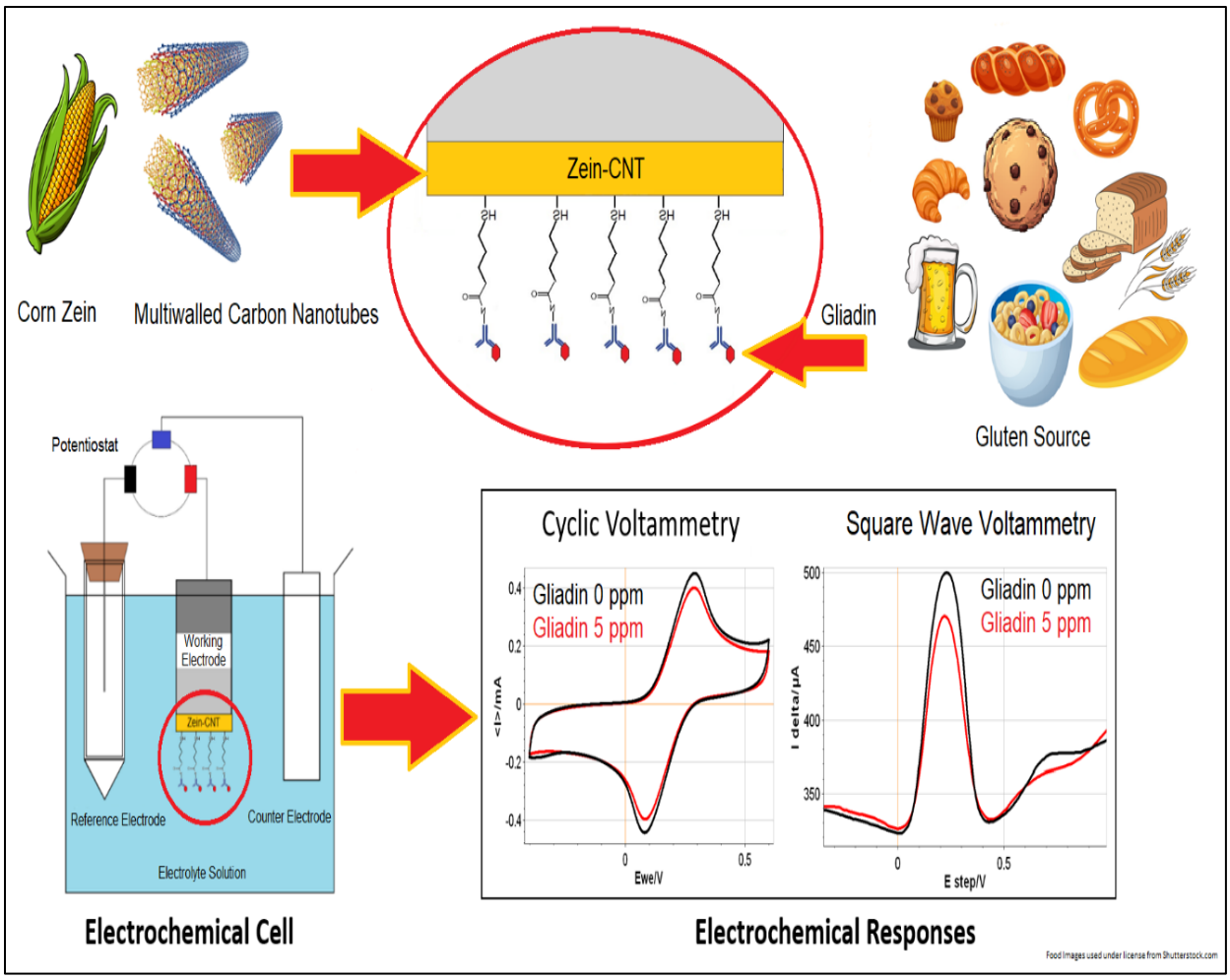

6.2 Introduction

The environmental limitation of many biosensors caused by fabrication using potent toxic chemicals such as 22-(3,5-bis((6-mercaptohexyl)oxy)phenyl)-3,6,9,12,15,18,21-heptaoxadocosanoic acid and 1,2-dithiolane-3-pentanoic acid (thioctic acid) [1] as anchoring platform to capture antibodies has created the motivation to look for natural materials to partly or completely replace these toxic chemicals without losing much sensitivity in detection of analytes. To this end, biosensors have been fabricated from different natural/biodegradable materials like a

natural rubber (ecoflex^{TM}), hard gelatin capsules [2], silk fibroin mats [3], cellulose paper [4] using FET, corn zein [5] using SERS and EIS with gold nanoparticles and silk [6] etc.

Zein is a prolamin of corn, that constitutes 50% protein in corn. It is insoluble in water, but soluble in other solvents like 70% ethanol or acetic acid. One of the earliest and most well-known model by Argos et al. 1982, proposed that zein constitutes of rod-like structures formed by α-helices that are connected by glutamine turns [7]. However, as zein is a biological material that can be extracted using different methods using different varieties of corn, there are wide variations in the tertiary and secondary structure analysis results [7]. Zein has GRAS (generally regarded as safe) status from the FDA and due to its biodegradability and amphiphilic film forming capability, it is a highly demanded polymer for production of biodegradable packaging, scaffolds in tissue engineering, fabrication of drug carrier nanoparticles and formation of eco-friendly biosensor platforms [7,8]. Zein, has been shown to be an excellent reagent delivery platform for biosensors and biokits based on alkaline phosphatase (ALP) activity/inhibition [9]. Zein has also proven to be an excellent biodegradable and low-cost material for capturing, stabilizing, and delivering reagents in various formats and matrices, thus resulting in different optical sensor applications [10]. Poly(ethyleneimine) crosslinked electrospun zein ultrafine fibers containing gold nanoparticles provided a substrate for use in cyclic voltammetry (CV) and square wave voltammetry (SWV) for highly sensitive detection of the plant metabolite catechol which is a carcinogen for animals [11]. Zein microspheres have also been combined with carbon black to anchor hemoglobin and fabricate an electroactive film that uses differential pulse voltammetry to detect hydrogen peroxide [12]. The high performance of the carbon black containing zein based biosensor is attributed to the large surface area of the porous zein microsphere film which effectively anchored hemoglobin [12]. However, this excellent study did not explore the conductive properties of zein films vs. zein microsphere films, in addition, influence of other carbon-based nanoparticle, and stability of the fabricated zein sensor was not reported, which are vital for sensor feasibility study. The COOH and NH_3 functional groups in zein, makes it a viable candidate for immobilizing bio recognition elements in electrochemical biosensors. These applications show the potential that zein offers as a platform for immobilization and delivery of bio-recognition elements.

Electrochemical biosensors offer the advantages of being inexpensive, user-friendly, rapid and most importantly they can be used in situ (with available portable versions) allowing rapid assay turnaround time in labeled or label free formats. This can potentially facilitate accurate and fast measurement of gliadin in wheat containing products (bread, cookies, bagels etc.), at levels

that can cause the allergic response in people suffering from celiac disease [13], leading to a large number of complications, such as growth retardation in children, decreasing bone mineral density in patients with osteoporosis, and miscarriage and infertility in women [1]. Unfortunately, avoidance of the allergen the only method of treatment for this disease. Over 3 million people suffer from celiac disease in the United States (U.S.) [14]. In 2013, the FDA released a definition of "gluten-free" as a food or beverage product that does not contain more than 20 ppm of gluten from cross contamination [15]. Enzyme linked immunosorbent assay (ELISA), is the official method for gluten detection and uses antibodies to capture the desired gluten analyte and detects the gluten concentration by a color change [16]. This method is time consuming and requires highly trained personnel. Gluten is therefore of interest as an analytical target for new biosensors that can detect it rapidly and with high sensitivity and specificity.

Researchers have recently attempted to find alternatives to ELISA method for determining the presence of gliadin in food materials. Nassef et al. 2008 [1] fabricated an immunosensor for gliadin comparing two different anchoring molecules. However, both the anchoring molecules are toxic and the self-assembled monolayer formation for both were time consuming (100 hours and 3 hours). In addition to that, the research does not investigate any stability or specificity tests with other food toxins or proteins. Portable gliadin immunochip was fabricated by Chiriacò et al. 2015 [17], using a microfluidic assembly for delivering solutions to the sensing areas functionalized with anti-gliadin antibodies. By using the electrochemical impedance spectroscopy (EIS) method, the researchers were successful in detecting gliadin from food sample, but their investigation did not explore biological capture molecules or did not test the stability of the sensor over time. Laube et al. 2011 [18], studied the development of an electrochemical magneto immunosensor through immobilization of gliadin on tosyl activated magnetic beads, using horse radish peroxidase (HRP) as enzymatic label, followed by subsequent capture of the magnetic beads onto graphite-epoxy composite magneto electrodes for electrochemical detection. Although the researchers were able to detect gliadin, these types of sensors can be complex, time consuming and costly.

Zein is a low-cost by-product of ethanol production, and zein-carbon-based nanocomposites have a large number of functional groups including COOH and NH_3 to successfully capture and anchor antibodies and aptamers, and can replace overcomplicated capturing methods and toxic immobilization chemicals that are currently being used in many biosensor applications. Therefore, the objective of this study was to demonstrate the feasibility of

using a zein based carbon nanotube containing electrochemical sensor to detect gliadin content at the sensitive level to meet FDA requirements. Zein has been utilized as an immobilization substrate that also enables the dispersion of highly conductive nanoparticles such as carbon nanotubes that can amplify the electrochemical signals for the sensitive detection of gliadin. This fabricated sensor may offer a suitable alternative to other sensors containing highly toxic chemicals as linker molecules.

6.3 Experimental Details

6.3.1 Materials

Zein, 11-mercaptoundecanoic acid (11-MUA), N-Hydroxysuccinimide (NHS) 98%, 1-Ethyl-3-(3-dimethylaminopropyl) carbodiimide (EDC) 98%, multiwalled carbon nanotubes (MWCNT) and Anti-gliadin (wheat) antibody, gliadin protein were purchased from Sigma-Aldrich (St. Louis, MO). Graphite flakes, potassium permanganate ($KMnO_4$), 96% sulfuric acid (H_2SO_4), phosphoric acid (H_3PO_4), 30% hydrogen peroxide (H_2O_2) and 70% Ethanol (140 proof (70%), Decon™ Labs) were purchased from Fisher Scientific. LAPONITE® RD clay was kindly donated by Byk Additives Ltd. (Cheshire, U.K.)[19]. StartingBlock™ T20 (PBS) Blocking Buffer was purchased form ThermoFisher Scientific (Waltham, MA).

6.3.2 Zein-nanocomposite Solution Preparation

First, Zein-nanocomposites with GO, LAP and CNTs were prepared to analyze their spectroscopic, microscopic and electrochemical performance. Graphene oxide was prepared using Tour's method [20]. The zein nanocomposite preparation method has been adapted from Xu et al. 2009 [21]. An aliquot of 50mg LAP, or 50mg GO or 50mg CNT was added to 50mL 70% ethanol, sonicated for 30 minutes and heated to 65°C. Then 1ml of 15 wt% zein in 70% ethanol solution was added to the nanocomposite solutions and stirred vigorously for 1 hour which caused it to completely dissolve into each solution. Each formulation was sonicated for 5 minutes to ensure complete dispersion and degassing. A glassy carbon electrode (GCE) used as the working electrode, was first polished with 0.3 and 0.05 μm alumina slurry on emery paper (# 1200), and then cleaned under sonication bath for 1 min and finally thoroughly rinsed with distilled water [22] (Step #1 in **Fig. 6.1**) . A drop casting technique was used to coat the electrode with the zein

solution containing LAP, GO and CNTs (Step #2 in **Fig. 6.1**). The thickness of the zein nanocomposite layer is important to the flow of electrical current so this layer was kept as thin as possible by depositing a 10 microliter drop on the surface of the electrode. This volume was the result of an optimization procedure testing 2, 3, 4, 5,10 and 15 microliter deposition, as shown in Figure S2. After dropping 10µL zein-LAP or zein-GO or zein-CNT solution on the top surface of the electrode it was dried for 30 minutes to obtain a film.

6.3.3 Preparation of Zein-Based Biosensor Assembly

The zein/CNT coated electrochemical sensor assembly was used to detect different concentrations of gliadin because in the first phase of experiments it was shown to have a superior electrochemical performance. The experiments to demonstrate its performance will be discussed in detail in the Results and Discussion section below. The gliadin was detected through an immunoassay using an antigliadin antibody previously tested for its specificity in our laboratory [23]. Gliadin antibodies (ANT) were bound to the surface of the zein nanocomposite sensors using the method described in Gezer et al. (2016a), with some modifications. First, Z-CNT coated electrodes were immersed in a 100 µL droplet of 2 M 11-MUA solution inside a centrifuge tube (Step #3 in **Fig. 6.1**) and incubated for 16 hours at 4^{o}C constant temperature in a refrigerator. Afterwards, the electrode was washed with 200 proof ethanol and immersed in a 100 µl droplet of a 1:1 solution of 0.4 M EDC and 0.1 M NHS and incubated for 45 min (Step #4 in Figure 1). The electrode was then washed with DI water, followed by immersion into a 30µl droplet of 5 µg/ml anti-gliadin solution for 30 minutes (step #5 in **Fig. 6.1**). This allowed the sensor surface to bind to the anti-gliadin protein before being washed with DI water to remove the excess unbound anti-gliadin protein. The residual -COOH groups were blocked with 10% PBS-Tween 20 (St. Louis, MO, USA) for 30 minutes. The target gliadin solution was prepared by adding 50 mg gliadin from wheat with 1 ml of 55% (v/v) ethanol and mixing for 2 hours at room temperature. After centrifuging the suspensions at 10000 X g for 5 min; the supernatants were collected and diluted with 10% PBS-Tween 20 to prepare 0.5, 1, 5, 10, 20, 50 and 100 ppm gliadin solution (Freedman et al., 1987). The Z-CNT electrode that had been functionalized with antibody was washed with DI water and placed in solutions of 0.5, 1, 5, 10, 20, 50 and 100 ppm gliadin for 30 minutes and washed with DI water and the electrodes were then used as a working electrode in the electrochemical cell connected to the potentiostat (step #6 in **Fig. 6.1**).

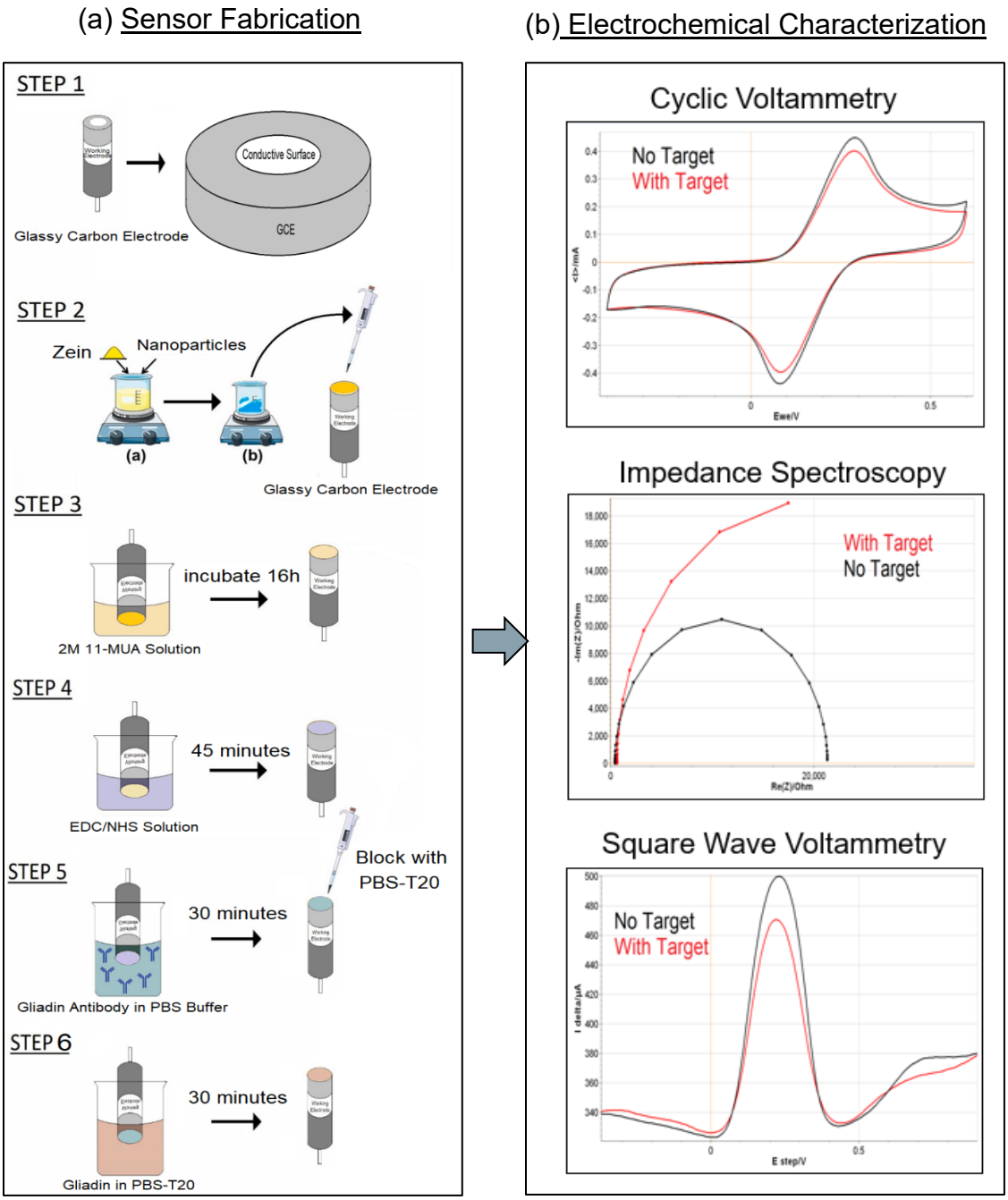

Fig. 6.1. (a) stepwise process of antibody immobilization and gliadin capture on the zein-CNT platform on working electrode (b) Ideal shapes of cyclic voltammetry, impedance spectroscopy, and square wave voltammetry signals, when functionalized electrode is used as a working electrode in potentiostat system. For colored images please refer to the online version of the article.

6.3.4 Fourier Transform Infrared Spectroscopy (FTIR)

Thermo-Nicolet Nexus 470 FTIR Spectrometer (Thermo scientific) was used to collect the ATR-FTIR spectra of zein, zein-GO, zein-LAP, zein-CNT, Gliadin, multiwalled CNT, with 64 scans, at 4 cm−1 resolution and wavenumber range of 4000- 800 cm−1. Other aspects of this technique has been described previously [20].

6.3.5 Transmission Electron Microscopy (TEM)

The LAP, GO, CNT, Z-LAP, Z-GO and Z-CNT samples were visualized using TEM. A Tecnai T20 TEM (FEI Company) with an acceleration voltage of 200 kV was used. Nanoparticle samples were prepared by dispersing the nanoparticles in 70% ethanol, sonicating for 5 min and then placing the dispersion on holey carbon TEM grids. TEM samples of Z-LAP, Z-CNT and Z–GO nanocomposites were prepared following a procedure published previously [8].

6.3.6 Electrochemical Characterization

Specificity tests were performed by testing the CV signals from gliadin 50 ppm, lactalbumin 50ppm, ovalbumin 50 ppm, acrylamide 50 ppm, formamide 50 ppm. The steps of Z-CNT deposition, linker molecule attachment and antibody immobilization were the same for all targets and has been described in section 2.3.

6.3.7 Electrochemical Characterization

Cyclic voltammetry (CV), square wave voltammetry (SWV) and electrochemical impedance spectroscopy (EIS) was performed in 5 mM $K_4[Fe(CN)_6]^{4-}/K_3[Fe(CN)_6]^{3-}$ electrolyte using a Biologic potentiostat (SP-150, Bio-Logic SAS, France). For electrochemical analysis, a three-electrode electrochemical cell was prepared, where the as-fabricated biosensor electrode was used as the working electrode, a Pt wire counter electrode, and an Ag/AgCl reference electrode. The cyclic voltammetry scans were recorded at 100mVs-1 scan rate, [12], in the potential range of −0.4 - 0.6 V vs. Ag/AgCl (3.0 M KCl). Testing with different scan rates of 25, 50 and 100 mVs^{-1} , the 100 mVs-1 scan rate gave the best signal as shown in Figure S1. Also 100 mVs^{-1} was used in previous zein electrochemical studies [12]. There was obvious voltammetric signal observed at bare GCE electrode in the potential of −0.4 - 0.6 V vs. Ag/AgCl (3.0 M KCl), which proved electron transfer on the electrode. Impedance spectra were recorded in the frequency range of 100

mHz to 300 kHz, with 10 mV amplitude at open circuit voltage (0CV). The square wave voltammetry, (SWV) measurements were recorded at a pulse amplitude of 35 mV and scan increment of -0.5–1.0 mV. Using the impedance data, the charge-transfer resistance (RCT-layer) of zein, zein-GO, zein-LAP, Z-CNT were analyzed using the Randles' model [24]. For Nyquist plots analysis, a Randles' modified equivalent circuit [Rs(CPE[RctZW])] was used, where, Rct is the charge transfer resistance, ZW is the Warburg impedance, CPE is a constant phase element and Rs is the solution resistance [12].

6.3.8 Specificity Test

Specificity tests were performed by testing the CV signals from gliadin 50 ppm, lactalbumin 50ppm, ovalbumin 50 ppm, acrylamide 50 ppm, formamide 50 ppm. The steps of Z-CNT deposition, linker molecule attachment and antibody immobilization were the same for all targets and has been described in section 2.3.

6.3.9 Stability Test

The stability and reproducibility of the sensor were tested, by testing CV current response of the bare glassy carbon electrodes, Z-CNT-Antibody modified electrode with no target and Z-CNT-Antibody modified electrode with 5 ppm gliadin over a period of four weeks. The electrochemical signals generated each week were compared to check reproducibility and stability of the sensor.

6.3.10 Statistical Analysis

For each of the zein nanocomposites, each of the different concentrations of targets, the experiments were repeated three times. Minitab 18 (one-way ANOVA) was used to statistically analyze and compare the data with 95% confidence level. Tukey's comparison tests were applied ($p < 0.05$), and the letter system was used throughout the paper to show significant difference such that different letters indicate significant difference between the adjacent values.

6.4 Results and Discussions

6.4.1 FTIR of Zein Nanocomposites

In order to estimate the electrochemical performance of the modified electrodes, CV was used as a method to detect the intensity of redox. **Fig. 6.2** shows cyclic voltammograms of bare glassy carbon electrode (GCE) modified electrode in 0.1 M acetate buffer solution (pH 5.0) at a scan rate of 100 mV/s. There was obvious voltammetric signal observed at bare GCE electrode in the potential of −0.4 – 0.6 V vs. Ag/AgCl (3.0 M KCl) (blue curve), which proved electron transfer on the electrode. Then when zein coated GCE was tested it failed to show any sign of electron transfer, as there were no redox peaks visible. Once zein was modified using LAP/GO we can see the redox peaks once again in the CV graphs. The Z/LAP modified electrode had the highest signal compared to the l-b-l Z/LAP or Z-GO modified electrode. This means that the oxygen functional groups available in the GO prevents good flow of electron, and the LAP coating on the zein did not adhere properly causing electrochemical characterization causing poor signal.

In FTIR the rise of new peaks or shift in existing peaks give useful information about formation of new physicochemical bonds which helps with the mechanistic understanding of the material chemistry. FTIR was performed on zein in ethanol, zein-CNT, zein-LAP, zein-GO and gliadin to understand the underlying chemistry of the different combinations of zein with different nanoparticles, as well as compare the peaks of zein which is a corn protein and used as an anchoring molecule in this study, with the peaks of gliadin which is a protein from gluten, used as the target molecule in this study. **Fig. 6.2** shows FTIR spectra of pristine gliadin, zein solutions in 70% ethanol, zein-Laponite®, zein-GO in 70%ethanol, zein-CNT and pristine multiwalled CNT. For pristine gliadin, the wide peak at 3400 cm-1 represents the -NH functional groups found in proteins. The –CH3 and –CH2 alkyl aliphatic side chains of the R groups of the amino acids of protein gave rise to the low intensity peak at 2850cm^{-1}. The Amide I peak at 1639 cm-1 is attributed to C=O and C=C stretching, and Amide II peak at 1450 cm-1 is attributed to -CN, -NH stretching.

In comparison to pristine gliadin powder, the FTIR spectra of zein in 70% ethanol, zein-LAP in 70% ethanol, zein-GO in 70%ethanol solutions had new peaks at 1098 cm^{-1} which resulted from the out of phase C-C-O stretch and two peaks between 900-800 cm^{-1} were attributed to the in phase C-C-O stretch of primary and tertiary alcohols [25]. From **Fig. 6.2** (a) it is clearly visible that gliadin and zein has identical peaks at similar positions, and because of this, spectroscopic

techniques like FTIR, Raman, UV-Vis will be unable to detect the presence of gliadin on a zein substrate sensor.

From **Fig. 6.2** (b) we can see that CNT has peaks at 1640 cm^{-1} due to vibrations of carbonyl (C=O, C-C) groups and 2887 cm^{-1} due to the stretching vibration of C–H bonds [26]. Peaks at 1640 cm^{-1} can be attributed to C=C, vibrations. As a result, the Z-CNT composite seems to only exhibit the prominent -NH peak and amide II peak coming from the zein protein.

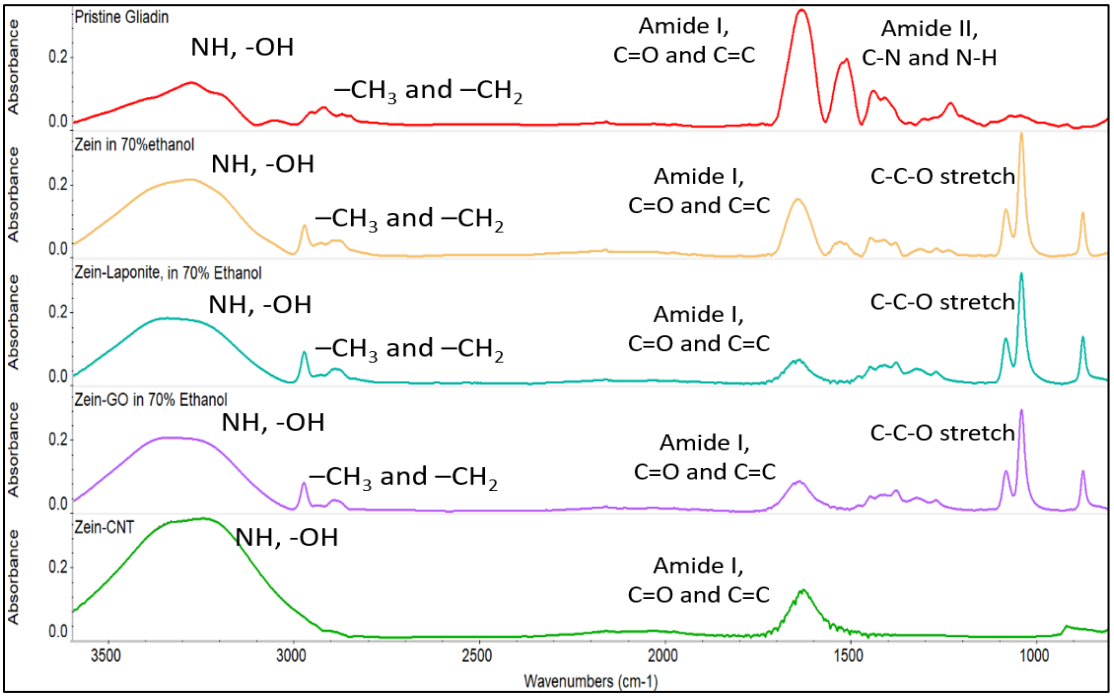

(a)

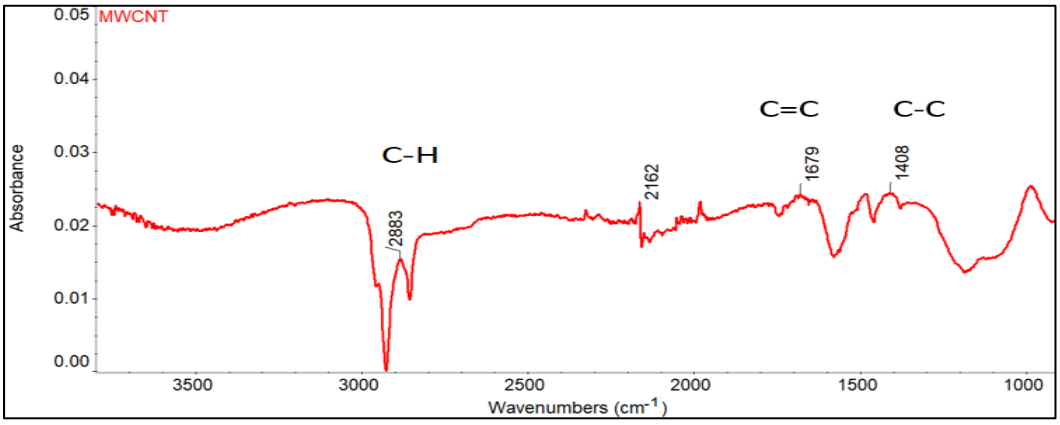

(b)

Fig. 6.2. FTIR spectra of (a) pristine gliadin, zein in 70% ethanol, zein-Laponite® in 70% ethanol, zein-GO in 70% ethanol, zein-CNT, (b) pristine multiwalled carbon nanotubes. For colored images please refer to the online version of the article.

6.4.2 TEM of Zein Nanocomposites

TEM images shown in **Fig. 6.3** (a-b), shows the MWCNTs have a fiber like structure. Larger magnification of the nanotubes show that multiple nanotubes are concentrically formed, as evidenced by the multiple parallel lines at the edges of the nanotubes, as well as the multiple inner circles at the ends of the tubes. The MWCNTs seemed to have on an average 6-8 tube walls, which agrees with the manufacturer specification. The manufacturer's description of MWCNT as having 10 nm × 4.5 nm average outer diameter × inner diameter was slightly less than the experimental values obtained 15 nm × 6.0 nm. When zein is added to the MWCNTs, they tend to create some aggregation, as seen from figure **Fig. 6.3** (c-d), but the parallel lines of the nanotubes can still be visible within the aggregations as indicated with red circles.

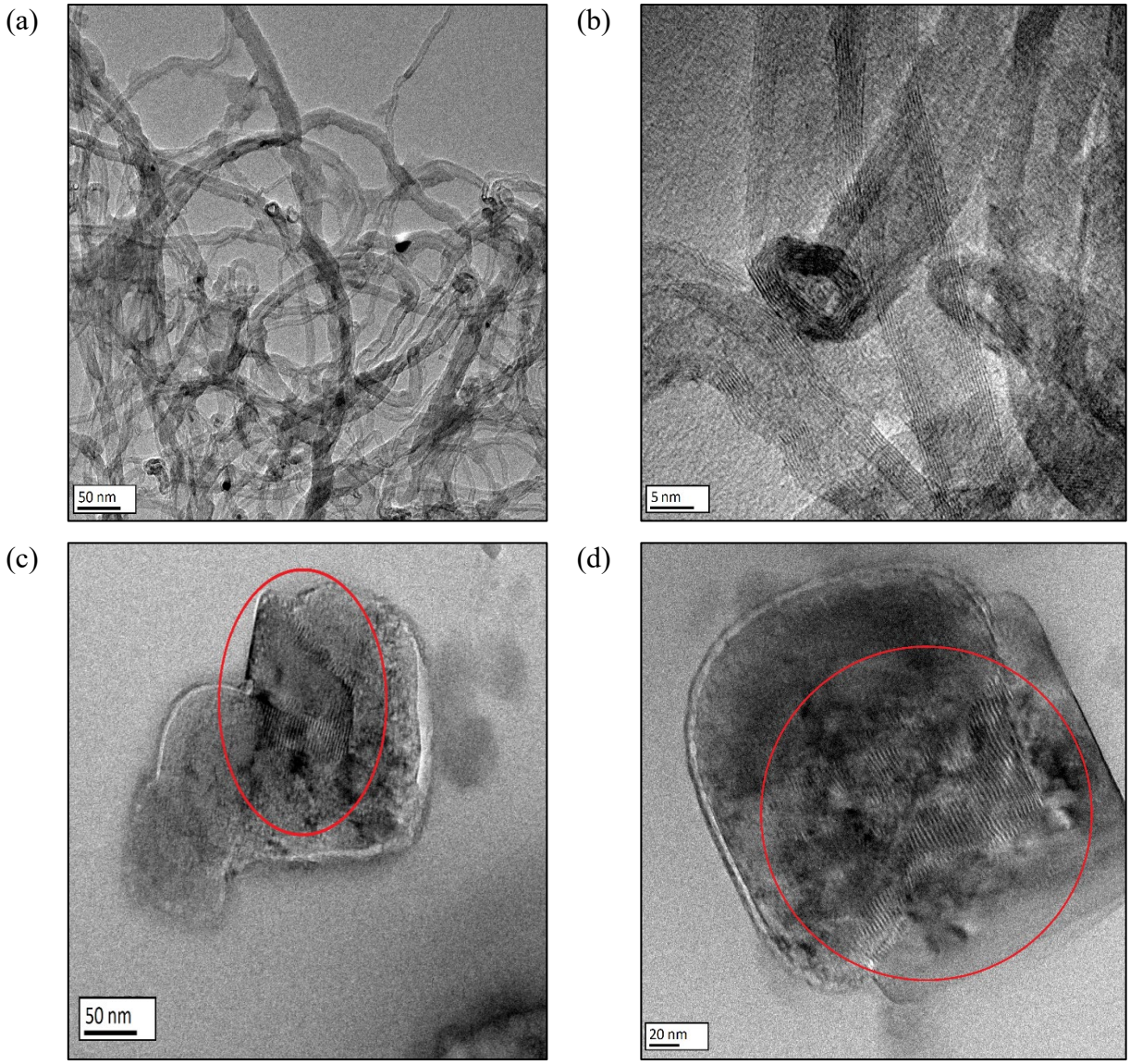

Fig. 6.3. TEM images of (a-b) Prisitne MWCNTs, (c-d) Z-CNT nanocomposites.

Fig. 6.4 (a) shows TEM images of GO prepared with a wrinkled morphology. Previous studies have also reported the appearance of large number of wrinkles in GO sheets [27]. Translucency of the GO sheets enable observation of stacked layers. Single or few layers of GO are indicated by the light-colored wrinkles, consistent with previous reports [28]. This usually means there is good degree of exfoliation of GO sheets, which is helpful in achieving efficient biopolymer/nanoparticle interactions [27] between Z and GO, enabling larger degree of conductivity through formation of networks. In **Fig. 6.4** (b), larger degree of wrinkled sheets with darker shades are more prevalent for Z-GO nanocomposites, suggesting that the higher the ratio

of GO sheets, the greater the likelihood of aggregate formation. Similar results were also found in our previous work [20]. In **Fig. 6.4** (c), we can see the individual fully exfoliated LAP nanoparticles, which are white streaks with an average 1 nm diameter and 20-30 nm length. The LAP nanoparticles appear to be oriented in a way that gives the appearance of 'house of cards'. For Z-LAP nanocomposite in **Fig. 6.4** (d), Laponite® nanoparticles appears to be in parallel alignment within small aggregates or domains, as evident from the dark streaks. Due to the presence of zein and a high Laponite® concentrations, the 'house of cards structure' is no longer feasible and more intercalation is visible [8].

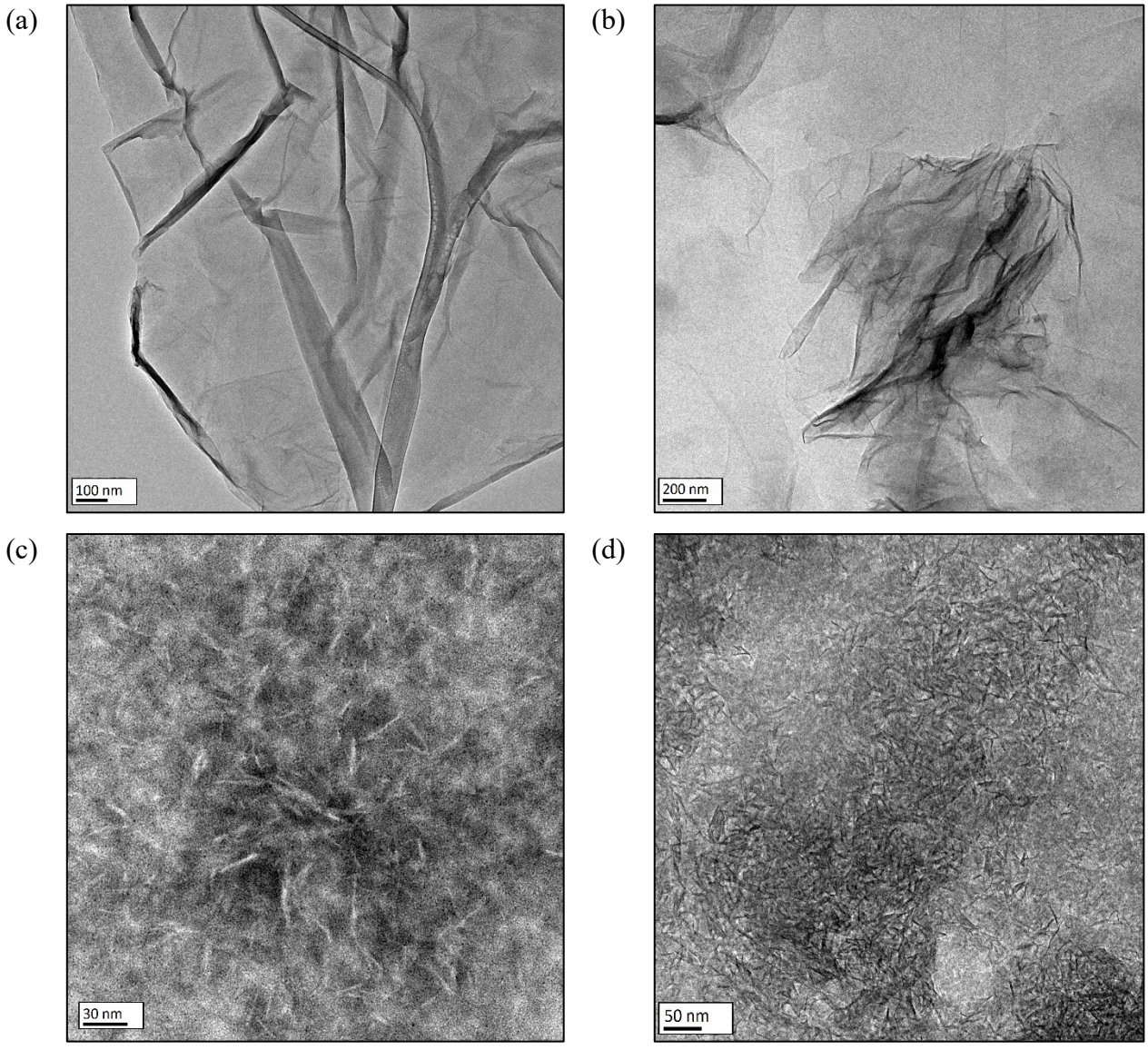

Fig. 6.4. TEM images of (a) GO sheets prepared in the laboratory, (b) Zein-GO nanocomposites, (c) Pristine LAP nanoparticles (d) Zein-LAP nanocomposite.

6.4.3 Electrochemical Characterization of Zein Nanocomposites

Electrochemical performance of the zein nanocomposite functionalized electrodes were estimated by applying CV as a method to detect the intensity of redox peaks. **Fig. 6.5** (a) shows cyclic voltammograms of bare glassy carbon electrode (GCE) in K3[Fe(CN)6] at a scan rate of 100 mVs-1. Zein coated GCE failed to show any sign of electron transfer, as there were no redox peaks visible. Once zein was modified using LAP/GO we can see the redox peaks once again in the CV graphs. The Z-GO modified electrode had higher signal compared to the Z-LAP modified electrode. But the highest signal was collected from Z-CNT coatings, which means that the oxygen functional groups available in the GO and Laponite® prevents good flow of electron, causing poor signal. The concentration of the nanoparticles GO, LAP, CNT were varied to optimize the electrochemical signal. The concentration of the nanoparticles was varied by 1%, 5% and 10% to determine which concentration would give higher signal without blocking the electrode and reducing the electrochemical signal. The upper limit concentration of nanoparticle loading was maintained at 10% to minimize nanoparticle usage while optimizing signal strength. Z-CNT had much stronger signal for CV response, compared to the Z-LAP and Z-GO which can be clearly seen from **Fig. 6.5** (b).

The Z-LAP, Z-GO and Z-CNT were further investigated using EIS technique as shown in**Fig. 6.5** (c). The Z-CNT had the highest redox signals in CV graph (**Fig. 6.5** (a)) and the lowest resistance in EIS curves. The charge transfer resistance Rct was calculated using the Z fitting method, which gave the value for bare GCE (500Ω), zein (36kΩ), zein-Laponite® (16kΩ), Zein-GO (11kΩ), Zein-CNT (94 Ω). Based on these findings, Z-CNT was selected as the matrix for antibody binding in the gliadin electrochemical sensor.

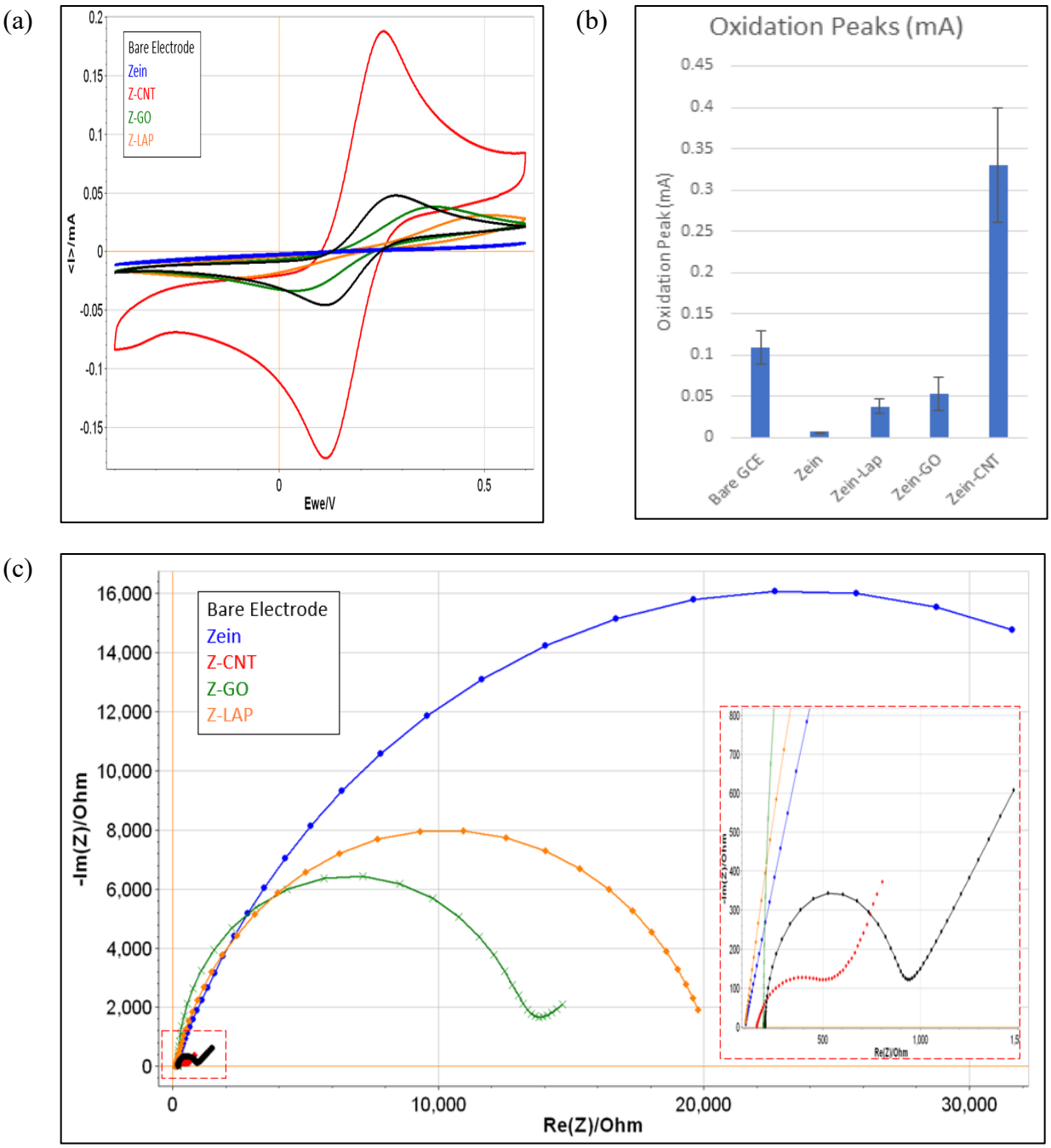

Fig. 6.5. (a) Cyclic voltammograms (CV) curves for bare electrode, zein, zein –LAP, Zein-GO, Z-CNT in 5 mM $K_4[Fe(CN)_6]^{4-}/K_3[Fe(CN)_6]^{3-}$ at 100 mVs^{-1} (b) Bar charts showing comparison of signal intensity (c) *Nyquist plots for* bare electrode, zein , zein –LAP, Zein-GO, *and Z-CNT*. For colored images please refer to the online version of the article.

6.4.4 Understanding the Sequential Immobilization of Biocomponents

To understand the electrochemical response of each of the immobilization steps, square wave voltammetry and cyclic voltammetry was applied in each of the sequential immobilization steps to understand the underlying chemistry as shown in **Fig. 6.6**. To obtain good repeatability and high sensitivity in measurement, it is imperative to identify proper linker compounds that are durable, can be easily prepared, and that form a strong linkage between the Z-CNT layer and the antibody, that maintains appropriate bond length for allowing high density packing of antibody at the biosensor surface. Although EDC has been known to provide a suitable linker compound for 3-mercaptopropionic acid (MPA), it is not very stable, and this may account for the poor performance of previous SAM piezo immunosensors [29]. Because the co-addition of NHS and EDC has proven to enhance the strength of the linker compounds, [30,31] and the successful use of 11-mercaptoundecanoic acid in our previous works [32], we have selected these materials and adopted the procedure in our current study. **Fig. 6.6** shows the schematic diagram depicting the stepwise procedures for the anchoring of antibodies onto the carboxylate-terminated Z-CNT on GCE electrodes. The method continued by means of a stepwise development and substitution of terminal EDC and NHS in succession to form the NHS ester preceding its substitution by the side-chain lysine residues of the gliadin antibody to shape the gliadin electrochemical sensor, after the blocking of nonspecific interaction by PBS-T20 [30].

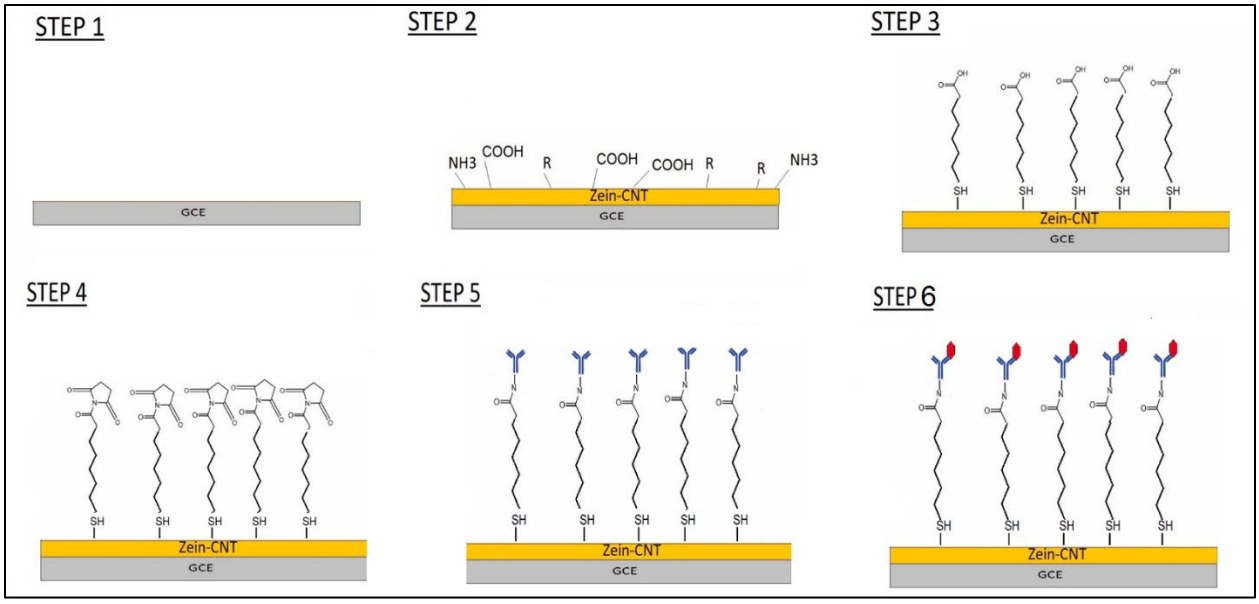

Fig. 6.6. Sequential immobilization of the antibody antibodies onto the carboxylate-terminated Z-CNT. Step 1: Bare electrode (GCE) with no functional group or binding ability, Step 2: Functionalization through deposition of Z-CNT, Step 3: -SH bond formation between zein and 11-MUA, Step 4: NHS ester formation due to addition of EDC:NHS, Step 5: substitution of NHS ester through lysine residue from gliadin antibody, Step 6: Capturing gliadin with gliadin antibody. For colored images please refer to the online version of the article.

Fig. 6.7 (a) shows the CV response of each step during immobilization of linker molecules MUA, EDC, NHS and antibody. First, we can see addition of Z-CNT on bare electrodes increases the current signal, which means presence of highly conductive CNT improves the current flow resulting in the higher current signal. On the other hand, the addition of zein with its large number of functional groups increases the possibility of binding. After the 16hour MUA treatment the signal goes down, meaning MUA interacts with Z-CNT which blocks the electron flow from CNT and reduces the current signal. Further addition of NHS/EDC and antigliadin antibody, results in even further lowering of the signal. **Fig. 6.7** (b) shows SWV response of sequential immobilization of biorecognition elements on the bare electrode designated for antibody immobilization and 5 ppm gliadin detection.

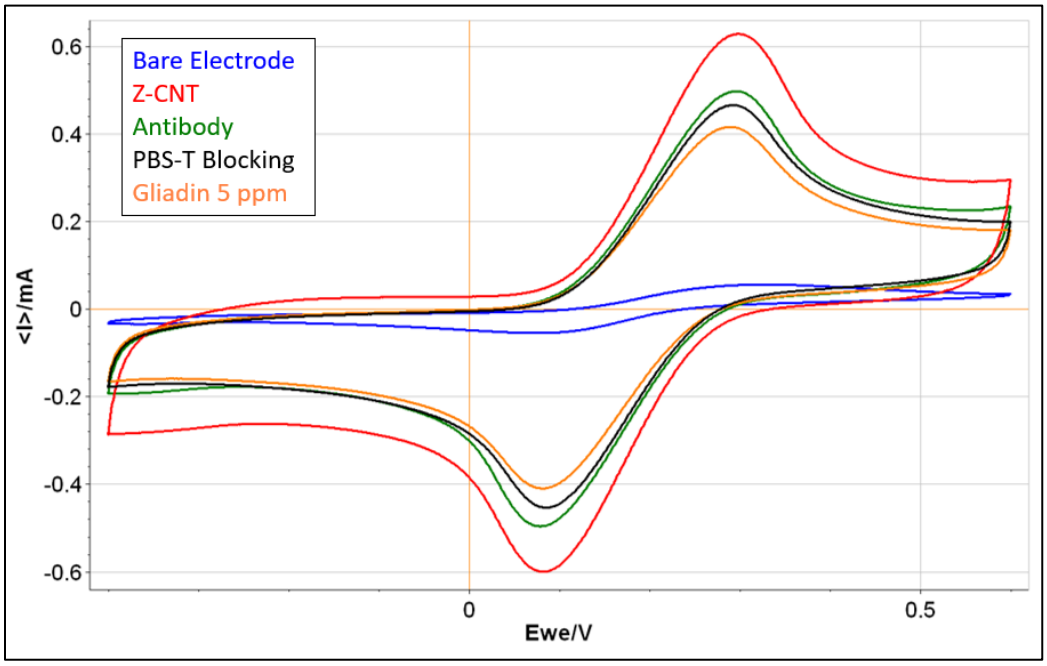

(a)

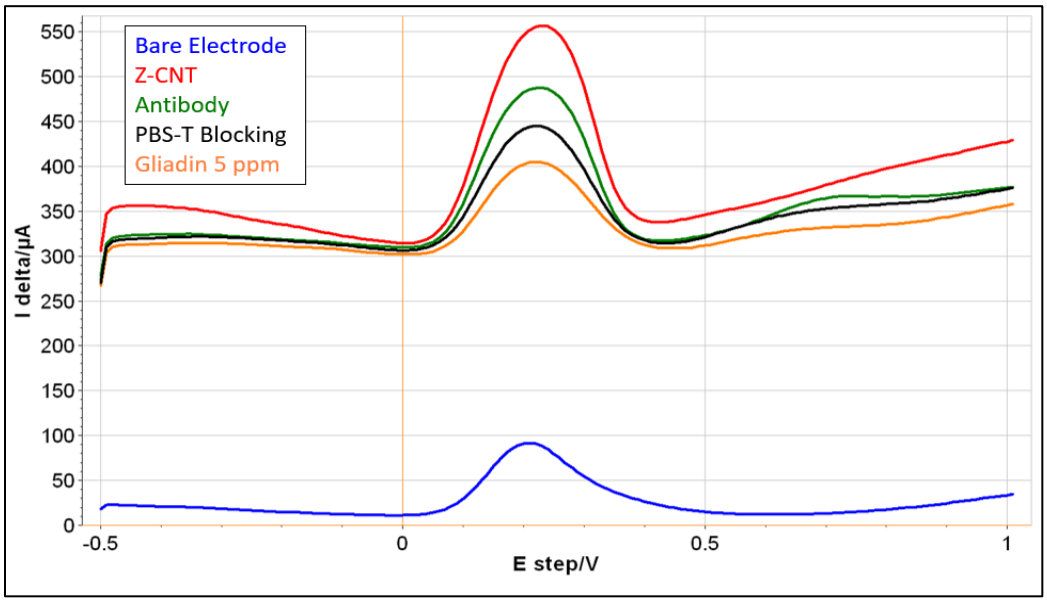

(b)

Fig. 6.7. (a) CV response of sequential immobilization of biorecognition elements on the bare electrode designated for antibody immobilization and 5 ppm gliadin detection, in 5 mM $K_4[Fe(CN)_6]^{4-}/K_3[Fe(CN)_6]^{3-}$ at 100 mVs^{-1}. (b) SWV response of sequential immobilization of biorecognition elements on the bare electrode designated for antibody immobilization and 5 ppm gliadin detection. For colored images please refer to the online version of the article.

6.4.5 Analytical Performance

The electrochemical reduction behavior resulting for the capturing of gliadin by antibody immobilized by zein was explored using CV techniques. Upon incubation in 20 ppm gliadin, the cyclic voltammogram of the Z-CNT-ANT/GCE changed dramatically with an increase of reduction peak current and a decrease of oxidation peak current in **Fig. 6.8** (a) So, the electrochemical response could be used as an efficient biosensor for detection of gliadin. In order to determine the significance of zein as a binding matrix of CNT, only CNT functionalized glassy carbon electrode with antibody and 20 ppm gliadin have also been tested. **Fig. 6.8** (a) shows that electrodes coated with Z-CNT-ANT showed a decrease in oxidation peak once 20ppm gliadin was added. This indicated that zein had successfully immobilized gliadin antibody and the gliadin antibody had captured gliadin analyte, causing the decrease in oxidation peak. On the other hand, the electrode only functionalized with CNT-ANT, showed an increase in oxidation peak once the 20 ppm gliadin was added. This is the opposite of what is expected and indicates that in the absence of zein, CNT fails to adhere the antibody to the electrode which subsequently results in the opposite trend in electrochemical response. **Fig. 6.8** (b) and (c) shows the CV response of Z-CNT in the presence of 0, 0.5, 1, 5, 10, 20, 50 and 100 ppm gliadin. In figure 8(b), we can see clear redox peaks for all the Z-CNT electrodes with 0, 0.5, 1, 5, 10, 20, 50 and 100 ppm gliadin. All the peaks are highly discernible and easily detectable, meaning the fabricated electrochemical sensor can detect the presence of gliadin with as low as 0.5 ppm. As 20 ppm loading is the FDA recommended value for gluten free food, the as fabricated sensor clearly detects gliadin at an acceptable concentration. **Fig. 6.8** (c) shows current signal difference between antibody loaded Z-CNT functionalized electrode (gliadin 0 ppm) and 0.5, 1, 5, 10, 20, 50 and 100 ppm gliadin. It can be known from the linear range of this biosensor to gliadin concentration was between 5 and 100 ppm, which can be described by a linear regression equation of I (mA) = 0.0138C+0.013 (ppm) (R^2 = 0.953). The limit of detection of as fabricated sensor was determined to be 0.5ppm, which is well below the FDA requirement for gluten free food.

A recent study discussing gliadin ELISA sensors have shown to detect gliadin within the range of 5.42 – 1.72 ppm [33], another study using competitive ELISA showed limit of detection of 1.36 mg prolamin/kg food [34]. The shortcoming of ELISA is that it is time consuming and requires highly trained personnel. A study discussing gliadin immune chip has reached a limit of detection of 1.5 ppm [17], which is higher than the LOD in current study. Pinto et al. has been

able to detect gliadin with an apta-PCR with the limit of detection of 0.1 ppm [35], which is lower than current study, however, one of the major drawbacks of PCR technique is the complexation of the process and the high cost of the equipment. Nassef et al. tested two different types of anchoring molecules: 22-(3,5-bis((6-mercaptohexyl)oxy)phenyl)-3,6,9,12,15,18,21-heptaoxadocosanoic acid (labeled as 1) and 1,2-dithiolane-3-pentanoic acid (thioctic acid), (labeled as 2), to fabricate an electrochemical sensor for gliadin. The anchoring molecule 1 took 100 hours to generate self-assembled monolayer, and anchoring molecule 2 took 3 hours. Using the '2' anchoring molecule they were able to fabricate a gliadin immunosensor with LOD of 0.01 ppm. In stark contrast, the anchoring molecule in this study, the Z-CNT nanocomposite are more cost effective, less complicated and it only takes 30 minutes to fabricate, while staying well below the FDA required gluten free standard 20 ppm (LOD 0.5 ppm).

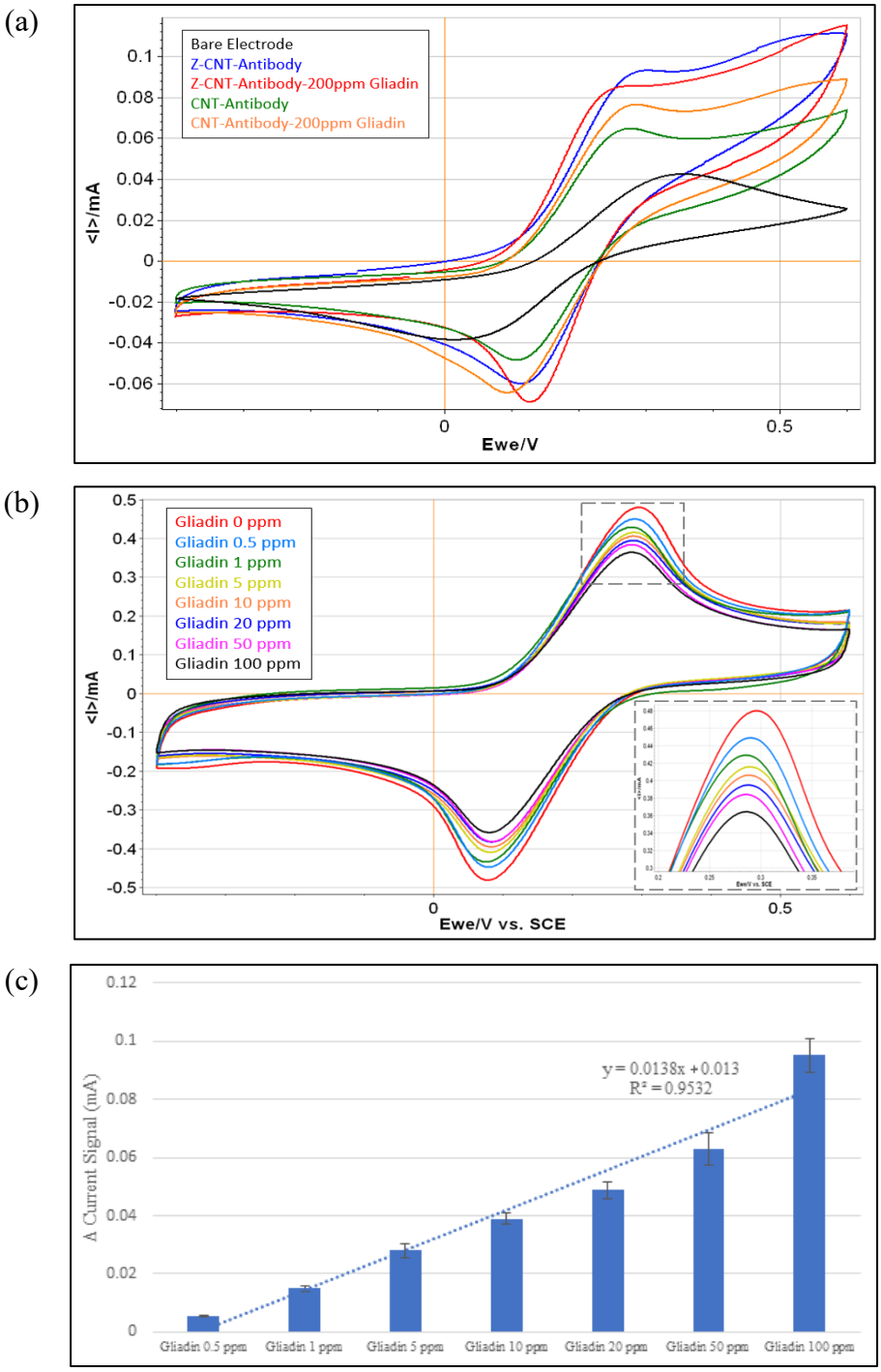

Fig. 6.8. (a) Cyclic voltammograms curves for bare electrode, Z-CNT-ANT with 0 ppm, 20 ppm and CNT-ANT with 0 ppm and 20 ppm (b) Z-CNT-ANT with 0, 5, 10, 20, 50 and 100 ppm gliadin 5 mM $K_4[Fe(CN)_6]^{4-}/K_3[Fe(CN)_6]^{3-}$ at 100 mVs^{-1}. (c) Current signal difference between antibody loaded Z-CNT functionalized electrode (gliadin 0 ppm) and 0, 0.5, 1, 5, 10, 20, 50 and 100 ppm gliadin. For colored images please refer to the online version of the article.

6.4.6 Specificity Test

In **Fig. 6.9** (a) selectivity test, comparison between Z-CNT coated electrode with no target, shows no difference in signal after addition of lactalbumin 50ppm, ovalbumin 50 ppm, acrylamide 50 ppm, formamide 50 ppm. However, when gliadin 50ppm is added the signal goes down, meaning the antibody has attached itself with the gliadin 50ppm which blocks some of the signal. When the oxidation peaks are compared for all the targets in **Fig. 6.9** (b), very low CV signals can be seen for lactalbumin, ovalbumin, acrylamide and formamide, but these are negligible compared to the signal intensity from gliadin. This proves that the fabricated sensor is highly selective towards gliadin, even in the presence of large concentrations of interfering molecules.

(a)

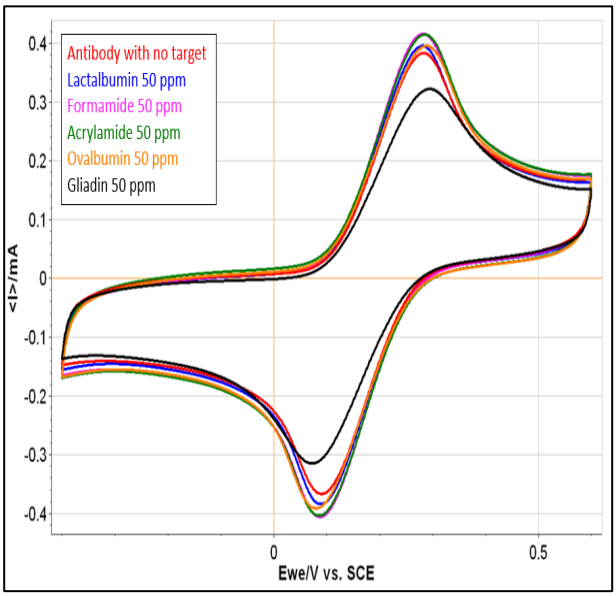

(b)

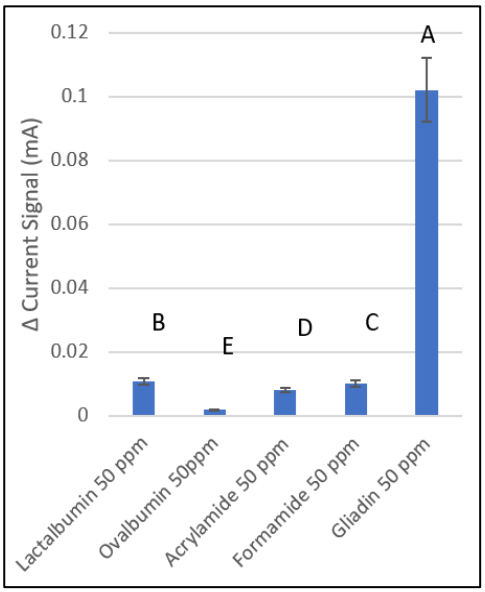

Fig. 6.9. (a) CV voltammograms comparison shows selectivity of the Z-CNT sensor, with lactalbumin 50ppm, ovalbumin 50ppm, acrylamide 50ppm, formamide 50ppm, and gliadin 50 ppm, in 5 mM $K_4[Fe(CN)_6]^{4-}/K_3[Fe(CN)_6]^{3-}$ at 100 mVs^{-1} (b) Comparison of current signal difference between antibody loaded Z-CNT functionalized electrode (gliadin 0 ppm) and lactalbumin 50ppm, ovalbumin 50ppm, acrylamide 50ppm, formamide 50ppm, gliadin 50 ppm. Different letters above error bars signify statistically significant differences according to Tukey's pairwise comparison ($p < 0.05$). For colored images please refer to the online version of the article.

6.4.7 Stability Test

The stability and reproducibility of the sensor were tested, by testing the same Z-CNT solution, linker molecule, antibody to detect 5 ppm gliadin over a period of four weeks. In **Fig. 6.10**, we can see the electrochemical signals generated each week and comparison of each week

signals are reproducible and have very small differences. This proves that the sensor is reproducible and the Z-CNT solution as well as the linker molecules and antibody is stable over a four-week period time.

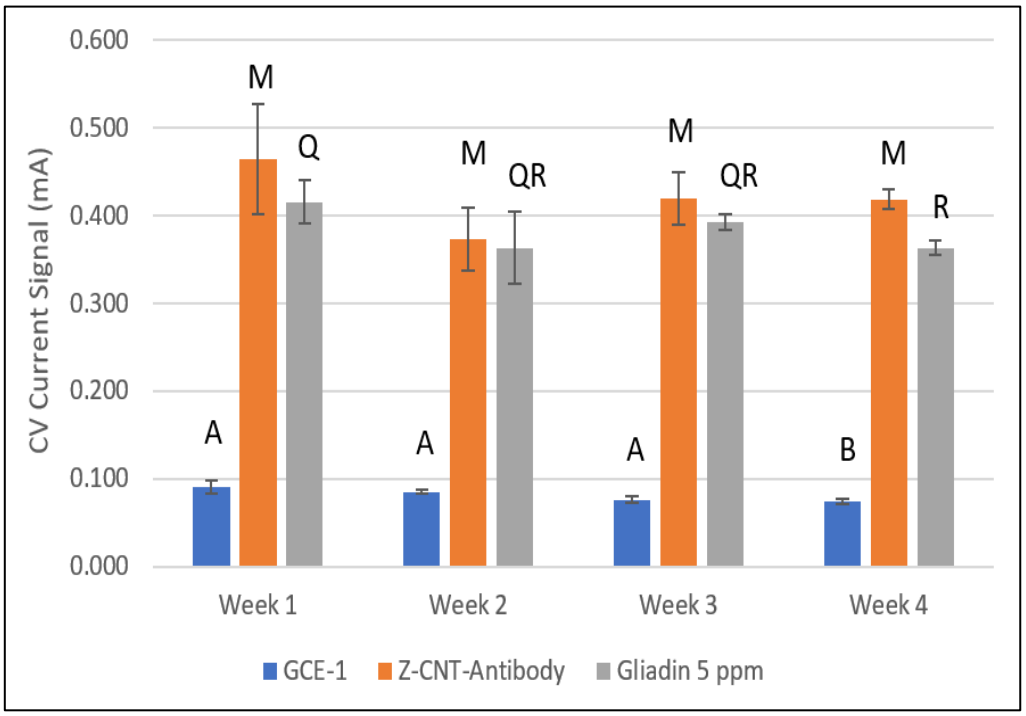

Fig. 6.10. CV current response of the bare glassy carbon electrodes, Z-CNT-Antibody modified electrode with no target and Z-CNT-Antibody modified electrode with 5 ppm gliadin over a period of four weeks, tested in 5 mM $K_4[Fe(CN)_6]^{4-}/K_3[Fe(CN)_6]^{3-}$ at 100 mVs^{-1} . Different letters above error bars signify statistically significant differences according to Tukey's pairwise comparison ($p < 0.05$). For colored images please refer to the online version of the article.

6.5 Conclusions

The objective of this study was to assemble a novel gliadin biosensor based on natural polymer composite nanomaterials. Novel biodegradable coatings made from zein using three different nanoparticles, graphene oxide, Laponite® and multiwalled carbon nanotubes using drop casting technique were tested for fabricating electrochemical sensors using cyclic voltammetry. It is critical that a protein from sustainable sources (zein) combined with a low level of carbon nanomaterial acts as framework for immobilization of biomolecules. Both cyclic voltammogram curves and square wave voltammogram curves indicated successful sequential immobilization of the biorecognition elements onto the Z-CNT coated electrode. Comparison of the CV and EIS curves indicated that Z-CNT gave higher and stronger signals compared to other nanomaterials

like graphene oxide and Laponite®. The Z-CNT biosensor was successfully able to give CV signals for gliadin toxins for as low as 0.5 ppm loading. Successful outcome of this research will lead to the use of zein, as a biodegradable platform for immobilization of different biorecognition elements, which can be extended to other matrices in biosensors.

Funding sources

This research was funded by the Scholle Family Endowment of Purdue University and their support is greatly appreciated.

Acknowledgements

The authors would like to thank Dr. Christopher Gilpin and Laurie Mueller for their assistance with TEM experiments, and Dr. Patricia Bishop and Dr. Hartmut Hedderich for their assistance with AFM and FTIR experiments. We will also like to thank Byk Additives Ltd. (Cheshire, U.K.) for donating LAPONITE® RD clay for our research.

6.6 References

1. Nassef HM, Bermudo Redondo MC, Ciclitira PJ, et al (2008) Electrochemical Immunosensor for Detection of Celiac Disease Toxic Gliadin in Foodstuff. Anal Chem 80:9265–9271. https://doi.org/10.1021/ac801620j

2. Irimia-Vladu M, Głowacki ED, Voss G, et al (2012) Green and biodegradable electronics. Materials Today 15:340–346. https://doi.org/10.1016/S1369-7021(12)70139-6

3. You X, Pak JJ (2014) Graphene-based field effect transistor enzymatic glucose biosensor using silk protein for enzyme immobilization and device substrate. Sensors and Actuators B: Chemical 202:1357–1365. https://doi.org/10.1016/j.snb.2014.04.079

4. Qian C, Sun J, Yang J, Gao Y (2015) Flexible organic field-effect transistors on biodegradable cellulose paper with efficient reusable ion gel dielectrics. RSC Advances 5:14567–14574

5. Gezer PG, Hsiao A, Kokini JL, Liu GL (2016) Simultaneous transfer of noble metals and three-dimensional micro- and nanopatterns onto zein for fabrication of nanophotonic platforms. J Mater Sci 51:3806–3816. https://doi.org/10.1007/s10853-015-9699-0

6. Chakravarty S, Gogoi B, Mandal BB, et al (2018) Silk fibroin as a platform for dual sensing of vitamin B12 using photoluminescence and electrical techniques. Biosensors and Bioelectronics 112:18–22. https://doi.org/10.1016/j.bios.2018.03.057

7. Argos P, Pedersen K, Marks MD, Larkins BA (1982) A structural model for maize zein proteins. J Biol Chem 257:9984–9990

8. Rouf TB, Schmidt G, Kokini JL (2018) Zein–Laponite nanocomposites with improved mechanical, thermal and barrier properties. J Mater Sci 1–16. https://doi.org/10.1007/s10853-018-2061-6

9. Jornet-Martínez N, Campíns-Falcó P, Hall EAH (2016) Zein as biodegradable material for effective delivery of alkaline phosphatase and substrates in biokits and biosensors. Biosensors and Bioelectronics 86:14–19. https://doi.org/10.1016/j.bios.2016.06.016

10. Bocanegra-Rodríguez S, Jornet-Martínez N, Molins-Legua C, Campíns-Falcó P (2018) Delivering Inorganic and Organic Reagents and Enzymes from Zein and Developing Optical Sensors. Anal Chem 90:8501–8508. https://doi.org/10.1021/acs.analchem.8b01338

11. Chen X, Li D, Li G, et al (2015) Facile fabrication of gold nanoparticle on zein ultrafine fibers and their application for catechol biosensor. Applied Surface Science 328:444–452. https://doi.org/10.1016/j.apsusc.2014.12.070

12. dos Santos Pereira T, Mauruto de Oliveira GC, Santos FA, et al (2019) Use of zein microspheres to anchor carbon black and hemoglobin in electrochemical biosensors to detect hydrogen peroxide in cosmetic products, food and biological fluids. Talanta 194:737–744. https://doi.org/10.1016/j.talanta.2018.10.068

13. Balakireva AV, Zamyatnin AA (2016) Properties of Gluten Intolerance: Gluten Structure, Evolution, Pathogenicity and Detoxification Capabilities. Nutrients 8:644. https://doi.org/10.3390/nu8100644

14. Barber EA (2018) Optimization of Zein Based Surface Enhanced Raman Spectroscopy Biosensor for the Detection of Gliadin as a Marker for Celiac Disease. Theses and Dissertations Available from ProQuest 1–173

15. Nutrition C for FS and A (2019) Gluten-Free Labeling of Foods. FDA

16. Koerner TB, Abbott M, Godefroy SB, et al (2013) Validation procedures for quantitative gluten ELISA methods: AOAC allergen community guidance and best practices. Journal of AOAC International 96:1033–1040

17. Chiriacò MS, de Feo F, Primiceri E, et al (2015) Portable gliadin-immunochip for contamination control on the food production chain. Talanta 142:57–63. https://doi.org/10.1016/j.talanta.2015.04.040

18. Laube T, Kergaravat SV, Fabiano SN, et al (2011) Magneto immunosensor for gliadin detection in gluten-free foodstuff: Towards food safety for celiac patients. Biosensors and Bioelectronics 27:46–52. https://doi.org/10.1016/j.bios.2011.06.006

19. Additives BYK (2014) Instruments. Laponite Performance Additives, Technical Information B-RI 21. BYK Additives, Ltd.: Cheshire, UK

20. Rouf TB, Schmidt G, Cakmak M, Kokini JL (2019) Design and mechanistic understanding of graphene oxide reinforced zein nanocomposites with improved mechanical, barrier and thermal properties. J Mater Sci 54:12533–12552. https://doi.org/10.1007/s10853-019-03817-w

21. Xu H, Dai H, Chen G (2010) Direct electrochemistry and electrocatalysis of hemoglobin protein entrapped in graphene and chitosan composite film. Talanta 81:334–338

22. Zheng W, Zheng YF (2007) Gelatin-functionalized carbon nanotubes for the bioelectrochemistry of hemoglobin. Electrochemistry Communications 9:1619–1623. https://doi.org/10.1016/j.elecom.2007.03.007

23. Ansari S, Bozkurt F, Yazar G, et al (2015) Probing the distribution of gliadin proteins in dough and baked bread using conjugated quantum dots as a labeling tool. Journal of Cereal Science 63:41–48. https://doi.org/10.1016/j.jcs.2014.12.001

24. Rushworth JV, Hirst NA (2013) Impedimetric Biosensors for Medical Applications: Current Progress and Challenges. Momentum Press

25. Lin-Vien D, Colthup NB, Fateley WG, Grasselli JG (1991) Alcohols and Phenols. In: The Handbook of Infrared and Raman Characteristic Frequencies of Organic Molecules. Elsevier, pp 45–60

26. Lotfi A, Karimi S, Hassanzadeh J (2016) Molecularly imprinted polymers on multi-walled carbon nanotubes as an efficient absorbent for preconcentration of morphine and its chemiluminometric determination. RSC Adv 6:93445–93452. https://doi.org/10.1039/C6RA22074F

27. Ghobadi S, Sadighikia S, Papila M, et al (2015) Graphene-reinforced poly (vinyl alcohol) electrospun fibers as building blocks for high performance nanocomposites. RSC Advances 5:85009–85018

28. Li M, Wu Z, Ren W, et al (2012) The doping of reduced graphene oxide with nitrogen and its effect on the quenching of the material's photoluminescence. Carbon 50:5286–5291. https://doi.org/10.1016/j.carbon.2012.07.015

29. Staros JV, Wright RW, Swingle DM (1986) Enhancement by N-hydroxysulfosuccinimide of water-soluble carbodiimide-mediated coupling reactions. Analytical Biochemistry 156:220–222. https://doi.org/10.1016/0003-2697(86)90176-4

30. Fung YS, Wong YY (2001) Self-Assembled Monolayers as the Coating in a Quartz Piezoelectric Crystal Immunosensor To Detect Salmonella in Aqueous Solution. Anal Chem 73:5302–5309. https://doi.org/10.1021/ac010655y

31. Nakajima N, Ikada Y (1995) Mechanism of Amide Formation by Carbodiimide for Bioconjugation in Aqueous Media. Bioconjugate Chem 6:123–130. https://doi.org/10.1021/bc00031a015

32. Gezer PG, Liu GL, Kokini JL (2016) Development of a biodegradable sensor platform from gold coated zein nanophotonic films to detect peanut allergen, Ara h1, using surface enhanced raman spectroscopy. Talanta 150:224–232. https://doi.org/10.1016/j.talanta.2015.12.034

33. Cavaletti L, Taravella A, Carrano L, et al (2019) E40, a novel microbial protease efficiently detoxifying gluten proteins, for the dietary management of gluten intolerance. Sci Rep 9:1–11. https://doi.org/10.1038/s41598-019-48299-7

34. Haas-Lauterbach S, Immer U, Richter M, Koehler P (2012) Gluten Fragment Detection with a Competitive ELISA. Journal of AOAC International 95:377–381. https://doi.org/10.5740/jaoacint.SGE_Haas-Lauterbach

35. Pinto A, Polo PN, Henry O, et al (2014) Label-free detection of gliadin food allergen mediated by real-time apta-PCR. Anal Bioanal Chem 406:515–524. https://doi.org/10.1007/s00216-013-7475-z

CHAPTER 7. CONCLUSIONS

Throughout the research that led to this dissertation, the potential of utilizing zein, a corn protein, as a biodegradable packaging material and a biosensor platform was investigated. First, both Laponite® and GO nanoparticles participated in covalent bonding with zein, during film formation using solvent casting techniques. For Laponite®, Si-N covalent bonding formed, through the Si-O groups of Laponite® with the -NH groups of β-sheets in zein, which was evident from the new 1000 cm^{-1} peak and decrease in α-helix and increase in β-sheets in the secondary structure analysis of zein- Laponite® nanocomposites. For GO, even though FTIR, FT-Raman and DSC indicated amidation reaction between -COOH groups of GO and -NH_2 groups of glutamine turns of zein, there were some indications of hydrogen bonding due to the downward shift in the amide I peak in FT-Raman, and the shift to lower temperatures of the endothermic peaks with increased GO addition. Initially the combined effect of the hydrogen and covalent bonding between zein and GO did improve the mechanical and thermal properties, however, the dispersive adhesion between the GO sheets were very strong and at higher loadings of GO (above 1 wt%) started to form significant aggregates.

For zein-Laponite® nanocomposites, Si-N covalent bonding formation significantly improved the mechanical strength, as 10wt% loading improved the tensile strength by 150% and Young's modulus by 180%, and decreased the water vapor barrier properties by 40%, indicating potential for zein nanocomposites to be extended for biodegradable packaging material as well as various functional film research. The combined hydrogen bonding and amidation reaction between zein and GO significantly improved the tensile properties, as only 3 wt% increased tensile strength by 80% increase, Young's modulus by 300%, and exhibited 20°C increase in 50% thermal degradation temperature. However, due to the aggregate formation at 1wt% GO concentration, the barrier properties showed a non-linear trend and started to decrease compared to the control zein films. Hence, zein-Laponite® nanocomposites showed greater promise in packaging application compared to Z-GO nanocomposites.

For both nanocomposite studies, the control plasticized zein film had a hydrophilic water contact angle of 50±5°. In spite of both GO and Laponite® being hydrophilic, addition of these nanoparticles increased surface hydrophobicity with the water contact angle of Z-5wt% Laponite and Z-2 wt% GO being 64° and 65° respectively. This phenomenon can be attributed to a number

of factors like the orientation of the nanoparticle within zein matrix, surface morphology, influence of oleic acid plasticizer. There were some indications of phase separation of the plasticizer, for zein-Laponite®, with the dark oleic acid spots in the TEM images, for Z-GO the disappearance of the 1447 cm^{-1} peak attributed to the zein-oleic acid bonding. The phase separated oleic acid could have traveled to the hydrophobic PDMS substrate on which zein was cast on and oriented its hydrophobic tail towards the surface which could have influenced the slight shift in the surface hydrophilic/hydrophobic balance. Nevertheless, the zein nanocomposite surface still remained mostly hydrophilic. This kind of surface property makes many practical applications possible, such as cell and tissue adhesion, microfluidic platforms, metal adhesion onto zein films to name a few.

The presence of different functional groups like -COOH, $-NH_2$, -R groups make zein an ideal candidate for immobilization application in electrochemical sensor assembly. On the other hand, the presence of functional groups like -OH, -COOH, -Si-O groups make Laponite® and graphene oxide less conductive than multiwalled carbon nanotubes, which only has C-C, C=C and C-H functional groups. Because of this, even though all three different types of zein-nanocomposite (zein-Laponite®, zein-GO and zein-CNT) films exhibited conductive properties, the zein-carbon nanotube functionalized films had the highest electrochemical signal. The alkyl groups of zein formed thiol bonding with the -SH groups of 11-MUA at the initial stage of sensor fabrication. Cyclic voltammetry proved to be a highly sensitive technique, with a potential to be an on-field method with hand-held portable versions of potentiostats. The zein sensor platform was successful in detection of 0.5 ppm gliadin, with a detection range of 5 ppm -100 ppm, which is well below the FDA requirement for gluten free food (20 ppm). The fabricated biosensor was highly selective for gliadin, even at higher concentrations of interfering analytes like formamide, acrylamide, ovalbumin and lactalbumin. The sensor was stable for a four-week period time, which indicated fabrication of a successful stable, selective and sensitive biosensor platform, which can be extended to other matrices in different biosensors.

APPENDIX A FITTING OF FTIR CURVES

Step 1. Frist the full spectra for the film is obtained using the FTIR. The full spectra obtained for zein-0%Laponite nanocomposite film is shown below:

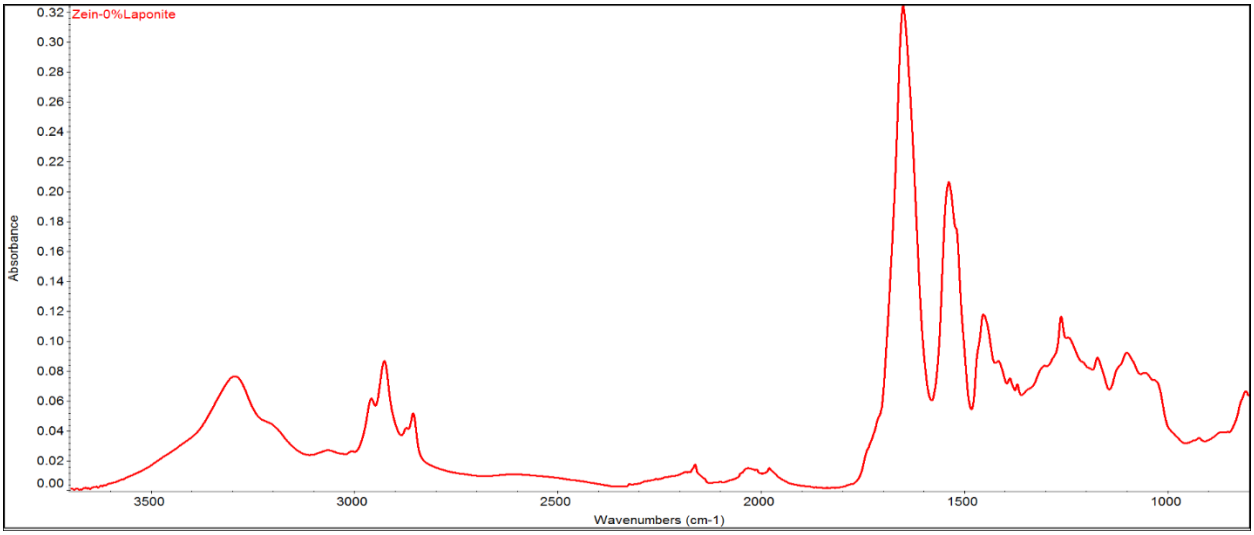

Step 2. Then to do the secondary structure analysis, the amide I region for protein, 1600-1700 cm^{-1} wavenumber is focused.

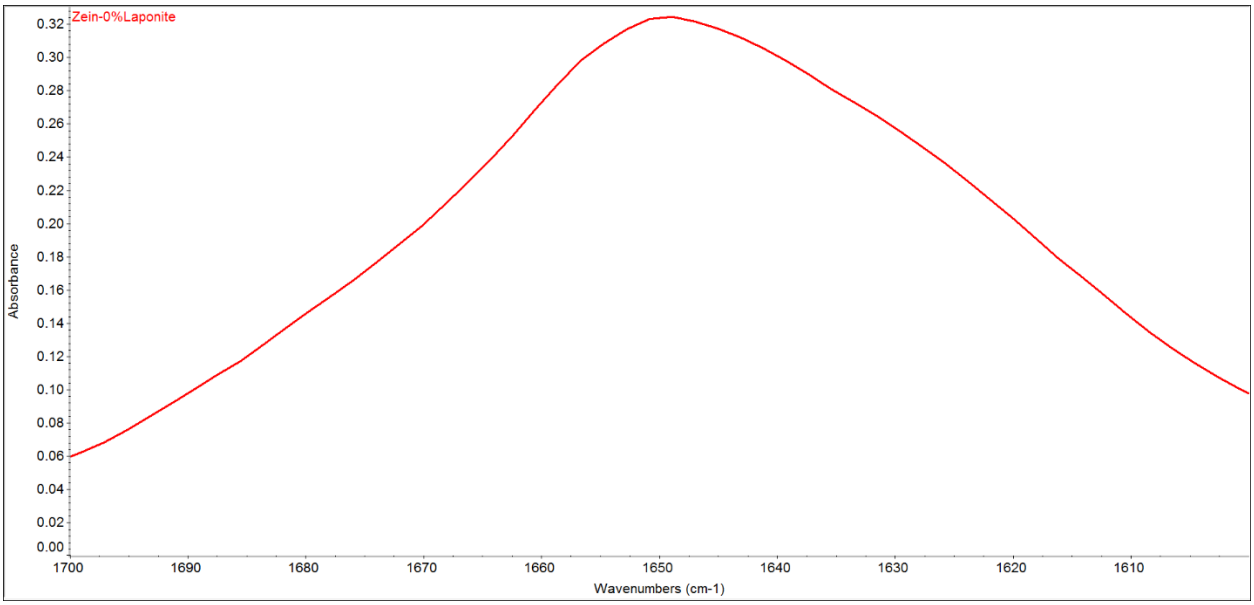

Step 3. Then Fourier self-deconvolution is used in that portion (1700 – 1600 cm^{-1} range), using the Omnic software.

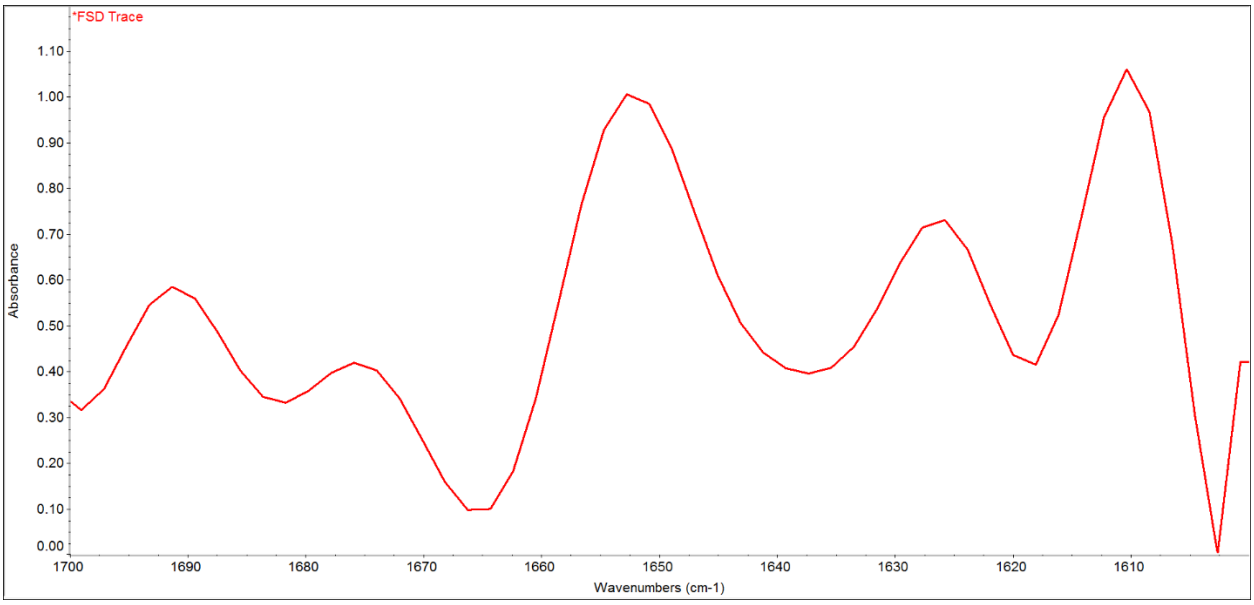

Step 4. The deconvoluted spectra is peak fitted using the 'Gaussian' peak fitting method, using the Omnic software, which gives 5-6 peaks.

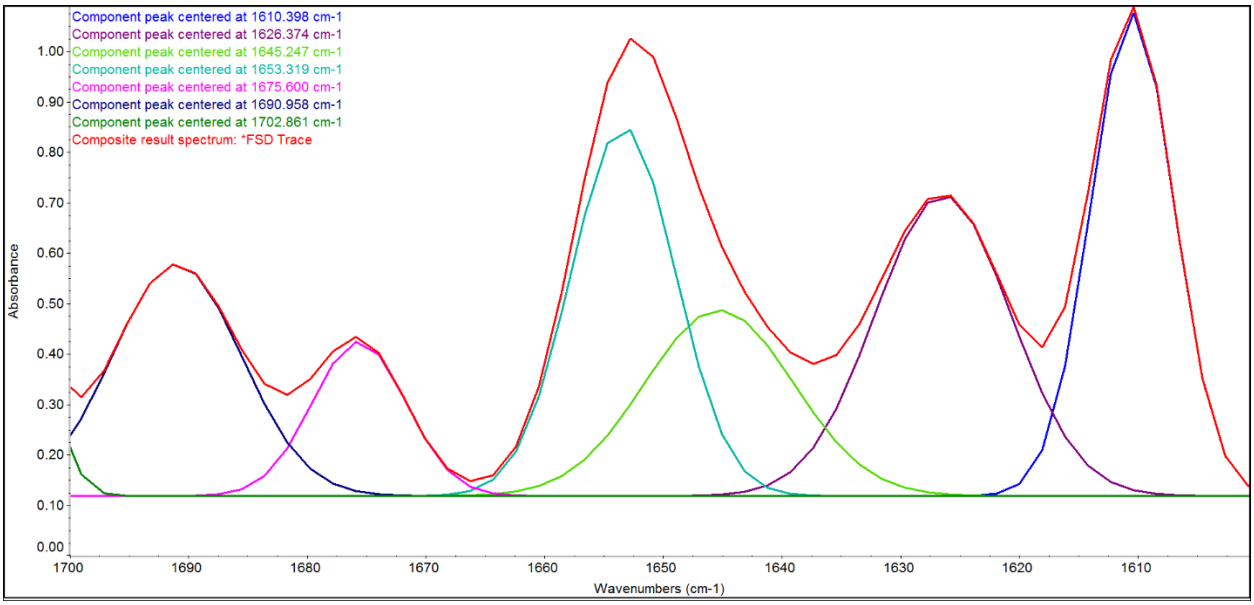

Step 5. Using the Omnic software, the height and area of each peak is calculated. According to the literature the peaks are assigned as α helix, β sheet, β turn, and the percentage of area under each peak is calculated. For Z-0%Laponite film, the % area under the peaks related to α helix, β sheet, β turn are shown below:

Peak #	Peak Type	Center X	Height	Area	%Area	Secondary Structure
1	Gaussian	1610.398	0.9595	8.4276	20.9933	β sheet
2	Gaussian	1626.374	0.5969	8.5426	21.2798	β sheet
3	Gaussian	1645.247	0.3689	5.8017	14.4521	α helix
4	Gaussian	1653.319	0.7331	8.0742	20.1130	α helix
5	Gaussian	1675.6	0.3066	3.0304	7.5488	β turn
6	Gaussian	1690.958	0.4603	6.2676	15.6127	β turn

APPENDIX B STRESS-STRAIN CURVES FOR Z-GO NANOCOMPOSITES

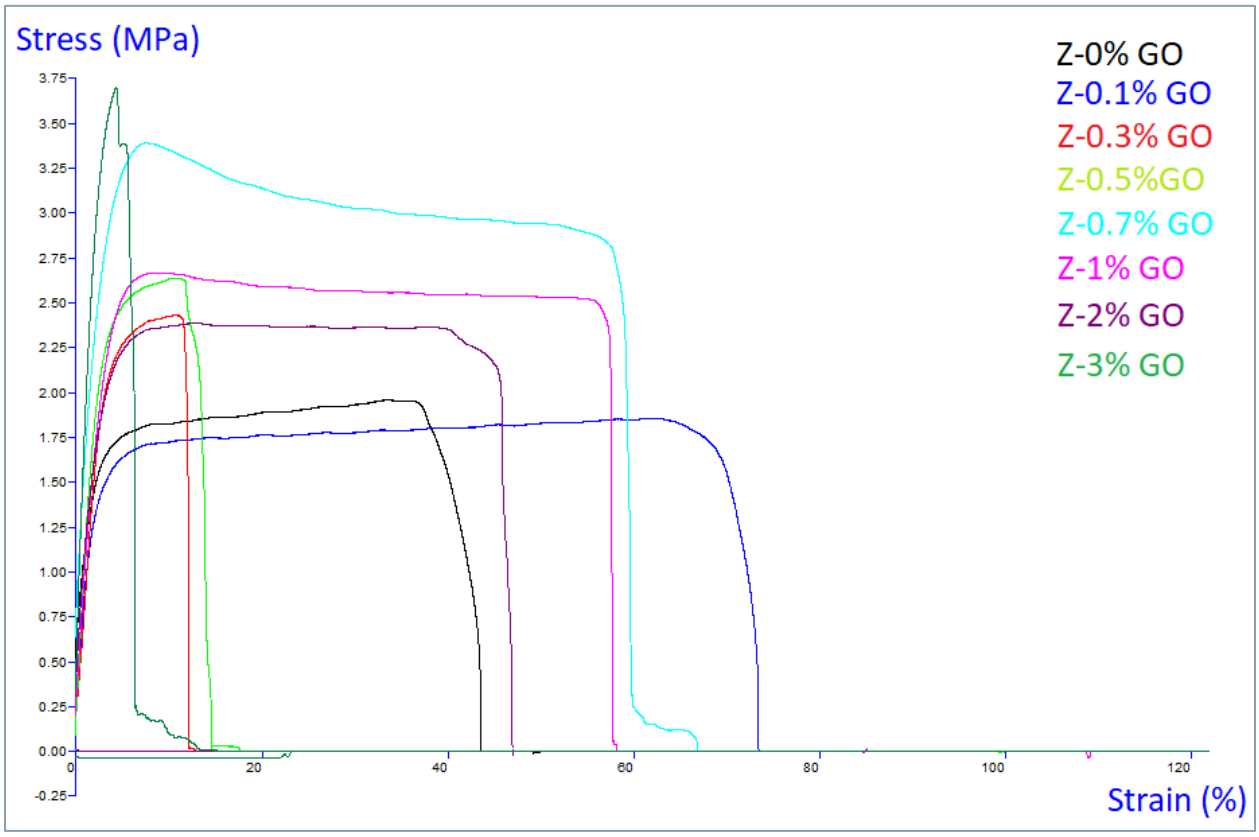

Fig. B-1 Stress-strain curves for zein-GO nanocomposites

APPENDIX C EFFECT OF THICKNESS ON SIGNAL INTENSITY

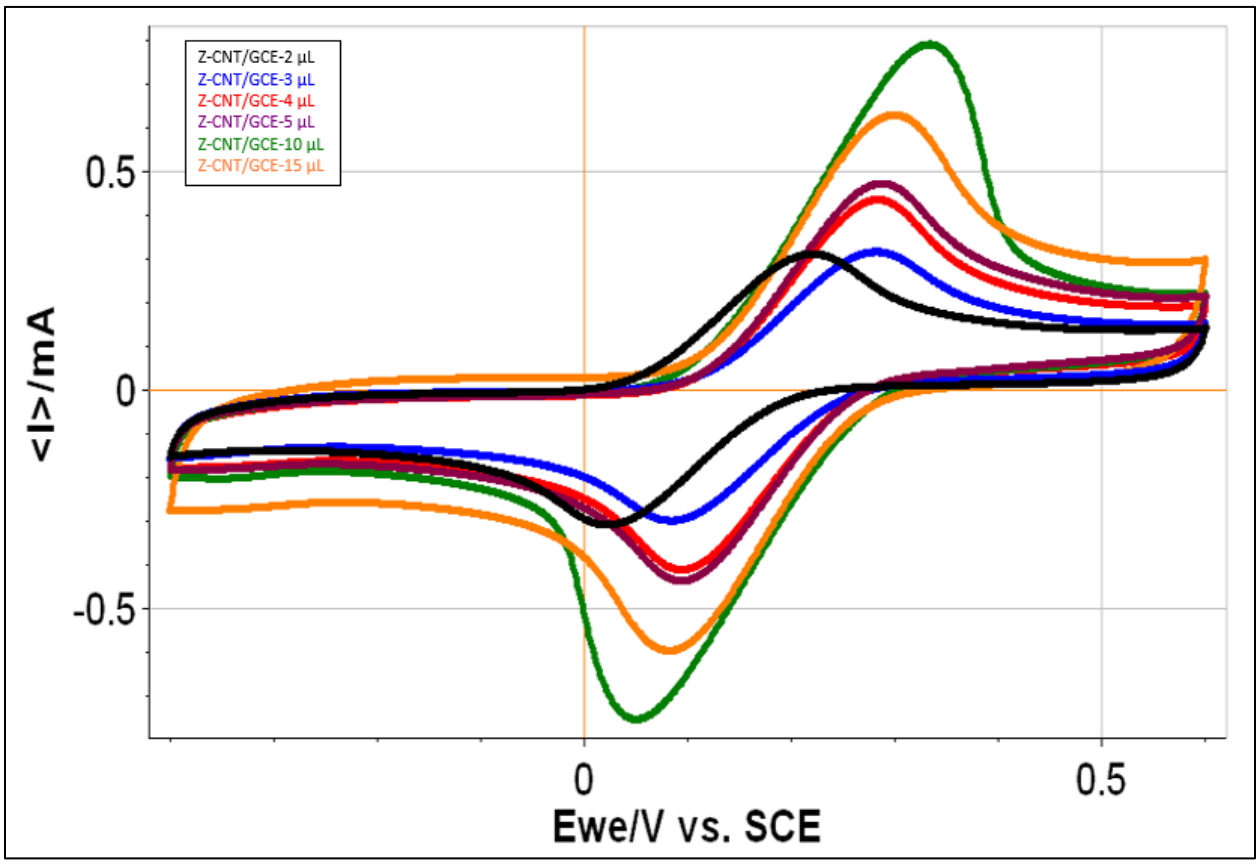

Fig. C-1. Cyclic voltammograms for different volumes of Z-CNT deposition for functionalization of glassy carbon electrode in in 5 mM $K_4[Fe(CN)_6]^{4-}/K_3[Fe(CN)_6]^{3-}$ at 50 and 100 mVs^{-1}.

APPENDIX D COMPARISON OF DIFFERENT SCAN RATES IN CV

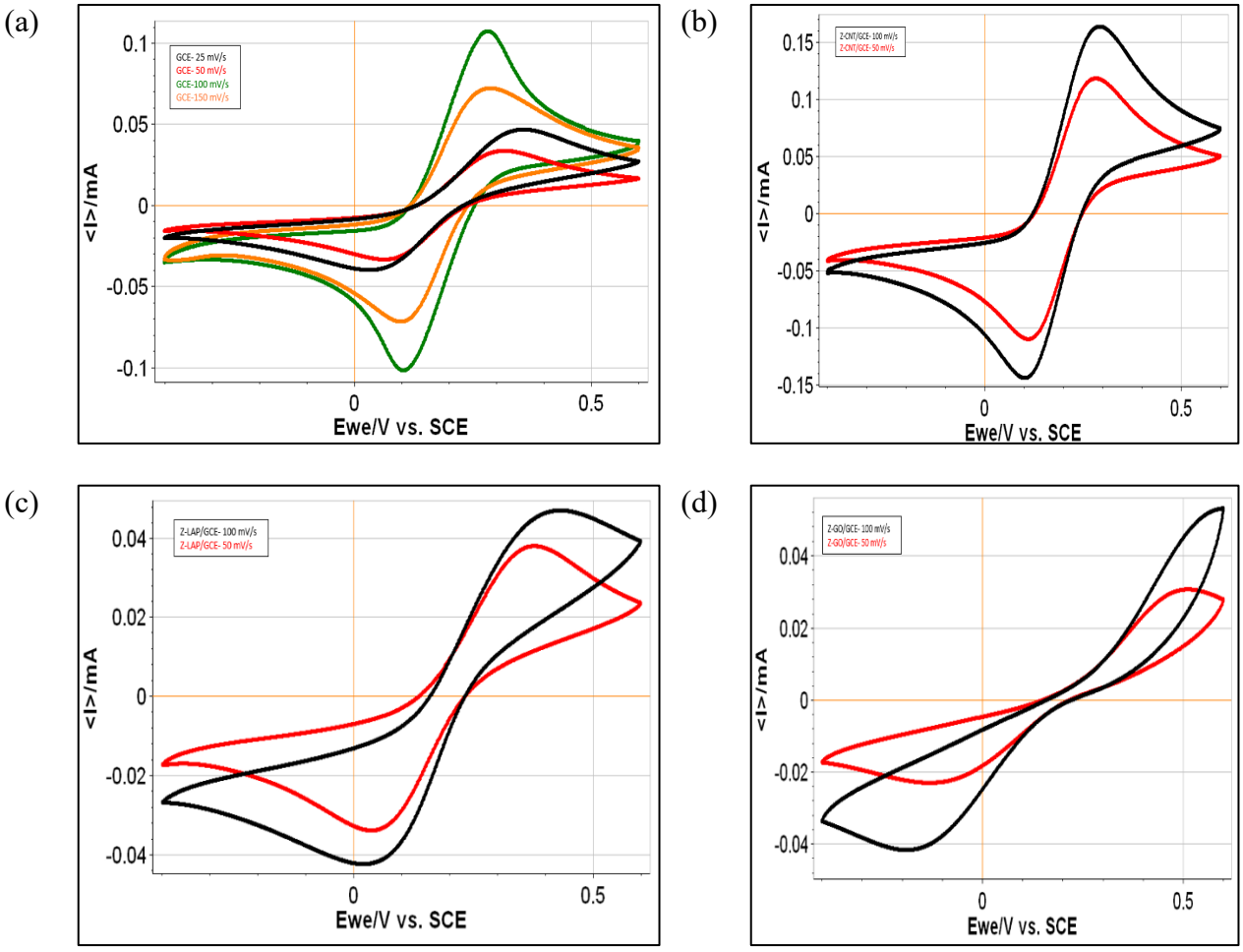

Fig. D-1. Cyclic voltammograms for (a) bare glassy carbon electrode (GCE) in 5 mM $K_4[Fe(CN)_6]^{4-}/K_3[Fe(CN)_6]^{3-}$ at 25, 50, 100 and 150 mVs^{-1}(b) Z-CNT functionalized electrode in 5 mM $K_4[Fe(CN)_6]^{4-}/K_3[Fe(CN)_6]^{3-}$ at 50 and 100 mVs^{-1} (c) Z-LAP functionalized electrode in 5 mM $K_4[Fe(CN)_6]^{4-}/K_3[Fe(CN)_6]^{3-}$ at 50 and 100 mVs^{-1} and (d) Z-GO functionalized electrode in 5 mM $K_4[Fe(CN)_6]^{4-}/K_3[Fe(CN)_6]^{3-}$ at 50 and 100 mVs^{-1}.

APPENDIX E PUBLISHED ABSTRACTS

Rouf, T. B., & Kokini, J. L. (2016). Biodegradable biopolymer–graphene nanocomposites. Journal of Materials Science, 51(22), 9915-9945.

Graphene's invention has catalyzed many new material applications in different fields. It has been used in combination with different biopolymers to design nanocomposites with improved mechanical, thermal, electrical, as well as, gas and water vapor barrier properties. This review focuses on the chemistry and synthesis of Graphene Oxide (GO) and sheds some light on the different ecological pathways available for graphene oxide synthesis and reduction. The major pathways for graphene incorporation into biopolymers include; 1) solution intercalation, 2) melt intercalation and 3) in situ polymerization. The fabrication, application and mechanisms of bonding between biodegradable biopolymers, like poly (lactic acid), cellulose, starch, chitosan, alginates, polyamides, and other biodegradable materials, with different forms of graphene including graphene oxide (GO), reduced graphene oxide (RGO), graphene nanoplatelets (GNP) etc. are the focus of this review. The paper has been organized according to different methods of incorporating graphene derivatives into biopolymers, in order to highlight the mechanisms for chemical bonding-physical changes that biopolymers and graphene nanofillers undergo during the method of preparation and the impact of chemical changes on end use properties. The information has been assembled, so that new conclusions can be drawn from the available data. The mechanism of enhancement of functional properties are evaluated using techniques including Fourier Transform Infrared Spectroscopy (FTIR), X-ray Diffraction (XRD), Raman, Scanning Electron Microscopy (SEM), Transmission Electron Microscopy (TEM), Atomic Force Microscopy (AFM) and the synergy resulting from the use of different spectroscopic techniques is discussed beyond what the individual authors have been able to interpret often from a few techniques. Effectiveness of solvents used, and reaction conditions have also been focused, in order to offer mechanistic understanding for the improvement of mechanical properties. The new observations and findings by comparing all relevant literature will help the reader to look at the whole spectrum of available methods and materials, in addition to focusing on the original biopolymer-graphene work.

Keywords Graphene ·Biopolymer · Poly (lactic Acid)· Starch · Cellulose · Chitosan · Alginate

Rouf TB, Schmidt G, Kokini JL (2018) Zein–Laponite nanocomposites with improved mechanical, thermal and barrier properties. J Mater Sci 1–16. https://doi.org/10.1007/s10853-018-2061-6

Zein, a prolamine of corn, is a bio-renewable resource that can potentially offer alternatives for petroleum-based polymers in many applications. Nanocomposite formation with addition of silicate nanoparticles (Laponite®) to zein films, cast from 70% ethanol solutions, significantly improved the mechanical, thermal and barrier properties. Based on FTIR findings, a mechanism for zein-Laponite® nanocomposite formation is proposed, which suggests Laponite® nanoparticles bind to zein molecules through Si-N bond formation. Structural characteristics investigated using AFM and TEM confirmed exfoliation of the nanoparticle. The changes in the surface energy of the films were evaluated using water contact angle measurements and showed increase in surface hydrophobicity. The Young's modulus and tensile strength increased with nanoparticle concentration. The glass transition temperature increased, and water vapor permeability decreased with only a small amount of Laponite®.

Keywords: Zein, Laponite®, TEM, FTIR, AFM, Water Vapor Permeability, DSC

Rouf TB, Schmidt G, Cakmak M, Kokini JL (2019) Design and mechanistic understanding of graphene oxide reinforced zein nanocomposites with improved mechanical, barrier and thermal properties. J Mater Sci 54:12533–12552. https://doi.org/10.1007/s10853-019-03817-w

Graphene oxide (GO)-based zein nanocomposite films with superior mechanical, barrier and thermal properties were fabricated by incorporating GO nanoparticles into corn protein zein (Z), through the solvent casting process. The study offers a mechanistic understanding of the effect of graphene oxide nanofiller on the physico-chemical properties of zein. TEM of the zein/graphene oxide (Z-GO) nanocomposites showed uniform dispersion of GO sheets up to 1%GO loading. Mechanisms for Z-GO nanocomposite formation through covalent and non-covalent bonding are developed based on FTIR, FT-Raman and DSC results. At only 3% loading, the Young's Modulus of a nanocomposite film increased by 300% and Tensile strength increased by 80%. The increases in mechanical property improvements are accompanied by surface roughness increases as indicated by AFM studies. Even though GO is hydrophilic, the Z-GO nanocomposite films showed hydrophobic tendencies. The amount and degree of exfoliation of GO as well as the relative orientation of GO nanoparticles within the zein film all play an important role in the physical property changes of the film. The films became less permeable with increasing amounts of GO addition, as shown by water vapor permeability tests. GO increased thermal stability as shown by TGA.

Keywords: Zein, GO, Packaging, TEM, FTIR, AFM, Water Vapor Permeability